Imperial College London

PhD Thesis

Role of phosphate and calcium in sol-gel bioactive glasses and silica/poly(caprolactone) hybrids

Hung-Kai Ting

November 2016

Department of Materials

Imperial College London

Declaration

I hereby certify that the work presented in this thesis is the result of my own investigations carried out at Imperial College London during the period from November 2012 to November 2016, except where otherwise stated.

The copyright of this thesis rests with the author and is made available under a Creative Commons Attribution Non-Commercial No Derivatives licence. Researchers are free to copy, distribute or transmit the thesis on the condition that they attribute it, that they do not use it for commercial purposes and that they do not alter, transform or build upon it. For any reuse or redistribution, researchers must make clear to others the licence terms of this work.

Hung-Kai Ting
November 2016

Abstract

There are currently no biomaterials that can 100% mimic the functions of living tissues. Sol-gel derived bioactive glasses (SiO_2-CaO-P_2O_5) bond with bone through formation of a hydroxycarbonate apatite (HCA) layer and are bioresorbable, releasing ions that can stimulate bone regeneration at genetic level. Here, structural analysis showed that hydroxyapatite (HA) formed within the glass, during sol-gel processing, due to orthophosphate units being formed after hydrolysis of the phosphate precursor.

The first aim was to produce a sol-gel bioactive glass that contains no pre-formed HA but with good bioactivity. Increasing the P_2O_5 to CaO ratio caused the formation of a phosphate glass network. Glass is brittle and cannot be used when a bone defect is subjected to cyclic loads. A second aim was to synthesise an inorganic/organic hybrid from the new sol-gel glass and polycaprolactone (PCL), which has lower stiffness and is bioresorbable. Calcium methoxyethoxide (CME) was investigated as an alternative precursor to incorporate calcium into the inorganic network of the hybrids at room temperature. The hybrid improved the mechanical properties over sol-gel glass. HCA formed on the surface of PCL hybrids just after 3 days of simulated body fluid (SBF) immersion. Cell culture study also showed the PCL hybrids could support good cell attachment and passed ISO standard cytotoxicity test. 3-D printing PCL hybrid scaffold was possible but challenging.

Acknowledgements

I would first like to express my deepest gratitude to my Supervisor, Prof. Julian Jones, for giving me the great opportunity to conduct my PhD in his lab. Throughout the time spent on of my PhD, Julian has always been thoughtful and provided experienced advices on my research. I would not have completed my PhD without his continuous support.

Secondly I wold like to thank a number of people for their generous assistance and advice during my PhD: Dr. John Hanna and Sam Page from University of Warwick for performing the solid state MAS-NMR and the help with the NMR data interpretation; Dr. Shu Chen from Imperial College London for taking TEM images of my sol-gel glass samples; Francesca Tallia from Imperial College London for the help with PCL hybrid synthesis and for providing helpful advice and knowledge of characterising the hybrid materials; Dr. Siwei Li from Imperial College London for conducting cell culture study on my hybrid materials; Xiaomeng Shi from Imperial College London for performing μCT on my 3D hybrid scaffolds. A very special thanks goes to Dr. Gowsihan Poologasundarampillai for welcoming me into the group and teaching me how to make sol-gel derived glass.

Finally, I would like to thank my mother for her endless support, both financially and psychologically, without her I would not have made it this far.

Contents

Declaration 2
Abstract 3
Acknowledgements 4
Contents 5
List of Figures 10
List of Table 20
List of abbreviations 22
1 Introduction 25
2 Literature review 27
2.1 Human bone 27
2.2 Bioactive ceramics and glasses 29
2.2.1 Introduction 29
2.2.2 Synthetic hydroxyapatite 30
2.2.3 Phosphate glasses 30
2.2.4 Melt-derived bioactive silicate glass 31
2.3 Sol-gel process and sol-gel derived bioactive glasses 34
2.3.1 Introduction 34
2.3.2 Mixing and gelation at room temperature 36
2.3.3 Aging of silica gels 39
2.3.4 Drying 40
2.3.5 Stabilisation and sintering of the silica gel 41
2.3.6 Calcium and phosphate incorporation into sol-gel derived glass 42
2.3.7 Sol-gel derived phosphate glass 43
2.4 HCA formation and glass bioactivity 45
2.5 Porous bioactive scaffolds 48
2.5.1 Introduction 48
2.5.2 Melt-derived bioactive glass scaffolds 48
2.5.3 Sol-gel derived bioactive foam scaffolds 50
2.6 Sol-gel bioactive organic/inorganic hybrids 52
2.6.1 Introduction 52
2.6.2 Class I hybrids 54
2.6.3 Strategies for Class II hybrids synthesis 54

2.6.4 Organic polymers for bioactive hybrids 57
2.6.5 Poly(ε-caprolactone) 62
2.6.6 Poly(tetrahydrofuran) 65
2.6.7 Calcium source for bioactive sol-gel hybrid 65
2.7 Objectives of the thesis 67
3 Characterisation methods 68
3.1 Particle size measurement 68
3.2 Nitrogen sorption: Surface area and pore size distribution 69
3.3 SBF dissolution and bioactivity 72
3.4 XRD 74
3.5 FTIR 75
3.6 Scanning electron microscope 75
3.7 Transmission electron microscope 76
3.8 Nuclear Magnetic Resonance 77
3.9 TGA/DSC 79
3.10 TRIS degradation study of PCL hybrids 79
3.11 Compression test 80
3.12 X-ray micro-computed tomography 81
4 Silicate based sol-gel glass containing phosphate 82
4.1 Introduction 82
4.2 Materials and methods 83
4.2.1 Materials 83
4.2.2 Synthesis of phosphate containing sol-gel glasses 83
4.2.3 Characterisation techniques 85
4.3 Results 86
4.3.1 Glass appearance 86
4.3.2 Nitrogen sorption 87
4.3.3 Particle sizes of TEP glass powders 90
4.3.4 SBF dissolution 91
4.3.5 FTIR-ATR 95
4.3.6 XRD 98
4.3.7 SEM 100
4.3.8 TEM 102

4.3.9 Solid state MAS-NMR 103
4.4 Discussion 106
4.4.1 Effect of phosphate (TEP) content on the structure of bioactive glass 106
4.4.2 Effect of water contact on the properties of bioactive glass 107
4.5 Conclusions 108
5 Sol-gel glass synthesised with alternative phosphate sources 109
5.1 Introduction 109
5.2 Materials and methods 110
5.2.1 Materials 110
5.2.2 Synthesis of sol-gel glasses with DEPETES and TBP 110
5.2.3 Characterisation techniques 111
5.3 Results 112
5.3.1 Glass appearance 112
5.3.2 Nitrogen sorption 112
5.3.3 Particle size of glass powder 115
5.3.4 SBF dissolution 116
5.3.5 FTIR of sol-gel glass made with different phosphate precursors 118
5.3.6 XRD 121
5.3.7 SEM 122
5.3.8 Solid state MAS-NMR 123
5.4 Discussion 125
5.4.1 Properties of DEPETES glass 125
5.4.2 Phosphate incorporation into silica network from DEPETES 125
5.5 Conclusions 128
6 Low temperature sol-gel derived bioactive glass 129
6.1 Introduction 129
6.2 Materials and method 130
6.2.1 Materials 130
6.2.2 CME preparation 130
6.2.3 Sample preparation 130
6.2.4 Characterisation techniques 132
6.3 Results 133
6.3.1 SBF dissolution of samples synthesised at 60°C 133

6.3.2 FTIR of sol-gel glasses/gels made with CME and DEPETES 135
6.3.3 XRD of sol-gel glasses/gels made with CME and DEPETES 136
6.3.4 Solid state MAS-NMR 137
6.4 Discussion 141
6.5 Conclusions 142
7 Calcium containing PCL hybrids 143
7.1 Introduction 143
7.2 Materials and methods 144
7.2.1 Materials 144
7.2.2 PCL diol oxidation 144
7.2.3 PCL hybrid preparation 146
7.2.4 3D printing 149
7.2.5 Cell culture study of PCL hybrids 150
7.2.6 Characterisation techniques 152
7.3 Results 153
7.3.1 Apatite formation on inorganic synthesised at low temperature 153
7.3.2 TGA-DSC 154
7.3.3 Compression test 155
7.3.4 SBF dissolution 162
7.3.5 TRIS degradation study 165
7.3.6 FTIR 167
7.3.7 XRD 170
7.3.8 Solid state MAS-NMR 172
7.3.9 Cell culture study 173
7.3.10 3D printing 175
7.3.11 SEM images of PCL hybrid powder particles 180
7.4 Discussion 182
7.4.1 Properties of calcium containing PCL hybrids 182
7.4.2 The role of calcium and phosphate in PCL hybrids 182
7.5 Conclusions 184
8 Conclusions and further work 185
8.1 Conclusions 185
8.2 Further work 187

9 Reference 188

List of Figures

Figure 2.1 Hierarchical structure of human bone (adapted from [1]). 27

Figure 2.2 the schematic of silica glass network formation (adapted from [18]). 29

Figure 2.3 Schematic of phosphate glass structure with additional network modifiers, Ca^{2+} and Na^{+} (adapted from [29]). 31

Figure 2.4 Bioactive map of melt-derived glass composition (in wt%) in the Na_2O-CaO-P_2O_5-SiO_2 system (all glasses in the diagram contain 6 wt% P_2O_5) [38]. 32

Figure 2.5 A flow chart of sol-gel process (adapted from [18] and [43]). 35

Figure 2.6 The hydrolysis of tetraethyl orthosilicate (TEOS) 36

Figure 2.7 Polycondensation of silicate tetrahedra to form silicate nanoparticles. 36

Figure 2.8 The mechanism of (a) acid-catalysed hydrolysis (b) base-catalysed hydrolysis [56]. 37

Figure 2.9 Schematic representation of acid-catalysed gel and base-catalysed gel (adapted from [57]). 37

Figure 2.10 Schematic of syneresis during aging [55]. 39

Figure 2.11 Schematic of a growing interparticle neck by coarsening [55]. 40

Figure 2.12 Schematic of cation exchange [20]. 45

Figure 2.13 Hydrolysis reaction of a Si-O-Si bond. 46

Figure 2.14 Condensation reaction of neighbouring Si-OH and form a SiO_2 rich layer. 46

Figure 2.15 Schematic of space holder method for melt derived glass scaffold [108]. 48

Figure 2.16 Schematic of gel-cast foaming of melt derived glass scaffold [108]. 49

Figure 2.17 A schematic of the sol-gel foaming process [107]. 51

Figure 2.18 Schematic of a conventional bioactive composite..... 52

Figure 2.19 Schematic of an organic/inorganic Class II hybrid material. 53

Figure 2.20 Chemical structure of PDMS..... 55

Figure 2.21 The chemical structures of commonly used coupling agents for Class II silica/polymer hybrid synthesis: GPTMS, ICPTES and APTES. 55

Figure 2.22 Chemical structure of bacterial synthesised γ-PGA. 59

Figure 2.23 Chemical structures of poly(lactic acid), poly(glycolic acid) and poly(lactide-co-glycolide). 61

Figure 2.24 Schematic of functionalisation of PCL diol with ICPTES for silica/PCL hybrid synthesis [150]. 63

Figure 3.1 Diagram of Mastersizer 2000E (adapted from the user manual of Mastersizer)..... 69

Figure 3.2 Different types of isotherms (adapted from [174])..... 70

Figure 3.3 Different types of hysteresis loops (adapted from [174])..... 71

Figure 3.4 Photography of compression test of a cylindrical silica/PCL hybrid monolith. 80

Figure 4.1 The chemical structure of TEP. 83

Figure 4.2 Appearance of sol-gel glasses made with 12R water ratio at (a) 4, (b) 8, (c) 12 and (d) 24 mol% P_2O_5, and the sol-gel glasses made with 4R water ratio at (e) 4, (f)8, (g)12 and (h) 24 mol% P_2O_5. (i) sol-gel glass made into disc shape with 4R water ratio at 24mol% P_2O_5. 86

Figure 4.3 Nitrogen adsorption-desorption isotherms of (a) sol-gel glasses made with 12R water ratio at 4, 8, 12 and 24 mol% P_2O_5 (b) sol-gel glasses made with 4R water ratio at at 4, 8, 12 and 24 mol% P_2O_5. 88

Figure 4.4 The pore size distributions of (a) sol-gel glasses made with 12R water ratio at 4, 8, 12 and 24 mol% P_2O_5 (b) sol-gel glasses made with 4R water ratio at at 4, 8, 12 and 24 mol% P_2O_5. 89

Figure 4.5 pH change profile of (a) sol-gel glasses made with 12R water ratio at 4, 8, 12 and 24 mol% P_2O_5 (b) sol-gel glasses made with 4R water ratio at at 4, 8, 12 and 24 mol% P_2O_5. 92

Figure 4.6 ICP profile of sol-gel glasses made with 12R water ratio at 4, 8, 12 and 24 mol% P_2O_5 (a) for 2 weeks (b) for the first 24 h of SBF dissolution. 94

Figure 4.7 SBF dissoluton profile of sol-gel glasses made with 4R water ratio at 4, 8, 12 and 24 mol% P_2O_5. 95

Figure 4.8 The FTIR spectra of sol-gel glasses made with 12R water ratio at (a) 4 (b) 8 (c) 12 and (d) 24 mol% P_2O_5 at different time point of SBF dissolution..... 97

Figure 4.9 The FTIR spectra of sol-gel glasses made with 4R water ratio at 4, 8, 12 and 24 mol% P_2O_5 after stabilisation..... 98

Figure 4.10 XRD patterns of sol-gel glasses made with 12R water ratio at (a) 4, (b) 8, (c) 12 and (d) 24 mol% P_2O_5 at different time point of SBF dissolution. 99

Figure 4.11 XRD patterns sol-gel glasses made with 4R water ratio at 4, 8, 12 and 24 mol% P_2O_5 after stabilisation..... 99

Figure 4.12 SEM images of TEP sol-gel glasses made with 12R water ratio at (a) 4, (b) 8, (c) 12 and (d) 24 mol% P_2O_5 after stabilisation..... 101

Figure 4.13 SEM images of TEP sol-gel glasses made with 12R water ratio at (a) 4 mol% (b) 8 mol% (c) 12 mol% and (d) 24 mol% P_2O_5 after 2 weeeks of SBF immersion. 101

Figure 4.14 SEM images of TEP sol-gel glasses made with 12R water ratio at (a) 4 mol% and (b) 8 mol% P_2O_5 after 8 h of SBF immersion. 102

Figure 4.15 Analytic TEM characterisation of TEP24p12r, the sol-gel glasses made with 12R water ratio at 24 mol% P_2O_5, heated at 700 C for X h. (a) a low magnification

bright field TEM (BFTEM) image reveals the presence of porous and film like structures in the sample. (b) a magnified BFTEM image further shows the morphology of the porous materals. (c, d) high resolution TEM (HRTEM) analysis of the porous and film like materials, respectively. Inserts in (c and d) show halo fast Fourier transform (FFT) patterns collected from the dashed boxed areas, respectively, indicate the amorphous nature of both the porous and film like materials. Representative STEM-EDS spectra collected from (e) the porous and (f) film like materials. (g) HAADF-STEM imag shows a porous particle sitting on the film like materials and the corresponding (h) STEM-EDS mapping of the boxed area in (g). 103

Figure 4.16 Solid state (a) ^{29}Si NMR (b) ^{31}P NMR of TEP sol-gel glasses made with 12R water ratio at 4, 8, 12 and 24 mol% P_2O_5 after stabilisation. 104

Figure 5.1 Chemical structure of (a) DEPETES (b) TBP. 110

Figure 5.2 The appearnce of sol-gel glass made with DEPETES at (a) 4 mol % (b) 8 mol% P_2O_5 and sol gel glass made with TBP at (c) 4 mol% (b) 8 mol% (e) 12 mol% (f) 24 mol % P_2O_5 after stabilisation at 700°C. 112

Figure 5.3 Nitrogen adsorption-desorption isotherms of sol-gel glass made with (a) DEPETES at 4 mol % and 8 mol% P_2O_5 (b) sol gel glass made with TBP at 4, 8, 12 and 24 mol % P_2O_5 after stabilisation at 700°C. 113

Figure 5.4 Pore size distributions of (a) sol-gel galsses made with DEPETES at 4 and 8 mol% P_2O_5 (b) sol-gel glasse made with TBP at 4, 8, 12 and 24 mol% P_2O_5. 114

Figure 5.5 pH change profile of of sol-gel glasses made with (a) DEPETES at 4 and 8 mol% P_2O_5 (b) TBP at 4, 8, 12 and 24 mol% P_2O_5. 116

Figure 5.6 ICP dissolution profiles of sol-gel glasses made with (a) DEPETES at 4 and 8 mol% P_2O_5 (b) TBP at 4, 8, 12 and 24 mol% P_2O_5. 118

Figure 5.7 FTIR spectra of sol-gel glasses made with DEPETES at (a) 4 mol% and (b) 8 mol% P_2O_5 at different time point of SBF dissolution. 120

Figure 5.8 FTIR spectra of sol-gel glasses made with TBP at 4, 8, 12 and 24 mol% P_2O_5 after stabilisation at 700°C. 120

Figure 5.9 XRD patterns of (a) DEPETES4p (b) DEPETES8p at different time points of SBF dissolution.....121

Figure 5.10 XRD patterns of sol-gel glasses made with TBP at 4, 8, 12, 24 mol% P_2O_5 after stabilisation at 700^oC.....122

Figure 5.11 SEM images of sol-gel glasses made with DEPETES at (a) 4 mol% (b) 8 mol% P_2O_5 after stabilisation (c) 4 mol% (d) 8mol%P_2O_5 after 8 h of SBF immersion (e) 4 mol% (f) 8 mol% P_2O_5 after 2 weeks of SBF immersion. 123

Figure 5.12 Solid state of DEPETES glasses (a) ^{29}Si NMR (b) ^{31}P NMR. 124

Figure 5.13 Incorporation of DEPETES into the silica glass network at room temperature. 126

Figure 5.14 Hydrolysis of phosphonate end of DEPETES and condensation reaction between two phosphonates. 127

Figure 6.1 Schematic of the reaction between calcium and 2-Methoxythanol.....130

Figure 6.2 Photograph of CME DEP4p 60c in SBF. 133

Figure 6.3 ICP SBF dissolution profile of the gels which contain 4 and 8 mol% of P_2O_5 made with CME and DEPETES at synthesis temperature of 60^oC. 134

Figure 6.4 pH change profile of the gels which contain 4 and 8 mol% P_2O_5.....134

Figure 6.5 FTIR spectra of (a) CME DEP 4p 60c before SBF (b) CME DEP8p 60c before SBF (c) CME DEP 4p 60c after 2 weeks of SBF dissolution (d) CME DEP 8p 60c after 2weeks of SBF dissolution. 135

Figure 6.6 FTIR spectra of CME DEP 4p glasses with different synthesis temperatures before SBF dissolution (a) CME DEP 4p 60c (b) CME DEP 4p 130c (c) CME DEP 4p 700c.....136

Figure 6.7 XRD patterns of (a) CME DEP 4p (b) CME DEP 8p glasses with different synthesis temperatures, 60^oC, 130^oC and 700^oC, before SBF dissolution.....137

Figure 6.8 XRD patterns of CME DEP 4p 60c and CME DEP 8p 60c after 2weeks of SBF dissolution. 137

Figure 6.9 Solid state ^{29}Si NMR for (a) CME DEP 4p (b) CME DEP 8p with different synthesis temperatures, 60ºC, 130ºC and 700ºC. 138

Figure 6.10 Solid state ^{31}P NMR for (a) CME DEP 4p samples (b) CME DEP 8p samples with different synthesis temperatures, 60ºC, 130ºC and 700ºC..... 140

Figure 7.1 Anelli's TEMPO catalysed oxidation mechanism (adapted from [209]). 145

Figure 7.2 Schematic of the PTFE mold for PCL hybrid aging and drying; and a photograph of the PTFE insert within a PMP mold during ageing..... 147

Figure 7.3 Mechanism of THF polymerisation [170]. 148

Figure 7.4 Hypothesised reaction mechanism of (a) THF polymerisation terminated by PCL-diCOOH (b) PCL-diCOOH compete with THF for GPTMS [170]..... 149

Figure 7.5 Schematic of the 3D grid like structure printing design. 149

Figure 7.6 XRD patterns of (a) 6040 glass 60c before SBF (b) CME TEP 4p 60c before SBF (c) 6040 glass 60c after 2weeks (d) CME TEP 4p 60c after 2 weeks of SBF dissolution. 153

Figure 7.7 FTIR spectra of (a) 6040 glass 60c before SBF (b) CME TEP 4p 60c before SBF (c) 6040 glass 60c after 2weeks (d) CME TEP 4p 60c after 2 weeks of SBF dissolution. 154

Figure 7.8 TGA and DSC curves of (a) 6040 PCL (b) TEP4p PCL (c) TEP8p PCL (d) TEP12p PCL. All PCL hybrids in this figure were made with a TEOS/PCL wt ratio of 80:20 (2.14 ml of TEOS and 500 mg of PCL diCOOH in 5 ml of THF) and the corresponding amount of CME and TEP.6040 PCL was synthesised by incorporating the silica glass of chemical composition 60 mol% SiO_2 and 40 mol% CaO into PCL (500 mg of PCL in 5 ml of THF) to make a hybrid, TEPXp PCL was synthesised by incorporating a silica glass of 60 mol% SiO_2 (from 2.14 ml TEOS), X mol% of P_2O_5

and (40-X) mol% of CaO into PCL hybrid (500 mg of PCL diCOOH in 5 ml of THF). 155

Figure 7.9 Compression test curves of pure 6040 glass (60 mol% SiO_2 and 40 mol% CaO) which was 100% inorganic, 6040 PCL hybrid made with 20wt% PCL (500 mg of PCL), 80wt% TEOS (2.14 ml of TEOS) and corresponding amount of CME (the hybrid contained 29.2 wt% of inorganic) and 6040 PCL hybrid made with 10 wt% PCL (500 mg of PCL), 90wt% TEOS (4.815 ml of TEOS) and corresponding amount of CME (the hybrid contained 50.4 wt% of inorganic). 6040 PCL was synthesised by incorporating the silica glass of chemical composition 60 mol% SiO_2 (from 2.14 ml or 4.815 ml of TEOS) and 40 mol% CaO (from the corresponding amount of CME) into PCL hybrid (500 mg of PCL diCOOH in 5 ml of THF). 156

Figure 7.10 Compression curves of calcium containing PCL hybrid monoliths (cylindrical) made in this work and CME free PCL hybrid monolith from Francesca Tallia. All PCL hybrids in this figure were made with a TEOS/PCL wt ratio of 80:20 (2.14 ml of TEOS and 500 mg of PCL diCOOH in 5ml of THF) and the corresponding amount of CME and TEP. The true inorganic/organic ratio difference between the calcium containing PCL hybrids used in the compression test was smaller than 1wt%, all of them contained 29 wt% to 30 wt% of inorganic. 6040 PCL was synthesised by incorporating the silica glass of chemical composition 60 mol% SiO_2 (from 2.14 ml of TEOS) and 40 mol% CaO into PCL hybrid (500 mg of PCL in 5 ml of THF), TEPXp PCL was synthesised by incorporating a silica glass of 60 mol% SiO_2 (from 2.14 ml TEOS), X mol% of P_2O_5 and (40-X) mol% of CaO into PCL hybrid (500 mg of PCL diCOOH in 5 ml of THF) 158

Figure 7.11 Cyclic loading stress-strain curves for 6040 PCL hybrid cylindrical monoliths. In each of the 10 cycles the 6040 PCL cylindrical monolith was compressed up to 10% of their initial height. 159

Figure 7.12 Cyclic loading stress-strain curves for 6040 PCL hybrid cylindrical monoliths. In each of the 10 cycles the 6040 PCL cylindrical monolith was compressed up to 20% of their initial height. 160

Figure 7.13 Cyclic loading stress-strain curves for 6040 PCL hybrid cylindrical monoliths. In each of the 10 cycles the 6040 PCL cylindrical monolith was compressed up to 30% of their initial height. 162

Figure 7.14 pH change profile of PCL hybrids made by incorporating different glass compositions into PCL hybrids. 6040 PCL was synthesised by incorporating the silica glass of chemical composition 60 mol% SiO_2 (from 2.14 ml of TEOS) and 40 mol% CaO into PCL hybrid (500 mg of PCL diCOOH in 5 ml of THF), TEPXp PCL was synthesised by incorporating a silica glass of 60 mol% SiO_2 (from 2.14 ml TEOS), X mol% of P_2O_5 and (40-X) mol% of CaO into PCL hybrid (500 mg of PCL diCOOH in 5 ml of THF). 163

Figure 7.15 ICP SBF dissolution profiles of 6040 PCL, TEP4p PCL, TEP8p PCL and TEP12p PCL. 6040 PCL was synthesised by incorporating the silica glass of chemical composition 60 mol% SiO_2 (from 2.14 ml of TEOS) and 40 mol% CaO into PCL hybrid, TEPXp PCL was synthesised by incorporating a silica glass of 60 mol% SiO_2 (from 2.14 ml TEOS), X mol% of P_2O_5 and (40-X) mol% of CaO into PCL hybrid (500 mg of PCL diCOOH in 5 ml of THF). 165

Figure 7.16 Diagram for TRIS buffer dissolution of PCL hybrids (a) 6040 PCL (b) TEP4p PCL (c) TEP8p PCL (d) TEP12p PCL. 6040 PCL was synthesised by incorporating the silica glass of chemical composition 60 mol% SiO_2 (from 2.14 ml of TEOS) and 40 mol% CaO (from the corresponding amount of CME) into PCL (500 mg of PCL in 5 ml of THF) hybrid, TEPXp PCL was synthesised by incorporating a silica glass of 60 mol% SiO_2 (from 2.14 ml TEOS), X mol% of P_2O_5 and (40-X) mol% of CaO into PCL hybrid (500 mg of PCL diCOOH in 5 ml of THF). 166

Figure 7.17 FTIR spectra of (a) 6040 PCL (b) TEP4p PCL (c) TEP8p PCL (d) TEP12p PCL at differnet time points of SBF dissolution. 6040 PCL was synthesised by incorporating the silica glass of chemical composition 60 mol% SiO_2 (from 2.14 ml of TEOS) and 40 mol% CaO (from the corresponding amount of CME) into PCL (500 mg of PCL in 5 ml of THF) hybrid, TEPXp PCL was synthesised by incorporating a silica glass of 60 mol% SiO_2 (from 2.14 ml TEOS), X mol% of P_2O_5 and (40-X) mol% of CaO into PCL hybrid (500 mg of PCL diCOOH in 5 ml of THF). 169

Figure 7.18 FTIR spectra of calcium free PCL hybrid (500 mg of PCL + 2.14 ml of TEOS) before and after 2 weeks of SBF dissolution 170

Figure 7.19 XRD patterns of (a) 6040 PCL (b) TEP4p PCL (c) TEP8p PCL (d) TEP12p PCL at differnet time point of SBF dissolution. 6040 PCL was synthesised by incorporating the silica glass of chemical composition 60 mol% SiO_2 (from 2.14 ml of TEOS) and 40 mol% CaO (from the corresponding amount of CME) into PCL (500 mg of PCL in 5 ml of THF) hybrid, TEPXp PCL was synthesised by incorporating a silica glass of 60 mol% SiO_2 (from 2.14 ml TEOS), X mol% of P_2O_5 and (40-X) mol% of CaO into PCL hybrid (500 mg of PCL diCOOH in 5 ml of THF). 171

Figure 7.20 XRD patterns of calcium free PCL hybrid (500 mg of PCL + 2.14 ml of TEOS) before and after 2 weeks of SBF dissolution. 171

Figure 7.21 Solid state (a) ^{29}Si NMR (b) ^{31}P NMR of the PCL hybrids..... 172

Figure 7.22 Metabolic activity of the preosteoblst cells after 24 hours of incubation with the dissolution products of each PCL hybrid. 174

Figure 7.23 Confocal microscopy images of the preosteoblast cells cultured on the surface of (a) 6040 PCL (b) TEP4p PCL (c) TEP8p PCL (d) TEP12p PCL. 175

Figure 7.24 Photograph taken during 3D printing. 176

Figure 7.25 Low magnification SEM images of 6040 PCL 3D printing scaffold with 3D printing setting: Z space: 0.18mm, horizontal/vertical road width: 0.8mm and printing speed: 10mm taken from (a) bottom (b) horizontal section (c) Top (d) vertical section of the scaffold. 178

Figure 7.26 Micro CT 3D image of a 3D printing scaffold with the following print setting: Z space: 0.18mm, Horizontal/vertical road width: 0.8mm and printing speed: 15mm s^{-1}. (a) whole scaffold (b) 1.8mmX1.8mmX1.8mm cube cropped from the inside the scaffold. 150X150X150 voxels, voxel size:12µm. 179

Figure 7.27 Compression curves of scaffolds with the print setting (a) Z space: 0.18mm, Horizontal/vertical channel width: 0.8mm (b) Z space: 0.18mm, Horizontal/vertical channel width: 1mm. 180

Figure 7.28 SEM images of (a) 6040 PCL (b) TEP4p PCL (c) TEP8p PCL (d) TEP12p PCL before SBF dissolution. 181

Figure 7.29 SEM images of (a) 6040 PCL before SBF dissolution; (b, c, d) 6040 PCL after 2 weeks of SBF dissolution. 181

List of Table

Table 2.1 The mechanical properties of cortical and trabecular bone [1]. 28

Table 3.1 The ingredients for 2000ml of SBF [178]. 73

Table 4.1 Chemical compositions of phosphate containing glasses made with TEP. . 84

Table 4.2 Modal pore sizes and surface areas of TEP bioactvive glasses. 90

Table 4.3 The particle sizes distribution if each TEP glass composition after grinding and sieving. 91

Table 4.4 wt% of calicum released from sol-gel glasses made with 12R water ratio at 4, 8, 12 and 24 mol% P_2O_5 within the first 30 mintues of SBF dissolution (Assuming calcium deposition started after 30 minutes of dissolution). 94

Table 4.5 The Q^n structures distributions and the degree of condensations of TEP sol-gel glassed made with 12R water ratio at 4, 8, 12, 24 mol% P_2O_5. 105

Table 5.1 Chemical compositions of phosphate containing glasses made with TBP and DEPETES. 111

Table 5.2 Surface areas of DEPETES glasses and TBP glasses. 115

Table 5.3 Particle size distribution of DEPETES glasses after grinding and sieving with a 38 μm sieve. 115

Table 5.4 The Q^n distributions and degree of condenstation of silica network in DEPETES glasses determined from ^{29}Si MAS-NMR spectra analysis. 124

Table 6.1 Chemical compositions and synthesis temperature of samples synthesised with CME and DEPETES. 131

Table 6.2 Chemical shift and relative proportions of T^n and Q^n species in each CME DEP glass synthesised with different synthesis temperatures. Degree of condensation for each sample was calculated from relative proportion of T^n and Q^n. 139

Table 7.1 The compositions of calcium containing PCL hybrids made in this work. * the ratio of TEOS/PCL in wt% where 2.14 ml (2 g) of TEOS and 500 mg of PCL were used. ** the sol of inorganic component for hybrid synthesis was prepared separately by mixing 2.14 ml of TEOS + corresponding amount of CME (CaO precursor) and TEP (P_2O_5 precursor) to make up the chemical composition (in mol%) shows in the table. 147

Table 7.2 Weight loss after 1 week of TRIS buffer dissoltuion, the inorganic ratios in the PCL hybrids before and after TRIS dissolution. 167

Table 7.3 T^n and Q^n distributions and degree of condensations of silica network in the PCL hybrids. 173

List of abbreviations

[X]: X ion concentration

µCT: X-ray Micro-Computed Tomography

3D: Three dimensional

45S5: 45 mol% SiO_2, 24.5 mol Na_2O, 24.5 mol% CaO and 6 mol% P_2O_5

58S: 60 mol% SiO_2, 36 mol% CaO and 4 mol% P_2O_5

ABS: acrylonitrile butadiene styrene

APTES: 3-aminopropyltrimethoxysilane

BSA: Bovine Serum Albumin

CME: Calcium methoxyethoxide

DABCO: 1,4-diazabicyclo[2,2,2]octane

D_c: Degree of condensation

DEPETES: Diethyl phosphatoethyl triethoxysilane

DI water: Deionised water

DMSO: dimethylsulfoxide

DSC: Differential Scanning Calorimetry

EDS: Energy Dispersive X-ray Spectroscopy

EDS: Energy dispersive X-ray spectroscopy

EDTA: ethylene diamine tetra-acetic acid

FCS: Foetal calf serum

FDA: The US Food and Drug Administration

FTIR- ATR: Fourier-transfer infrared spectroscopy - Attenuated Total Reflectance

GPTMS: 3-(glycidyloxypropyl)trimethoxysilane

HA: Hydroxyapatite

HCA: Hydroxycarbonate apatite

ICP-OES: Inductively coupled plasma optical emission spectroscopy

ICPTES: 3-isocyanatopropyltriethoxysilane

KBr: Potassium bromide

MAS-NMR: Magic Angle Spinning Nuclear Magnetic Resonance

MSC: Mesenchymal stem cell

MTT: 3-(4,5-dimethylthiazol-2-yl)-2,5-diphenyltetrazolium bromide

$\mathbf{M_w}$: Molecular weight

$\mathbf{N_c}$: Network connectivity

PBS: Phosphate Buffer solution

PCL: Poly(ε-caprolactone)

PDLLA: DL-poly(lactic acid)

PDMS: Polydimethoxysilane

PE: polyethylene

PGA: Poly(glycolic acid)

PLA: Poly(lactic acid)

PLGA: Poly(lactic-co-glycolide)

PLLA: L-poly(lactic acid)

polyTHF: Poly(tetrahydrofuran)

PSF: polysulfone

PTFE: Polytetrafluoroethylene

PU: polyurethane

PVA: Polyvinyl alcohol

SBF: Simulated Body Fluid

SEM: Scanning Electron Microscope

TBP: Tributyl phospahte

TEM: Transmission Electron Microscope

TEMPO: 2,2,6,6-tetramethyl-1-piperidinyloxy

TEOS: Tetraethyl orthosilicate

TEP: Triethyl phosphate

TGA: Thermogravimetric analysis

THF: Tetrahydrofuran

TMS: Tetramethylsilane

XRD: X-ray Diffraction

ZDEC: zinc diethyldithiocarbamate

β-TCP: Tricalcium phosphate

γ-PGA: Poly(γ-glutamic acid)

1 Introduction

Due to improvements in public health the average life-span of humans has increased. Therefore, there is a need to maintain a high standard of life in an aging population. Orthopaedic trauma and degenerative diseases are the very common problems that the elderly population faces. Bone is a natural organic/inorganic nanocomposite of cells, collagen fibres (organic) and biological (calcium deficient) hydroxyapatite (inorganic) [1]. Bone is able to heal by itself if the defect is small, but a treatment is needed if the bone defect is large [2, 3]. There are two alternative treatments: transplantation and implantation.

When the patient's own tissue is harvested from a donor site and transplanted it to a host site, the graft is called autograft [4]. The most commonly bone autograft is harvested from the iliac crest. Autografting is the gold standard bone transplantation procedure as it is the patient's own tissue, so it will not trigger any immune reaction, but the autograft from a donor site is very limited and it creates a defect at the donor site. Therefore, there is a need to develop new materials which can overcome those limitations. Artificial biomaterials are the solution.

The first generation biomaterials were designed to provide the suitable mechanical properties that match the replaced tissue with minimum toxic response in the host, metal alloys used in joint replacement are a good example [5]. Those early biomaterials had several problems, such as interfacial stability with living tissue, due to fibrous encapsulation, and mismatch of physical properties across the interface and production of wear debris [6]. Therefore, the emphasis in field of biomaterials shifted from bioinert to bioactive [7]. The second generation biomaterials were developed. Those bioactive materials were able to elicit a controlled action and reaction in the physiological environment, particularly bonding to bone without fibrous encapsulation [5]. But both first and second generation materials were not able to respond to changes in surrounding environment such as physiological load or biochemical stimuli. To overcome this, biomaterials should be bioactive and biodegradable (third generation biomaterials). Instead of replacing the damaged bone with artificial material, third generation biomaterials, such as bioactive glass, are able trigger the regeneration of specific tissue at genetic level with controlled degradation [8-10].

Bioactive glasses bond with bone through the formation of a bone-like apatite surface layer [11] and stimulate bone growth through the release of ions that stimulate bone

cells at the genetic level [9, 10]. Bioactivity can now be defined as the “stimulation of a positive biological response from cells”.

Sol-gel bioactive glass is a promising third generation biomaterial for bone regeneration. While sol-gel glasses were first developed in 1991 [12], the atomic scale structure has not been fully understood. An aim here was to understand the structure evolution during synthesis of sol-gel derived silicate glasses containing calcium and phosphate and to optimise the synthesis method for optimal bioactivity and controlled ion release.

As glasses are brittle, they need to be made more flexible if they are to be used in sites where they need to share load with the host bone. One method to achieve this is to introduce polymers into the sol-gel process. A second aim was to optimise the calcium and phosphate precursors used in the sol-gel process for low temperature synthesis. A third aim was incorporate bioresorbable polymers into the sol-gel process and to maintain the apatite forming ability of the bioactive glass.

2 Literature review

2.1 Human bone

Bone is a connective tissue which provides the physical support to the whole body and physical protection to the organs. There are two types of bone tissues at the macroscopic level, cortical (compact) bone and trabecular (spongy or cancellous) bone (Figure 2.1). Cortical bone is a dense compact structure and forms the outer shell of most bones; it facilitates the main functions of bone mentioned above. Trabecular bone is highly porous and has a much higher surface area to mass ratio than compact bone. Trabecular bone can be found at the ends of the long bone, and it is highly vascular and contains red bone marrow for blood cell production [13].

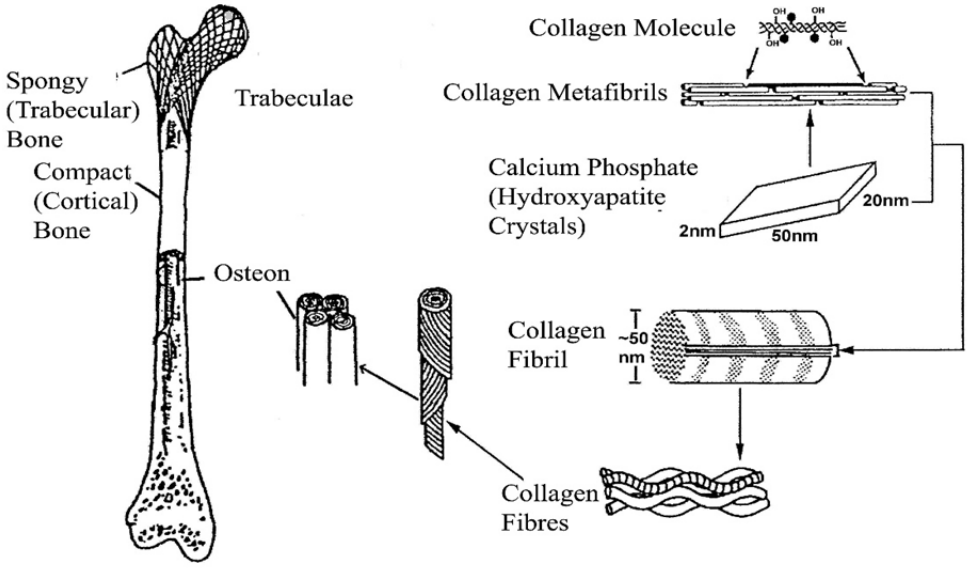


Figure 2.1 Hierarchical structure of human bone (adapted from [1]).

Bone is a natural nanocomposite which is composed of inorganic bone mineral crystals (biological hydroxyapatite (HA)), organic collagen and cells, where the organic collagen molecules are covalently linked to each other and bone mineral crystals are at the gaps of these collagen molecules (Figure 2.1) [14, 15]. The organic phase contributes to the toughness of bone and distributes the loads to the inorganic minerals. The inorganic bone minerals take the majority of compressive load.

The types of cells in bone include osteocytes, osteoclasts and osteoblasts. Osteocytes are the most abundant cell in the bone. They maintain the bone structure and recycle calcium salts in the bone matrix. Osteoclasts are the bone destroyers; secreting acid and enzymes to decompose the bone matrix and release the calcium and phosphate ions.

Osteoclasts play a very important role in maintaining the homeostasis in the blood. Osteoblasts are the bone producers and play an important role in bone regeneration. Osteoblasts produce bone matrix and can also deposit the calcium salts in matrix. When osteoblasts are surrounded by calcified matrix, they lose their bone production property and become osteocytes in order to maintain the bone structure. [1, 16, 17]

Bone responds to the mechanical load and can remodel itself. At high loading sites, osteoblasts are active and produce bone matrix to densify the bone; at low load sites, osteoclasts degrade the bone matrix faster than osteoblasts produce it [17]. In addition, the activity of the osteoclasts is also regulated by the concentration of ions in the blood stream.

Understanding the mechanical properties of human bone is important for bond grafting scaffold development. The mechanical properties of cortical and trabecular bone are summarised in Table 2.1. However, the mechanical properties of bone strongly depend on the age and type of bone tested [13].

Table 2.1 The mechanical properties of cortical and trabecular bone [1].

Mechanical property	Cortical bone	Trabecular bone
Compressive strength (MPa)	100-230	2-12
Tensile strength (MPa)	50-150	10-20
Stain to failure (%)	1-3	5-7
Young's (tensile) modulus (GPa)	7-30	0.5-0.05

2.2 Bioactive ceramics and glasses

2.2.1 Introduction

A bioactive material can be defined as "a material that stimulates beneficial response from the body" [18]. In 1994, Larry L. Hench [19] further classified bioactive materials into two types, Class A and Class B, according to their bioactivities. "Class A bioactive materials, such as 45S5 bioactive glass, lead to both osteoconduction and osteostimulation as consequence of rapid reaction on the surface of the bioactive material" [20, 21]. Class B bioactive materials can stimulate osteoconduction only, such as synthetic HA. An osteoconductive material is defined as a material that bond to bone and capable of stimulating formation and growth of the bone on the implant surface from the interface of the bone and the implant.

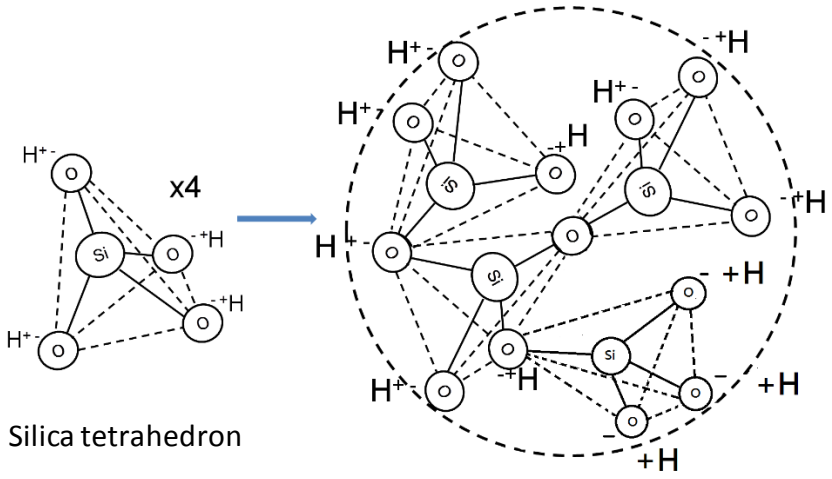


Figure 2.2 the schematic of silica glass network formation (adapted from [18]).

Glass is one of the commonly used materials in daily life. Glass is a network of atoms which link together through covalent bonds with oxygen, and as the atoms in the networks are randomly arranged, i.e. amorphous[22]. Silica (Figure 2.2) is the most commonly used glass network former.

The properties of glass depend on the glass composition, and certain compositions can make glass become bioactive and bio-degradable. Bioactive glass is able to reinforce the bone regeneration by having a silica content low enough that the glass can degrade in aqueous conditions, releasing certain ions to the surroundings.

2.2.2 Synthetic hydroxyapatite

Synthetic HA is one of widely used calcium phosphate biomaterials in orthopaedic applications such as filling of bone defects. Synthetic HA ($Ca_{10}(PO_4)_6(OH)_2$) has a composition similar to the mineral component of bone, which is a hydroxycarbonate apatite (HCA) with chemical composition of $Ca_{8.3}(PO_4)_{4.3}(CO_3)_x(HPO_4)_y(OH)_{0.3}$ where x increases with age and y decreases with age [23]. HA is bioactive and biocompatible [24], but the bioactivity of synthetic HA is relatively lower than bioactive glass, because of the lower dissolution rate of synthetic HA when compare to bioactive glass [25, 26]. When a bioactive glass bone graft is implanted, the components of the bioactive glass are used up by new bone therefore the repaired tissue will be bone. Unlike bioactive glass, the implanted HA bone graft will remain on the implantation site for a long time and result in a composite of new bone reinforced by the implanted HA [24].

Tricalcium phosphate (β-TCP, $Ca_3(PO_4)_2$) is an osteoconductive material that can be used in conjunction with synthetic HA to improve the resorbability of HA in orthopaedic applications [27]. The mixture of synthetic HA and β-TCP forms the biphasic calcium phosphate and the bioactivity of this materials can be controlled by manipulating the HA/ β-TCP ratio [27, 28].

2.2.3 Phosphate glasses

The network former in the phosphate based glass is P_2O_5 and the basic unit in the phosphate glass structure is orthophosphate tetrahedron (PO_4^{3-}). Each orthophosphate tetrahedron can covalently link to three other phosphate tetrahedral groups via bridging oxygen and form a phosphate glass structure as shown in Figure 2.3 [29]. Phosphate based glasses are found to be much more soluble than silicate based glasses, of similar content of network former, and can offer a more controlled rate of degradation, therefore phosphate glasses can potentially be used as sutures, as carrier in drug delivery and also in bone fracture fixation applications without the need for further removal surgery [30, 31]. The solubility of the phosphate glasses can be tailor-made to suit the end application by altering the glass structure [32, 33]. As reported by Ahmed *et al.* [31], the dissolution rate of a ternary-based P_2O_5-CaO-Na_2O glass decreases with increasing CaO content due to the cross-link formation between the non-bridging oxygen of two different phosphate chains by Ca^{2+} and that improved the phosphate network strength. The ternary-based P_2O_5-CaO-Na_2O glass with certain glass

composition showed a good biological response [34], the high Ca^{2+} containing P_2O_5-CaO-Na_2O glasses up-regulated the proliferation of the cells and the expression of bone antigens. Whereas highly soluble P_2O_5-CaO-Na_2O glasses with a lower level of Ca^{2+} inhibited growth and bone antigen expression.

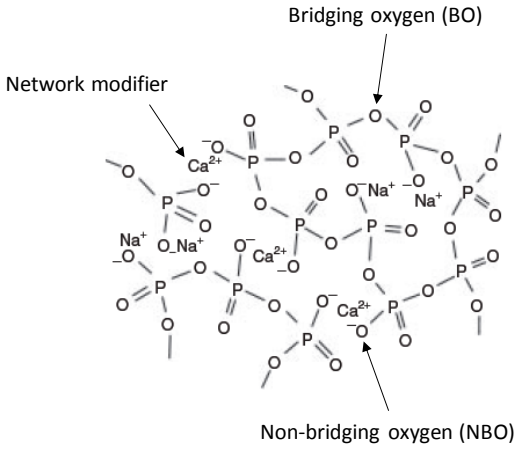


Figure 2.3 Schematic of phosphate glass structure with additional network modifiers, Ca^{2+} and Na^{+} (adapted from [29]).

2.2.4 Melt-derived bioactive silicate glass

In melt-quench process, the glass components are mixed and melted at high temperature (usually above 1300ºC), then the molten glass is quenched in a mold or in water.

Bioglass®, also known as 45S5, was the first material found to bond with bone after implantation and it was discovered by Professor Larry Hench in 1969. 45S5 is a silica based melt-derived glass with glass composition of (46.1 mol% SiO_2, 24.4 mol% Na_2O, 26.9 mol% CaO and 2.6 mol% P_2O_5). [35] The first paper about 45S5 Bioglass was published in 1972 which summarised both *in vitro* and *in vivo* studies of 45S5 [11]. The *in vitro* tests showed that formation of hydroxycarbonate apatite was found on the surface of 45S5 glass in test solutions that did not contain calcium and phosphate ions. The interfacial HCA crystals were also observed *in vivo*, which contributed to the strong interfacial bond to bone.

The glass composition can affect the bioactivity of the glass and only certain compositions of silica based glass are capable of bonding to bone via HCA formation on the surface. The compositional dependence of bone bonding and soft-tissue bonding for melt-derived Na_2O-CaO-P_2O_5-SiO_2 glass system is shown in Figure 2.4. The glasses

in Region A can form a strong bond to bone, where the bioactivity (rate of bone bonding) of the glasses in Region A decreases when the SiO_2 content of the glass lies between 52 mol% to 60 mol%. When the SiO_2 content exceeds 60 mol%, the glasses are bioinert and lie in Region B. Glasses in Region C are resorbable and usually disappear 10 to 30 days after implanted. SiO_2 content in the glasses lie in Region D is too low for a glass network to form therefore glasses in Region D are not technically practical. [35-37] Glasses lie within Region E, such as 45S5, (at the middle of Region A) demonstrate highest bioactivity which can form strong bonds with soft tissue (collagenous tissue) as well as the inorganic part of bone [38, 39].

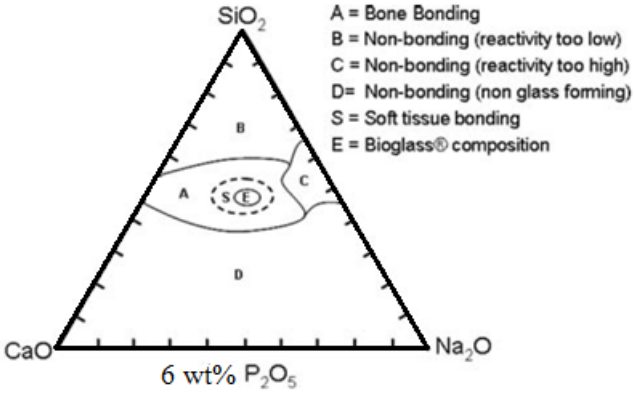


Figure 2.4 Bioactive map of melt-derived glass composition (in wt%) in the Na_2O-CaO-P_2O_5-SiO_2 system (all glasses in the diagram contain 6 wt% P_2O_5) [38].

However, there are several disadvantages of using the traditional melt-quench method for bioactive glass synthesis:

1. It is difficult to make a melt derived glass with high purity. It is primarily because of the high processing temperature required for melting and homogenisation. The low purity is also related to the chemical composition of traditional melt derived glass (e.g. 45S5) which contains low silica and high alkali. The composition is very reactive chemically which can easily pick up other multiple cations as impurity and the crucible might also dissolve into glass at high temperature. In addition, several processing steps, including fritting, grinding and sieving etc., expose melt derived glass powders to potential contaminants. [12] The bioactive bone bonding ability of bioactive glasses has been shown to be very sensitive to a small amount of impurity in the glass. As reported by Hench and Greenspan [40], a small amount of Al^{3+} can eliminate bone bonding for bioactive glasses.

2. The compositional range for the glass to be bioactive is narrow. Melt derived glasses which contain more than 60 mol% of SiO_2 are not bioactive because higher the SiO_2 content in the glass, the higher the network connectivity which reduces the dissolution rate in body fluid.

3. Melt derived glass cannot be readily made into porous scaffold and certain compositions cannot be made into scaffold without crystallising during sintering. Such as 45S5, because of the narrow sintering window of 45S5 (temperature gap between glassy transition temperature and its onset temperature for crystallisation) the crystallisation during sintering cannot be avoided and the crystallisation greatly reduce the bioactivity [41].

2.3 Sol-gel process and sol-gel derived bioactive glasses

2.3.1 Introduction

Sol-gel process is a wet chemical technique which offers an alternative route to synthesis bioactive glasses but with a lower processing temperature than melt-quench method therefore most disadvantages of high temperature melt-quench method can be eliminated. Alkoxide precursors can be hydrolysed and the products of hydrolysis can undergo polycondensation to form silica nanoparticles, which can then assemble to form a silicate network, in the form of a wet gel [42]. When the gel is dried and thermally stabilised, a nanoporous glass remains. Unlike melt derived bioactive glasses, sol-gel derived glasses have higher purity and homogeneity, because SiO_2 network forms under continuous stirring at low temperature. [43] The glasses with similar composition synthesised via two routes have differences in their structures but have very similar mechanism by which bioactivity is achieved [44, 45].

In addition, due to the wet nature of sol-gel process and the way nanoparticles assemble, nanopores are formed and the SiO_2 network formation is disrupted by protons (H^+) in the sol [43]. The unique nanoporosity improves the cellular response and increases surface area greatly (two orders of magnitude higher than melt derived glass with similar composition) [46]. Sol-gel derived glasses have a wider bioactive composition range up to 90 mol% SiO_2 because of their unique nanoporosity and lower connectivity of the SiO_2 network when compare to melt derived glass [12, 43]. The sol-gel process also allows simplification the glass composition. The role of Na_2O in melt derived glass is to lower the melting point, and also increase the solubility of the melt derived glass, which is important to bioactivity. However there is no melting is required in sol-gel process and the high surface area increases the solubility of the glass significantly therefore sodium can be eliminated from the composition of sol-gel derived glass [18]. The absence of Na_2O in the glass can avoid the rapid change in interfacial pH observed with melt derived glass [47].

The first sol-gel derived bioactive glass, 58S, was synthesised in 1991 by Li *et al* [12], with the composition of 60 mol% SiO_2, 4 mol% P_2O_5 and 36 mol% CaO. Sol-gel derived 58S glass has the excellent bioactivity both *in vitro* and *in vivo* [48, 49]. The highly porous texture of 58S causes fast dissolution rate and rapid apatite formation *in vitro*. As reported by Sepulveda *et al* [44], 58S powders were covered by highly crystalline apatite within the first hour of dissolution in SBF. Studies by Bielby *et al.*

[50, 51] suggest the dissolution products from 58S increase the proliferation of both murine and human osteoblasts, and stimulates osteoblast associated gene expression in differentiation culture of murine embryonic stem cells. Christodoulou *et al.* [52] showed the ionic dissolution products from 58S stimulated the expression of various genes in human fetal osteoblasts.

The composition of sol-gel derived bioactive glass can be simplified into a binary CaO-SiO_2 system [53]. Glasses with different molar ratio of SiO_2 : CaO (from 90:10 to 50:50) were made and studied by Saravanapavan *et al.* and the 70S30C (70 mol% SiO_2 and 30 mol% CaO) appeared to have the highest bioactivity compare to other compositions, in terms of HCA formation in SBF [54].

Sol-gel process involves mixing of the raw materials, gelation at room temperature, aging, drying and stabilisation. Sintering is then applied to remove interconnected nanopores for certain applications. Steps of sol-gel process are summarised in Figure 2.5.

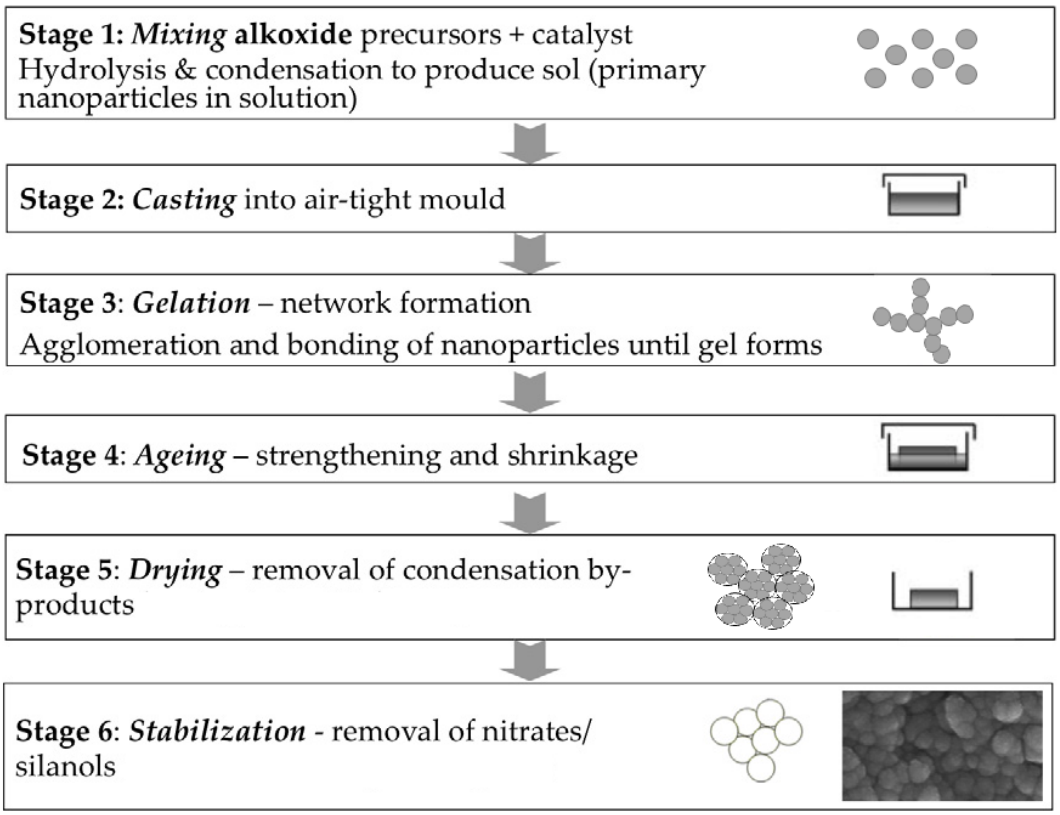


Figure 2.5 A flow chart of sol-gel process (adapted from [18] and [43]).

2.3.2 Mixing and gelation at room temperature

The first step of sol-gel process is mixing of all the raw materials with water and catalyst to prepare a liquid "sol". At this stage, hydrolysis and polycondensation reactions of the network former take place simultaneously to initiate the formation of glass network. Tetraethyl orthosilicate (TEOS) is the most widely used silica precursor for making the Si based sol-gel glass therefore TEOS is taken as an example in this section. TEOS is insoluble in water, but it can be hydrolysed to form silicate tetrahedron (Figure 2.6), then the repeating polycondensations of silicate tetrahedra (Figure 2.7) leads to the formation of primary nanoparticle which disperse in the liquid "sol".

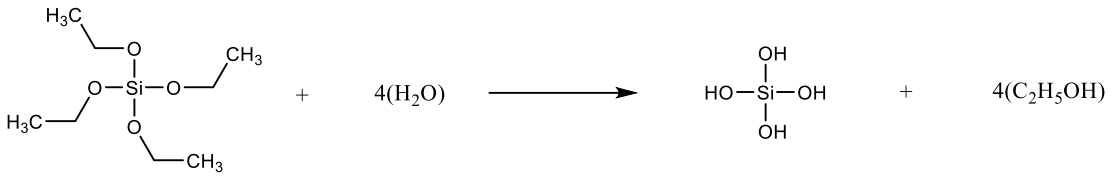


Figure 2.6 The hydrolysis of tetraethyl orthosilicate (TEOS)

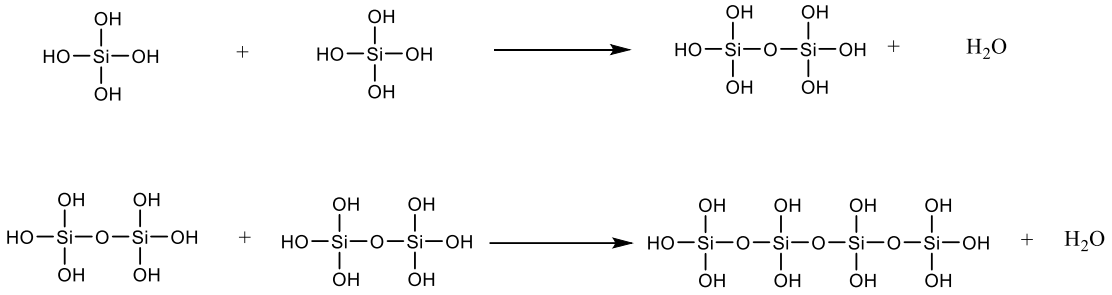


Figure 2.7 Polycondensation of silicate tetrahedra to form silicate nanoparticles.

The hydrolysis and polycondensation reactions can be catalysed either by an acid (e.g. HNO_3) or a base (e.g. ammonia). Different types of catalysis affect the final properties and structures of the glass.

Under acidic conditions, the oxygen in silanol groups are attacked by protons (H^+) and then protonated, which makes the Si atom in the silanol groups more electrophilic thus more susceptible to attack by water (Figure 2.8a). Because the oxygen of the silanol groups at the end of the chains have the higher partial negative charge than those in the middle of the chains, the acid-catalysed condensation is directly preferentially toward the ends of the chain [55]. As a result the silica tends to form the less branched silica

structure under acidic condition and then the linear silica chains entangle to form additional branches (Figure 2.9). [56]

Under basic conditions, the OH^- groups in the sol attack the Si atoms directly (Figure 2.8b) and because the Si atoms in the middle of the chains have higher partial positive charge than the Si atoms at the end of the chins, the base-catalysed condensation is directed toward the middle of the chains, resulting in the formation of more compact and highly branched silica species (Figure 2.9). [55]

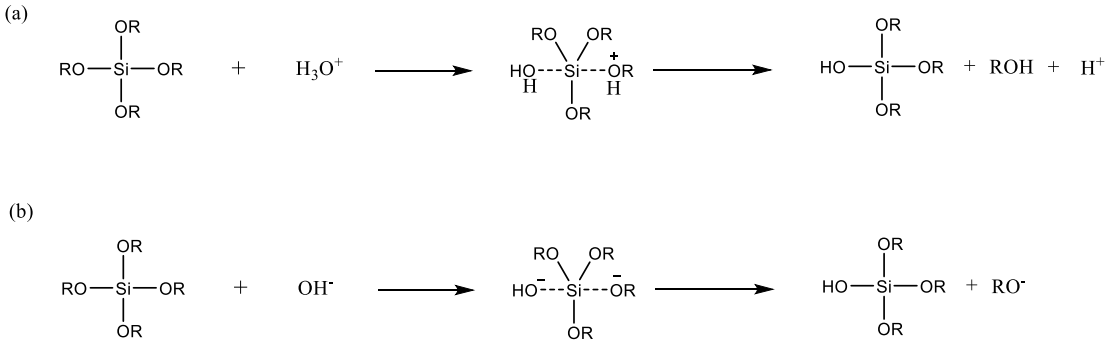


Figure 2.8 The mechanism of (a) acid-catalysed hydrolysis (b) base-catalysed hydrolysis [56].

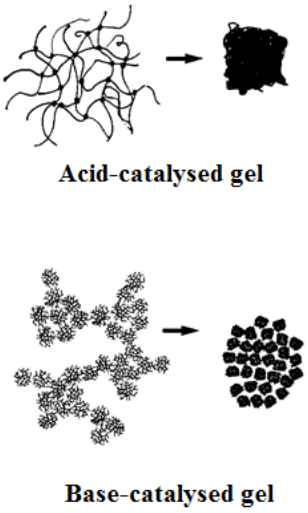


Figure 2.9 Schematic representation of acid-catalysed gel and base-catalysed gel (adapted from [57]).

In addition, silicate tetrahedra exhibit different polymerisation behaviours at different pH. Above pH 7, the SiO_2 particles are negatively charged and repel each other and do not collide to each other, therefore the particles in sol tend to grow in size rather than aggregate and fuse together, so base-catalysis is usually used to form individual dense nanoparticles[58, 59]. Whereas under acidic condition, SiO_2 particles bear very little

ionic charge thus no electrostatic repulsion of particles take place, so the SiO_2 particles aggregate into three-dimensional network resulting in gel formation [58]. Sol-gel bioactive glasses are usually synthesised by using acid-catalysis, where SiO_2 particles in the sol fuse to each other and the interstitial spaces between the particles become nanopores. [59]

pH of the sol can also affect the rates of hydrolysis and polycondensation reactions. The rate of condensation is minimised when the pH is near the isoelectric point of SiO_2 (pH=2.2) and the hydrolysis reaches its lowest rate when the pH is around 7 [60]. The rate of hydrolysis increases at pH lower or higher than 7 and the rate of hydrolysis is faster under acid-catalysis rather than base-catalysis [61].

After mixing, the liquid sol is cast into an air tight mold prior to gelation, and the mold must be made of a material that will not adhere to the gel, such as polytetrafluoroethylene, PTFE. At gelation, the viscosity of the sol increases with time due to the agglomeration of primary nanoparticles and continuous formation of Si-O-Si bonds, eventually a gel is formed. [43, 62] Gelation of the sol is mainly associated with the condensation reaction therefore the gelation time can be affected by pH of the sol, where the sols have a maximum gelation time when pH is around 1.5 to 3 (near isoelectric point of SiO_2) and the minimum gelation time when pH is around 6. [58]

Water ratio (R, molar ration of water : TEOS) is the other factor that can affect the gelation time. Because water is produced as the by-product of the condensation reaction the minimum amount of water required to complete hydrolysis and polycondensation to form a silica network is a R value of 2 [55]. When R water ratio increases from 2 to 4, the gelation time of sol decreases significantly because there are more water molecules available for hydrolysis. But because of the dilution effect when the R ratio excesses 7 the gelation time increases as R ratio increases. [55, 63]

Additional substances can be incorporated into SiO_2 glass network to suit the end application by adding corresponding precursors into the sol during mixing, e.g. calcium and phosphate are usually incorporated into the SiO_2 glass network to make the glass bioactive. Incorporations of calcium and phosphate will be discussed in section 2.3.6.

2.3.3 Aging of silica gels

After mixing and gelation at room temperature, the gel is aged in an air tight mold at room temperature or at slightly higher temperature (60°C) for a period of time (hours or days). Aging involves the changing in the structure of the cast gel by several simultaneous reactions which contain polycondensation, syneresis and coarsening. [55] Polycondensation (Figure 2.7) continues to increase the concentration of Si-O-Si bonds which leads to create a more cross-linked structure. Syneresis is the shrinkage of the gel network which caused by the condensation reaction of neighbouring Si-OH groups, resulting in expulsion of liquid by-product from the pores (Figure 2.10). [55, 62]

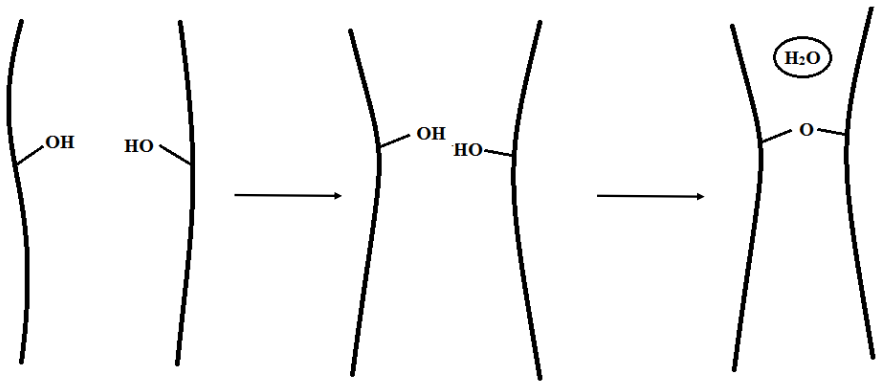


Figure 2.10 Schematic of syneresis during aging [55].

Coarsening is the process of dissolution and reprecipitation driven by differences in solubility between the surfaces with different curvatures. Since the convex surface is more soluble than concave surface, the dissolution materials from the convex surface will reprecipitate on the concave surfaces at the region of interparticle necks, therefore the thickness of interparticle necks increase and then fill up the small pores in the gel, resulting in the decrease in the surface area but increase in the average pore size of the gel (Figure 2.11). [55, 62]

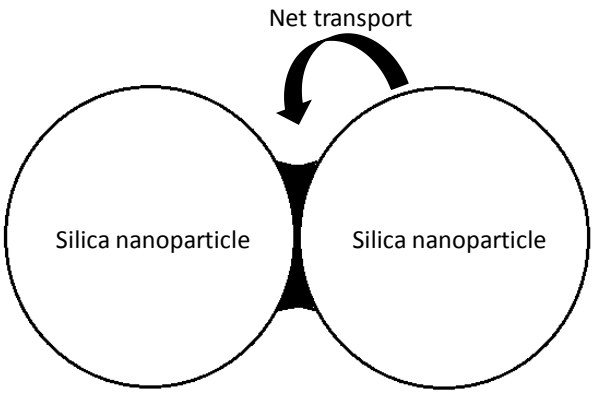


Figure 2.11 Schematic of a growing interparticle neck by coarsening [55].

Many processing parameters can affect aging by affecting the three reactions descried above, such as temperature which affect the rate of condensation reactions. The polycondensation is faster at higher temperature. The rate of syneresis is determined by many factors, including temperature, the concentration of reactive Si-OH groups and chemical environment etc. The coarsening can be affected by pH, since solubility of silica is higher at high pH therefore the rate of coarsening of silica gel is also faster at high pH. [62]

After aging, a solid wet gel remains immersed in its liquid by-products. The strength of the gel increases during aging, therefore the aged gel should be strong enough to resist cracking during drying. Extending the aging time can reduce the chance of cracking during drying.

2.3.4 Drying

During drying, all the liquid by-products and solvents are removed to leave a xerogel with an interconnected nanoporous structure behind. Drying can be separated into 4 stages: stage 1 – 3 and the cooling stage. At the first stage of drying (stage 1), the gel shrinks because the capillary force draws the solid network together as the liquid evaporates [64]. Most of the changes in the volume, weight, density and structure of the gel take place during the first stage. In classical large-pore system (pore > 20 nm) the first stage is also called the constant rate period, because the evaporation rate per unit area of the drying surface is independent of time [65]. Evaporation rate is not constant but decreases with time, because the pore radii change during drying thus cause the reductions in the vapour pressure of the liquid in the small pores. [66] The

strength of the network increases during the first stage of drying and once it reaches the critical point, the strength of the network is sufficient to resist further shrinkage and it also means stage 1 ends.

In stage 2, the pores in the gel are partially empty and the surfaces of the pores are covered by liquid films, therefore liquid flows to the outer surface of the gel by the gradient in capillary stress and then evaporates. Stage 2 is also call the first falling rate period because the rate of evaporation decreases in stage 2. [62]

It reaches the third stage of drying (stage 3) when the pores are empty and the liquid films on the surfaces of the pores cannot be sustained. At stage 3 the remaining liquid evaporates within the pores and then diffuses to the outer surface in gas phase. The evaporation rate decreases again at this stage therefore stage 3 is also called as the second falling rate period. [67] During the cooling, the dry gel gains weight due to condensation occurs within the pores.

During drying, the inside and outside of the drying gel have different shrinkage rates, which generates a tensile drying stress σ_x. The tensile drying stress increases with the thickness of the gel, evaporation rate and viscosity of the liquid. Additionally, the tensile drying stress is also strongly correlated to the permeability of the network (which is strongly depends on the pore size, where the smaller pores have lower permeability), where tensile stress increases as the permeability of the network decreases. [55]

Since the tensile drying stress is proportional to the evaporation rate, cracking can be avoided by carefully controlling the drying process to slow down the liquid evaporation rate. In addition, the thinner the gel the lower the tensile drying stress thus reduce the chance of cracking during drying.

2.3.5 Stabilisation and sintering of the silica gel

The aim of stabilisation is to remove the reactive surface Si-OH groups by further formation of Si-O-Si bonds in the network. This can be done either by using chemical or, more commonly, by heat treatment. Hydrogen bonded pore water, organic residuals and toxic by-products (e.g. nitrate from calcium nitrate) are also removed by thermal stabilisation. During thermal stabilisation, the network becomes more highly-connected therefore the mechanical strength of the gel is enhanced and surface area is reduced. [62]

At around 170°C the surface Si-OH groups start condensing and the physisorbed water is eliminated. When heating the gel in 170°C - 400°C range, the dehydration is reversible and when the temperature reaches 400°C the organic residuals start to decompose. Above 400°C, shrinkage and sintering initiate, which results in the irreversible dehydration and the number of the existing hydroxyl groups is inversely proportional to stabilisation temperature. [68]

A glass without nanoporosity is required for some applications and this can be achieved by heating the gel to a higher temperature. If the glass is heated above its glass transition temperature but below crystallisation onset, the remaining hydroxyl groups are removed by reacting with each other (condensation), which can eventually eliminate the pores within the gel. [68]

For certain glass compositions, calcium nitrate is used as the calcium precursor and toxic nitrate is decomposed during thermal stabilisation. As reported by Arcos *et al* [69], nitrates decompose at 680°C (4.7 mol% of $Ca(NO_3)_2$ remained in 58S after the glass was heated to 600°C, and 0.6 mol% remained when heated to 700°C) and the glass transition temperature (T_g) for sol-gel 58S glass is around 785°C. When heating above T_g the porosity of the sol-gel glass is greatly reduced. The onset crystallisation tends to occur at lower temperature when a lower heating rate is used, therefore to synthesise an amorphous and nanoporous sol-gel derived 58S glass, the stabilisation temperature must be lower than T_g, but higher than the temperature for nitrate decomposition to eliminate toxic nitrite (stabilisation temperature used in this project was 700°C).

2.3.6 Calcium and phosphate incorporation into sol-gel derived glass

The glass composition in this project was based on 58S glass therefore 58S is used as an example to explain the calcium and phosphate incorporation in this section. The presences of Ca^{2+} and PO_4^{3-} in sol-gel derived 58S glass play the important role in HCA formation and its bioactivity. The conventional calcium and phosphate precursors for sol-gel glasses are calcium nitrate tetrahydrate and triethyl phosphate (TEP) respectively. As reported by Lin *et al.* [42], calcium nitrite dissolves in the aqueous sol and is not incorporated in the silicate network at room temperature. After drying, Ca^{2+} and NO_3^- are deposited on the surface of silica nanoparticles but without incorporating into the silica network. The calcium can only be incorporated into the silica glass network by diffusion when the temperature is above 400°C [42]. Ca^{2+} acts as the

network modifier which disrupts the silica network formation by ionic bonding to the non-bridging oxygen thus reduce the network connectivity (N_c) of the silica network. The disruption is necessary for the glass to be degradable and bioactive [70]. The network connectivity (N_c) describes the average number of bridging oxygen atoms (Si-O-Si) per silicon, and the bioactivity of a glass can sometimes be predicted from its N_c [71]. Calcium methoxyethoxide (CME) is an alternative calcium precursor for sol-gel bioactive glasses and it has been proved to be able to incorporate calcium into the silica network at room temperature thus to produce the sol-gel glass with higher homogeneity [72].

TEP can be hydrolysed in aqueous solution and form orthophosphate (PO_4^{3-}). The orthophosphate is incorporated into silica network by charge balancing with calcium ions and cannot be integrated into the silica network alone (no Si-O-P bonds are found) [73-75]. Increasing the phosphate content in the glass increases the N_c as calcium has higher affinity to coordinate phosphate rather than silicate, so there are less calcium ions to modify the silicate network [76].

2.3.7 Sol-gel derived phosphate glass

Phosphate based glass is commonly synthesised via melt-quench route (section 2.2.3) but the high processing temperature can cause high loss of the volatile phosphate precursor or the decomposition of bioactive molecules during glass synthesis. An alternative synthesis route, sol-gel process can also be used to make bioactive phosphate glasses. Carta *et al.* [77] showed that the atomic structures of sol-gel and melt-quenched P_2O_5-CaO-Na_2O glasses are similar, therefore the similar dissolution properties and bioactive behaviour are expected for both sol-gel and melt-quenched phosphate glasses. In their study, the phosphate precursor for sol-gel derived phosphate glasses was a mixture of monoethyl phosphate ($OP(OEt)(OH)_2$) and diethyl phosphate ($OP(OEt)_2(OH)$), which was prepared by reacting phosphorus pentoxide (P_2O_5) with anhydrous ethanol under nitrogen atmosphere. Then the solution of calcium methoxide ($Ca(OCH_3)_2$) and sodium methoxide ($NaOCH_3$) in anhydrous ethylene glycol was added drop-wise into the ethylphosphate precursor to make the sol, and followed by the heat treatments (aged at 90°C, dried at 150°C, ground and left at 180°C then finally calcined at 400°C).[77, 78]

As recently reported by Foroutan *et al* [79], the sol-gel derived $(P_2O_5)_{55}$-$(CaO)_{25}$-$(Na_2O)_{(20-x)}$-$(TiO_2)_x$ glasses for bone tissue engineering applications were successfully synthesised and studied (X=0, 5, 10 or 15). In their work, sol was prepared by first mixing n-butyl phosphate (1:1 molar ratio of mono-n-butyl phosphate and di-n-butyl phosphate) in 2-methoxyethanol, followed by the dropwise addition of titanium isopropoxide and calcium methoxyethoxide (CME). Then the sodium precursor, sodium methoxide, was added into the mixture. Finally, n-dimethyl formamide (n-DMF) was added into the solution. The resultant solution gelled within 5 minutes after n-DMF was added then aged at room temperature for 3 days, following the drying stage (60ºC for 7 days, 120ºC for 4 days, 170ºC for 2 days and 220ºC for 1 h). The results obtained by the group suggested that the phosphate glasses containing 5 or 10 mol% of TiO_2 exhibited ideal dissolution rate for cell attachment (human osteoblast-like osteosarcoma cells), easily metabolised dissolution products and high surface area, therefore had the potential to be used in bone tissue engineering applications.

Most of the published literature on bulk sol-gel phosphate glasses were with ethylphosphate (mixture of mono- and di-ethyl phosphate) or n-butyl phosphate (mixture of mono- and di-butyl phosphate) as the phosphate precursor [77-90]. Additionally, as recently reported by Foroutan *et al* [91], TEP was as the phosphate precursor to synthesis ternary P_2O_5-CaO-Na_2O glass system at low temperature.

2.4 HCA formation and glass bioactivity

Bioactive glasses, such as melt-derived 45S5 and sol-gel 58S (section 2.3), have been showed to be able to bond with bone and also stimulate bone growth away from the bone/glass interface. Furthermore, the study done by Vrouwenvelder *et al* showed that the osteoblast cells divide more rapidly on bioactive glass than on synthetic HA [92]. It was believed that glasses must contain both CaO and P_2O_5 in order to be bioactive and capable of triggering HCA formation [93], but later it was proved that the P_2O_5 free SiO_2-CaO based glasses were also bioactive and able to induce HA formation, because the phosphate ions required for the apatite formation was supplied by the fluid [94, 95]. As reported by Vallet-Regi *et al.* [96] apatite crystals formed on the surface of SiO_2-CaO-P_2O_5 glass were larger when compared to the P_2O_5 free SiO_2-CaO glass, suggesting the calcium with additional P_2O_5 promote the apatite growth *in vitro*.

The mechanism of bioactivity involves 11 stages of reactions. The first five reactions occur rapidly on the glass side of interface regardless of whether the tissue is present or not, and result in HCA crystal layer formation on the surface of the glass. The following six additional reactions are necessary for the tissue to bond with HCA layer on the surface of the bioactive glass. The 11 stages of reactions occur on the surface of bioactive glass are: [20, 37, 97, 98]

Stage 1: Once implanted, rapid ion exchange of alkali-metal cations (Ca^{2+} and Na^+) with H^+ from body fluid occurs, releasing cations to the fluid (Figure 2.12). The pH of the surrounding fluid increases as the H^+ in the fluid are replaced by cations which increases the [OH^-] in body fluid. [20]

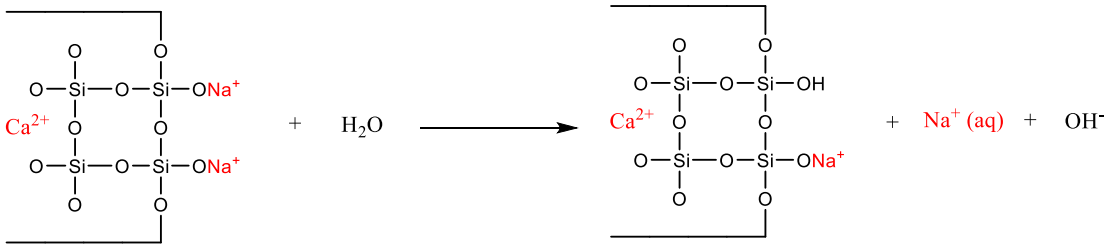


Figure 2.12 Schematic of cation exchange [20].

Stage 2: Hydrolysis of Si-O-Si bonds (Figure 2.13) followed by soluble silica release in form of $Si(OH)_4$ to the surrounding solution, leaving Si-OH bonds behind. Stage 1 and 2 occur rapidly within 1 or 2 h for 45S5 Bioglass®.

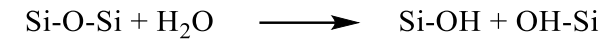


Figure 2.13 Hydrolysis reaction of a Si-O-Si bond.

Stage 3: Condensations and polymerisations of neighbouring Si-OH resulting in formation of a SiO_2 rich layer on the surface. (Figure 2.14)

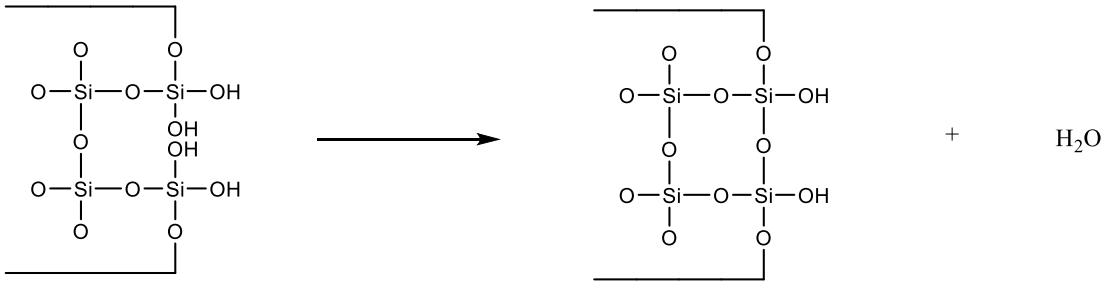


Figure 2.14 Condensation reaction of neighbouring Si-OH and form a SiO_2 rich layer.

Stage 4: Ca^{2+} and PO_4^{3-} ions from the inside of glass and the fluid migrate to the SiO_2 rich layer on the surface, nucleating at Si-OH site and forming an amorphous $CaO\text{-}P_2O_5$ film on top of SiO_2 rich layer.

Stage 5: The amorphous $CaO\text{-}P_2O_5$ film is then crystallised by incorporation of OH^- and CO_3^{2-} anions from the fluid in order to form a HCA layer. Stage 3 to stage 5 occur within 8 to 24 h for 45S5 Bioglass.

Stage 6-11: Adsorption and desorption of biological growth factors to the HCA layer, activating differentiation of osteoprogenitor cells to osteoblasts that generate extra-cellular matric to form bone.

There are two kinds of interactions that happen between bioactive glass and tissue throughout the whole bioactive bonding process, which are extracellular and intracellular interactions. The extracellular interaction is determined by the surface structure of the implanted material, such as surface nanoporosity, surface charge and hydrophobic behaviour, which play an important role in adsorption of proteins and collagen [99]. Various studies suggest that the absorbed growth factors and morphogenetic proteins maintain their biological function, resulting in the stimulation of bone cells at the surface of the implant [100, 101]. Another study done by Green *et al* suggests that the HCA crystallinity on the surface of the implant can probably affect the differentiation of stem cell. [102]

The intracellular interaction is mainly caused by the dissolution products released from the implanted material. As stated by Hench, the HCA formation on the surface of bioactive glass is useful for bioactive behaviour but it is not critical, but the ionic dissolution productions released by the bioactive glass which stimulate the bone regeneration at genetic level is the key to be bioactive [35]. Previous work has already proved that the ionic dissolution products from bioactive glass (e.g. 45S5) can up-regulate the gene expression of bone specific proteins [9, 10]. Soluble silicon plays an important role in tissue repair and osteogenesis [97]. As an early study on chicken done by Carlisle showed that the silicon deficiency in the diet retarded the normal growth and skeletal development and these abnormalities could be corrected by a silicon supplement [103]. Solutions of high silicon concentration can induce osteoblast proliferation and the expression of TGF-β mRNA in human osteoblast-like cells. [104] Other than soluble silicon, it has also been shown that increase the extracellular Ca level also induce osteoblast proliferation [105] and the influx of P into the osteoblast can trigger osteopontin protein synthesis, a protein facilitates the attachment of bone cells (osteoblast and osteoclast) to extracellular matrix allowing them to perform their functions during osteogenesis [106].

2.5 Porous bioactive scaffolds

2.5.1 Introduction

In order to repair large defects, bioactive scaffolds are needed to provide a template to support tissue regeneration rather than the powder or granule forms [107]. Ideally the template for bone regeneration should consist of two factors: 1. the interconnected macropore structure with pore size larger than 100 μm to allow vascularised bone ingrowth and ensure the nutrient delivery to the centre of regenerating tissues. 2. The presence of micropores (pore size < 2 nm) or mesopores (2 nm < pore size < 50 nm) for cell adhesion and biological metabolites absorption.

2.5.2 Melt-derived bioactive glass scaffolds

There are various methods to make a porous melt derived bioactive glass scaffold, including space holder method, polymer foam replication, gel-cast foaming and robocasting method (3D printing). Space holder method is the simplest method to produce a melt derived porous scaffold (Figure 2.15). In space holder method, glass slurry (glass particle and solvent) is mixed with space holder particle (usually use combustible polymer for glass scaffold, e.g. poly(methyl methacrylate)), then heat treatment is applied to remove the space holder particles and sinter the glass particles. The scaffold made with space holder method has low pore interconnectivity.[108]

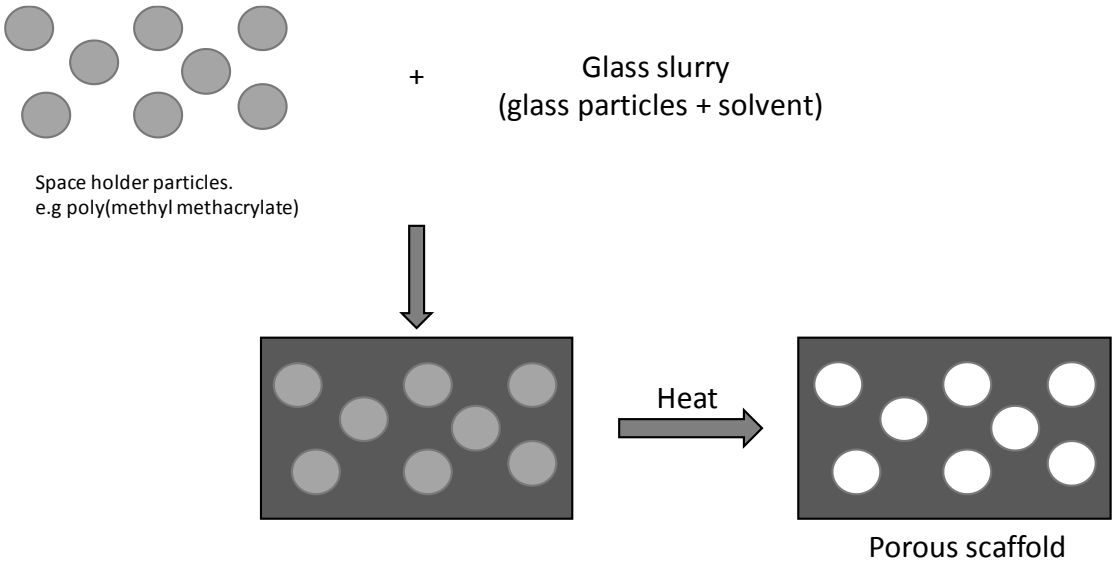


Figure 2.15 Schematic of space holder method for melt derived glass scaffold [108].

Polymer foam replication improves the interconnectivity of the scaffold (when compare to the scaffold made from space holder method) and the scaffolds with different pore sizes can be easily made by using the polymer foam with different pore size. In polymer foam replication method, a polymer foam (usually polyurethane foam) is immersed into glass slurry (glass particle and solvent) to form a glass slurry coating on porous polymer foam. It is important to ensure the polymer foam is well coated, any excess glass particle/slurry need to be removed before heat treatment (excess glass particles will block the pores). Then heat treatment is applied to remove the polymer foam and sinter the glass particles. The main disadvantage of polymer foam replication is that it leaves hollow struts after polymer is removed which reduce the mechanical properties of the scaffold significantly [108, 109].

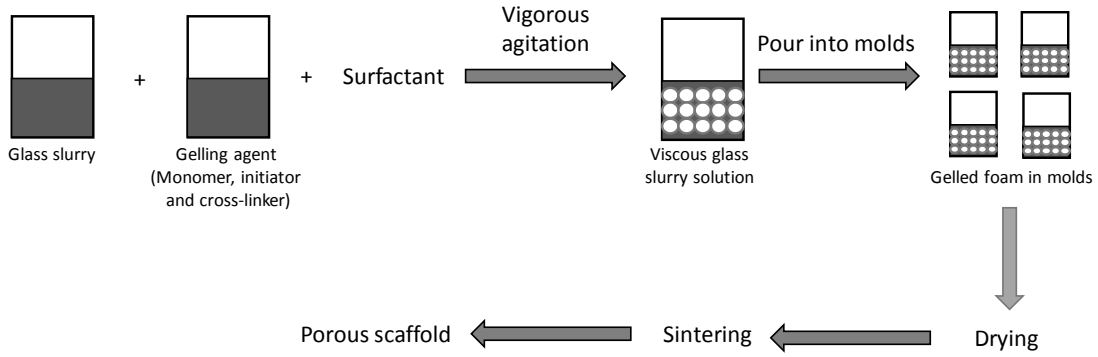


Figure 2.16 Schematic of gel-cast foaming of melt derived glass scaffold [108].

To produce a scaffold with interconnecting pores and sufficient mechanical properties, gel-cast foaming technique is the solution. For gel-cast foaming, solution is prepared by mixing glass particles slurry (glass particles < 38 μm + water) and the gelling agent which contains monomer (e.g. acrylamide), cross-linker and water. Surfactant, initiator and catalyst are then added into the solution followed by vigorous agitation to foam. The viscosity of slurry increases during agitation due to *in situ* polymerisation which fixes the bubbles in place. The foam is then poured into moulds just prior to gelation, followed by drying and sintering. The schematic of the gel-cast foaming process is shown in Figure 2.16. Gel-cast foaming produces excellent scaffolds but the process is complex therefore it is difficult to up-scale the production. The amount of glass particles in the slurry can affect the resultant foaming scaffold: if there are too little glass particles the foam might slump before sintering, whereas too much glass particles in the slurry make it difficult to foam. The main limitation of gel-cast foaming is that,

for the surfactant to function, water is needed in the slurry, therefore the glass particle in slurry starts reacting with the water and might form a HCA layer on the surface of the glass particle. [41, 108]

As reported by Fu *et al* [110] melt-derived bioactive glass can be made into porous scaffolds (60% porosity) with compression strength similar (136 MPa) to human cortical bone by robocasting (3D printing) method. The glass composition 6P53B (in mol%: 51.9 SiO_2, 9.8 Na_2O, 1.8 K_2O, 15.0 MgO, 19.0 CaO and 2.5 P_2O_5) was used in the study to expand the sintering window thus prevent crystallisation during heat treatment. The inks were prepared by dispersing 30 vol% of 6P53B glass particles (D_{50} = 1.2 μm) in 20 wt% Pluronic F-127 solution, then corn syrup was added to enhance adhesion between particle filaments. The inks were then used to 3D print the porous scaffolds. After 3D printing, the scaffolds were air-dried for 24 h and then heated to 700^{o}C to sinter the glass particles.

2.5.3 Sol-gel derived bioactive foam scaffolds

Sepulveda *et al.* [107] showed that the sol-gel bioactive foam scaffolds meet the two requirements described above. Macropore diameters of 58S foam scaffolds were in the range of 500 μm with the interconnecting window size range from 2 – 100 μm and the nanopores with average pore size of 15 nm. [107] The scaffolds for bone regeneration must also provide sufficient mechanical support when implanted. As reported by Poologasundarampillai *et al.* [111], the compressive strength of Sol-gel 70S30C foam scaffolds can be improved to 4.56 MPa, which is within the range of compressive strength of human trabecular bone (2 – 12 MPa), by increasing the sintering temperature to 800^{o}C.

Bioactive glass can be made into porous scaffold without crystallising using sol-gel, because the silica networks start to form at room temperature thus the glass transition temperature does not need to be surpassed to produce the porous scaffold [18]. During sol-gel foaming process, the liquid sol is prepared as described in section 2.3.2, then surfactant (e.g. Teepol® detergent) and a gelling agent (e.g. Hydrofluoric acid, HF) were added into the sol prior to vigorous agitation. Agitation is applied to produce spherical bubbles in the sol, and once the sol turns gel the spherical bubbles become permanent in the gel. Polycondensation takes place during agitation and the viscosity of the sol starts to rise more steeply when gelling agent is added, just at the instant before the

gelling point, the foamed sol is casted into molds followed by a series of heat treatments, including aging, drying and stabilisation. The schematic of the sol-gel foaming process is shown in Figure 2.17.

Amorphous bioactive scaffolds with interconnected pore structures can be synthesised by using sol-gel foaming process [41], but the process is complex. The timing when the foam is casted into molds need to be controlled carefully. If the foam is casted into the molds too early, the foamed sol is not gelled enough and will collapse in the mold. Whereas if leave for too long, the foamed sol turns into gel before casting into molds and the heat treatments cannot be applied.

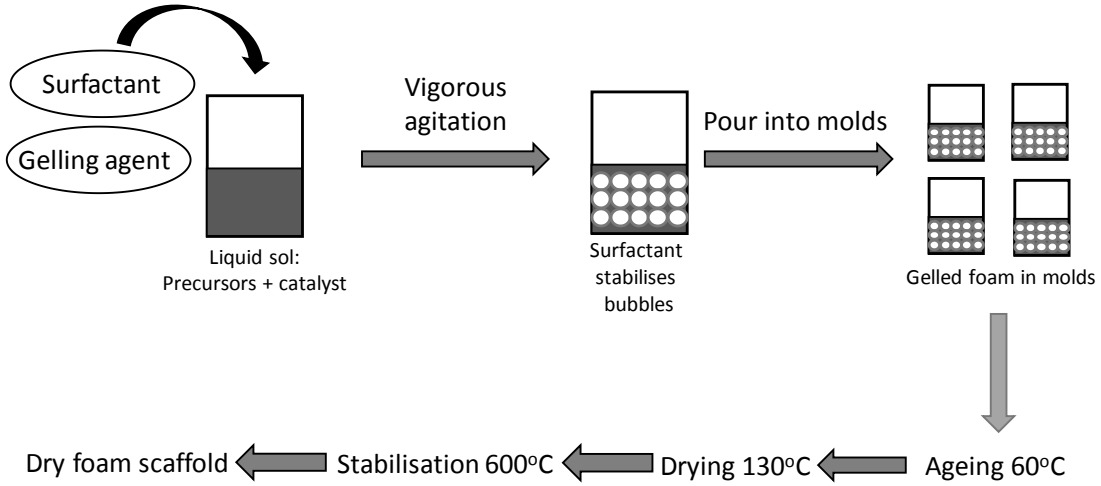


Figure 2.17 A schematic of the sol-gel foaming process [107].

2.6 Sol-gel bioactive organic/inorganic hybrids

2.6.1 Introduction

Bioactive glass has excellent biological properties and can be made into porous scaffolds to mimic the porous structure of natural bone, for many applications bioactive glasses work really well. But bioactive glass is a brittle material and are not suitable to be applied at the defect sites that are under cyclic loads. Therefore, there is a need to introduce flexibility and toughness into the bioactive glass.

The obvious engineering solution is bioactive composite materials of bioactive glass particles (or fibres) and bioresorbable polymer matrix (Figure 2.18). The most commonly used organic polymers for composite are saturated aliphatic polyesters, including poly(lactic acid) (PLA) [112, 113], poly(glycolic acid) (PGA) and their copolymer poly(lactic-co-glycolide) (PLGA) [114] as they are approved by the US Food and Drug Administration (FDA) and their monomeric components can be completely removed from the body [18, 115]. However, they degrade rapidly once the degradation starts because of self-catalysed hydrolysis of ester bonds in the polyester. The hydrolysis of ester bonds creates carboxylic groups which reducing the local pH and the flowing hydrolytic reactions are catalysed at low pH [18, 115]. Therefore, bioresorbable polymer and bioactive glass particles (or fibres) degrade at different rates [116], the polymer may degrade faster, which can cause instability of the composite scaffold and migration of bioactive glass particles *in vivo*. In the bioactive composite, bioactive glass particles or fibres are buried in the bioresorbable polymer matrix as two distinguishable phases. The amount of bioactive glass expose to the surrounding is limited thus the bioactivity is reduced significantly [117, 118].

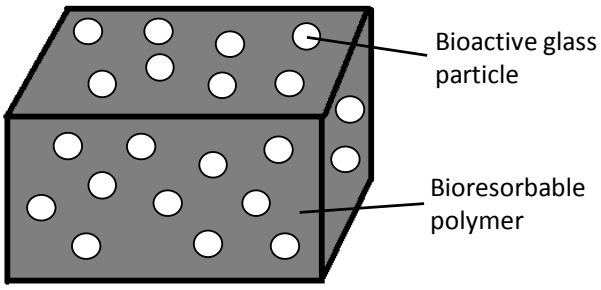


Figure 2.18 Schematic of a conventional bioactive composite.

Organic/inorganic hybrid is a newer material which has the potential to overcome the problems associated with bioactive composites. The organic component (polymer) and

the inorganic component (bioactive glass) interact with each other at nanoscale to form interpenetrating networks. The two components are indistinguishable above the nanoscale therefore the hybrid combines the properties of two components and can be seen as one material when implanted. The properties of hybrid can be tailored to suit the end application by manipulating the organic/inorganic ratio and the sources of organic and inorganic components.

Bioactive hybrids are synthesised via sol-gel processing without the heat treatments of stabilisation and sintering. The drying temperature is usually below 60^{o}C. The synthesis of bioactive hybrids is complex and several challenges need to be overcome, such as calcium incorporation at low temperature.

Bioactive hybrids can be classified into two families, Class I and Class II according to the interactions between the inorganic and organic components. The interactions between organic and inorganic in a Class I hybrid are hydrogen bonds and physical bonding, including van der waals force and molecular entanglements therefore Class I hybrids dissolve rapidly in aqueous environments [119, 120]. In Class II hybrids (Figure 2.19), the inorganic and organic components are chemically linked together via covalent bonds [120].

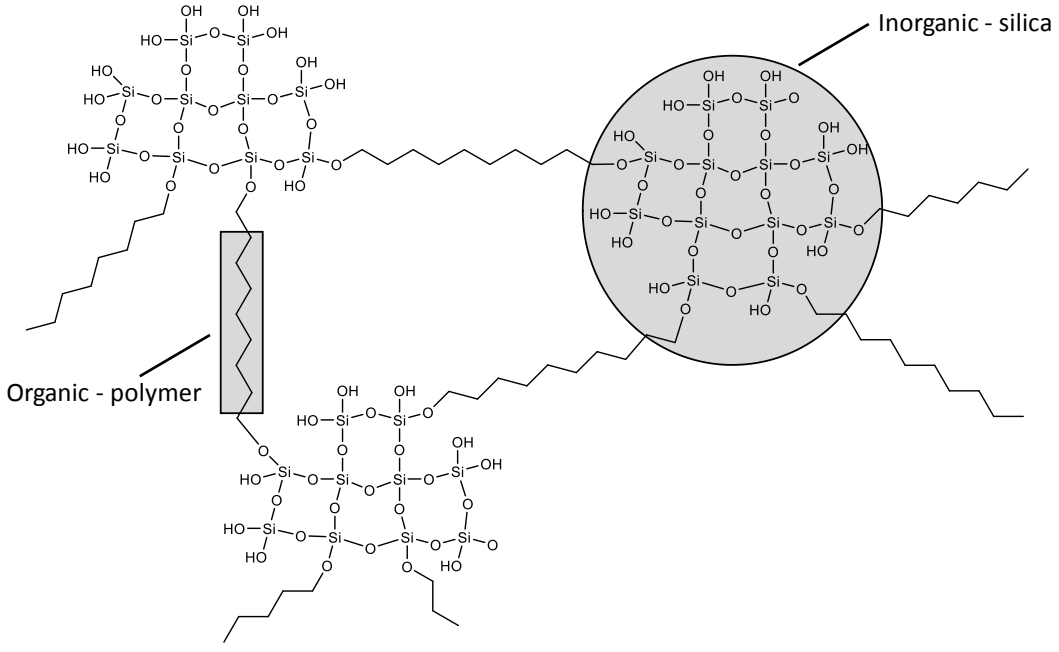


Figure 2.19 Schematic of an organic/inorganic Class II hybrid material.

2.6.2 Class I hybrids

Class I hybrids are synthesised by incorporating a soluble polymer into the inorganic sol and the organic polymer is mechanically entrapped within inorganic silica network during network formation. The organic polymer chains are also hydrogen bonded to Si-OH groups of the inorganic silica network. [119]

Polyvinyl alcohol (PVA) is one of the organic polymers that is used to synthesis Class I hybrid, because it is biocompatible, soluble in water and the hydroxyl groups on the polymer chains lead to the formation of hydrogen bonds with Si-OH groups on the inorganic silica. Pereira *et al.* [121] produced PVA hybrid foam scaffolds by incorporating PVA with molecular weight (M_w) of 16 kD_a into inorganic 70S30C glass composition, where $CaCl_2$ and TEOS were used as calcium and silica precursors respectively. They proved that the PVA hybrid foam scaffolds were lower stiffness than 70S30C glass foam scaffold and the strain to failure (compression) was improved from around 1 % to between 6% and 8% for PVA hybrid scaffold. The bioactivity of PVA hybrids were also studied by several groups [122] with HCA layer formed on the surface of calcium containing PVA hybrids after 24 h of immersion in SBF. Gomide *et al.* [123] showed that the cell proliferation and osteogenic differentiation of mesenchymal stem cells (MSCs) increased *in vitro* when PVA hybrid (50 wt% 70S30C + 50 wt% PVA) was present, as compared to the MSCs without the presence of hybrid. PVA is non-biodegradable but water soluble, therefore PVA with molecular weight lower than 50 kD_a (the kidney threshold for clearance of water soluble polymer) can be easily excreted by kidney [18, 124].

2.6.3 Strategies for Class II hybrids synthesis

Two strategies can be applied for Class II silica/polymer hybrid synthesis: a coupling agent is used to link the polymer and silica network, or a silane containing polymer, such as polydimethoxysilane (PDMS), can be used directly to covalently link to silica without the aid of coupling agent. [18]

PDMS has a silica backbone with organic side groups and a methyl group at each end of PDMS (Figure 2.20). PDMS is not soluble in water or ethanol. But during the sol-gel process, the terminal methyl group is hydrolysed in sol to form a silanol group, which then reacts (condensation) with the other silanol groups from inorganic silica network (hydrolysed TEOS) to covalently link the PDMS with silica network [119,

125-128]. Although the coupling of PDMS and TEOS are excellent but PDMS is not a degradable polymer. For tissue engineering applications, a biodegradable polymer with non-toxic degradation products is preferable, therefore coupling agent is used to broaden the types of polymers that can be used in Class II hybrid synthesis.

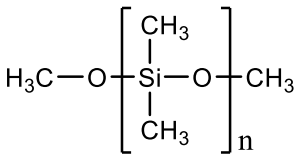


Figure 2.20 Chemical structure of PDMS.

Since the sol-gel process is used for hybrid synthesis, the polymer used must be soluble in the sol. Therefore, a suitable solvent needs to be used to produce a homogenous hybrid. The solubility of polymer can also be increased by using a coupling agent which link the polymer with inorganic silica. [129]

A coupling agent for silica/polymer hybrid synthesis is usually a short chain polymer which contains three alkoxysilane groups on one end of the chain and a functional group that can react with the polymer on the other end. The alkoxysilane end can be hydrolysed and then can condense with the silanol groups of inorganic silica. The polymer must contain a nucleophilic group, such as -OH, -COOH or -NH_2, in order to bond to the coupling agent. 3-(glycidyloxypropyl)trimethoxysilane (GPTMS), 3-isocyanatopropyltriethoxysilane (ICPTES) and 3-aminopropyltrimethoxysilane (APTES) are the most commonly used coupling agents for Class II silica/polymer hybrid synthesis (Figure 2.21).

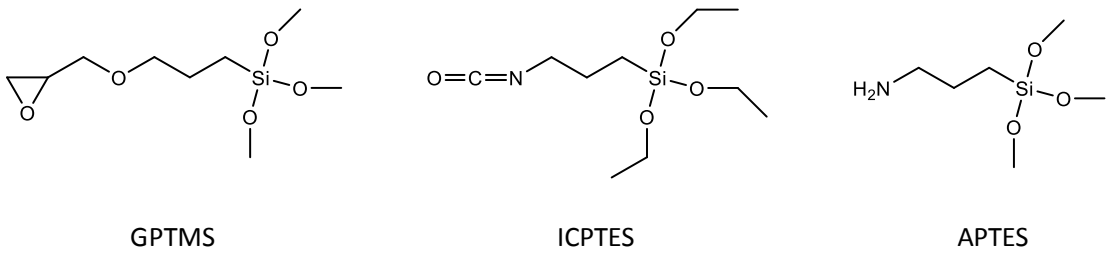


Figure 2.21 The chemical structures of commonly used coupling agents for Class II silica/polymer hybrid synthesis: GPTMS, ICPTES and APTES.

For the polymers which contain carboxylic acid functional groups (-COOH), such as gelatin, GPTMS is usually used as the coupling agents, where the epoxy ring of GPTMS

opens and reacts with the -COOH group on the polymer to form an ester linkage [130, 131]. Some polymers have been chemically modified in order to react and bond with the coupling agent, such as polysulfone (PSF) and acrylonitrile butadiene styrene (ABS). As reported by Guiver *at al.* [132] PSF can be converted into carboxylated polysulfone (C-PSF) via a two-stage reaction with n-bytyllithium, CO_2 dry ice and diluted HCl. The C-PSF can then functionalised by GPTMS for hybrid synthesis [133]. Hsu *et al.* [134] showed that -COOH and -$CONH_2$ groups on ABS can be made via oxidation of ABS with hydrogen peroxide. The two functional groups (COOH and $COONH_2$) allowed ABS to be functionalised with GPTMS for hybrid synthesis. Polymers containing amino groups can also be functionalised with GPTMS.

ICPTES and APTES are preferred when a -OH functional groups containing polymer is chosen, such as DL-lactide oligomers can be functionalised by ICPTES and then undergo hydrolysis and condensation to form cross-linked polymers [135]. ICPTES only react with the terminal hydroxyl groups, therefore the amount of crosslinking in the hybrid depends on the molecule weight of the polymer. The crosslinking of the hybrid can be increased by using the polymer with lower molecular weight [119].

GPTMS and ICPTES have no severe influence on the silica network formation and structure. They are not involved in the formation of inorganic silica network and the basic inorganic network is nearly exclusively built from the Si precursor [136]. Whereas APTES has a large influence on the inorganic silica network formation and structure because of the presence of basic amine group (-NH_2) on APTES, which can act as a catalyst for condensation. Because of the hydrogen bonding ability of APTES, the hydrogen bonds form between the -NH_2 groups of APTES and Si-OH groups of the inorganic silica, consequently promote network formation. Furthermore, the hydrolysis and condensation of TEOS can be catalysed by the -NH_2 of APTES. [137]

The coupling agent can be used prior to sol-gel process to functionalise the polymer or it can be used during sol-gel process to react with the organic and inorganic phases simultaneously.

2.6.4 Organic polymers for bioactive hybrids

For bone tissue engineering applications, the bioresorbable materials with appropriate properties, such as biocompatibility and bioactivity, are preferred. Bioactive hybrids synthesised with biodegradable or bioresorbable polymers are able to achieve the requirements. The commonly used polymers are summarised in this section.

Collagen

Type I collagen is the natural polymer found in bone therefore it is sensible to use collagen as the organic phase in hybrid synthesis for bone tissue engineering applications. Collagen has excellent mechanical properties due to its triple helix of polypeptide chains[119]. These polypeptide chains are held together by hydrogen bonds between the NH_2 and COOH groups along the chain but also by covalent bonds. The presence of NH_2 and COOH groups also allow functionalisation for hybrid synthesis. The other reason for choosing collagen for hybrid synthesis is due to its excellent biocompatibility. Collagen can be degraded by specific enzymes which attack the triple helix molecule, and after the triple helix comes apart, the other enzymes in the body attack the individual polypeptide chains. Collagen is usually prepared from living organism, including bovine and porcine, therefore there is a risk of transferring diseases. [119]

As reported by Heinemann *et al.* [138], a silica/collagen hybrid material can be synthesised by using the fibrillary collagen obtained from cattle hides and TEOS as the silica precursor. They stated that under neutral pH the positive charged amine groups of collagen acts as preferred nuclei for polycondensation of negatively charged silica species. The silica-collagen hybrid material has been proven to be biocompatible as it is able to support the adhesion, proliferation, and osteogenic differentiation of human mesenchymal stem cell (MSC). However only small amount of collagen can be incorporated into the hybrid system as collagen has low solubility. Additionally, the source of collagen is the other problem, as collagen is xenogenous. Although the immuno-rejection of non-human collagen is uncommon when compare to transplantation of organ, but there is still a chance of 3-5% that non-human collagen can cause immune response [119, 139].

Gelatin

Gelatin is obtained from partial hydrolysis of collagen, which involves the breakdown of the backbone chain and the rupture of the cross-links that hold the polypeptide chains together [140, 141]. The commercially available gelatins are the heterogeneous mixture of polypeptides with a molecular mass range from several kDa to more than 1000 kDa [140]. They can be prepared from a variety of animal sources, such as pig skin and bovine bone etc. The chemical structure of gelatin is similar to collagen therefore gelatin is also enzymatically degradable and contains functional groups (NH_2 and COOH) which can react with the coupling agent for Class II hybrid synthesis.

Mahony *et al.* [131] created silica/gelatin hybrids using TEOS with GPTMS as the coupling agent, then successfully made the hybrid material into porous scaffolds via a novel sol-gel forming and freeze drying approach. The epoxy ring of the GPTMS reacts with the carboxylic acid group of gelatin thus covalently link the gelatin with silica network formed from TEOS. The important discovery was that the congruent dissolution of the silica/geltin hybrid was achieved by increasing the amount of GPTMS cross-linking between organic and inorganic phases. The stiffness of the porous hybrid scaffold also increased as the amount GPTMS crosslinking increased. The hybrid scaffolds (interconnect diameters $\approx 200\ \mu m$) made with 60 wt% gelatin and molar ratio of GPTMS : gelatin of 500 was very flexible and elastic, with a linear-elastic region up to 34 % strain, when doubling the GPTMS cross-linking (molar ratio of GPTMS : gelatin = 1000) caused a 360 % increase in stiffness (young modulus) of the hybrid scaffold with interconnect diameters of 200 μm. The dissolution and mechanical properties of the hybrid material developed by the author are highly tailorable and that allows the hybrid materials to be used as the regenerating scaffolds for both hard and soft tissue.

Poly(γ-glutamic acid)

Poly(γ-glutamic acid) (γ-PGA) is a naturally occurring anionic biopolymer made up of repeating units of L-glutamic acid, D-glutamic acid or both [142]. The repeating units of γ-PGA are linked via peptide bonds between amino groups and γ-carboxylic acid groups to form a linear polymer (Figure 2.22). γ-PGA can be produced using bacteria, especially those of *Bacillus* species, such as *Bacillus subtilis* [142, 143]. The polymer has the potential to be use in food and medical applications due to its biodegradable

(undergo both hydrolytic and enzymatic degradation), non-toxic and non-immunogenic properties [142]. The free acid form of γ-PGA is not water soluble therefore it cannot be used directly in sol-gel process for hybrid synthesis. Because γ-PGA is anionic, the COO^- groups of γ-PGA can be ionic bonded to a variety of cations, including calcium and sodium, in order to form a water soluble γ-PGA salt [119, 142].

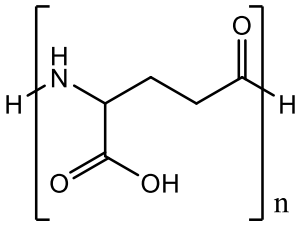


Figure 2.22 Chemical structure of bacterial synthesised γ-PGA.

Poologasundarampillai *at al.* [144] successfully synthesised calcium containing silica/ γ-PGA hybrids via sol-gel process by using GPTMS as the coupling agent. In the study, free acid form of γ-PGA and GPTMS were reacted in dimethylsulfoxide (DMSO) prior to sol-gel process. The functionalised γ-PGA then mixed with hydrolysed TEOS to allow the formation of silica/ γ-PGA hybrid. The γ-PGA hybrid materials were found to be non-toxic to the osteosarcoma cells and allowed cells to attach on the surface of the material. However, DMSO solvent must be removed during processing as the long-term effects of DMSO in vivo are unknown [119]. Hence Valliant *et al.* [145] incorporated γ-PGA into sol-gel process by converting free acid form of γ-PGA into calcium γ-PGA salt which is soluble in water. In order to prepare calcium γ-PGA salt, the free acid form of γ-PGA was reacted with $Ca(OH)_2$ in deionised water. Calcium γ-PGA salt acts as both calcium and organic sources in the hybrid system. The resulting hybrids exhibited excellent compressive strength and had the uniform distributions of Ca and Si ions.

Poly(glycolic acid), Poly(lactic acid) and poly(lactide-co-glycolide)

Poly(glycolic acid) (PGA) and Poly(lactic acid) (PLA) are synthetic saturated aliphatic polyesters which are bioresorbable and biocompatible. The chemical properties of PLA and PGA allow hydrolytic degradation via de-esterification. The monomers of PGA

and PLA, glycolic acid and lactic acid, are non-toxic to human body and can be removed by natural pathways. [115]

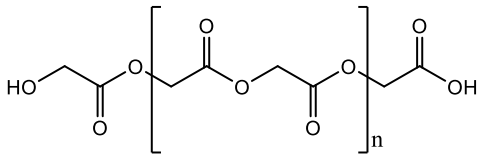
PGA can be synthesised via different routes, including polycondensation of glycolic acid and ring-opening polymerisation of glycolide. PGA is a highly crystalline polymer (45 - 55 % crystalline) with a melting point of 220 - 225^{o}C and a glass transition temperature of 35 - 40^{o}C. Due to the high degree of crystallisation, PGA is not soluble in most organic solvents and water, but the terminal carboxyl group and hydroxyl group allow PGA to be modified by coupling agent in sol-gel process. [146] PGA requires around 6 to 12 months to be completely absorbed, where the sutures of PGA lose about 50% of their strength after 2 weeks and 100% at 4 weeks. [115, 146] The degradation products of PGA are eliminated via the citric acid cycle or can excreted directly in urine [146].

Synthesis of PLA is similar to PGA, where it can be synthesised by using lactic acid or lactide as the monomer. The most common route to synthesis PLA is the ring opening polymerisation of lactide. Lactide is the cyclic dimer of lactic acid, which exists as two optical isomers, D and L, where L-lactide is naturally occurring isomer [146]. Therefore, the common PLA exists as L-PLA (PLLA) which is synthesised from pure L-lactide. PDLLA is synthesised from racemic mixture of D-lactide and L-lactide. PLLA and PDLLA have different mechanical properties and degradation rate. PLLA is a semi-crystalline polymer (around 37% crystalline) which exhibits high tensile strength and low elongation and consequently a high young modulus that makes then more suitable for load-bearing applications, such as in orthopaedic fixation. PDLLA is an amorphous polymer due to the random distribution of both D- and L- lactic acid in PDLLA which makes it unable to arrange into a crystalline structure. PDLLA has lower tensile strength and higher elongation when compare to PLLA [146]. PLLA degrades at a much lower rate than PDLLA, the implanted PLLA bone plates and screws required more than 2 years to be completely absorbed [147], where the degradation time for PDLLA is around 6 to 12 months [115]. The degradation products of PLA can be converted into carbon dioxide and water in citric acid cycle [146].

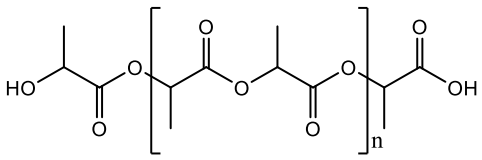
The presence of a methyl group makes PLA more hydrophobic than PGA and sterically hinders the ester bonds from hydrolytic cleavage therefore PLA degrades slower than PGA. The properties of the polymer can be tailored by altering the molecular weight of the polymer or copolymerisation with other monomers. Copolymes of L-lactide with

glycolid or D,L-lactide is prepared to disrupt the crystallinity in order to increase the degradation rate. In addition, high molecular weight PGA exhibits high strength and young modulus, therefore it is too stiff to be used as sutures. Glycolide can be copolymerised with other monomer to soften the resulting material. [146]

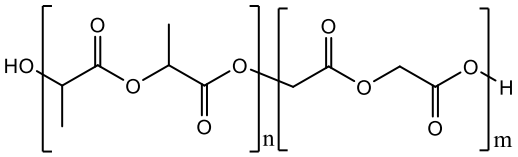
Copolymer of PLA and PGA, poly(lactide-co-glycolide) (PLGA), can be synthesised by copolymerisation of lactide and glycolide. The chemical structures of PLA, PGA and PLGA are shown in Figure 2.23.



Poly(glycolic acid)



Poly(lactic acid)



Poly(lactide-co-glycolide)

Figure 2.23 Chemical structures of poly(lactic acid), poly(glycolic acid) and poly(lactide-co-glycolide).

PLGA has a wide range of degradation rate which is governed by the composition of chains (proportions of L-lactic acid, D-lactic acid and glycolic acid). But there is no a linear relationship between the PLGA chains composition and its mechanical and degradation properties. The relationship between PLGA composition and degradation time is schematically illustrated as a U-shape graph, where the PLGA contains 50% of glycolide and 50% of D,L-lactide degrades faster than either homopolymer (PGA and PLA). Furthermore, PGLA copolymer of L-lactide with 25-70 % of glycolide are amorphous because the regularity of the polymer chain is disrupted by other the other monomer. [146] PGLA is also degradable and degradation products are glycolic acid and lactic acid molecules which can be completely removed from the body.

There are some major drawbacks to the use of these polymers including the formation of acidic degradation products in vivo which can cause an inflammation response.

These polymers also underdo bulk erosion with autocatalysis therefore can sometimes cause scaffolds to fail prematurely. [115]

Rhee *et al.* [148] synthesised calcium containing Class II PLGA/ICPTES hybrid monoliths using $Ca(NO_3)_2$ as the calcium precursor. Two PLGA copolymer compositions were used for hybrid synthesis in the study, the high (50 % PLA 50 % PGA) and low (90% PLA 10% PGA) degradable PLGA. They found the hybrid synthesised with high degradable PLGA showed no HCA formation after 28 d of immersion in SBF, whereas the hybrid with low degradable PLGA exhibited HCA formation ability after 3 d of immersion in SBF. They stated that the fast release of acidic degradation products from high degradation PLGA hybrid lowered the pH of SBF thus inhibited the nucleation and growth of HCA crystal. However, the mechanical properties of the hybrids were not reported.

2.6.5 Poly(ε-caprolactone)

Poly(ε-caprolactone) (PCL) is known to be a biocompatible, bioresorbable and semi-crystalline synthetic aliphatic polyester which has the melting point around 58 - 63^{o}C and glass transition temperature of -60^{o}C [146]. PCL can be used in a wide range of biocompatible scaffold fabrications as it is a FDA approved polyester [149]. PCL is prepared from ring opening polymerisation of cyclic ε-caprolactone and it can be blended with other polymers, such as PLA and PLGA, to alter the degradation or mechanical properties of the resulting material [149]. PCL is insoluble in water, therefore for sol-gel hybrid synthesis, PCL and coupling agent are reacted in the selected solvent prior to sol-gel process, such as tetrahydrofuran (THF) or toluene. Many studies have been done on the hybrids with PCL as their organic phase [150-159].

Class II silica/PCL hybrids

Silica/PCL hybrid was first synthesised by Tian *et al*. [156] using TEOS, PCL diol and ICPTES. The biocompatibility and biodegradability of the silica/PCL hybrids have also been investigated in the other early study done by Tian *et al.* [157]. In the study, fibroblasts were used to evaluate the biocompatibility of the silica/PCL hybrid materials (contained different amount of PCL: 15%, 30% and 50% PCL, pure PCL polymer used as control) where cells attached to the surfaces of all the silica/PCL hybrids but not on

pure PCL polymer. The silica/PCL hybrids were shown to be degradable in porcine esterase solution thus confirmed the potential of biodegradability of the hybrid materials.

Calcium containing silica/PCL hybrids were synthesised by Rhee *et al.* [150] by covalently linking α,ω-hydroxyl poly(ε-caprolactone) (PCL diol) with silica network using ICPTES as the coupling agent. 1,4-diazabicyclo[2,2,2]octane (DABCO) and toluene were used as the catalyst and solvent respectively. The functionalisation of PCL diol with ICPTES is schematised in Figure 2.24. The study shows that the degradability of the silica/PCL hybrid system mostly comes from the PCL phase. However, the calcium source was calcium nitrate tetrahydrate, so the calcium was not in silica network and the toxic nitrate could not be removed at low temperature.

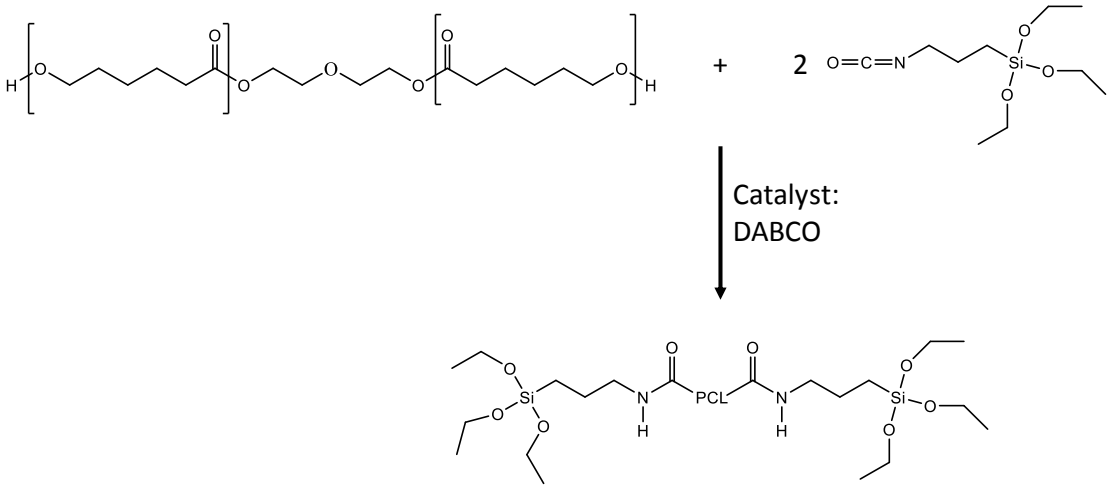


Figure 2.24 Schematic of functionalisation of PCL diol with ICPTES for silica/PCL hybrid synthesis [150].

The effect of the molecular weight of PCL on the properties of silica/PCL hybrid was also investigated [151]. The PCL hybrid containing low molecular weight PCL (around 2.3 kDa) degraded faster and released the ionic dissolution products (Ca and Si) faster than the hybrid containing high molecular weight PCL (around 6.6 kDa) despite the higher amount of cross-linking. It was proposed that the molecular weight of the polymer might have a stronger effect than cross-linking to the properties of the hybrid. In addition, the nucleation and growth of apatite crystals are faster and more uniform when low molecular weight PCL is used, because the silica-rich domains are more evenly distributed and well dispersed in the PCL hybrid made with low molecular weight PCL. The amount of PCL content in the silica/PCL hybrid is an important factor that not just affects the degradability, but also bioactivity and mechanical property of

the hybrid. Another study done by Rhee [152] suggests that the silica/PCL hybrid contained higher amount of PCL (80 wt% of PCL) had lower apatite formation rate in SBF and showed a polymer like ductile-tough fracture behaviour, whereas the PCL hybrid with lower amount of PCL (40 wt% of PCL) had higher apatite formation rate but a more stiff and brittle mechanical property. The silica/PCL hybrid contained 60 wt% PCL and 40 wt% TEOS had the intermediate values of bioactivity and mechanical properties. This PCL hybrid (40 wt% PCL) had a tensile strength of 21 MPa and a young modulus of 600 MPa, while the strain to failure was around 50 %, which are comparable to human trabecular bone, therefore the PCL hybrid have the potential to be used as a bone repairing material. ICPTES was used as the coupling agent in Rhee's study and it made the PCL hybrid system unsuitable for 3D printing scaffold fabrication since other literature suggested that the gelling time for the PCL hybrid system was around 2 d and which is too long for 3D printing scaffold fabrication [156]. Therefore, a different protocol was used to synthesis PCL hybrid in this project.

Degradation of PCL

Despite more than 1000 papers about PCL based biomaterials have been published during the last 10 years, only a small number of publications have included the study of degradation and resorption kinetics of the PCL scaffolds [149]. However, it is widely accepted that PCL undergoes hydrolytic degradation which breaks the ester bond within the PCL chain. The slow degradation of PCL allows it to be used in long-time degradation applications. The degradation rate of PCL is highly dependent on the molecular weight of the polymer. From several degradation studies of PCL [149, 160-165], it can be concluded that PCL undergo a two-stage degradation process *in vivo*: first stage involves random chain scission by hydrolytic cleavage of the ester linages which cause a decrease in molecular weight of the PCL without deformation. The second stage starts when the molecular weight of PCL has reduced to approximately 5000 Da, resulting in a significant weight loss of the PCL material and PCL implant start to fragment. Jenkins *et al.* [162, 163] suggested that the degradation of PCL occurs preferentially in the loosely packed amorphous regions as water can diffuse more easily into amorphous regions and hydrolytically degrade the PCL from the amorphous regions. Shih *et al. [164]* showed higher weight loss rate *in vitro* (in PBS) from PCL with lower degree of crystallinity. It has been proved that the degradation by-products

of PCL (low molecular weight PCL and caproic acid monomer) do not trigger any residual side effects and can be completely excreted from the body [160]. The low molecular weight PCL fragments (less than 3000 Da) undergo intracellular degradation inside the phagosomes of macrophages and giant cells, then the hydrolysis intermediates 6-hydroxyl caproic acids enter the citric acid cycle and are eliminated from the body [149, 166].

2.6.6 Poly(tetrahydrofuran)

Poly(tetrahydrofuran) (polyTHF) is not a common polymer to be used in bioactive hybrid synthesis for bone regeneration because it is not degradable but is biostable [167, 168]. A biostable material is considered to be the material where physiological interactions do not lead to the change in properties of the material and loss of function [169]. In the PCL hybrid system used in the project, tetrahydrofuran (THF) was used as the solvent for PCL functionalisation. Polymerisation of THF was observed by Francesca Tallia [170] during the PCL functionalisation stage because of the presence of epoxy ring (of GPTMS) and $BF_3O(C_2H_5)_2$ during the functionalisation of PCL. The details of polymerisation of THF will be discussed in section 7.2.3.

2.6.7 Calcium source for bioactive sol-gel hybrid

Calcium plays an important role in HCA formation which provides bonding with the bone. Furthermore, the calcium ions released from bioactive glass has also been shown to be capable of inducing osteoblast proliferation [105]. Therefore, it is essential to incorporate calcium into the bioactive hybrid for bone regeneration.

Calcium nitrate is the conventional calcium precursor for sol-gel bioactive glass but it is not suitable to be used in sol-gel hybrid synthesis as the toxic nitrate by-product can only be removed when heated to the temperature above 400^{o}C [42]. This heat treatment cannot be applied in sol-gel hybrid synthesis as the organic polymer will be burned off at such a high temperature. In addition, the calcium from calcium nitrate only incorporated into the silica network at the temperature higher than 400^{o}C [42]. (section 2.2.6)

The alternative water soluble calcium precursor, calcium chloride, has been widely used to produce the calcium containing hybrids, including silica/calcium/phosphate/PCL

hybrid [171], silica/calcium/PVA hybrid [172] and silica/calcium/γ-PGA hybrid [144], because calcium chloride does not produce toxic by-product when used in sol-gel process. The problem with using calcium chloride as the calcium source has been noticed by Poologasundarampillai *et a.l* [144]. They stated that calcium was not incorporated into the material (silica/calcium/γ-PGA hybrid) but instead recrystallised on the surface as calcium chloride. Therefore, a new calcium precursor is needed for sol-gel hybrid synthesis.

Calcium methoxyethoxide (CME) is the calcium alkoxide which has been shown to have the potential to be used in sol-gel bioactive hybrid synthesis. As reported by Pereira *et al.* [172] sol-gel glass synthesised with CME presented a much higher homogeneity than calcium nitrate derived sol-gel glass, indicating an improvement in calcium incorporation when CME is used. Poologasundarampillai *et al.* [173] successfully synthesised the silica/calcium/γ-PGA hybrid using CME as the calcium source. He stated that calcium from CME was well incorporated into the both organic and inorganic phases of the hybrid at room temperature and resulted in a homogenous silica/calcium/γ-PGA hybrid. The ionic crosslinking of γ-PGA by calcium was observed in the CME derived hybrid, hence steady releases of calcium and γ-PGA were observed. Additionally, the ionic crosslinking of γ-PGA by calcium also resulted in an improvement in compressive strength of the hybrid material. Cell culture study was also conducted by the author, human bone marrow derived mesenchymal stem cells (hMSCs) were used in the study. The result of cell culture study shows no cytotoxic effect was induced by the CME derived hybrid. However, CME is found to be highly reactive to water and hydroxyl groups, it will induce “rapid gelation” when mixing with aqueous sol and it is the main challenge to use CME in sol-gel process. But once controlled, the rapid gelation is beneficial for certain application, such as fabrication of 3D printing hybrid scaffold. The mechanism of rapid gelation of CME when reacts with water is still unknown, it might be because of the colloidal suspension of calcium oxide which makes the sol become gel-like rather than a real gel.

2.7 Objectives of the thesis

The aim of this thesis was to synthesise a porous hybrid scaffold with controlled ions release and optimal bioactivity. In order to achieve the aim, the objectives of this thesis were therefore to:

1. Understand the structure evolution during synthesis of sol-gel derived silicate glasses containing calcium and phosphate where sol-gel derived silicate glasses containing different ratios of calcium to phosphate. **(Chapter 4: silicate based sol-gel glass containing phosphate);**

2. Investigate the effect of alternative phosphate precursors (DEPETES and TBP) on the structures and properties of the sol-gel derived silicate glass in order to have controlled ions release from the sol-gel glasses. **(Chapter 5: sol-gel glass synthesised with alternative phosphate sources);**

3. Optimise the calcium and phosphate precursor used in the sol-gel process for low temperature synthesis **(Chapter 6: low temperature sol-gel derived bioactive glass);**

4. Incorporate the suitable bioactive glass into a bioresorbable polymer (PCL hybrid system developed by Francesca Tallia) to synthesise the bioactive hybrid materials. Then to fabricate porous 3D scaffolds with the bioactive hybrid material using 3D printing technique **(Chapter 7: calcium containing PCL hybrids).**

3 Characterisation methods

3.1 Particle size measurement

All the samples were ground into powders and sieved to particle size smaller than 38 μm using a sieve shaker. The particle size distributions for TEP glasses and DEPETES glasses samples were measured using Malvern Mastersizer 2000E (Figure 3.1). Mastersizer 2000E determines the size of a particle from the scattering pattern produced when it passes through a laser beam in an optical bench. Each size of particle will have its own characteristic scattering pattern. Theories used by the Mastersizer 2000E are Mie theory and Fraunhofer model. Mastersizer works backward from the theories and calculates the size of particles that created the scattering pattern in optical bench.

The Fraunhofer model assumes the particle is a solid, opaque disc of a known size when passing through a laser beam. But this model is only suitable for certain particles and does not describe the scattering exactly if the particles are not disc shape or when the particles are transparent. Mie theory is able to predict the light scattering patterns of all materials under all conditions, but it assumes the particle is spherical and the user knows some specific information about the particle, such as the size of the particle, refractive index and its absorption.

Good sample preparation is important and a representative sample must be taken. For dry sol-gel glass powders, if stored for too long, the larger particles tent to rise to the top of the container and the smaller particles stay at the bottom of the container. Therefore, here, sol-gel glass powders were well mixed before a measurement was taken. Dry sol-gel glass powders were mixed with deionised water in a centrifuge tube and placed it in sonication bath to disperse the powder particles evenly. Then the powder-water mixture was introduced into the sample dispersion unit of Mastersizer 2000E until it reached the correct concentration (Mastersizer detects the concentration in real time), then the powders were delivered to the optical bench. In the optical bench, the scattering pattern of the prepared sample was collected by the detector array and raw data was analysed by the Malvern software, using the two theories mentioned above.

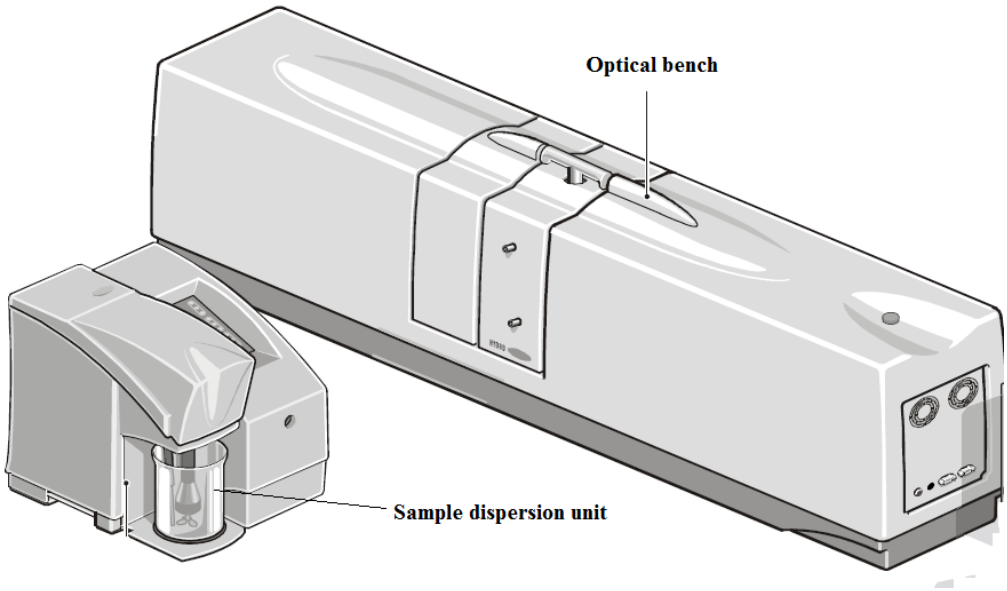


Figure 3.1 Diagram of Mastersizer 2000E (adapted from the user manual of Mastersizer).

3.2 Nitrogen sorption: Surface area and pore size distribution

Nanoporosity of phosphate containing glasses was analysed by nitrogen sorption, using the Quantachrome AUTOSORB-6 (AS-6). Before measurement, the sample was transferred into a 9 mm sample tube and degassed using AUTOSORB degasser at room temperature over night to remove any contaminant from the surface of the glass particles, e.g. water vapour and physically adsorbed gases. After degassing, the sample tube was filled with helium and weighed before starting the measurement. The technique was not carried out on hybrids as they were determined not to be mesoporous due to low volume of adsorbed nitrogen. AS-6 operates by measuring the quantity of nitrogen adsorbed onto or desorbed from the sample at 77K (the temperature of liquid nitrogen). Nitrogen condenses onto the surface of a material as relative pressure (P/P_o) in the sample tube increases, and the amount of absorbed nitrogen is measured. The adsorbate nitrogen initially forms a monolayer that cover the surface of the material, as the pressure increases more nitrogen is absorbed and form multiple layers until all the pores in the material have been filled. Plotting relative pressure (P/P_o) against volume of nitrogen absorbed generates the absorption isotherm. The adsorbate nitrogen is then desorbed when the pressure goes down and the desorption isotherm is also recorded. Different materials can exhibit different types of isotherms, according to the shape of isotherm they have been classified into six types by International Union of Applied Chemistry (IUPAC) [174] as shown in Figure 3.2.

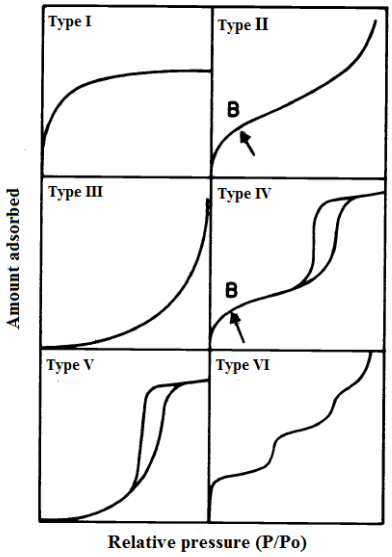


Figure 3.2 Different types of isotherms (adapted from [174]).

Type I, II, III and VI isotherms have the overlapping adsorption and desorption curves, a reversible isotherm indicates that the rates of nitrogen adsorption onto and desorption from the material are the same at a given pressure. Type I isotherms are usually given by a microporous material having relatively small external surface area [174]. Type II shows monolayer to multilayer adsorption, point B indicates finishing of the monolayer coverage and the beginning of the multilayer adsorption. The Type III isotherms are rare and they are caused by the adsorbate-adsorbate interactions, for example, nitrogen adsorbed onto polyethylene. Type VI isotherm shows the stepwise multilayer adsorption on a non-porous surface. The adsorption and desorption curves of Type IV and V do not overlap because of the delay desorption, where the adsorption and desorption curves form a hysteresis loop. Type V isotherms are not common and hysteresis loop of Type IV isotherms can be further classified into four groups as shown in Figure 3.3. [174]

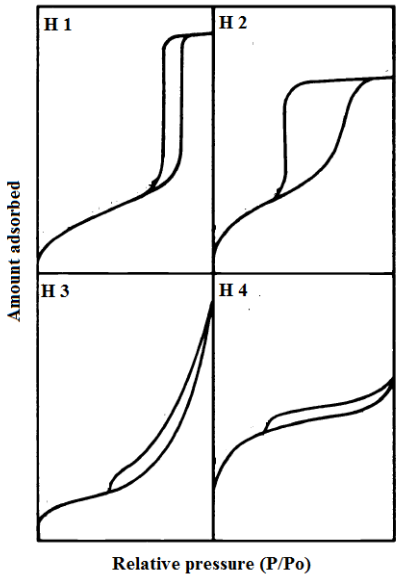


Figure 3.3 Different types of hysteresis loops (adapted from [174]).

The shapes of hysteresis loops are often used to identify the pore structures of the adsorbent material. Type H1 loops are attributed to agglomerates of uniform spherical particles, giving narrow distribution of pore sizes. Porous glasses tend to give type H2 loops, but the pore size and shape are not well defined. In the past Type H2 loop was attributed to pores with narrow necks and wide bodies (ink-bottle pores), but it is now being recognised as an over simplified picture of the system. Type H3 loop is often associated to aggregates of plate-like particles giving rise to slit-shape pores and type H4 loops is often attributed to narrow slit-like pores. [174]

The surface areas of the sol-gel glasses were determined by using the Brunauer Emmett Teller (BET) method. For most solid adsorbent, using nitrogen as the adsorbate, the adsorption isotherm plot is nearly linear between relative pressure (P/P_o) of 0.05 to 0.30, and BET method use the linear region of adsorption isotherm which associates with monolayer formation to determine the surface area of a material. The linear form of the equation is shown below (Equation 3.1) [175]:

$$\frac{1}{\nu[(P_o/P)-1]} = \frac{C-1}{\nu_m C}\left[\frac{P}{P_o}\right] + \frac{1}{\nu_m C} \qquad (3.1)$$

Where P is the equilibrium pressure, P_o is the saturation pressure, ν is the volume of gas adsorbed at a relative pressure P/P_o, ν_m is the volume of gas adsorbed when entire adsorbent surface is covered with a complete unimolecular layer, and C is the BET constant.

The BET plot of $\frac{1}{v[(P_o/P)-1]}$ (on the y-axis) against relative pressure P/P_o (on the x-axis) gives a straight line with gradient s and intercept i, where $s = \frac{C-1}{v_m C}$ and $i = \frac{1}{v_m C}$. The volume of monolayer, v_m, can be calculated from the gradient and intercept of the BET plot, where $v_m = \frac{1}{s+i}$. The total surface area S_t is then expressed as $\left[\frac{v_m \ N \ A_{cs}}{V}\right]$, where v_m is the volume of monolayer, N is Avogadro's number (6.023×10^{23} molecule mol^{-1}), V is molar volume of nitrogen gas and A_{cs} is the cross-section area of nitrogen (A_{cs} for hexagonal close-packed nitrogen monolayer at 77K is 0.162 nm^2). The specific surface area S can be expressed as $S=S_t/w$, where w is the sample weight. [175] Assuming a cylindrical pore geometry, pore size distributions are measured by applying Barrett Joyner Halenda (BJH) model to the desorption branch of the isotherm with the aid of Kelvin equation (Equation 3.2) [176, 177]:

$$r_K = \frac{2\sigma^{lg} v^l}{RT \ \ln(P/P_o)} \tag{3.2}$$

Where r_K is the Kelvin radius, σ^{lg} is the surface tension of the liquid condensate (8.85 ergs cm^{-2} for nitrogen at 77K), v^l is the molar volume (34.7cm^3 mol^{-1} for liquid nitrogen), R is the gas constant (8.314×10^7 ergs deg^{-1} mol^{-1}), T is the boiling point (77K for nitrogen) and P/P_o is the relative pressure. By using the appropriate constants for nitrogen the Kelvin radius can be expressed as (Equation 3.3):

$$r_K = \frac{4.15}{log(P_o/P)} \tag{3.3}$$

3.3 SBF dissolution and bioactivity

Simulated body fluid (SBF) has similar pH (pH 7.4) and ion concentrations to natural blood plasma. Investigation into apatite formation on the surface of a material in SBF is the first approach to predict *in vivo* bone bonding ability of a material. The dissolution rate (ion releases) of a material in SBF and its pH buffering ability are also important in predicting in vivo bone bioactivity of a material. SBF used in this work was prepared by following Kokubo's protocol [178]. The ingredients of SBF were added into 1600 ml of 37°C deionised water in a specific order and then filled the bottle with deionised

water to 2000 ml, finally adjust the pH to 7.40 at 37°C with 1 M HCl. The amounts of the ingredients for 2000 ml of SBF preparation are listed in Table 3.1. The chemicals used to prepare SBF in this work were all purchased from Sigma-Aldrich and used as purchased.

Table 3.1 The ingredients for 2000ml of SBF [178].

Order	Ingredients	Amount
1	NaCl (99.5%)	15.992 g
2	$NaHCO_3$ (>99.5%)	0.700 g
3	KCl (99%)	0.448 g
4	$K_2HPO_4 \cdot 3H_2O$ (99%)	0.456 g
5	$MgCl_2 \cdot 6H_2O$ (99%)	0.610 g
6	HCl (1M)	70 ml
7	$CaCl_2 \cdot 2H_2O$ (99%)	0.736 g
8	Na_2SO_4	0.142 g
9	$(CH_2OH)_3CNH_2$ (99.8%)	12.114 g

Jones *et al.* showed [179] that the optimal concentration for sol-gel derived 58S is 1.5 g L^{-1} in SBF. If the concentration of 58S in SBF exceeded 1.5 g L^{-1}, the inhibition of HCA formation was found to occur. Therefore, in this work 150 mg of glass sample in powder form was immersed in 100 ml of SBF and placed in a shaking incubator at 37°C and 120 rpm shaking speed [180]. 1 ml of SBF supernatant was collected for Inductively coupled plasma optical emission spectroscopy (ICP-OES) analysis at 0, 0.5, 1, 2, 4, 8, 24, 72, 168 and 336 h time points and replaced by 1 ml of fresh SBF. The pH of the SBF at each time point was also measured using pH meter with a thermal probe (Oakton pH 11 meter with Oakton general-purpose glass pH probe, Ag/AgCl electrode, and Oakton ATC probe). The pH meter was calibrated at pH 4, pH 7 and pH 10 before the measurements. Three SBF dissolution tests were done for each sample composition with mean and standard deviation values reported.

The powder samples were collected using filter paper (particle retention: 5 – 13 μm), washed with deionised water followed by acetone rinse and then dried at 40°C oven. The dry post-SBF immersion powder samples were ready for charactering tests, such as XRD and FTIR.

Inductively coupled plasma optical emission spectroscopy (ICP-OES) is the analytical technique for measuring the elemental concentrations in a solution. The sample solution is turned into aqueous aerosol by a nebuliser using argon as the carrying gas. Then the atoms in the sample are excited and ionised by passing the sample aerosol through the ICP flame. The electrons in the excited atoms then spontaneously revert to their ground state or a lower excitation state, emitting the radiation at specific wavelength, and the emitting radiation is then measured by the optical emission spectrometer. The frequency of the radiation is characteristic of the element. The concentration of elements in the sample solution is determined by comparing the intensity of the emission with that for standard solutions (calibration curve is obtained before sample analysis). [181]

Si, Ca and P concentrations of the sample immersed SBF at each time point were analysed by ICP-OES. In this work, ICP-OES was carried out using Thermo Scientific iCAP 6000 Series ICP. Before analysis, each solution was diluted by a factor of 10 with 2 M nitric acid (1 ml of sample solution + 9 ml of 2 M nitric acid) and standard solutions contain Si, Ca and P were prepared at 0, 2, 10 and 20 μg ml^{-1} for the calibration.

3.4 XRD

X-ray diffraction (XRD) reveals the information about the crystal structure of a material. XRD is based on the scattering (diffraction) of the X-ray beam as it hits the sample. Specific crystalline structures can diffract X-ray and give a unique diffraction pattern according to Bragg's law (Equation 3.4) [182]:

$$n\lambda = 2d \sin\theta \tag{3.4}$$

Where n is an integer, λ is the wavelength of the X-ray, d is the distance between atomic planes and θ is the angel of incidence. XRD patterns of a material can be affected by many factors, such as the shape of the crystal unit cell, the spacing between the atomic planes and the type of atoms.

XRD was carried out on samples before and after SBF dissolution with a desk top diffractometer, Bruker D2 PHASER, using a step scanning with Cu radiation, at 30 kV and 10 mA, with 0.030^{o} 2θ step size and a count rate of 0.5 s per step, from 6^{o} to 70^{o} 2θ. XRD is able to provide the information about the presence of crystal apatite structure in the samples, therefore XRD data was important to investigate the apatite formation on samples after immersion in SBF.

3.5 FTIR

Fourier-transfer infrared spectroscopy (FTIR) detects the covalent bonds with dipole moments in the sample. Covalent bonds with dipole moments can absorb infrared and vibrate. Only the infrared which has the specific energy (wavenumber) that matches the gap of the vibrational energy states of the functional group in the sample is absorbed, providing a correlation between the wavenumber of absorbed infrared and structure of the molecule. A plot of IR intensity against path difference is called an interferogram. Then the interferogram is Fourier transformed to give a spectrum. A complete spectrum for a specific wavelength is collected by translating the moving mirror back and forth once. [183]

Here, FTIR spectra were collected before and after SBF dissolution using Nicolet iS10 FTIR machine with the diamond ATR accessory in the range 400 – 4000 cm^{-1}. FTIR-ATR is able to characterise the powder sample without further preparation. FTIR-ATR can only scan the surface of the powder sample, but it is still capable of providing reliable data as the powder samples were homogeneous.

3.6 Scanning electron microscope

SEM is the technique that can reveal surface morphology of a material at nanometer level. The sample is scanned by the non-destructive electron beam and the electrons bombard the sample surface creating secondary electrons emitted from the sample surface which contribute to the formation of SEM image. Backscattered electrons are also detected and used to form the backscattered electron images [184]. SEM requires the samples to be conductive, otherwise the electron beam will charge it up and distort the SEM image, therefore for bioactive glasses or hybrids a chromium coating is needed.

In this work, LEO Gemini 1525 FEG-SEM was used to image the surface morphology of powder samples, with beam voltage of 3 ～ 5 kV and working distance of 5 mm ～ 10 mm, before and after SBF dissolution. JEOL JSM 6010LA was used to investigate the macroporous structures of the 3D printing PCL hybrid scaffolds with beam voltage of 20 kV and working distance of 12 ～ 13 mm. Samples for SEM were prepared by coating with 10 nm thick chromium on the powder samples and 20 nm thick chromium on the 3D printing scaffolds.

3.7 Transmission electron microscope

TEM is the technique that can reveal the inner morphology of a material. In TEM, a beam of electron is transmitted through a thin specimen (less than 100nm). Each electron passing through the specimen has a number of possible fates: 1. Directly transmitted through the specimen without interacting with any atom. 2. It is deflected but without losing energy (elastically scattered electrons and backscattered electrons) 3. It loses a significant amount of energy as it passes through (inelastically scattered electrons), as a result secondary electrons or X-ray may be emitted [185, 186]. The scattering of the incident beam by the specimen results in the contrast of TEM image. In mass-thickness dominated TEM image, the lighter region in a TEM image is where more electrons have been transmitted through (i.e. regions where the sample is thinner or contain less heavy atoms) and the darker region in a TEM image is where less electron have been transmitted through.

Energy dispersive X-ray spectroscopy (EDS) is the analytical tool that usually applied with TEM and SEM to give the information about the atomic composition of the sample. When the incident high energy electron is inelastic scattered by an atom in the sample, it loses the corresponding energy and ejects the electron from an inner shell (lower energy shell) while creating an electron hole (the energy loss from the incident electron is transferred to the ejected electron). The electron from an outer shell (higher energy shell) then move to the lower energy shell to fill the electron hold, the energy difference between the higher energy shell and lower energy shell is emitted as X-ray which is then collected by EDS microprobes. As different element emits X-ray with a different wavelength, therefore the quantitative atomic composition of the region of

interest can be determined by analysing the X-ray emission spectrum (wavelength against intensity).

Sample was milled and dispersed in ethanol by sonication (30 seconds) before drop casted on a 300 mesh holeycarbon Cu grid (TAAB).

In this work, the TEM images were taken by Dr Shu Chen using Jeol 2100F scanning/transmission electron microscope (S/TEM) operated at 200 kV, fitted with a X-MaxN Silicon Drift Detector with a detector sizes of 80 mm^2.

3.8 Nuclear Magnetic Resonance

Nuclear Magnetic Resonance (NMR) is a powerful technique that can reveal the chemical structure of a molecule in solution or in the solid state. In solution state NMR, the spectra consist of a series of sharp peaks, due to averaging of anisotropic NMR interactions by rapid random tumbling. Whereas, in solid state NMR, the peaks in the spectra are very broad as the effects of anisotropic interactions are observed. Therefore, a special technique, such as Magic Angle Spinning (MAS), is needed to increase the resolution of solid state NMR spectra. When the solid sample is spun at the magic angle (54.74^o) the orientation-dependent interactions are averaged thus the peak width is reduced. However only solid state NMR was applied in this project.

Although there are many different NMR spectrometers the theory of NMR is common to all NMR spectrometers.

The nuclear spin (I) is the fundamental property of the atomic nucleus. The nuclear spin (I) has values of $0, \frac{1}{2}, 1, \frac{3}{2}, 2 \ldots.,$ etc. [187]. The value of nuclear spin (I) is determined by the number of protons and neutrons in the nucleus, a nucleus with even numbers of both protons and neutrons has I=0, therefore has 0 nuclear magnetic moment (μ). Nuclear magnetic moment (μ) is directly proportional to the nuclear spin (I), $\mu = \frac{\gamma I h}{2\pi}$, where γ is the nuclear gyromagnetic ratio and h is the plank constant. In an NMR spectrometer, the sample is exposed to a strong magnetic field (B_0) and a radiofrequency energy. When a magnetic field is applied, the nuclear moments orient themselves either orientate for the lower energy state which is with the magnetic field or the higher energy state which is against the magnetic field. Then when a radiofrequency is applied, the radiofrequency energy can excite the lower energy orientation to higher energy orientation. As nuclear moments realign in a preferred

lower energy orientation, a radiofrequency energy is released and detected by the NMR spectrometer. The frequency of the radiation that nuclei absorb and emit is the resonant frequency (v), which can be expressed as $v = \frac{\gamma B_0}{2\pi}$, where B_0 is the applied magnetic field [187]. However, the resonance frequency is perturbed by the chemical shielding interaction which induces the change in resonance frequency. Thus, combination of the chemical environment and the property of the nucleus affect the final resonant frequency. This allows the chemical structure of a molecule to be revealed. [187, 188]. ^{29}Si and ^{31}P solid state MAS-NMR were done by Sam Page from the University of Warwick.

Magic Angle Spinning ^{29}Si Solid State Nuclear Magnetic Resonance (MAS-NMR) measurements were performed at 7.0 T using a Varian/Chemagnetics InfinityPlus spectrometer operating at Larmor frequencies of 59.6 MHz. These experiments were performed using a Bruker 7 mm HX probe which enabled a MAS frequency of 5 KHz to be implemented. For ^{29}Si single pulse MAS NMR, flip angle calibration was performed on kaolinite from which a π/2 pulse time of 5.5 μs was measured. All measurements were undertaken with a π/2 tip angle along with a delay between subsequent pulses of 240 s. For heteronuclear ^{1}H decoupling the nutation frequency was equal to 50 kHz. All ^{29}Si centre of gravity (apparent) shifts were reported against the IUPAC recommended primary reference of Me_4Si (1% in $CDCl_3$, δ 0.0 ppm), via a kaolinite secondary in which the resonance has a known shift of -92.0 ppm [189].

For ^{31}P MAS-NMR measurements were performed at 9.4 T using a Bruker Avance III spectrometer operating at Larmor frequency of 161.4 MHz. These experiments were performed using a Bruker 4 mm HX probe which enabled a MAS frequency of 12 KHz to be implemented. For ^{31}P single pulse MAS-NMR, flip angle calibration was performed on ammonium dihydrogen phosphate (ADP) from which a π/2 pulse time of 2.5 μs was measured. All measurements were undertaken with a π/2 tip angle along with a delay between subsequent pulses of 30 s. For heteronuclear ^{1}H decoupling the nutation frequency was equal to 100 kHz. All ^{31}P center of gravity (apparent) shifts were reported against the IUPAC recommended primary reference of H_3PO_4 (neat, δ 0.0 ppm), via a ADP secondary in which the resonance has a known shift of 0.99 ppm [189].

^{29}Si was applied to determine the distributions of Q^n and T^n structures of Si-O species in sol-gel glasses/gels and PCL hybrids. Q^n corresponds to the structure of $Si(OSi)_n$

$(OR)_{4-n}$ and T^n corresponds to the structure of C-$Si(OSi)_n(OR)_{3-n}$, where R is Ca or H here. The degree of condensation (D_c) can be calculated using the following equation (Equation 3.5) [190]:

$$D_c(\%) = \left[\frac{T^1\% + 2T^2\% + 3T^3\%}{3}\right] + \left[\frac{Q^1\% + 2Q^2\% + 3Q^3\% + 4Q^4\%}{4}\right] \quad (3.5)$$

^{31}P NMR data was used to investigate the phosphate incorporation from different phosphate precursors at different mol% of P_2O_5.

3.9 TGA/DSC

Thermogravimetric analysis (TGA) and differential scanning calorimetry (DSC) are the branches of thermal analysis. TGA examines the mass change of a sample as it is heated (weight loss with temperature). TGA was used to determine the organic/inorganic ratio of a polymer/glass hybrid material in this work. But not all thermal events bring about a change in the mass of the material, for example melting and crystallisation [191]. DSC simultaneously measures the difference in the amount of energy required to increase the temperature of the sample and reference to determine the heat flux of the sample. DSC can be used to observe subtle physical transformation, such as melting, glass transition and crystallisation of a material. DSC can also be used to determine the temperature when organic polymer in a glass/polymer hybrid is decomposed and removed.

In this work, TGA-DSC was carried out on PCL hybrids using NETZSCH STA 449 C Jupiter. The sample for TGA-DSC analysis was in powder form and heated from room temperature to 750°C in air at 10°C min^{-1}.

3.10 TRIS degradation study of PCL hybrids

Cylindrical PCL hybrid monolith was immersed in TRIS buffer solution for a week to investigate the degradation of PCL hybrid. Weight loss after 1 week of immersion in TRIS buffer was determined. The true organic/inorganic ratios of the PCL hybrids before and after TRIS dissolution were determined using TGA-DSC when heated to 750°C at 10°C min^{-1} heating rate. TRIS buffer solution was prepared following the protocol modified from [192], where 15.090 g of TRIS (hydroxymethyl) amino

methane ($(CH_2OH)_3CNH_2$) was dissolved in 1800 ml of deionised water, adding 44 ml 1N HCl, left at 37ºC overnight, filled to a total volume of 2000 ml with deionised water and then adjusted the pH to 7.40 at 37ºC with 1 M HCl.

3.11 Compression test

Compression testing was carried out on cylindrical PCL hybrid monoliths and PCL hybrid 3D printing scaffolds using Zwick/Roell Z010 machine with the test speed of 1 mm min^{-1} and 5 N pre-load (pre-load speed = 1 mm min^{-1}). Cyclic loading (compressive) testing was also carried out on the cylindrical 6040 PCL hybrid monoliths using the same machine with the cycle (loading and unloading) speed of 1 mm min^{-1}, cycle number of 10, 3 minutes time interval between each cycle (hold time), deformation of 10, 20 or 30 % and 5 N pre-load (pre-load speed = 1 mm min^{-1}). During the cyclic loading test, the 6040 PCL cylinders were compressed and then started unloading when the deformation of the specimen reached the preset value (10, 20 or 30%). The hold time between each cycle allows the deformation to recover before starting the next cycle.

The bottom and top surfaces of the test sample (hybrid cylinder) were flattened using SiC paper, then placed between two compression platens as shown in Figure 3.4.

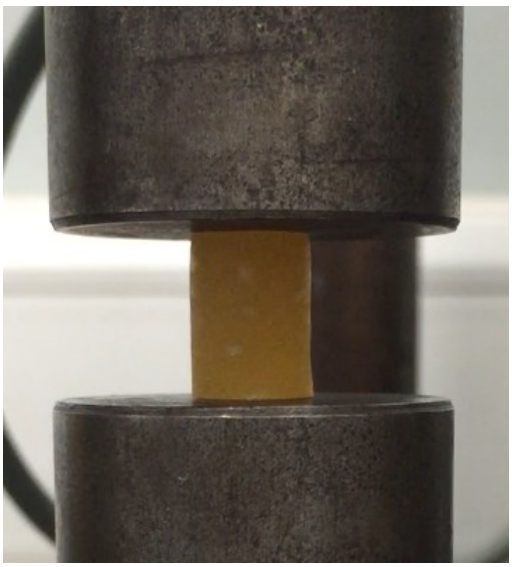


Figure 3.4 Photography of compression test of a cylindrical silica/PCL hybrid monolith.

3.12 X-ray micro-computed tomography

μCT was used to analyse the macroporosity of a PCL hybrid 3D printing scaffold. The scaffold was scanned using a commercial μCT device, Phoenix X-ray Systems and Services GmbH, Wunstorf, Germany, at 40kV and 150 μA, and with a voxel size of 12 μm. The 3-D image micro CT image of the scaffold was obtained using Avizo 9.0 (Visualization Science Group, Merignac Cedex, France).

2D grey scale images were obtained from X-ray CT scan, a $3\times3\times3$ media filter was applied to all micro CT images to remove noise and make the boundary clear. Thresholding was applied to the grey scale images to segment out each voxels as strut or background according to their intensity, the threshold value was determined by using the lowest value between strut and background peaks. The grey scale images were then converted into binary images and the binary images were used to form the 3D image of the scaffold. The porosity of the scaffold is the fraction of bulk volume V that is not occupied by solid matter. Porosity, ϕ, can be expressed as (Equation 3.5):

$$\phi = \frac{V - V_S}{V} = \frac{V_P}{V} = \frac{Pore\ \ Volume}{Total\ \ Bulk\ \ Volume} \tag{3.6}$$

Where V_s is the volume of solid and V_p is the pore volume. To determine the porosity of the scaffold, a cube has a size of $300\times300\times300$ voxels was cropped from the centre of the scaffold. The number voxels labelled as strut in the cropped cube was used to calculate V_s and the total bulk volume, V, was $(300\times12)^3$ μm^3.

4 Silicate based sol-gel glass containing phosphate

4.1 Introduction

One of the original sol-gel derived bioactive glass compositions was 58S (60 mol% SiO_2. 36 mol% CaO and 4 mol% P_2O_5) [12], which rapidly releases calcium into body fluid, increasing the pH of surrounding environment that can cause damage to surrounding tissue. Release of phosphate from the glass can buffer the pH changes and the additional phosphate may promote HCA formation [96]. However, a decrease in pH can also inhibit HCA formation. Our preliminary investigation of the 58S glass found that HA formed after stabilisation stage of sol-gel process because of the reaction between free calcium ions and orthophosphate from the TEP hydrolysis with the presence of water of the sol. It has never been stated clearly in any study that the HA forms during 58S glass synthesis when TEP and calcium nitrate are used. The formation of HA may increase the burst release of calcium from the glass and may reduce the buffering potential. Therefore, the aim of this work was to investigate the effect of TEP concentration, and therefore phosphate content, on the structure and dissolution of the glass. In order to achieve the aim, TEP glass with different CaO to P_2O_5 ratio were made and studied. Additionally, effect of water content (R ratio) in the sol-gel process on the structure and dissolution of glass was also investigated in this chapter.

4.2 Materials and methods

4.2.1 Materials

Tetraethyl orthosilicate (TEOS, 98%), nitric acid (HNO_3, 69%), calcium nitrate tetrahydrate ($Ca(NO_3)_2 \cdot 4H_2O$, 99%) and triethyl phosphate (TEP, 99%) were used in sol-gel bioactive glass synthesis. The chemicals used in SBF preparation are listed in section 3.3. All the chemicals were purchased from Sigma-Aldrich. HNO_3 was diluted in deionised water to make the concentration of 2 M and all the other chemicals were used as purchased.

4.2.2 Synthesis of phosphate containing sol-gel glasses

The glass compositions made in this work were based on 58S glass but with different ratio of CaO to P_2O_5. The first objective was to investigate how the CaO to P_2O_5 molar ratio can affect the properties of glass and if HA formation during glass synthesis can be prevented by increasing the phosphate content in glass. The phosphate precursors used to make the phosphate containing glasses was TEP (Figure 4.1). In addition, low water containing sol-gel glasses were also made to investigate if the HA formation during glass synthesis can be suppressed by reducing the amount of water in the glass sol. The samples are named after their compositions and the phosphate precursor used: sample TEPXp12r and TEPXp4r are of chemical composition 60mol% SiO_2, (40-X) mol% CaO and X mol% of P_2O_5. R ratio (molar ratio of water : TEOS) for TEPXp12r is 12, for TEPXp4r is 4. The chemical composition of each sample is summarised in Table 4.1.

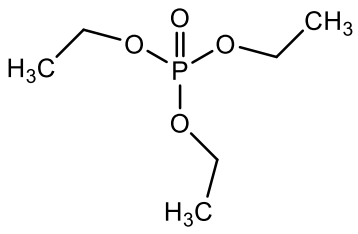


Figure 4.1 The chemical structure of TEP.

Table 4.1 Chemical compositions of phosphate containing glasses made with TEP.

Sample	SiO_2 (mol%)	P_2O_5 (mol%)	CaO (mol%)	Water ratio (R ratio)
TEP4p12r	60	4	36	12
TEP8p12r	60	8	32	12
TEP12p12r	60	12	28	12
TEP24p12r	60	24	16	12
TEP4p4r	60	4	36	4
TEP8p4r	60	8	32	4
TEP12p4r	60	12	28	4
TEP24p4r	60	24	16	4

All the samples in this chapter were prepared by using an acid-catalysed sol-gel protocol [62]. The sol-gel process contains 6 stages: mixing, casting, ageing, drying and stabilisation. During mixing all the precursors were added into deionised water in a specific order. First, TEOS, deionised water (DI water) and 2 M nitric acid (1/6 amount of DI water) were mixed. After 1 h of stirring, the phosphate precursor (TEP) was added into the hydrolysed TEOS. Finally, calcium nitrate tetrahydrate was added into the solution after 1 h. After all the precursors were mixed, the sol was left stirring at room temperature for another 1 h. During aging, the sol was sealed in a screw top PTFE jar and heated to 60^{o}C for 72 h at 5^{o}C min^{-1} heating rate. After aging, sol became a wet gel. Drying was carried out by unsealing the PTFE jar and heating the wet gel to 130^{o}C for 40 h with a three stage heating schedule: 1. heating from room temperature to 60^{o}C at 0.5^{o}C min^{-1} and holding at 60^{o}C for 20 h. 2. from 60^{o}C to 90^{o}C at 0.1^{o}C min^{-1} and holding at 90^{o}C for 24 h. 3. Heating from 90^{o}C to 130^{o}C at 0.1^{o}C min^{-1} and holding at 130^{o}C for 40 h. After drying, the dry gel was transferred into a ceramic container and ready for stabilisation. During stabilisation, the dry gel was heated to 700^{o}C by a 3-

stage schedule: Heating from room temperature to 100°C at 1°C min^{-1} followed by heating up to 300°C at 0.5°C min^{-1} and holding at 300°C for 2 h. Then heating from 300°C to 700°C at 1°C min^{-1} and holding at 700°C for 5 h. After stabilisation the phosphate containing glasses were ready for characterisation.

4.2.3 Characterisation techniques

All the samples were ground in a ball mill and sieved to particles size smaller than 38 μm by a sieve shaker. Grinding and sieving allowed comparison between samples in terms of dissolution rate, bioactivity and surface area, which all can be affected by the size of powder particles. Therefore, particle size of each glass powder was measured by particles sizer. The characterisation techniques used in this chapter were nitrogen sorption, XRD, FTIR, SEM, TEM with EDS, MAS-NMR, SBF dissolution study and ICP-OES (Chapter 3).

4.3 Results

4.3.1 Glass appearance

Glass appearance was the first thing investigated after the sol-gel bioactive glasses were made. A PTFE jar was used for the sol-gel process. PTFE is a hydrophobic material, so the risk of contamination during the sol-gel process can be minimised, but glasses with highest TEP concentration became black after stabilisation (Figure 4.2, d, and h). The reason for the black glass was carbon (carbon black) entrapment in the glass and lack of oxygen. After stabilisation, all the organics were burned off as CO_2 gas. A lack of oxygen during stabilisation can leave carbon black as there is not enough oxygen to oxidise the organic completely. Figure 4.2 shows all TEP glasses were white after stabilisation apart from TEP24p glass; it is mainly because the increase in TEP increased the amount of organic that had to be removed. In addition, if the pores of the glass are too small the carbons can be trapped in the glass due to the low oxygen diffusion into the inner of glass. According to the nitrogen desorption results (section 4.3.2), the glass with high phosphate content had smaller pores, which would also inhibit organic removal and oxygen diffusion.

A small disc of TEP24p glass remained white after stabilisation, because the carbon had a shorter path to exit from the small disc of glass, and oxygen diffusion path was shorter.

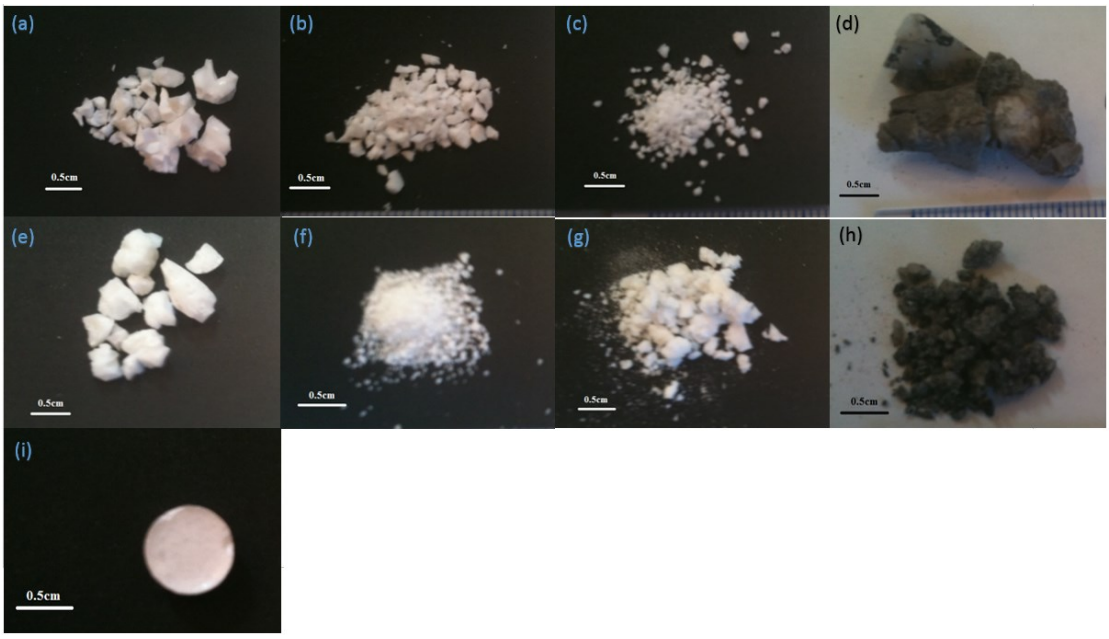


Figure 4.2 Appearance of sol-gel glasses made with 12R water ratio at (a) 4, (b) 8, (c) 12 and (d) 24 mol% P_2O_5, and the sol-gel glasses made with 4R water ratio at (e) 4, (f)8, (g)12 and (h) 24 mol% P_2O_5. (i) sol-gel glass made into disc shape with 4R water ratio at 24mol% P_2O_5.

4.3.2 Nitrogen sorption

The isotherm and the shape hysteresis loop provide information about the porosity of sol-gel glass (section 3.2). The isotherms for 12R to 4R were really similar (Figure 4.3), indicating that reducing water content from 12R to 4R did not really change the nanoporosity of the TEP bioactive glass. The total volume of nitrogen adsorbed dropped as the phosphate content increased from 4 mol% to 24 mol%, suggesting the increase in the ratio of phosphate to calcium decreased the pore volume of the glass. Very little nitrogen was absorbed into 24p glasses (Figure 4.3), therefore all the glasses which contained 24 mol% of phosphate were not porous. Calcium acts as the Si network modifier and can disrupt the Si network formation, therefore the glasses with higher phosphate content contained less calcium and a more connected Si glass network and lower nanoporosity level, which will be discussed in section 4.3.9. The Si network of TEP24p glass was highly condensed and the pore size of the TEP24p glass was too small for carbon atom to be removed from the glass. The trapped carbon black might also block the pores and make the TEP24p glass (both 4R and 12R water ratio) even less porous.

The hysteresis loops of those isotherms were all type H2 loops but in such systems the pore size distribution and shape are not well defined. It was suggested that Type H2 loop was attributed to the ink-bottle shape pores but the assumption has been proved inaccurate according to Lin et al. [42]

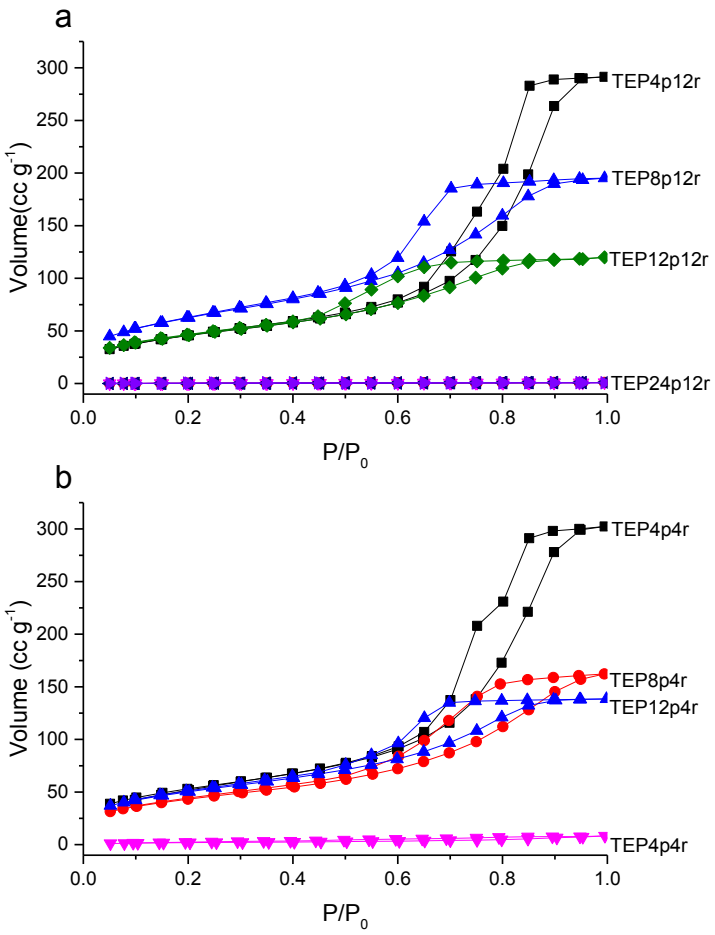


Figure 4.3 Nitrogen adsorption-desorption isotherms of (a) sol-gel glasses made with 12R water ratio at 4, 8, 12 and 24 mol% P_2O_5 (b) sol-gel glasses made with 4R water ratio at at 4, 8, 12 and 24 mol% P_2O_5.

Figure 4.4 shows the pore size distributions of the glasses and Table 4.2 shows the modal pore size of each glass. The results confirm that the glasses with 24 mol% of phosphate were non-porous. In general, the nanopores in TEP glasses decreased in diameter as phosphate content increased (Figure 4.4). The TEP4p12r had a much wider range of nanopore size distribution (from 5 nm to 15 nm) than TEP8p12r and TEP12p12r. Most of the nanopores in TEP8p12r are around 7 nm in diameter and around 5 nm in diameter in TEP12p12r. (Figure 4.4a)

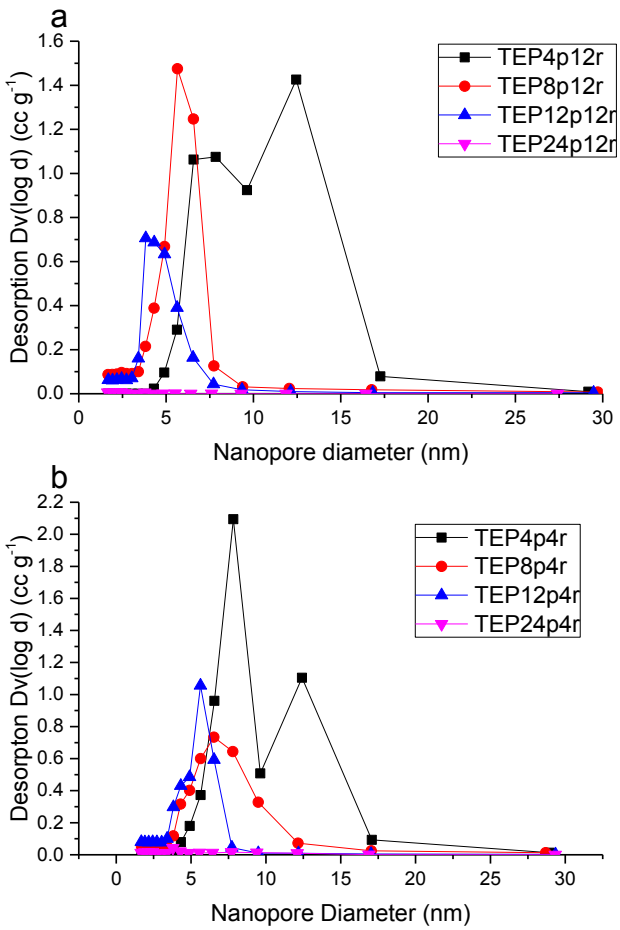


Figure 4.4 The pore size distributions of (a) sol-gel glasses made with 12R water ratio at 4, 8, 12 and 24 mol% P_2O_5 (b) sol-gel glasses made with 4R water ratio at at 4, 8, 12 and 24 mol% P_2O_5.

The HCA formation, degradation rate and the amount of protein absorb to the bioactive glass are all dependent on the surface area of the bioactive glass [42]. The surface area of each bioactive glass was also shown in Table 4.2. The surface area of a bioactive glass is determined by its pore volume and the size of the nanopores. The higher the pore volume the greater the surface area of the glass. With an equal pore volume, the smaller pores will give a greater surface area. The pore size distributions and isotherms show that the glass had larger nanopores also had a greater pore volume. Therefore, there is not a strong correlation between the phosphate content and surface area. The surface areas of the glasses with 24 mol% phosphate are much lower than other glasses as 24p glasses were not porous.

Table 4.2 Modal pore sizes and surface areas of TEP bioactvive glasses.

Bioactive glass	Modal pore size (nm)	Surface area (m^2 g^{-1})
TEP4p12r	Bimodal pore size distribution: 7.5 and 12.5	163.0
TEP8p12r	7	224.8
TEP12p12r	5	162.9
TEP24p12r	Non-porous	1.2
TEP4p4r	Bimodal pore size distribution: 7.5 and 13	188.6
TEP8p4r	6	154.0
TEP12p4r	4	178.0
TEP24p4r	Non-porous	7.4

4.3.3 Particle sizes of TEP glass powders

Before dissolution study, all the TEP glasses were ground by ball mill and sized by 38 μm sieve; the particle size of each TEP glass powder was measured (only TEP glasses with 12R water ratio were analysed). Each glass composition was measured twice; the average values and standard deviations were shown in Table 4.3. D(v,0.1), D(v,0.5) and D(v,0.9) are standard percentile readings from the particle sizer analysis. D(v,0.1) is the size of particle below which 10% of the sample lies; D(v,0.5) is the size in microns at which 50% of the sample is smaller and 50% is larger; D(v,0.9) is the size of particle below which 90% of the sample lies. As Table 4.3 shows, all the TEP glasses powders had D(v,0.5) value smaller than 17.3μm and D(v,0.1) smaller than 4.5μm. All the TEP glass powders had D(v,0.9) smaller than 39.3 μm. It was noticed that the size of the powder after grinding and sieving decreased when the phosphate content in 12R water TEP glass increased. The powders of TEP4p12r had the largest D(v,0.9) (39.3μm) and powder of TEP24p12r had the smallest D(v,0.9) (29.9μm).

Table 4.3 The particle sizes distribution if each TEP glass composition after grinding and sieving.

Sample	D(v,0.1)/µm	D(v,0.5)/µm	D(v,0.9)/µm
TEP4p12r	4.56	17.3	39.3
Standard deviation	0.03	0.09	0.46
TEP8p12r	3.91	15.4	37.5
Standard deviation	0.07	0.57	0.67
TEP12p12r	4.00	15.6	37.6
Standard deviation	0.22	1.48	2.76
TEP24p12r	3.82	11.5	29.9
Standard deviation	0.13	0.05	1.36

4.3.4 SBF dissolution

The pH of the SBF supernatant was monitored during SBF dissolution (Figure 4.5), as pH is the important factor that can affect the HCA formation and the activities of cells. All the TEP (4R and 12R) glasses changed the pH of surrounding SBF rapidly within first 24 h of dissolution and then slowly levelled off. The pH of SBF was 7.4 at time point 0. The pH profile indicates a strong correlation between glass composition and the pH changes of SBF. The pH of TEP4p12r and TEP8p12r were 7.8 and 7.5 respectively after 1 week of dissolution in SBF. The pH of TEP12p12r dropped slightly to 7.3 and TEP24p12r lowered the pH of SBF to 7.1 1 week after SBF immersion (Figure 4.5a). As phosphate content in the glass increased, the pH of SBF during dissolution decreased. During SBF dissolution, Ca^{2+} from the glass was rapidly exchanged by H^+ from the SBF and that increased the pH of surrounding as H^+ ions in SBF being replace by cations. The phosphate released from the glass and caused the pH to go down. In order to form HCA, OH^- and $(CO_3)^{2-}$ need to be incorporated into the amorphous calcium phosphate layer[37, 98]. Therefore, the low pH is not favourable for HCA formation as the concentration of OH^- in SBF is lower.

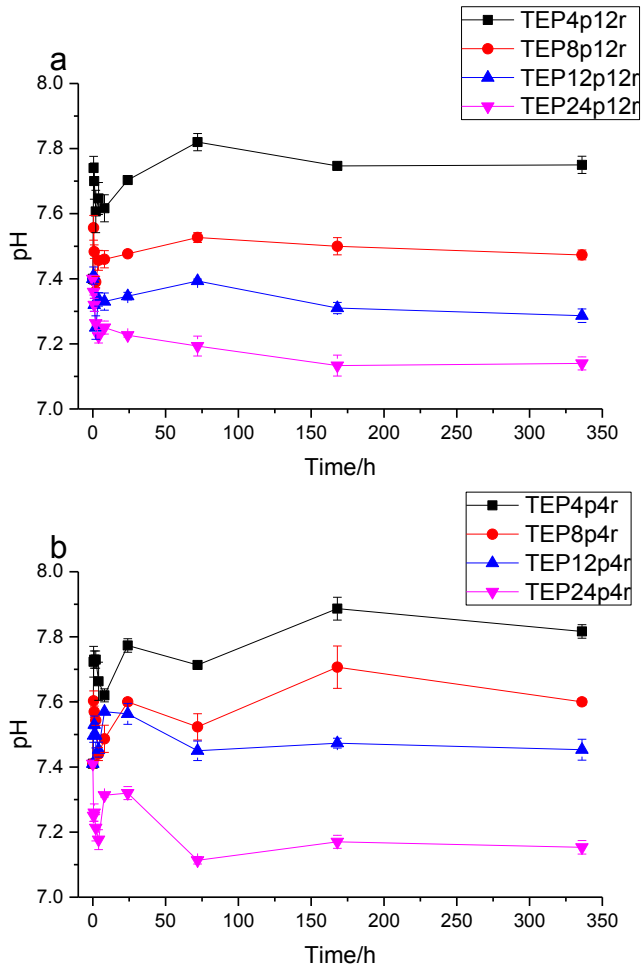


Figure 4.5 pH change profile of (a) sol-gel glasses made with 12R water ratio at 4, 8, 12 and 24 mol% P_2O_5 (b) sol-gel glasses made with 4R water ratio at at 4, 8, 12 and 24 mol% P_2O_5.

Calcium content of the glass decreased as phosphate increased, which would be expected to reduce the calcium release rate. The ICP results show the elemental concentrations (Ca, P and Si) in the SBF at different time points of SBF dissolution. As Figure 4.6 and Figure 4.7 show, the R ratio did not really affect the ion release from the sol-gel glasses. The 4R glasses and 12R glasses gave the similar dissolution profile (Figure 4.6 and Figure 4.7).

The dissolution profiles indicate that all the TEP glasses released Ca and P ions rapidly as soon as they were immersed in SBF (Figure 4.6 and Figure 4.7). The rapid increases in the concentration of Ca and P ions happened during the first 30 minutes of SBF dissolution. Then the concentrations of Ca started dropping gradually after 30 minutes of immersion. The drop in the concentration of calcium was caused by the deposition of calcium and phosphate ions to form amorphous calcium phosphate. The

concentration of Ca in SBF increased from 100 μg ml^{-1} to around 220 μg ml^{-1} after 30 minutes of dissolution for TEP4p12r, 150 μg ml^{-1} for TEP8p12r, 140 μg ml^{-1} for TEP12p12r and 130 μg ml^{-1} for TEP24p12r (Figure 4.6). Assuming calcium deposition started after 30 minutes of dissolution, the amount of calcium (in μg) released from the TEP glasses during the first 30 minutes of dissolution can be calculated by the following equation:

$$\left[[Ca](at\ \ 0.5\ \ h) - 100\right] \times 100\ = \text{Ca} \qquad (4.1)$$

The total amount of calcium (in μg) that a TEP glass contains can also be calculated by the equation:

$$150000\mu g \times (wt\%\ \ of\ \ CaO\ \ in\ \ glass) \times \frac{40}{56} = \text{Ca}_t \qquad (4.2)$$

The wt% of calcium released from the TEP glass to SBF was calculated by $(\frac{Ca}{Ca_t}) \times 100\%$ (the wt% of CaO is shown in Table 4.4).

In general, the amount of calcium released decreased as phosphate content of the glass increased. The wt% of calcium released for each TEP glass also decreased as phosphate content increased (Table 4.4) from 4P to 12P. The wt% of calcium released from TEP24p12p (24.8 wt%) at 30 minutes should be lower than the TEP8p12r (17 wt%) as TEP8p12r had much greater pore volume and surface area than TEP24p12r. But the data show the opposite results. Phosphate glass formed during synthesis of TEP24p (section 4.3.9) and the phosphate glass in 24p degraded faster, taking calcium with it.

The concentration of P in SBF started decreasing just after 1 h of dissolution, it suggests that the phosphate deposition was really fast and it also provides an evidence of HCA formation (Figure 4.6). The ICP profile for TEP12p12r was slightly different to others; the concentrations of calcium and phosphate ions started dropping significantly from 24 h of dissolution until 168 h of dissolution and then stayed constant. This is an indication of amorphous calcium phosphate formation, followed by the HCA formation.

The Si profile can be used to indicate the degradation rate of the glasses. As Figure 4.6 shows, the higher the phosphate content, the slower the Si released from the glass. It is because the Si glass network was more connected as the percentage of network modifiers was lower. The phosphate network was separate. The nanoporosity level was also lower in high phosphate containing glasses (TEP24p12r was not really porous,

refer to section 4.3.2).

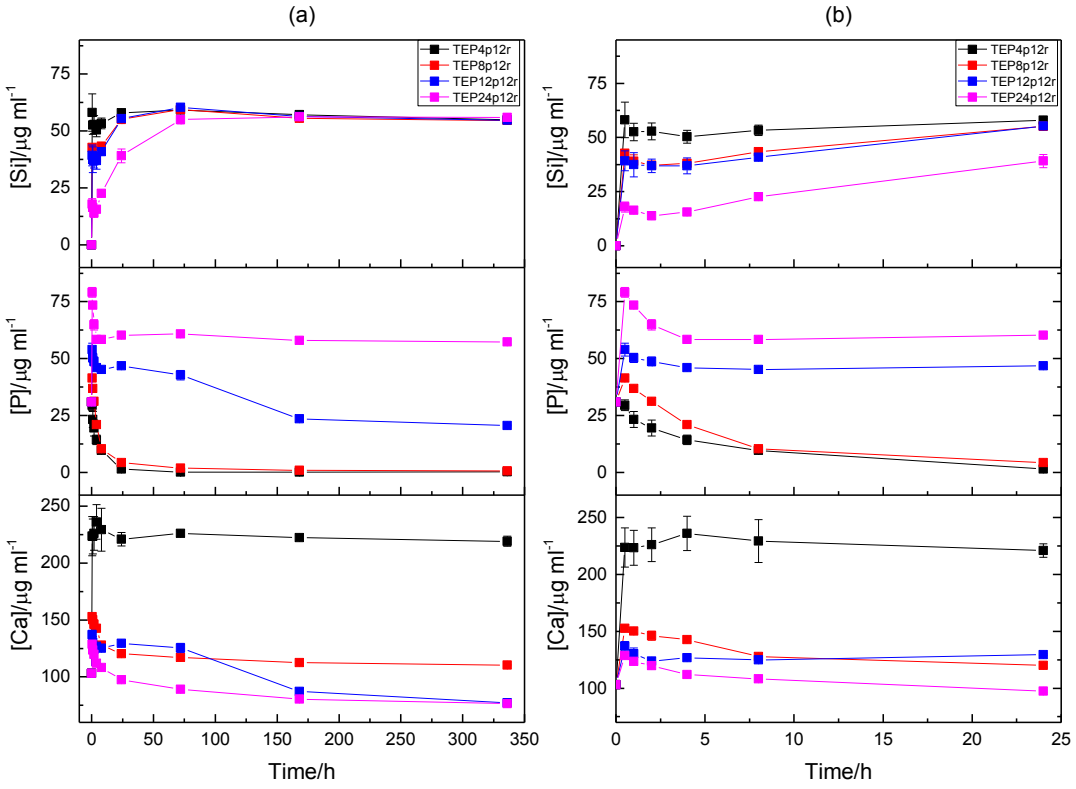


Figure 4.6 ICP profile of sol-gel glasses made with 12R water ratio at 4, 8, 12 and 24 mol% P_2O_5 (a) for 2 weeks (b) for the first 24 h of SBF dissolution.

Table 4.4 wt% of calicum released from sol-gel glasses made with 12R water ratio at 4, 8, 12 and 24 mol% P_2O_5 within the first 30 mintues of SBF dissolution (Assuming calcium deposition started after 30 minutes of dissolution).

Sample	Wt% of Ca released
TEP4p12r	34.3
TEP8p12r	17.0
TEP12p12r	16.4
TEP24p12r	24.8

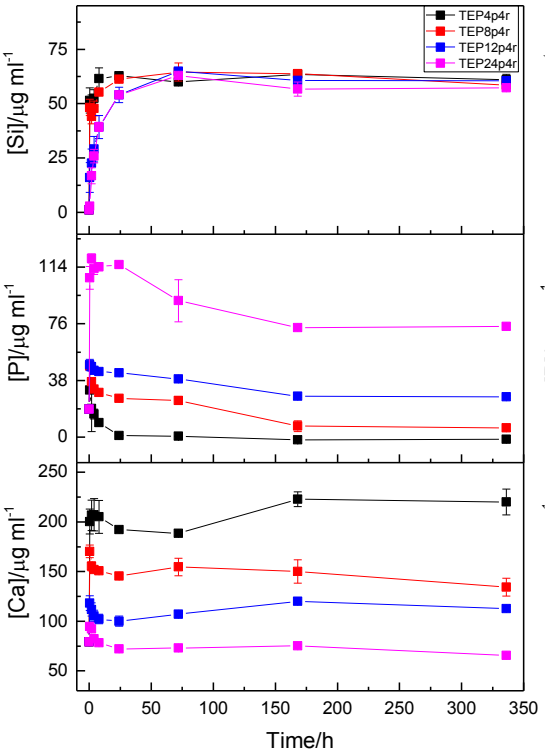


Figure 4.7 SBF dissoluton profile of sol-gel glasses made with 4R water ratio at 4, 8, 12 and 24 mol% P_2O_5.

4.3.5 FTIR-ATR

In the FTIR spectra (Figure 4.8), the formations of most bands were caused by the combinations of stretching vibrational modes of SiO_4 and PO_4 tetrahedra. "The band at 470 cm^{-1} is attributed to the vibration of the bridging oxygen atoms perpendicularly to the Si-O-Si plane, and the band at 800 cm^{-1} is caused by the bending motions of oxygen atoms alone the bisector of Si-O-Si groups [193]. The shoulder around 1200 cm^{-1} is attributed to the stretching vibration of Si-O-Si. The peak around 1150 cm^{-1} is attributed to the stretching vibrational motion of $Si-O^-$ bond in the Q^3 tetrahedral unit, and the shoulder around 950 cm^{-1} is assigned to the stretching vibration of two non-bridging oxygen atoms in the Q^2 tetrahedral unit of Si-O-Si [194, 195]. A weak Si-OH band at 960 cm^{-1} is superposed over the Q^2 tetrahedral Si-O-Si band [196, 197]. The double bands at 546 cm^{-1} and 585 cm^{-1} are attributed to the P-O asymmetric bending motion in the orthophosphates of crystal HCA, and the other band at 1010 cm^{-1} is corresponding to P-O stretching vibration of PO_4^{3-}. [197, 198] The P-O bending double bands (546 cm^{-1} and 585 cm^{-1}) and the P-O stretching band (1010 cm^{-1}) are the important indicators of the presence of HCA. Furthermore, a C-O stretching single peak at 862cm^{-1} and the

carbonate (CO_3^{2-}) band at 1400cm^{-1} indicates the apatite formed was HCA [72].

Figure 4.8 shows that orthophosphate formed in TEP4p12r, TEP8p12r and TEP12p12r during the glass synthesis as the three bands at 546 cm^{-1}, 585 cm^{-1} and 1010 cm^{-1} were observed in the spectra. But for TEP24p12r glass, before SBF dissolution, there is a broad shoulder at 550 cm^{-1} observed on the FTIR spectrum (Figure 4.8) and it can be the indication of amorphous phosphate formation during the glass synthesis.

Increasing relative intensity of the 546 cm^{-1} and 585 cm^{-1} bands, following SBF immersion, can be attributed to HCA formation. Comparing the FTIR spectra before and after SBF dissolution, the results suggest that HCA started forming on TEP4p12r and TEP8p12r just after 8 h of SBF dissolution and HCA started to form on TEP12p12r after 1 week of SBF dissolution. For TEP24p12r, a single band at 550 cm^{-1} became more intense gradually during SBF dissolution and it can be taken as an indication of the formation of more amorphous calcium phosphate during SBF dissolution.

The hypothesis was that reducing the water content during glass synthesis can reduce the level of HA formation during glass synthesis. But Figure 4.9a shows that reduction in water content did not stop the formation of HA during glass synthesis as the double bands at 546cm^{-1} and 585cm^{-1} were observed in the FTIR spectra for TEP4p4r and TEP8p4r.

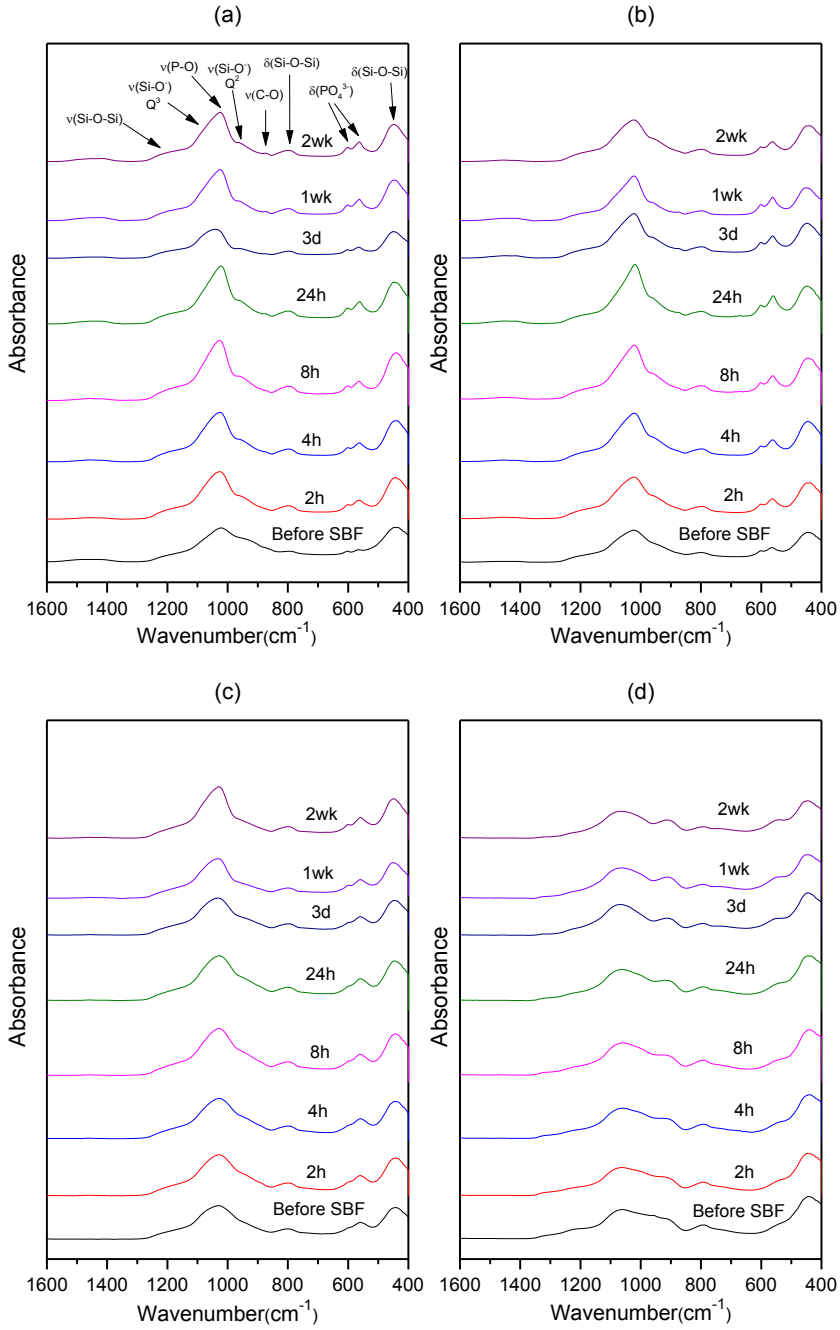


Figure 4.8 The FTIR spectra of sol-gel glasses made with 12R water ratio at (a) 4 (b) 8 (c) 12 and (d) 24 mol% P_2O_5 at different time point of SBF dissolution.

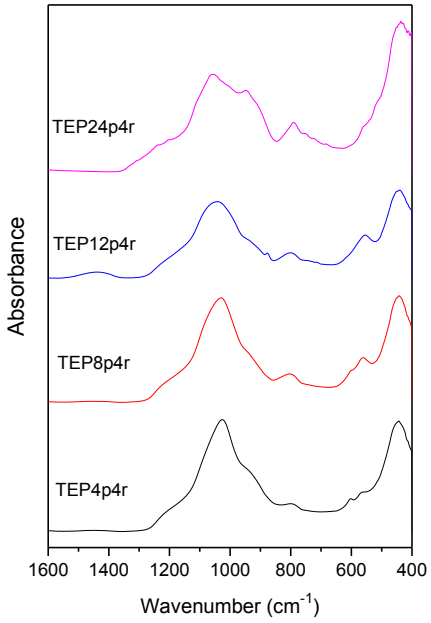


Figure 4.9 The FTIR spectra of sol-gel glasses made with 4R water ratio at 4, 8, 12 and 24 mol% P_2O_5 after stabilisation.

4.3.6 XRD

XRD was used to reveal the information of crystal structure of the bioactive glass before and after SBF dissolution. The peaks at 25.7°, 31.78° and 32.19° 2θ are the primary peaks for HCA. The peaks at 38.8°, 46° and 49.3° are also attributed to crystal HCA. [197, 199, 200] The XRD patterns confirmed the presence of HA in TEP4p12r, TEP8p12r and TEP12p12r glasses before SBF dissolution. But the level of crystallised HA in TEP12p12r was lower than TEP4p12r and TEP8p12r. There was no HA found in TEP24p12r according to the XRD pattern (Figure 4.10). The XRD pattern shows that TEP4p12r and TEP8p12r were able to form HCA after 8 h of soaking in SBF, but it took 1 week for TEP12p12r to form HCA. There was no HCA formed on TEP24p12r during SBF dissolution.

Figure 4.11 suggest that reduce the water content during the sol-gel did not affect the HA formation during glass synthesis neither.

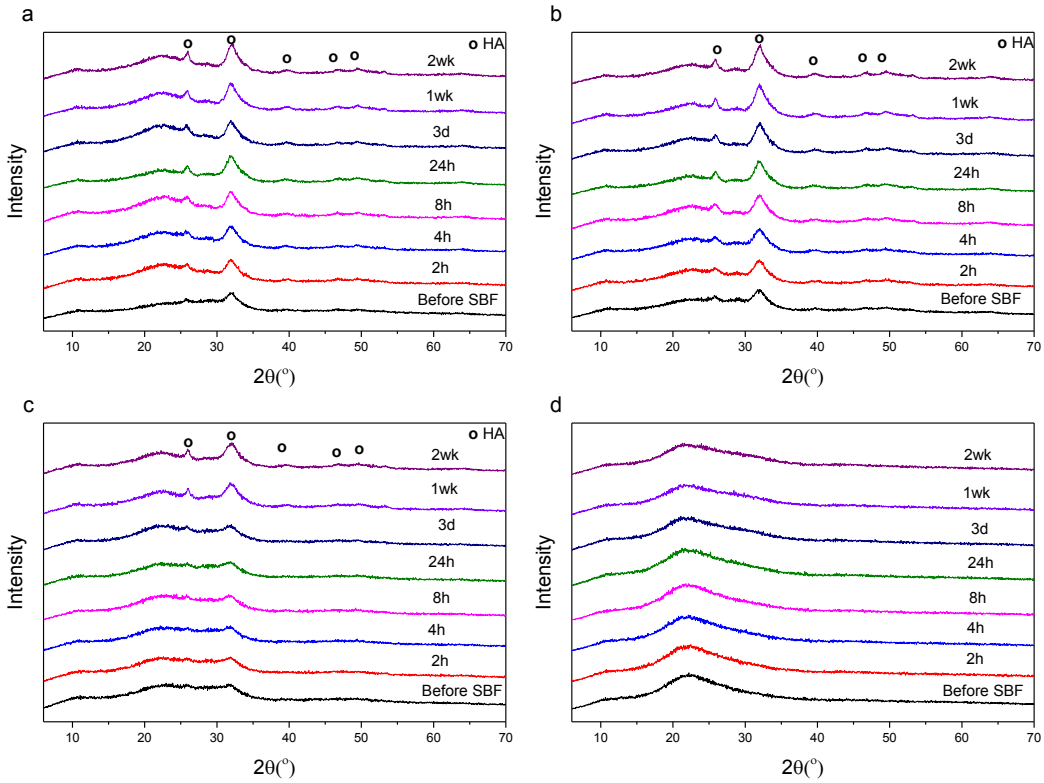


Figure 4.10 XRD patterns of sol-gel glasses made with 12R water ratio at (a) 4, (b) 8, (c) 12 and (d) 24 mol% P_2O_5 at different time point of SBF dissolution.

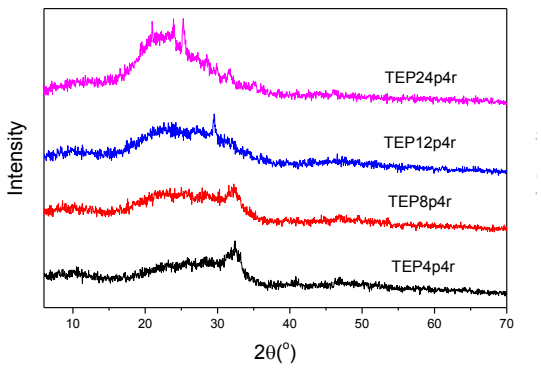


Figure 4.11 XRD patterns sol-gel glasses made with 4R water ratio at 4, 8, 12 and 24 mol% P_2O_5 after stabilisation.

4.3.7 SEM

SEM was used to examine the surface microstructure of TEP glasses. HCA exhibits a rod shaped structure under SEM microscope. Nanotopography of TEP4p12r, TEP8p12r and TEP12p12r can be seen on the SEM images (Figure 4.12). There were two different types of microstructures were found in TEP24p12r. One had a similar nanoporous structures to other TEP glasses; the other one with a flat smooth surface and was not porous. It indicates a phase separation happened during the glass synthesis of TEP24p12r. There might be two glass networks were formed in TEP24p12r, silica network and phosphate network.

XRD confirmed that HA was found within TEP4p12r, TEP8p12r and TEP12p12r glass before SBF dissolution but no HA can be seen from the SEM images. It suggests that the HA formed during the glass synthesis was inside the glass but not on the surface of glass.

Typical structures of HCA could be seen on the surface of TEP4p12r, TEP8p12r and TEP12P12r after 2 weeks of soaking in SBF (Figure 4.13a, b and c). For TEP4P12r and TEP8P12r, the HCA structure was even found on the surface just after 8 h of SBF dissolution (Figure 4.14). However, there was no HCA structure could be seen on TEP24p12r after 2weeks of soaking in SBF by using SEM. XRD and FTIR data has previously confirmed that TEP12p12r is able to trigger HCA formation after 1 week of SBF dissolution. But the amount of HCA formed on TEP12p12r during SBF dissolution might be lower than TEP4P12r and TEP8P12r, therefore it was more difficult to be found under SEM.

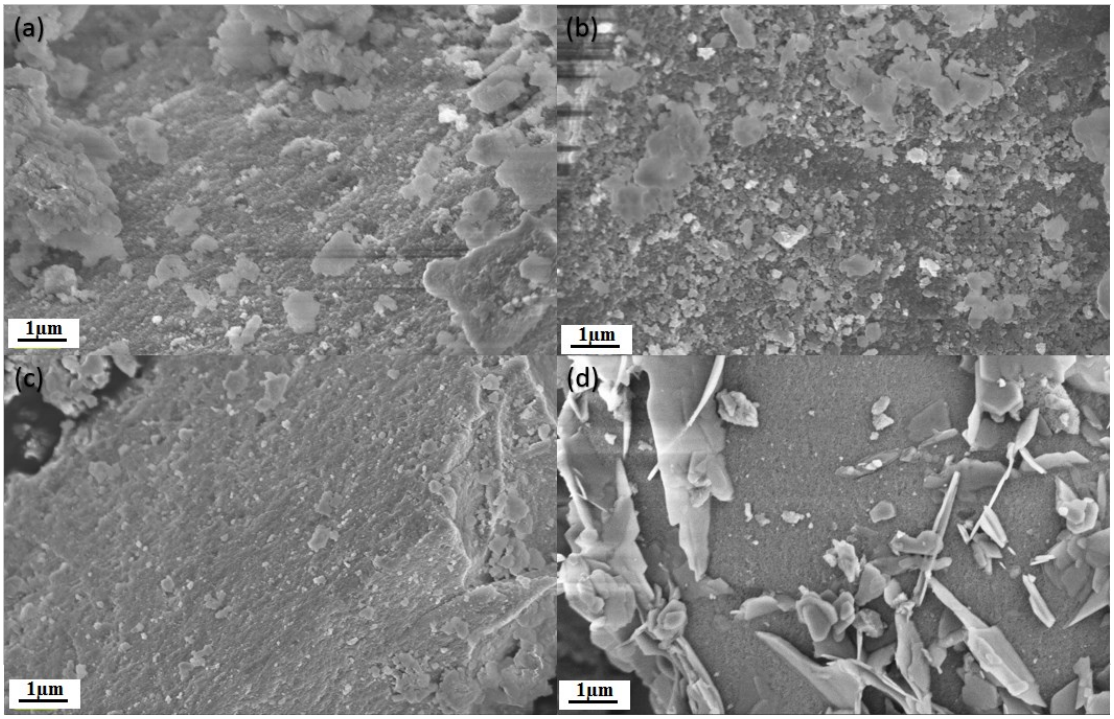


Figure 4.12 SEM images of TEP sol-gel glasses made with 12R water ratio at (a) 4, (b) 8, (c) 12 and (d) 24 mol% P_2O_5 after stabilisation.

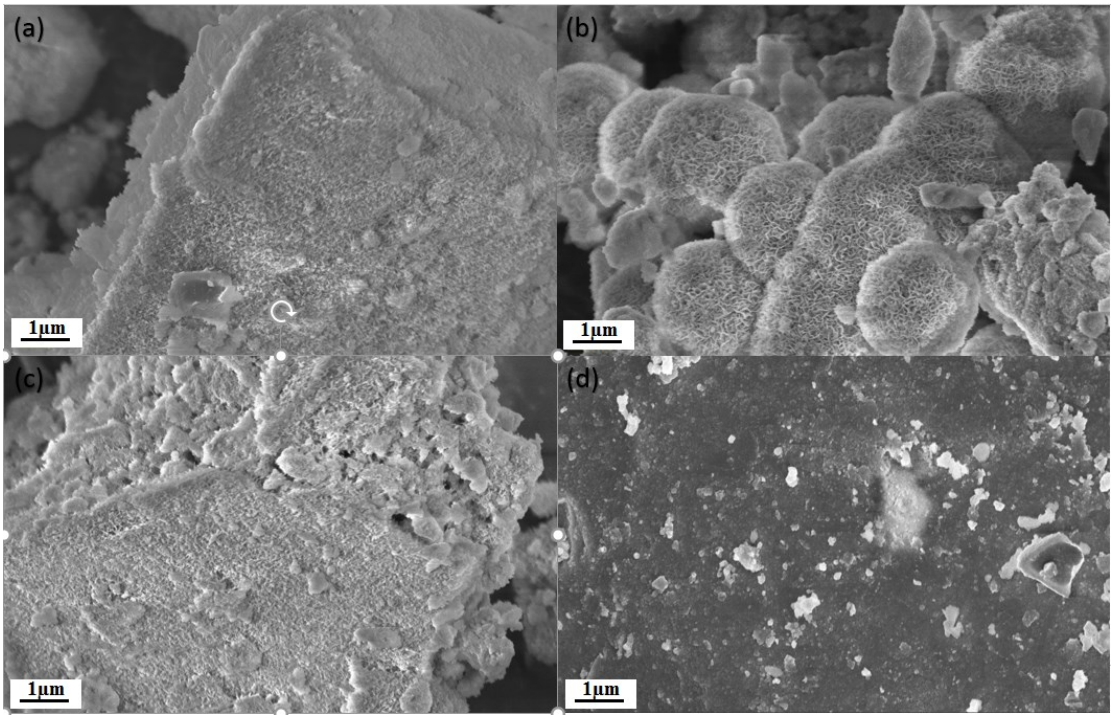


Figure 4.13 SEM images of TEP sol-gel glasses made with 12R water ratio at (a) 4 mol% (b) 8 mol% (c) 12 mol% and (d) 24 mol% P_2O_5 after 2 weeeks of SBF immersion.

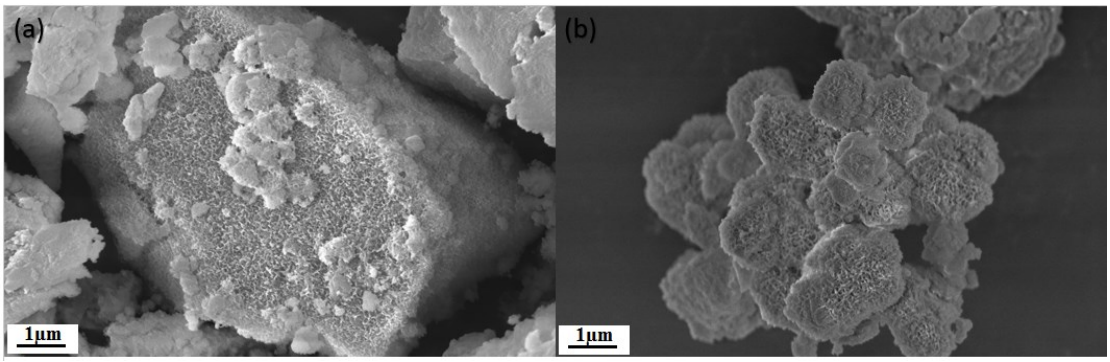


Figure 4.14 SEM images of TEP sol-gel glasses made with 12R water ratio at (a) 4 mol% and (b) 8 mol% P_2O_5 after 8 h of SBF immersion.

4.3.8 TEM

As there were two different structures were found in TEP24p12r using SEM, TEP24p12r was examined under TEM and EDS element mapping. The TEM image confirmed that there were two different structures in TEP24p12r, the nanoporous particle and the flat non-porous film (Figure 4.15a). The halo in Figure 4.15c and d indicate the amorphous nature of both nanoporous particle and flat non-porous film found in TEP24p12r. STEM-EDS spectra and mapping suggest that the nanoporous particle was probably silica glass with calcium and phosphate evenly distributed in it (Figure 4.15e and h). The flat non-porous film was likely to be the phosphate glass with calcium incorporated in the glass network (Figure 4.15f and h). The presence of non-porous phosphate glass can also reduce the overall nanoporosity of TEP24p12r glass.

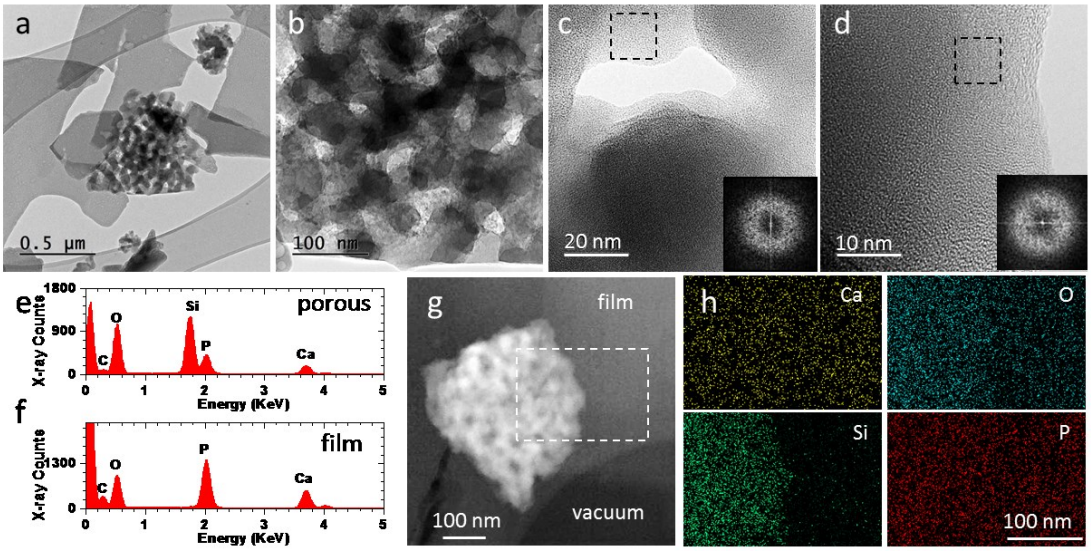


Figure 4.15 Analytic TEM characterisation of TEP24p12r, the sol-gel glasses made with 12R water ratio at 24 mol% P_2O_5, heated at 700 C for X h. (a) a low magnification bright field TEM (BFTEM) image reveals the presence of porous and film like structures in the sample. (b) a magnified BFTEM image further shows the morphology of the porous materals. (c, d) high resolution TEM (HRTEM) analysis of the porous and film like materials, respectively. Inserts in (c and d) show halo fast Fourier transform (FFT) patterns collected from the dashed boxed areas, respectively, indicate the amorphous nature of both the porous and film like materials. Representative STEM-EDS spectra collected from (e) the porous and (f) film like materials. (g) HAADF-STEM imag shows a porous particle sitting on the film like materials and the corresponding (h) STEM-EDS mapping of the boxed area in (g).

4.3.9 Solid state MAS-NMR

The ^{31}P solid state NMR revealed the phosphate component in TEP bioactive glasses. The peak between 2.5 to 0 $\delta(^{31}P)$/ppm is the orthophosphate peak and the peak between -9δ to -11 $\delta(^{31}P)$/ppm is attributed to pyrophosphate ($P_2O_7^{4-}$). The broad peak at -27 $\delta(^{31}P)$/ppm is assigned to the polyphosphate in the bioactive glass (Figure 4.16b). [201] The ^{31}P NMR spectra suggest that when the phosphate content is high enough, a phosphate network can form during glass synthesis. Only orthophosphate was found in TEP4p12r and TEP8p12r, corresponding to the HA formed during glass synthesis. When the phosphate content increased to 12 mol%, pyrophosphate was found in the glass but not polyphosphate, and it was a sign of phosphate network formation. When the phosphate content was 24 mol%, most phosphates formed polyphosphate, the phosphate network, instead of forming HA during glass synthesis. Therefore, there was no HA found in TEP24p12r glass after stabilisation. This matches the XRD and FTIR data (Figure 4.8 and Figure 4.10). Less HA was found in TEP12p12r after stabilisation when compared to TEP4p12r and TEP8p12r, because phosphates started to form

pyrophosphate during glass synthesis.

Figure 4.16 shows the ^{29}Si NMR spectra and it provides the information about Q^n structures of Si-O species in each glass (section 3.8). The Q^n structures distribution and the degree of condensation (D_c) of Si-O species are summarised in Table 4.5.

A higher D_c means more condensation reactions occurred during glass synthesis in order to form a highly connective Si glass network. Table 4.5 suggests that the glass with higher amount of phosphate had a more connective Si glass network (higher D_c), the D_c of TEP24p12r was 94.3% and the D_c of TEP4p12r was only 56.5%. Because calcium acts as the network modifier, the glass with higher phosphate content contained less calcium in it therefore a denser Si network can be formed during glass synthesis. ^{29}Si NMR agrees with the nitrogen sorption data and provide the explanation for nonporous TEP24p12r.

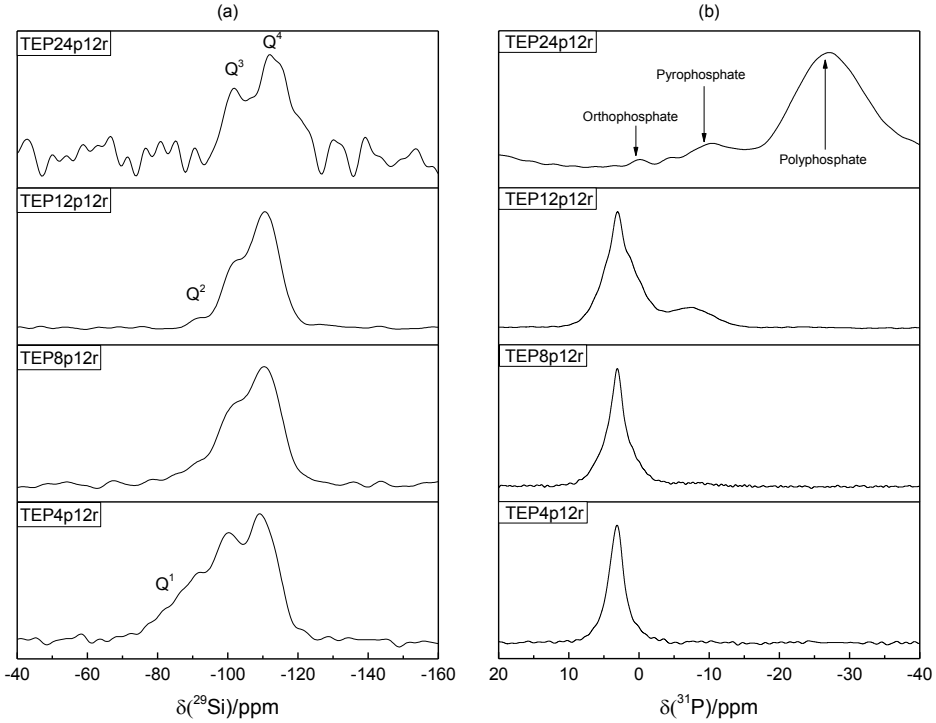


Figure 4.16 Solid state (a) ^{29}Si NMR (b) ^{31}P NMR of TEP sol-gel glasses made with 12R water ratio at 4, 8, 12 and 24 mol% P_2O_5 after stabilisation.

Table 4.5 The Q^n structures distributions and the degree of condensations of TEP sol-gel glassed made with 12R water ratio at 4, 8, 12, 24 mol% P_2O_5.

Sample	Q^1		Q^2		Q^3		Q^4		D_c[%]
	δ [ppm]	I [%]	δ [ppm]	I [%]	δ [ppm]	I [%]	δ [ppm]	I [%]	
TEP4p12r	-82.4	29.1	-92.3	32.7	-100.3	21.0	-109.2	17.1	56.5
TEP8p12r	-82.4	2.5	-93.7	13.7	-100.9	18.5	-110.0	65.3	86.7
TEP12p12r	-	-	-92.0	3.4	-101.2	25.7	-110.7	71.0	92.0
TEP24p12r	-	-	-	-	-101.4	23.0	-112.9	77.0	94.3

4.4 Discussion

4.4.1 Effect of phosphate (TEP) content on the structure of bioactive glass

The traditional sol-gel derived 58s glass (same composition as TEP4p12r) are bioactive but HA formed during glass synthesis when TEP and calcium nitrate were used. It is because the calcium ions from calcium nitrate cannot be incorporated into the silica network until the gel is heated to 400^{o}C. Therefore, the free orthophosphates and calcium ions are available for the HA formation; the hydroxyl groups from excess water in the sol-gel process allow the HA formation. The formation of HA during glass synthesis locks in the calcium and phosphate content. The calcium and phosphate released from the glass may therefore be released as HA nanoparticles rather than free ions. ICP cannot distinguish between free ions and nanoparticles. By increasing the phosphate content in sol-gel derived TEP4p12r (58S) glass, the level of preformed HA decreased (substitute calcium with phosphate). When the phosphate content was 12 mol%, the phosphate in the glass started forming pyrophosphates, the presence of pyrophosphate in TEP12p12r was the first sign of phosphate network formation. When the phosphate content reached 24 mol%, most of the phosphate formed the phosphate network during glass synthesis therefore less free orthophosphate were available for HA formation.

Increasing the phosphate content in the glass (to 24 mol%) can prevent HA formation during glass synthesis. But the high phosphate containing glass, TEP24p12r, lost its nanoporosity and bioactivity and did not form HCA in SBF. TEP4p12r and TEP8p12r were highly bioactive, they were able to trigger HCA formation just after 8 h of soaking in SBF. TEP12p12r took 1 week for HCA to form during SBF dissolution. The pH played an important role in HCA formation during SBF dissolution. OH^- and CO_3^- need to be incorporated into amorphous calcium phosphate layer to form crystallised HCA. But TEP24p12r reduced the pH of surrounding SBF too much, inhibiting crystallisation. It also explains why HCA formed slower on TEP12p12r than on TEP4p12r and TEP8p12r.

In conclusion, increasing the phosphate content in the glass can prevent the HA formation during glass synthesis but also reduces the bioactivity of the glass. However, calcium release and pH burst can be controlled through increasing phosphate content.

4.4.2 Effect of water contact on the properties of bioactive glass

The formation of HA during glass synthesis is caused by the reaction between free orthophosphate and calcium ions with the presence of water during sol-gel process. The hypothesis of the project was that a reduction in water content during sol-gel process can prevent the formation of HA during glass synthesis. But from all the data obtained, reduction in water content did not stop HA formation during glass synthesis and it did not affect any property of the glass. TEP glasses with 12R water ratio and TEP glasses with 4R water ratio gave very similar results for all the charactering tests.

4.5 Conclusions

1. HA formed in low phosphate containing glasses (4 mol% and 8 mol%) during glass synthesis when calcium nitrate and TEP were used as the precursors.

2. Increasing the phosphate content in the glass could prevent the HA formation during glass synthesis. When phosphate content was increased to 12 mol%, pyrophosphates formed within the glass during glass synthesis which could be a sign of phosphate network formation. However, HA still formed in the glass containing 12 mol% of phosphate during glass synthesis.

3. When the phosphate content in the sol-gel glass was increased to 24 mol%, phosphate network formed during glass synthesis instead of forming HA. But the high phosphate glass was no longer nanoporous and could not induce HCA formation in SBF.

4. Reducing the water content from 12R to 4R during sol-gel process could not prevent HA formation during glass synthesis.

5 Sol-gel glass synthesised with alternative phosphate sources

5.1 Introduction

The previous chapter suggested that high phosphate content in sol-gel derived bioactive glass can prevent the formation of HA during glass synthesis, but the high phosphate content also inhibits the HCA formation in SBF. Therefore, alternative phosphate precursors, Diethyl phosphatoethyl triethoxysilane (DEPETES) and tributyl phosphate (TBP) were used. The hypothesis was that because of the nature of DEPETES, there will not be any orthophosphate formed during the sol-gel process, and can therefore prevent HA formation during glass synthesis. TBP has a chemical structure similar to TEP and so was also investigated. The aim was to investigate how the alternative phosphate precursors affect the glass structure and properties.

5.2 Materials and methods

5.2.1 Materials

Tetraethyl orthosilicate (TEOS, 98%), nitric acid (HNO_3, 69%), calcium nitrate tetrahydrate ($Ca(NO_3)_2 \cdot 4H_2O$, 99%), tributyl phosphate (TBP, 99%) and Diethyl phosphatoethyl triethoxysilane (DEPETES, 92%) were used in sol-gel bioactive glass synthesis. Materials used for SBF preparation in this section were the same as described in Section 3.3. DEPETES was purchased from Fluorochem and all other chemicals were purchased from Sigma-Aldrich. HNO_3 was diluted in deionised water to make the concentration of 2 M and all the other chemicals were used as purchased.

5.2.2 Synthesis of sol-gel glasses with DEPETES and TBP

Samples in this chapter were prepared by using acid-catalysed sol-gel protocol [62] via the same route as described in section 4.2.2, mixing at room temperature, aging at 60°C, drying at 130°C and stabilisation at 700°C, but with alternative phosphate precursors, TBP and DEPETES (Figure 5.1).

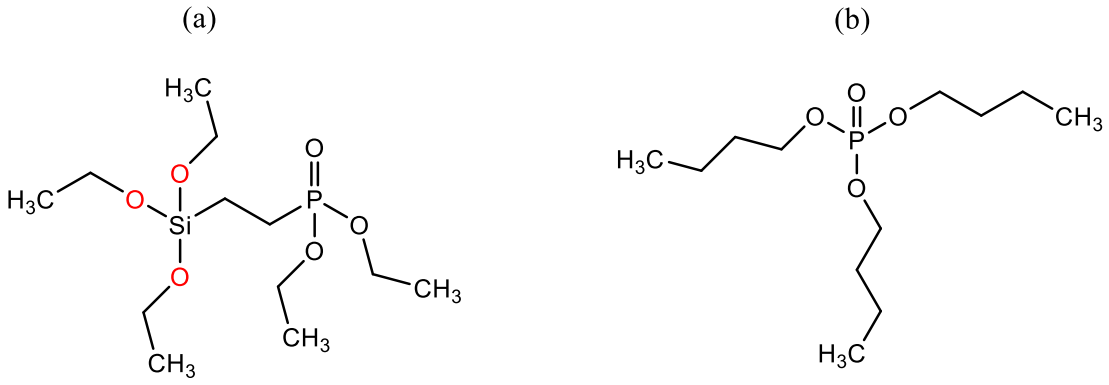


Figure 5.1 Chemical structure of (a) DEPETES (b) TBP.

It was noticed that there was a phase separation between TBP and hydrolysed TEOS solution when the R water ratio was 12, but TBP dissolved in the sol which contained 4R water ratio, therefore TBP glasses were made with 4R water ratio. TBP has longer carbon chains than TEP and which makes the hydrolysis of TBP more difficult than TEP. When water ratio was 4, most of water molecules were used to hydrolyse TEOS and ethanol was released as the by-product of the hydrolysis reaction. TBP is miscible

in ethanol and the rest of the water molecules (water was restored by polycondensation of silica tetrahedral) in the sol could slowly hydrolysed the TBP to orthophosphate.
The samples are named after the phosphate precursor used and their composition: TBPXp and DEPETESXp are of chemical composition 60 mol% SiO_2, X mol% P_2O_5 and (40-X) mol% CaO, the R water ratio for TBPXp glasses is 4 and for DEPETESXp is 12. The chemical composition of each sample in this chapter is shown in Table 5.1.

Table 5.1 Chemical compositions of phosphate containing glasses made with TBP and DEPETES.

Sample	SiO_2 (mol%)	P_2O_5 (mol%)	CaO (mol%)	Water ratio (R ratio)
TBP4p	60	4	36	4
TBP8p	60	8	32	4
TBP12p	60	12	28	4
TBP24p	60	24	16	4
DEPETES4p	60	4	36	12
DEPETES8p	60	8	32	12

5.2.3 Characterisation techniques

Samples made in this chapter were ground into power and sieved via the same route as described in section 4.2.3. SBF dissolution study was carried out on the powder samples. The characterisation techniques used were FTIR-ATR, XRD, MAS-NMR, nitrogen sorption, ICP-OES and SEM. Chapter 3 contains the detail of each technique used in this chapter.

5.3 Results

5.3.1 Glass appearance

Photographs of DEPETES glasses are shown in Figure 5.2. DEPETES4p was white after stabilisation, but DEPETES8p turned grey after stabilisation. This was caused by carbon black trapped in DEPETES8p. During stabilisation, carbon atoms can leave the glass as carbon dioxide when oxygen gas is present but sometimes some carbon black remained in the glass after stabilisation as there was not enough oxygen to oxidise the organic completely. The mechanical (handling) strength of both DEPETES glasses was low after stabilisation at 700ºC.

For TBP glasses contains 24mol% of phosphate (Figure 5.2f) was completely black, TBP8p and TBP12p were partially black (Figure 5.2d and e). Only TBP4p glass was completely white after stabilisation. (Figure 5.2c) It is because TBP contains more carbon atoms then TEP.

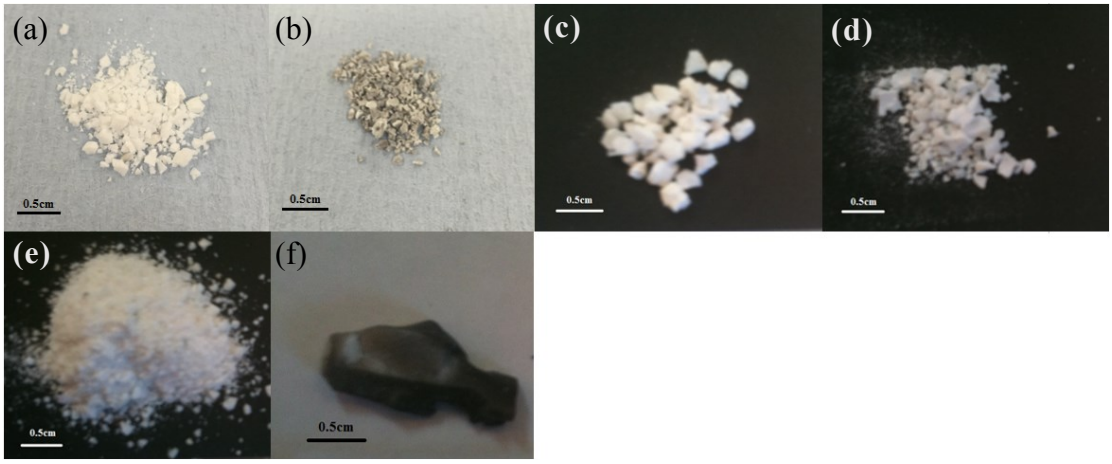


Figure 5.2 The appearnce of sol-gel glass made with DEPETES at (a) 4 mol % (b) 8 mol% P_2O_5 and sol gel glass made with TBP at (c) 4 mol% (b) 8 mol% (e) 12 mol% (f) 24 mol % P_2O_5 after stabilisation at 700°C.

5.3.2 Nitrogen sorption

The isotherms (Figure 5.3) suggest that the DEPETES4p had a greater pore volume then DEPETES8p, because the calcium (network modifier) content in DEPETES8p was lower, therefore the Si glass network in DEPETES8p was more connected. The hysteresis loops for DEPETES4p was type H2 (refer to section 3.2). Because DEPESTE8p glass did not absorb nitrogen well, it was difficult to assign the hysteresis loop to one of the five characteristic hysteresis loops, but it was more likely to be type

H2 or type H4. The DEPETES glasses adsorbed less nitrogen than corresponding TEP glasses (1 g of DEPETES4p absorbed around 160 cc and 1 g of TEP4p12r absorbed around 300 cc of nitrogen), it might be because phosphate from DEPETES incorporated into the Si glass network in a different way to the phosphate from TEP did.

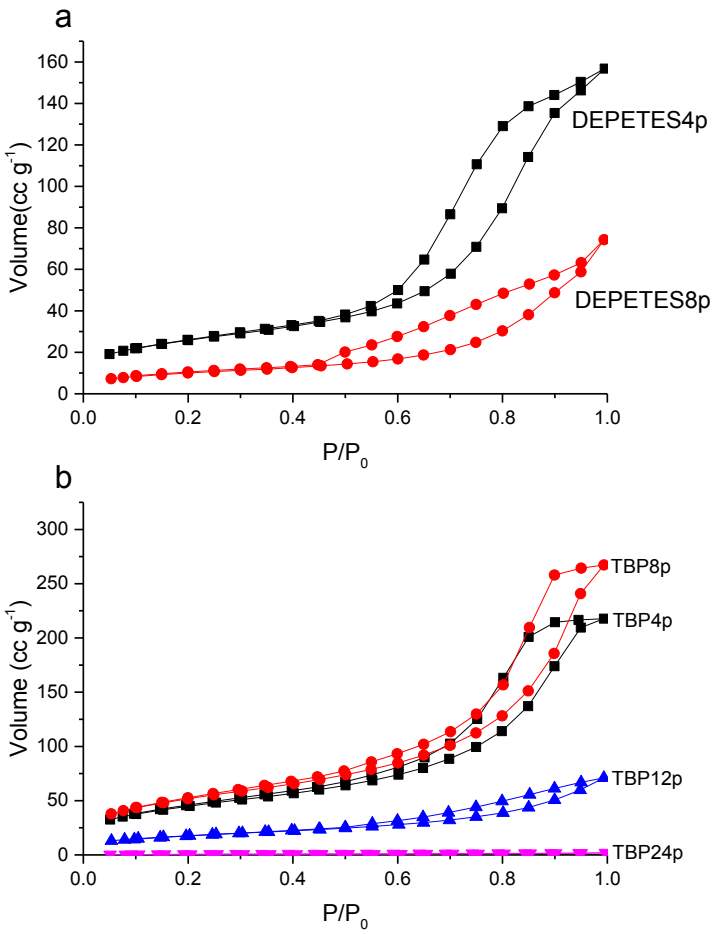


Figure 5.3 Nitrogen adsorption-desorption isotherms of sol-gel glass made with (a) DEPETES at 4 mol % and 8 mol% P_2O_5 (b) sol gel glass made with TBP at 4, 8, 12 and 24 mol % P_2O_5 after stabilisation at 700°C.

Figure 5.4a shows the pore size distributions for DEPETES4p and DEPETES8p. DEPETES4p had slightly larger pores then DEPETES8p. The DEPETES4p had a modal pore size at 7.5 nm and DEPETES8p had a wide range of pore size distribution from 5 nm to 12 nm. But the density of the nanopores in DEPETES8p was much lower than DEPESTS4p, suggesting that DEPETES8p is much less porous then DEPESTE4p. For the TBP glasses, TBP4p and TBP8p had similar pore size distribution, the size of the nanopores in both glasses are distributed from 5nm to 17.5nm. Modal pore size of

TBP8p (12.5nm) is slightly bigger then TBP4p (10nm) (Figure 5.4b). The TBP12p (Figure 5.3b, around 50cc of nitrogen was absorbed by 1 g of TBP12p) is much less porous when compare to TEP12p12 and TEP12p4r (refer to Figure 4.3 around 150cc of nitrogen was adsorbed by 1 g of TEP12p4r). That is because of TBP contains more carbon atoms then TEP, therefore during the stabilisation, not all the carbon atoms were removed and the trapped carbon black blocked the nanopores therefore reducing the nanoporosity of the glass. The only unexpected data was that TBP4p glass had lower pore volume then TBP8p glass and the cause of that is still unknown.

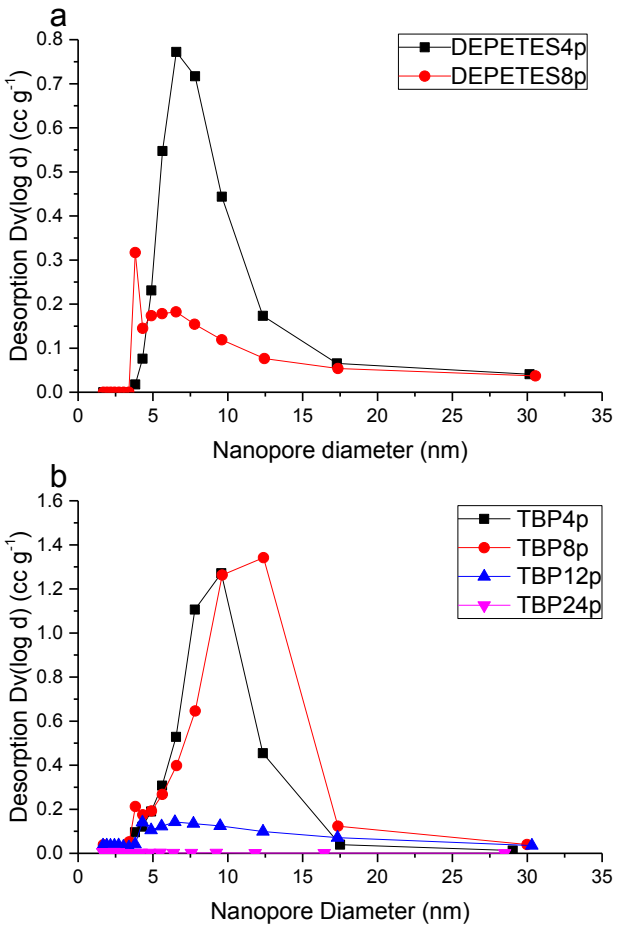


Figure 5.4 Pore size distributions of (a) sol-gel galsses made with DEPETES at 4 and 8 mol% P_2O_5 (b) sol-gel glasse made with TBP at 4, 8, 12 and 24 mol% P_2O_5.

The surface area of the glass is determined by the total pore volume and the size of the nanopores in the glass. Smaller pores and larger total pore volume can give a higher surface area. The surface area of the glass was calculated by BET method. The surface area of DEPETES4p (91.1 m^2 g^{-1}) was larger than DEPETES8p (35.7 m^2 g^{-1}) as the DEPETES4p had similar range of pore size distribution but larger total pore volume (Table 5.2).

Since all the TBP glasses had similar pore size distribution (from 5 nm to 17 nm), the surface area of TBP glass was purely dependent on the pore volume of the glass, TEP glass with the largest pore volume had the largest surface area (surface area: TEP8p > TEP4p > TEP12p > TEP24p, Table 5.2 and Figure 5.3).

Table 5.2 Surface areas of DEPETES glasses and TBP glasses.

Bioactive glass	Surface area (m^2 g^{-1})
DEPETES4p	91.1
DEPETES8p	35.7
TBP4p	161.2
TBP8p	185.5
TBP12p	62.8
TBP24p	2.2

5.3.3 Particle size of glass powder

90% of both DEPETES4p and 8p glass powder particles were smaller than 38 µm. DEPETES4p had a D(v,0.9) of 34.8 µm, compared to 25.0 µm for DEPETES8p.

Table 5.3 Particle size distribution of DEPETES glasses after grinding and sieving with a 38 µm sieve.

Sample	D(v,0.1)/µm	D(v,0.5)/µm	D(v,0.9)/µm
DEPETES4p	4.00	15.6	34.8
Standard deviation	0.36	1.06	0.26
DEPETES8p	3.11	10.0	25.0
Standard deviation	0.06	0.07	0.10

5.3.4 SBF dissolution

The pH of SBF at time point 0 was 7.4, both DEPETES glasses induced rapid pH increase as soon as they were soaked into SBF, which then slightly dropped after 24 h of SBF dissolution and stopped fluctuating after 168 h. It can be an indication of rapid calcium release from the DEPETES glass by cation exchange with H^+ ions in SBF. The phosphate content was released as phosphate species which buffered the pH increase by calcium ions. The pH of SBF for DEPETES4p was 7.95 at 8 h time point, which was higher than DEPETES8p (pH 7.65). Then the pH for DEPETES4p dropped to 7.85 and then levelled off after 1 week; for DEPETES8p the pH of SBF dropped to 7.55. The pH difference between DEPETES4p and DEPETES8p was caused by higher calcium and lower phosphate content in DEPETES4p.

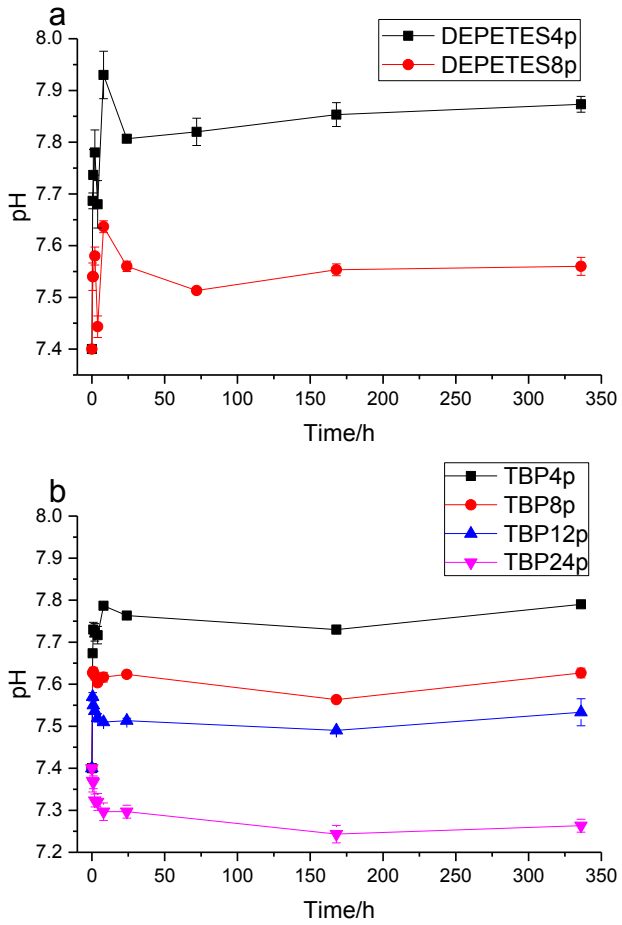


Figure 5.5 pH change profile of of sol-gel glasses made with (a) DEPETES at 4 and 8 mol% P_2O_5 (b) TBP at 4, 8, 12 and 24 mol% P_2O_5.

The SBF profile suggests that the calcium and phosphate deposition occurred as soon as the DEPETES glasses were immersed in SBF (Figure 5.6). The concentration of

calcium in DEPETES8p SBF started to drop gradually toward 40 μg ml^{-1} just after 1 h of dissolution. For DEPETES4p, the concentration of calcium in SBF increased significantly from 100 ppm to 190 ppm after 30 mins of dissolution then started dropping gradually and reaching 125 μg ml^{-1} at 3 d time point. For both DEPETES4p and 8p, the concentration of phosphorus dropped to 0 ppm rapidly within 3 days of SBF dissolution. The phosphorus level in DEPETES4p reaching 0 μg ml^{-1} after 24 h of dissolution and phosphorus level in DEPETES8p SBF dropped to 0 after 3 d of dissolution as DEPETES4p had lower phosphate content. This indicates the ions released from the glass and calcium phosphate deposition on the surface of the glass were happening simultaneously. In addition, the calcium phosphate deposition started as soon as the DEPETES glasses were immersed in SBF. For the DEPETES4p the rate of phosphate deposition was faster than it was released from the glass. For DEPETES8p, the calcium from SBF deposited faster than it was released from the glass as the calcium concentration in SBF started going down from the 30 min time point.

The Si profile indicates the degradation rate of DEPETES glasses. DEPETES4p degraded slightly faster than DEPETES8p (surface area: 35.7 m^2 g^{-1}) as DEPETES4p (surface area: 91.1 m^2 g^{-1}) had a larger surface area (Table 5.2). The silica network of DEPETES4p was less dense than DEPETES8p and that also made the DEPETES4p glass to degrade faster (refer to NMR data from section 5.3.8).

TBP glasses have a very similar dissolution profile to TEP glasses (Figure 4.6), so change the phosphate precursor from TEP to TBP did not really affect the ions releases of the glasses.

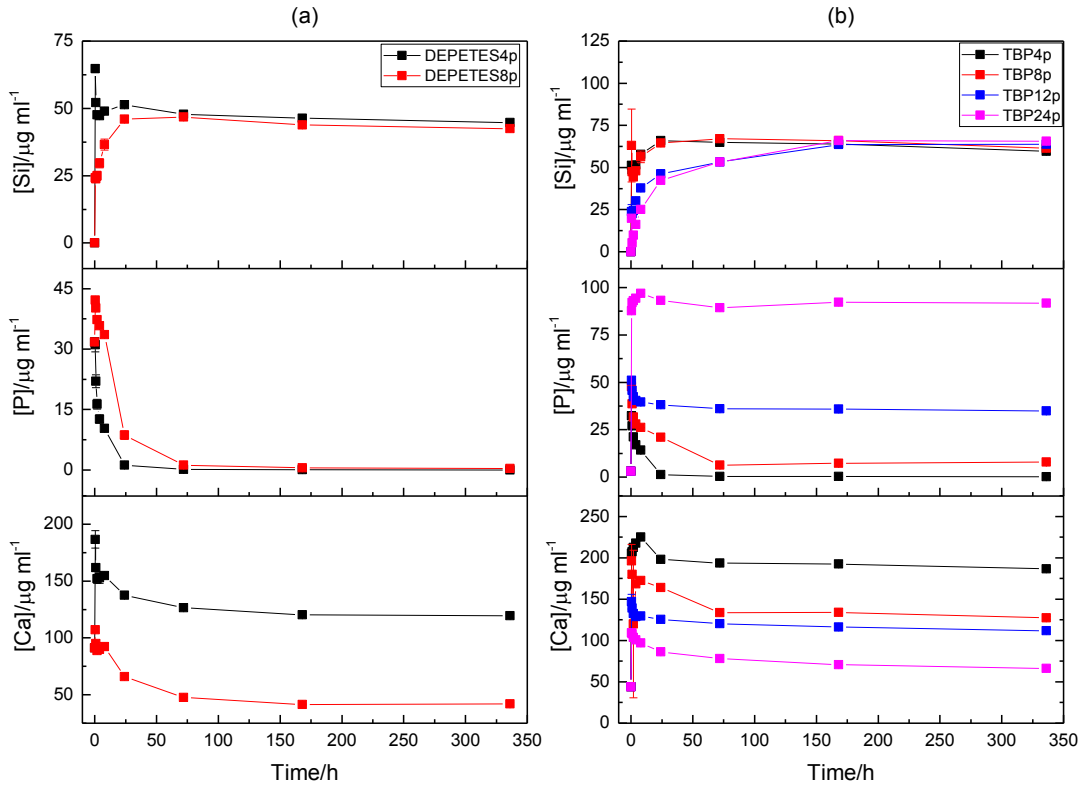


Figure 5.6 ICP dissolution profiles of sol-gel glasses made with (a) DEPETES at 4 and 8 mol% P_2O_5 (b) TBP at 4, 8, 12 and 24 mol% P_2O_5.

5.3.5 FTIR of sol-gel glass made with different phosphate precursors

From the FTIR spectra obtained (Figure 5.7), post-stabilisation DEPETES4p did not give the P-O bending bands at 546 cm^{-1} and 585 cm^{-1}, that correspond to orthophosphate, suggesting that there was no HA formed during glass synthesis. But a broad absorbance band at around 570-600 cm^{-1} was found in the FTIR spectrum for DEPETES8p before SBF, which can be attributed to amorphous calcium phosphate or HA with poor crystallinity in post-stabilisation DEPETES8p. A small amount of HA in glass might also be able to induce a weak band at 570-600cm^{-1}. XRD data is needed to confirm the presence of HA in post-stabilisation DEPETES8p. The FTIR spectrum for DEPETES4p shows that the amorphous calcium phosphate formed on the surface of the glass after 30 mins of SBF dissolution as the broad band at 570-600cm^{-1} appeared on the FTIR spectrum after 30 mins of SBF immersion. After 24 h of SBF dissolution, the P-O bending double bands (546cm^{-1} and 585cm^{-1}) were found on FTIR spectra for both DEPETES4p and 8p, indicating the formation of HCA on DEPETES4p and 8p after 24 h of SBF dissolution. The P-O stretching band at 1010cm^{-1} also became sharper gradually during SBF dissolution. The C-O stretch single band at 862cm^{-1} provides the

evidence for HCA formation by carbonate incorporation. DEPETES8p induced the HCA formation in the same way as DEPETES4p did, but the presence of the broad peak at 570-600cm^{-1} in the FTIR spectrum of post-stabilisation DEPETES8p (before SBF) makes it difficult to indicate HCA formation at any time point before 24 h of SBF dissolution, therefore XRD data is needed. For both DEPETES4p and 8p, the P-O bending double bands (546cm^{-1} and 585cm^{-1}) and the P-O stretching band (1010 cm^{-1}) were much sharper after 24 h of SBF dissolution than after 8 h dissolution. It suggests that the crystallisation of amorphous calcium phosphate to form HCA mainly occurred between 8 h and 24 h of SBF dissolution. It matches the ion concentration profile of DEPETES4p as concentration of phosphorus dropped to 0 ppm after 24 h of SBF dissolution. From the dissolution profile obtained (Figure 5.6), a hypothesis was made: "because there were more phosphates deposited on DEPETES8p than on DEPETES4p with excess of calcium in SBF, it might lead to more HCA formed after 2 weeks of SBF dissolution on DEPETES8p." The FTIR data supports the hypothesis as the P-O bending double bands (546 cm^{-1} and 585 cm^{-1}) and the P-O stretching band (1010 cm^{-1}) had higher relative intensity at 2 weeks SBF soaked DEPETES8p compared to 2 weeks SBF soaked DEPETES4p (Figure 5.7). In addition, changing the phosphate precursor from TEP to TBP also did not affect the HA formation during glass synthesis. (Figure 5.8)

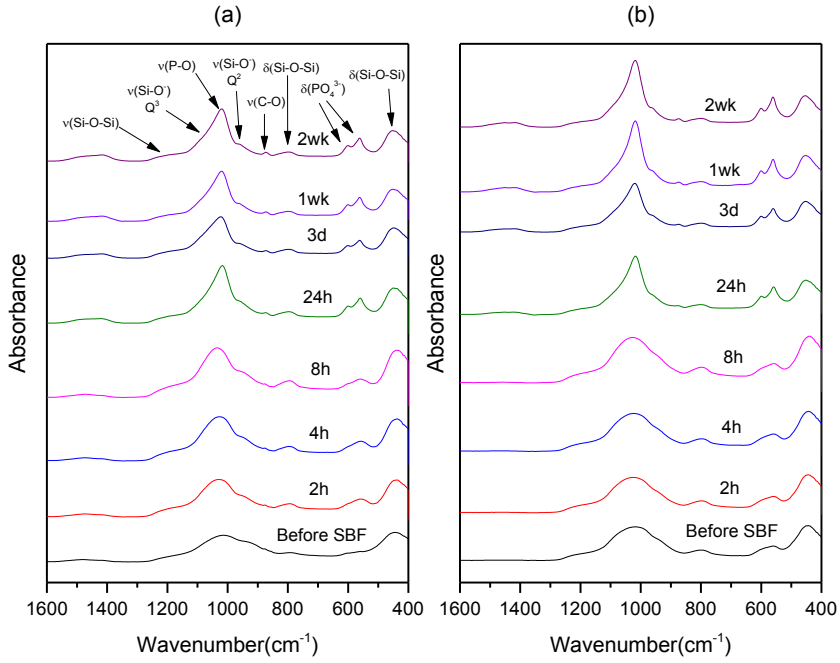


Figure 5.7 FTIR spectra of sol-gel glasses made with DEPETES at (a) 4 mol% and (b) 8 mol% P_2O_5 at different time point of SBF dissolution.

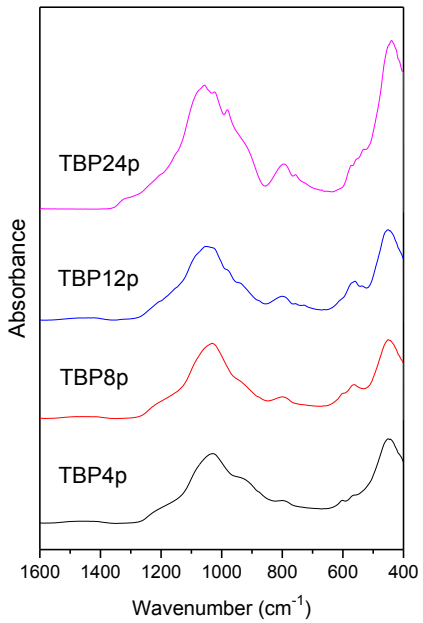


Figure 5.8 FTIR spectra of sol-gel glasses made with TBP at 4, 8, 12 and 24 mol% P_2O_5 after stabilisation at 700°C.

5.3.6 XRD

XRD provides the information about crystal structure of bioactive glasses. The peaks at 25° and 32° 2θ are the primary peaks for HCA and other then that the peaks at 38°, 46° and 49° 2θ are also attributed to the HCA. In addition, a broad peak at 30° 2θ can be found in the XRD patterns of amorphous calcium phosphate [202]. The XRD pattern of post-stabilisation DEPETES8p in Figure 5.9b expresses a broad peak at around 30° 2θ, and it can be attributed to a tiny amount of amorphous calcium phosphate in DEPETES8p before SBF dissolution and this matches the FTIR data obtained. XRD pattern of DEPETES4p before SBF shows that none of HA was found in post-stabilisation DEPETES4p (Figure 5.9a). Furthermore, the HCA peaks of XRD patterns became much sharper for both DEPETES glasses after 24 h of SBF dissolution when compare to 8 h SBF soaked DEPETES glasses. It matches the FTIR results and also suggests that the crystallisation of amorphous calcium phosphate mainly occurred between 8 h to 24 h of SBF dissolution. It also matches the dissolution profile (Figure 5.6a), the concentration of phosphate in the SBF dropped significantly between 8 h to 24 h of SBF dissolution. For DEPETES4p, the HA peak at 32° 2θ and weak amorphous calcium phosphate peak at 30° 2θ appeared on the XRD pattern after 2 h of SBF dissolution, it is taken as an indication of rapid formation of amorphous calcium phosphate and HCA after 2 h of SBF dissolution.

The XRD patterns (Figure 5.10) also suggest that changing the phosphate precursor from TEP to TBP did not prevent the HA formation during glass synthesis stage.

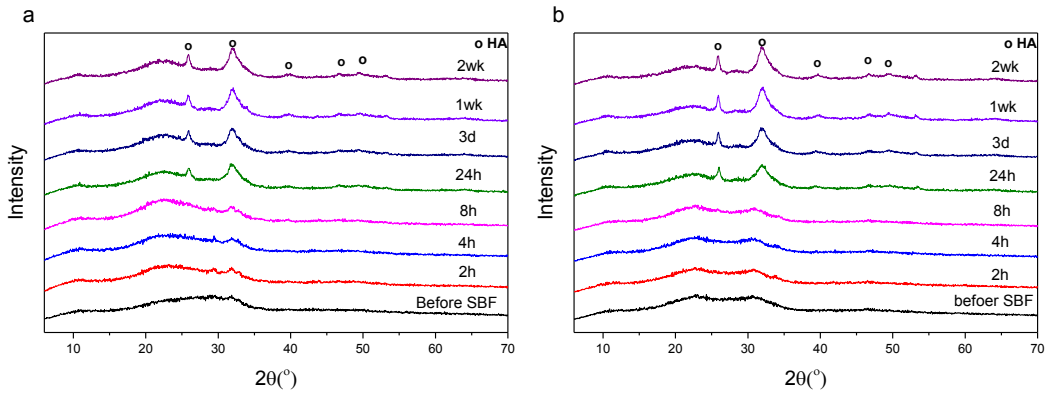


Figure 5.9 XRD patterns of (a) DEPETES4p (b) DEPETES8p at different time points of SBF dissolution.

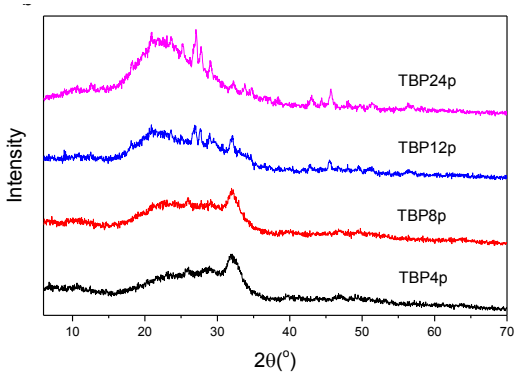


Figure 5.10 XRD patterns of sol-gel glasses made with TBP at 4, 8, 12, 24 mol% P_2O_5 after stabilisation at 700°C.

5.3.7 SEM

SEM images reveal the surface topography of bioactive glass. The SEM images of DEPETES glasses before SBF dissolution (Figure 5.11a and b) showed that both DEPETES glasses had very similar surface topography and only one type of topography was found in both DEPETES4p and 8p glasses. There was no apparent phase separation during the glass synthesis of DEPETES glasses. Both DEPETES 4p and 8p induced HCA formation during SBF dissolution and the HCA structure was visible under SEM after just after 8 h of SBF dissolution (Figure 5.11c and d). In addition, when looking at the DEPETES glasses under SEM, it was noticed that HCA was well spread on the surface of both DEPETES glasses after 2 weeks of SBF dissolution. But the HCA on DEPETES glasses after 8 h seemed sparse and heterogeneously distributed. As XRD and FTIR data suggest, the majority of HCA was formed between 8 h to 24 h after soaked in SBF.

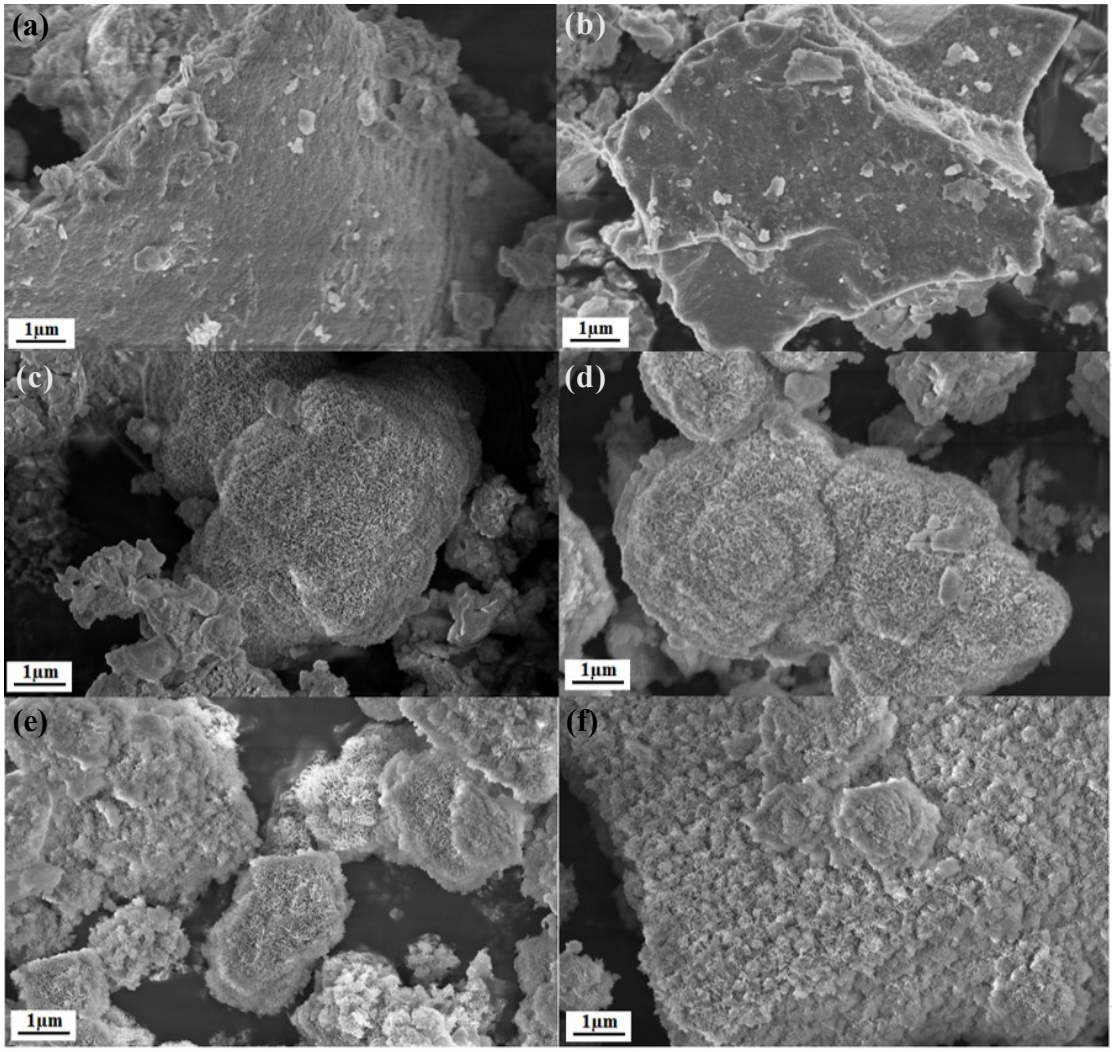


Figure 5.11 SEM images of sol-gel glasses made with DEPETES at (a) 4 mol% (b) 8 mol% P_2O_5 after stabilisation (c) 4 mol% (d) 8mol%P_2O_5 after 8 h of SBF immersion (e) 4 mol% (f) 8 mol% P_2O_5 after 2 weeks of SBF immersion.

5.3.8 Solid state MAS-NMR

The silica glass network in DPETES8p was more connected than the network in DEPETES4p, as shown by the greater degree of condensation (Table 5.4). Because of the lower amount of calcium in DEPETES8p, a denser silica network was formed in DEPETES8p. It explains the low porosity of DEPETES8p. There was a strong correlation between the degree of condensation and the porosity of bioactive glass, the higher the degree of condensation the lower the porosity of bioactive glass.

The result of ^{31}P NMR gives the information about phosphate components in the glass. Pyrophosphate was found in both DEPETES4p and 8p glasses (Figure 5.12b). It is an unexpected result as there was no pyrophosphate formed when the phosphate content was lower than 12 mol% in TEP glasses. For DEPETES glass, 4 mol% of phosphate

was enough to form pyrophosphate in the glass. When the phosphate content was 8 mol% the difference in the amount of pyrophosphate was obvious between DEPETES8p and TEP8p glass. This unexpected result of ^{31}P NMR further suggest that the phosphate from DEPETES might be incorporated into Si glass network in the different way as TEP did.

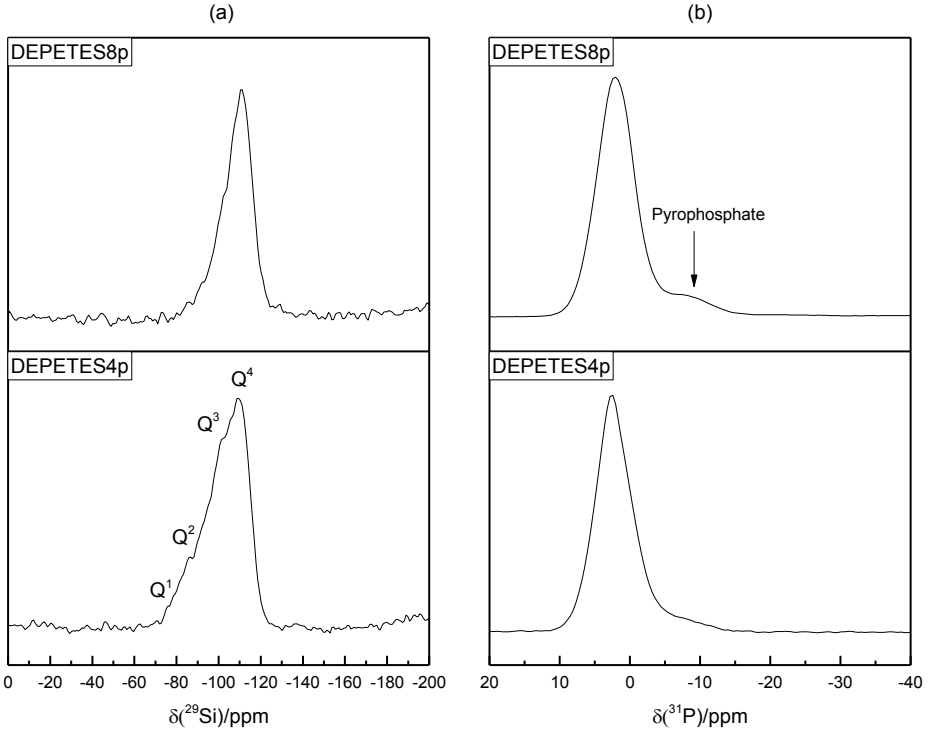


Figure 5.12 Solid state of DEPETES glasses (a) ^{29}Si NMR (b) ^{31}P NMR.

Table 5.4 The Q^n distributions and degree of condenstation of silica network in DEPETES glasses determined from ^{29}Si MAS-NMR spectra analysis.

Sample	Q^1		Q^2		Q^3		Q^4		D_c[%]
	δ [ppm]	I [%]	δ [ppm]	I [%]	δ [ppm]	I [%]	δ [ppm]	I [%]	
DEPETES4p	-81.6	21.1	-92.9	24.1	-101.3	26.2	-110.5	28.6	65.6
DEPETES8p	-84.6	1.9	-92.7	7.2	-100.4	14.2	-110.8	76.7	91.4

5.4 Discussion

5.4.1 Properties of DEPETES glass

Chapter 4 showed that in TEP glasses an increase in phosphate content can prevent HA formation during glass synthesis but the high phosphate containing TEP glass lost its bioactivity. By changing the phosphate precursor from TEP to DEPETES, HA formation during glass synthesis was successfully prevented. From the XRD and FTIR data obtained, there was no HA detected in both DEPETES4p and 8p glasses before SBF dissolution, but a small amount of amorphous calcium phosphate was found in post-stabilisation DEPETES8p. The hypothesis about DEPETES glasses (because of the nature of DEPETES, there will not be any free orthophosphate formed during sol-gel process, therefore can prevent the HA formation during glass synthesis) was proven. Both DEPETES glasses (4p and 8p) and TEP glasses (TEP4p12r and TEP8p12r) were able to induce a sufficient amount of HCA formation (to be found under SEM) after 8 h of SBF dissolution. DEPETES8p had a denser silica glass network than DEPETES4p, the results were as expected. But surprisingly the glass network of DEPETES glass was much more connected than the corresponding TEP glass, reducing the nanoporosity and surface area of DEPETES glasses (1 g of DEPETES4p had surface area of 91.1m^2 and 160cc of nitrogen absorbed; 1 g of TEP4p12r had surface area of 163m^2 and around 300cc of nitrogen absorbed). Even though DEPETES glasses still exhibited promising bioactivity during SBF dissolution.

DEPETES4p and DEPETES8p had very similar rates of HCA formation in SBF. Both can induce the formation of a sufficient amount of HCA for SEM just after 8 h of SBF dissolution. But according the results obtained, the amount of HCA formed on DEPETES8p after 2 weeks of SBF dissolution was slightly higher.

5.4.2 Phosphate incorporation into silica network from DEPETES

DEPETES glasses lost their mechanical (handling) strength after 700^{o}C of stabilisation. This in combination with the difference in degree of condensation suggests that phosphate from DEPETES was incorporated into silica glass network in a different way as it was from TEP precursor. For TEP, phosphate was in the form of orthophosphate, charge balanced with calcium ions. Phosphate from TEP was free in the sol until calcium started incorporating into silica network, which occurred at 400°C (when

calcium nitrate is used as the calcium precursor). But because of the chemical structure of DEPETES, the triethoxysilane end of DEPETES was hydrolysed and followed by the condensation reaction with hydrolysed TEOS (Figure 5.13). DEPETES was incorporated into the glass network by forming Si-O-Si covalent bonds with silica network (Figure 5.13). The phosphonate end of DEPETES was also be hydrolysed and formed P-O-P bonds with other hydrolysed phosphonate from DEPETES by condensation reactions (Figure 5.14). After stabilisation, the carbon chain in DEPETES was broken and exited glass as carbon dioxide. The breakage of carbon chains reduced the connectivity of silica network and leave the orthophosphates and pyrophosphates in glass. That is why DEPETES glass lost their mechanical strength after stabilisation and it can also explain the presence of small amount of pyrophosphate in post-stabilisation DEPETES glasses. Figure 5.13 and Figure 5.14 illustrate the possible reactions of DEPETES and TEOS. In order to further confirmed the theory, low temperature DEPETES need to be made and studied.

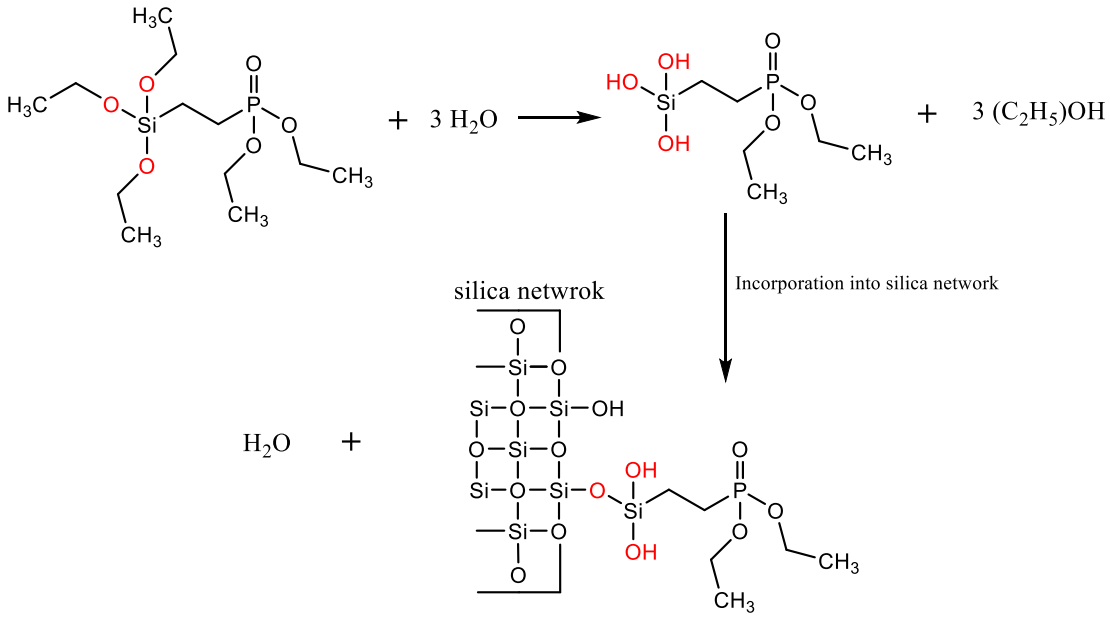


Figure 5.13 Incorporation of DEPETES into the silica glass network at room temperature.

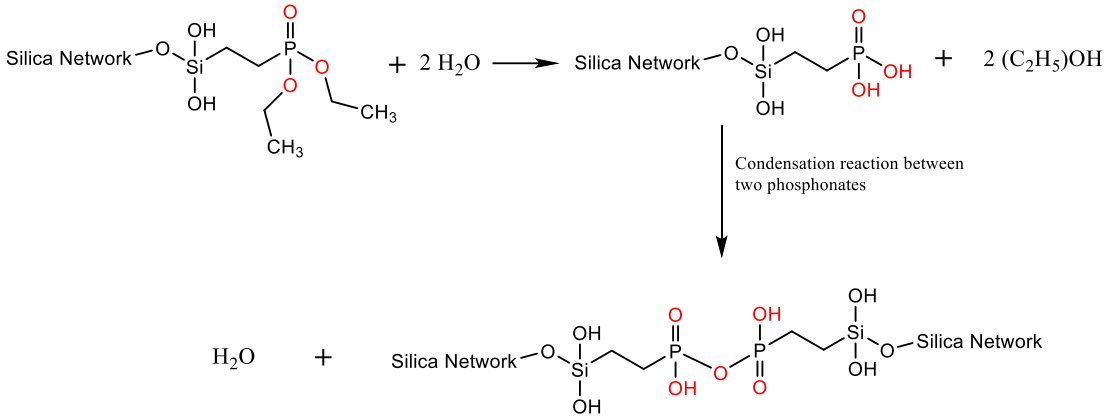


Figure 5.14 Hydrolysis of phosphonate end of DEPETES and condensation reaction between two phosphonates.

5.5 Conclusions

1. HA formation during glass synthesis was inhibited by changing the phosphate precursor from TEP to DEPETES.

2. Both DEPETES4p and DEPETES8p were able to induce HCA formation in SBF but without or with very little amount of preformed HA.

3. Both DEPETES4p and DEPETES8p glasses lost their mechanical (handling) strength after stabilisation.

4. Changing the phosphate precursor from TEP to TBP could not prevent HA formation during glass synthesis. TEP glasses and TBP glasses had very similar properties.

6 Low temperature sol-gel derived bioactive glass

6.1 Introduction

In order to incorporate a bioactive glass composition into a PCL based hybrid, some preliminary experiments were carried out. The heat treatments of sol-gel process can burn the organic in a hybrid material, therefore in order to choose a suitable glass composition for PCL hybrid system, some bioactive glass compositions were dried at low temperature (60^{o}C) and compared to post-stabilisation (700^{o}C) sol-gel derived bioactive glass. Apatite formation of the low temperature synthesised samples were tested by SBF dissolution. Calcium nitrate cannot be used in low temperature sol-gel process because the calcium from calcium nitrate only incorporates into glass network when the temperature is above 400°C [42, 203]. The calcium precursor used in this work was calcium methoxyethoxide (CME), it has been proven that the calcium from CME can be incorporated into glass network at room temperature [72]. The phosphate precursors used here was DEPETES.

In addition, Chapter 5 reported that, when DEPETES was used, the stabilisation heat treatment broke the carbon chains of DEPETES and weakened the mechanical (handling) strength of DEPETES bioactive glass. Investigation of DEPETES glasses with different synthesis temperatures (60^{o}C, 130^{o}C and 700^{o}C) were needed to determine how the drying temperature affected the structure-property relationships of the gels/glasses.

6.2 Materials and method

6.2.1 Materials

2-Methoxyethanol (anhydrous, 99.8%), calcium pieces (< 1 cm, 99%), tetraethyl orthosilicate (TEOS, 98%), nitric acid (HNO_3, 69%), pure ethanol (anhydrous, 200 proof, > 99.5%) and diethyl phosphatoethyl triethoxysilane (DEPETES, 92%) were used in sol-gel bioactive glass synthesis. Materials used for SBF preparation in this section were the same as described in Section 3.3. All chemicals were purchased from Sigma-Aldrich. 2-Methoxyethanol and calcium pieces were used in calcium methoxyethoxide (CME) formation. HNO_3 was diluted in deionised water to make the concentration of 2 M and all the other chemicals were used as purchased.

6.2.2 CME preparation

Calcium methoxyethoxide (CME) was prepared following the method described by Pickup *et al.* [88]. 4 g of calcium pieces was reacted with 96 ml of 2-methoxyethanol under argon atmosphere at 80°C in a 250 ml round bottom flask for at least 24 h (Figure 6.1). Then the resultant solution was centrifuged at 6000 rpm for 15 minutes to remove unreacted calcium metal. To determine the concentration of CME in the resultant solution, 1 ml the solution was transferred into a platinum crucible and heated to 1050°C for 12 h where all the solvent evaporated and CME converted to CaO. The concentration of CME in the resultant solution was then calculated using the following equation: [CME]= mass of CaO/molecular weight of CaO. This revealed that the concentration of CME solutions used in this chapter was around 1M.

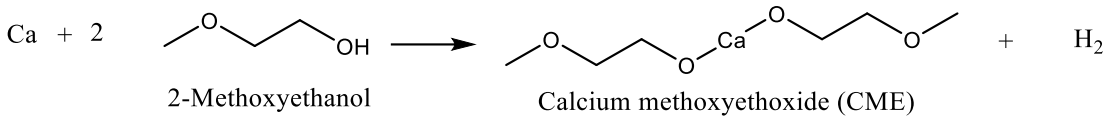


Figure 6.1 Schematic of the reaction between calcium and 2-Methoxythanol.

6.2.3 Sample preparation

In this chapter, various sol-gel derived glasses/gels were synthesised with CME as the calcium precursor and DEPETES as the phosphate precursor at different ratio of P_2O_5 to CaO (4 and 8 mol% of P_2O_5), with different synthesis temperatures (60°C, 130°C

and 700ºC). Samples are named after their compositions and synthesis temperature: CME DEPXp Yc indicates that the sample contains 60 mol% of SiO_2, X mol% of P_2O_5, (40-X) mol% of CaO and with synthesis temperature of YºC. The chemical composition of each sample is summarised in Table 6.1.

Table 6.1 Chemical compositions and synthesis temperature of samples synthesised with CME and DEPETES.

Sample	SiO_2 (mol%)	P_2O_5 (mol%)	CaO (mol%)	Water ratio (R ratio)	Synthesis Temperature (ºC)
CME DEP4p 60c	60	4	36	2	60
CME DEP8p 60c	60	8	32	2	60
CME DEP4p 130c	60	4	36	2	130
CME DEP8p 130c	60	8	32	2	130
CME DEP4p 700c	60	4	36	2	700
CME DEP8p 700c	60	8	32	2	700

The CME containing samples were synthesised by first mixing TEOS, CME and ethanol (molar ratio of ethanol : TEOS was 2:1) in a hermetic PTFE jar for 1 h at room temperature, then adding DEPETES into the sol. Because CME is highly reactive with water, it will form gel as soon as it contacts with water. Therefore, ethanol was used as a co-solvent to prevent immediate gelation when adding water into the sol. After at least 3 h of being stirred, deionised water (R=2) and 2 M nitric acid (1/6 amount of DI water) were added into the sol to hydrolyse the TEOS and CME. The sample sol was then stirred at room temperature for the other 30 minutes before heat treatment. Calcium from CME started to incorporate into the silica at this stage by condensation reactions between hydrolysed TEOS, $(OC_2H_5)_3SiOH$, and hydrolysed CME, $HOCa(OCH_2CH_2OCH_3)$, forming SiO-Ca^{2+}-OSi nonbridging oxygens [72].

Samples with synthesis temperature of 700ºC were taken through the full sol-gel heat treatment (aged at 60ºC, dried at 130ºC and stabilised at 700ºC). Samples with synthesis temperature of 130ºC were taken through the heat treatment without stabilisation (aged

at 60ºC and dried at 130ºC) and then left in the 60ºC oven until they were completely dried. The samples with synthesis temperature of 60ºC were aged at 60ºC for 72 h and dried at 60ºC. The protocols for aging, drying and stabilisation were the same as described in section 4.2.1.

6.2.4 Characterisation techniques

The characterisation techniques used in this chapter were SBF dissolution, ICP-OES, FTIR and XRD, as described in Chapter 3.

6.3 Results

6.3.1 SBF dissolution of samples synthesised at 60°C

CME DEP4p 60c and CME DEP8p 60c powders were immersed in SBF for 2 weeks in order to investigate their bioactivity (HCA forming ability) and pH buffering ability. During the SBF dissolution study, both CME DEP 60c samples seemed to absorb water and became gel-like when immersed in SBF (Figure 6.2).

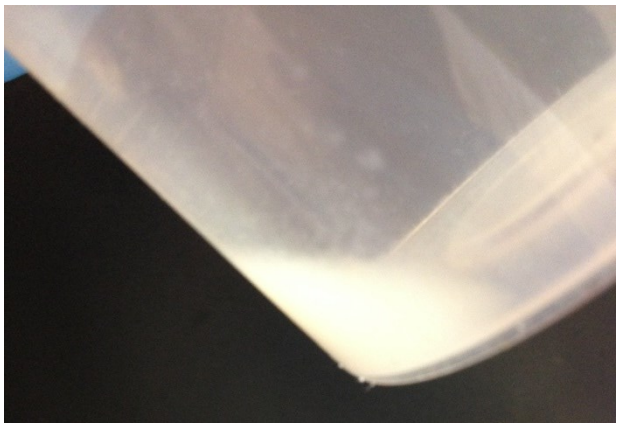


Figure 6.2 Photograph of CME DEP4p 60c in SBF.

Figure 6.3 shows that the silica, calcium and phosphate were rapidly released to the SBF from both CME DEP 60c samples. The silicon level rose significantly and then dropped slightly after 24 h of dissolution. The silicon level in the SBF containing low temperature CME DEP gel (CME DEP 4p 60c and 8p 60c) immersed was much higher than SBF exposed to post-stabilisation TEP glasses and DEPETES glasses, therefore it suggests that some low temperature CME DEP gel fell apart in SBF and the debris was taken with the SBF supernatant for ICP analysis, therefore, the actual ions levels were lower than the ICP profile. Both calcium and phosphorus level in SBF started dropping after 2 h of SBF dissolution, showing that the deposition of calcium and phosphate was happening.

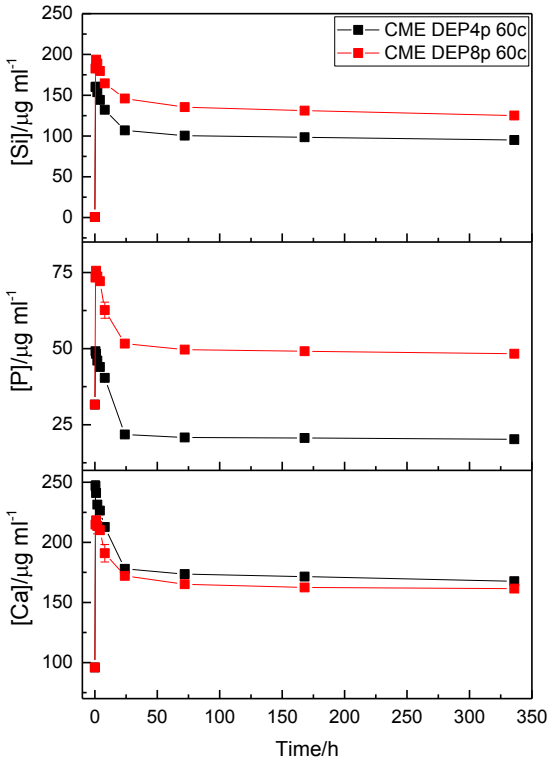


Figure 6.3 ICP SBF dissolution profile of the gels which contain 4 and 8 mol% of P_2O_5 made with CME and DEPETES at synthesis temperature of 60°C.

The pH changes in the SBF were also recorded. CME DEP 4p 60c immersed SBF and CME DEP 8p 60c immersed SBF had very small difference in pH during dissolution (pH of CME DEP 4p 60c SBF was around 0.05 higher). It suggests that the phosphates in the CEM DEP 60c glasses might be released as DEPETES therefore the phosphate from CEM DEP 60c glasses could not buffer the pH of surrounding.

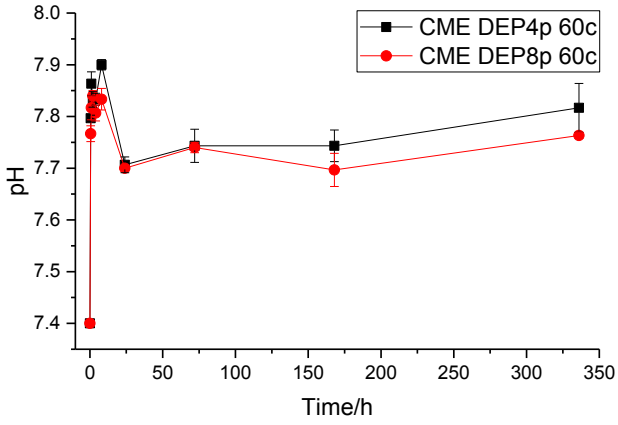


Figure 6.4 pH change profile of the gels which contain 4 and 8 mol% P_2O_5 made with CME and DEPETES at synthesis temperature of 60°C in SBF.

6.3.2 FTIR of sol-gel glasses/gels made with CME and DEPETES

All FTIR spectra were collected from CEM DEP 60c samples before and after 2 weeks of SBF dissolution (Figure 6.5). The appearances of the double P-O bending bands (571 cm^{-1} and 602 cm^{-1}) and P-O stretching (1040 cm^{-1}) in FTIR spectra after SBF dissolution indicates the formation of orthophosphate, which is likely to be HCA, during SBF dissolution. The presence of C-O stretching and bending peaks at 875 cm^{-1} and 1450 cm^{-1} respectively supports this.

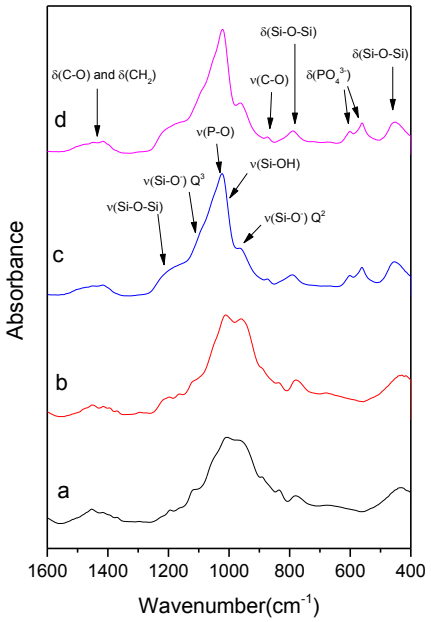


Figure 6.5 FTIR spectra of (a) CME DEP 4p 60c before SBF (b) CME DEP8p 60c before SBF (c) CME DEP 4p 60c after 2 weeks of SBF dissolution (d) CME DEP 8p 60c after 2weeks of SBF dissolution.

In order to study the phosphate incorporation from DEPETES, CME DEP gels/glasses with different synthesis temperatures (60ºC, 130ºC and 700ºC) were made and their molecular structures were investigated by FTIR. The broad band from 3000 cm^{-1} to 3700 cm^{-1} (OH group asymmetric stretching) indicates water, including residual hydroxyl functional groups. The small band at 1600 cm^{-1} (H-O-H deformation) indicates the molecular water in the CME DEP 4p 60c composition [200, 204]. Most of the bands from 2750 cm^{-1} to 3000 cm^{-1} are assigned to the hydrogen bonded OH groups. The presence of those few bands in the FTIR spectrum of CME DEP 4p 60c suggest that not all the water and ethanol molecules were removed from the low temperature synthesised CME DEP 4p sample. When the drying temperature increased to 130ºC, the relative intensities of those OH bands were reduced significantly,

suggesting that heating a CME DEP 4p sample to 130°C removed the water and ethanol residuals in CME DEP 4p. The bands from 1250 cm^{-1} to 1500 cm^{-1} were attributed to CH_2 bending vibrations [205, 206] from DEPETES. When CME DEP 4p was heated to 700°C the CH_2 peaks disappeared, indicating the high temperature broke the carbon chain in DEPETES. The FTIR spectra for CME DEP 8p (60°C, 130°C and 700°C) are very similar to CME DEP 4p, therefore only CME DEP 4p with different synthesised temperatures are shown here.

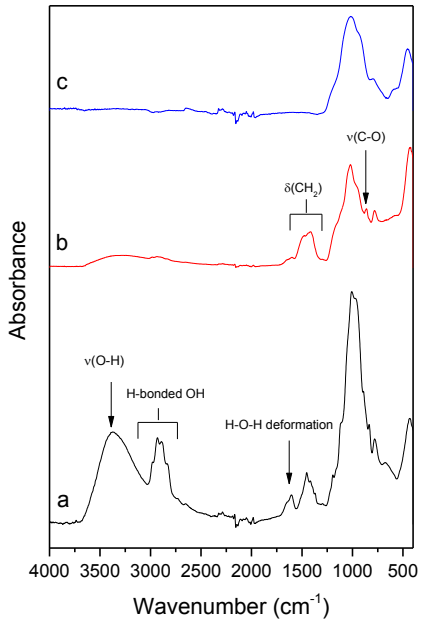


Figure 6.6 FTIR spectra of CME DEP 4p glasses with different synthesis temperatures before SBF dissolution (a) CME DEP 4p 60c (b) CME DEP 4p 130c (c) CME DEP 4p 700c.

6.3.3 XRD of sol-gel glasses/gels made with CME and DEPETES

Chapter 5 showed that using DEPETES as the phosphate precursor in sol-gel derived bioactive glass can prevent the formation of free orthophosphate in sol and also suppresses the formation of HA during glass synthesis. A small amount of amorphous calcium phosphate was found in DEPETES8p glass after 700°C stabilisation. Figure 6.7 shows that there was no crystalline HA or amorphous calcium phosphate found in CME DPE 4p 700c and CME DEP 8p 700c before SBF dissolution. It indicates that by using CME as the calcium precursor can further prevent HA formation during glass synthesis. Because calcium from CME can be incorporated into glass network at room temperature therefore there is no (or very little amount of) free calcium ions in sol, and leads to no HA or calcium phosphate formation during glass synthesis.

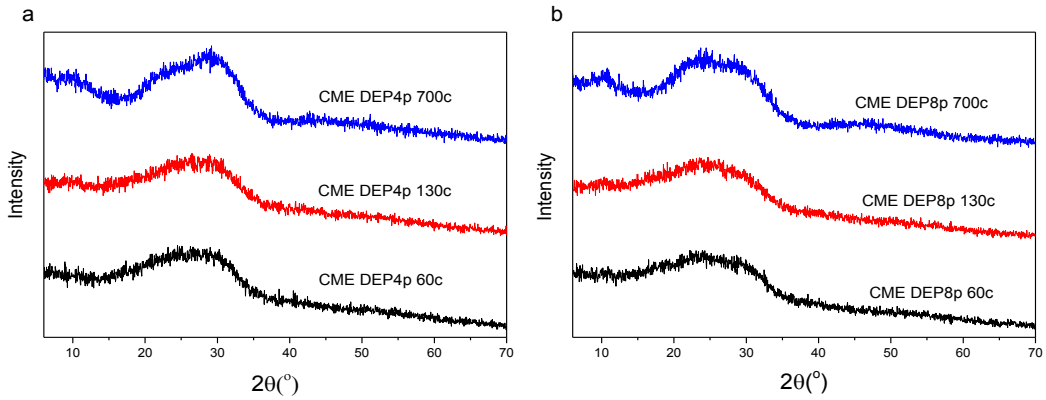


Figure 6.7 XRD patterns of (a) CME DEP 4p (b) CME DEP 8p glasses with different synthesis temperatures, 60ºC, 130ºC and 700ºC, before SBF dissolution.

CME DPE 4p 60c and CME DEP 8p 60c were immersed in SBF for 2 weeks and then the crystal structures of those two glasses were investigated by XRD. The peaks at 25.7º, 31.78º, 32.19º, 38.8º, 46º, 49.3º and 54º 2θ were all attributed to crystal HCA [197, 199, 200]. Figure 6.8 indicates the HCA formed on both CEM DEP 4p 60c and CME DEP 8p 60c after 2 weeks of SBF dissolution. It suggests that both low temperature CME DEP gels were bioactive and capable of inducing HCA formation in SBF.

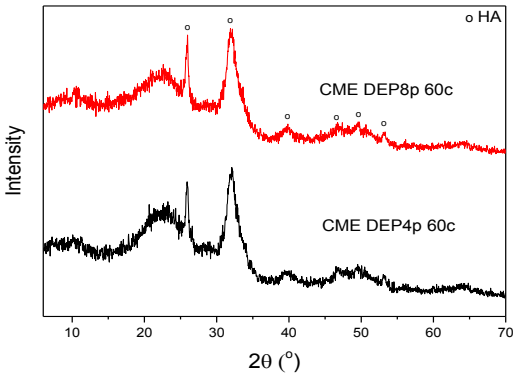


Figure 6.8 XRD patterns of CME DEP 4p 60c and CME DEP 8p 60c after 2weeks of SBF dissolution.

6.3.4 Solid state MAS-NMR

Solid state NMR was carried out to reveal the chemical structures of CME DEP glasses/gels when heated to different temperatures. ^{29}Si NMR provides the information about T^n and Q^n structures of silica network in CME DEP glasses/gels. Figure 6.9 indicates that T^n silica species were only found in CME DEP 4p and 8p when the synthesis temperature was below or equal to 130ºC, but not in the high temperature synthesised CEM DEP glasses (700ºC). It further confirms the theory that DEPETES

incorporates into sol-gel derived glass by forming Si-O-Si bonds with silica network, but the high temperature (above 400°C) breaks the carbon chain in DEPETES. Therefore, there were no T^n species found in high temperature synthesis CME DEP 4p 700c and CME DEP 8p 700c. The bands for T^n species were stronger in CME DPE 8p than in CME DEP 4p, it was because there was more DEPETES in CME DEP 8p samples and therefore more T^n species.

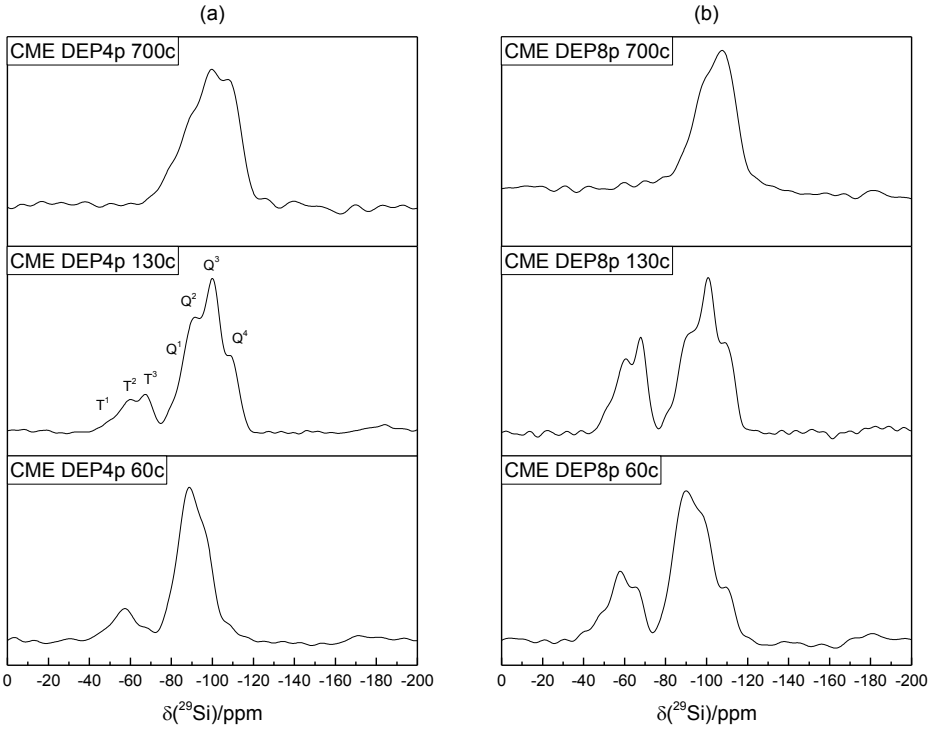


Figure 6.9 Solid state ^{29}Si NMR for (a) CME DEP 4p (b) CME DEP 8p with different synthesis temperatures, 60°C, 130°C and 700°C.

Table 6.2 shows the relative proportion of T^n and Q^n species in each CME DEP sample, the degree of condensation for each sample was calculated using Equation in section 3.8.

The degree of condensation increased when the glass synthesis temperature increased, suggesting that the silica networks in low temperature (60°C) CME DEP gels were low in connectivity, so they became gel-like when immersed in SBF. When comparing the degree of condensation between CME DEP 4p and CME DEP 8p glasses/gels, in general CME DEP 8p glasses/gels had higher degree of condensation than CME DEP 4p glasses/gels (D_c of CME DEP 4p 60c was 49.8% and D_c of CME DEP 8p 60c was

63.0%). This was because the calcium acts as a silica network modifier and the calcium contents in CME DEP 4p (60c, 130 and 700c) were higher (36 mol% calcium in CME DEP 4p and 32 mol% calcium in CME DEP 8p), therefore the silica networks in CME DEP 4p glasses/gels were less connected than in CME DEP 8p. However, calcium ions can only interfere the silica network formation when they enter the silica network by ionic bonding to the silica network. As Table 6.2 shows, that silica network in CME DEP 4p 60c had lower degree of condensation than CME DEP 8p 60c, it indicates that the calcium from CME could incorporate into the silica glass network at low temperature (60^{o}C).

Table 6.2 Chemical shift and relative proportions of T^n and Q^n species in each CME DEP glass synthesised with different synthesis temperatures. Degree of condensation for each sample was calculated from relative proportion of T^n and Q^n.

Sample	T^1		T^2		T^3		Q^1		Q^2		Q^3		Q^4		D_c[%]
	δ	I	δ	I	δ	I	δ	I	δ	I	δ	I	δ	I	
	[ppm]	[%]	[ppm]	[%]	[ppm]	[%]	[ppm]	[%]	[ppm]	[%]	[ppm]	[%]	[ppm]	[%]	
CME DEP 4p 60c	-50.3	5.6	-58.2	8.6	-67.8	2.0	-79.5	6.8	-88.9	55.6	-98.0	16.1	-108.0	5.2	49.8
CME DEP 4p 130c	-50.8	3.1	-59.4	6.9	-67.9	7.2	-81.3	5.5	-90.4	29.2	-100.3	33.9	-109.9	14.3	68.5
CME DEP 4p 700c	-	-	-	-	-	-	-82.9	17.4	-91.5	21.2	-99.5	21.5	-108.8	39.9	71.0
CME DEP 8p 60c	-50.6	9.2	-58.4	10.2	-66.6	7.8	-82.0	5.9	-89.4	34.0	-99.4	24.0	-110.4	8.9	63.0
CME DEP 8p 130c	-52.7	4.5	-59.8	11.4	-68.0	15.3	-82.0	2.3	-91.0	22.6	-100.7	26.9	-110.0	16.9	73.4
CME DEP 8p 700c	-	-	-	-	-	-	-79.6	4.0	-88.5	5.2	-96.9	22.9	-108.1	68.0	88.8

^{31}P NMR provide the information about the phosphorous components in CME DEP glasses with different synthesis temperatures. The two peaks between 20 ppm to 40 ppm in the ^{31}P NMR for low temperature (60^{o}C and 130^{o}C) synthesis CME DEP samples were assigned to the phosphonates from the silica network bound DEPETES (Figure 6.10) [207]. One of the peaks was attributed to a single phosphonate from the DEPETES bound to the silica network. Some condensation reactions happened and formed P-O-P bonds between two silica network bound DEPETES molecules, and the second peak was assigned to the P-O-P group from two linked DEPETES molecules (Figure 6.10a). Instead of phosphonates, only orthophosphate and pyrophosphate were

found after high temperature synthesis of CME DEP glasses (CME DEP 4p 700c and CME DEP 8p 700c). It further confirms that the carbon chains in DEPETES molecules were broken, leaving the orthophosphates and pyrophosphates when heated the CME DEP glasses to 700ºC. There was no evidence of Si-O-P bonds formation once the carbon chain was removed.

A small peak at around 0 ppm was found in ^{31}P NMR for CME DEP 4p 60c and CME DEP 8p 60c. The corresponding phosphorous molecule to that small peak is still unknown. It could be the peak for orthophosphate. But because of the nature of DEPETES, there should not be any orthophosphate formed when the synthesis temperature was 60ºC. In addition, the small peak at around 0 ppm became much weaker when the increased the synthesis temperature to 130ºC, therefore the peak should not be attributed to orthophosphate.

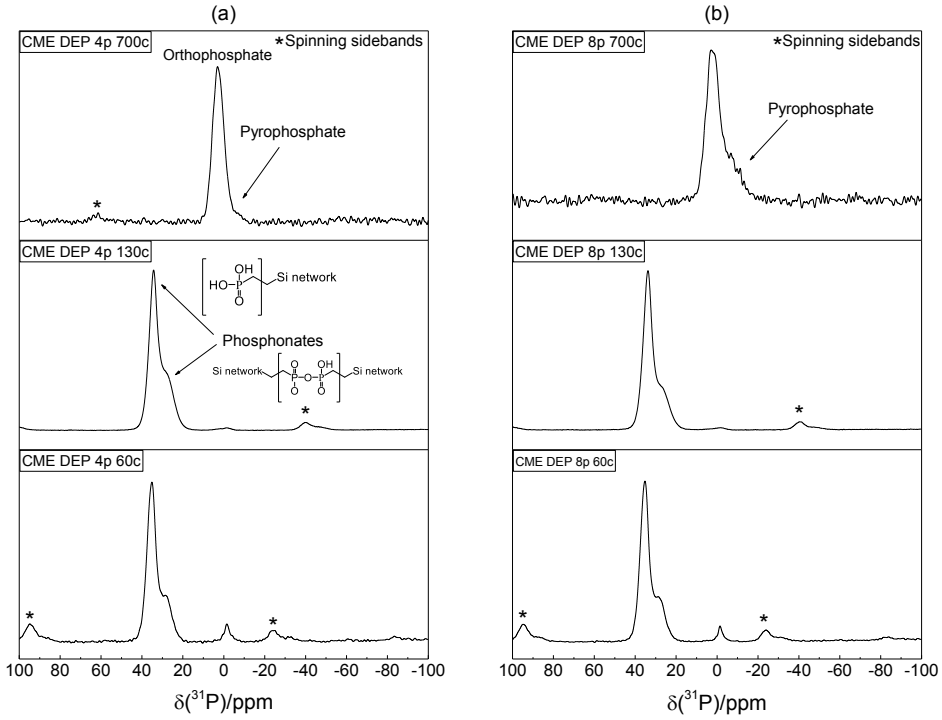


Figure 6.10 Solid state ^{31}P NMR for (a) CME DEP 4p samples (b) CME DEP 8p samples with different synthesis temperatures, 60ºC, 130ºC and 700ºC.

6.4 Discussion

Low temperature synthesised CME DEP 4p 60c and CME DEP 8p 60c were confirmed to be capable of inducing HCA formation when immersed in SBF. CME was found to be a potential calcium precursor to be used in low temperature synthesis of hybrids as it incorporated into the silica network at a temperature lower than 60^{o}C. But DEPETES is not a suitable phosphate precursor to be used in low temperature synthesis. As the pH change profile suggests that the phosphate content in the low temperature CME DEP glasses (60^{o}C) could not really buffer the pH of surrounding environment because the phosphate content might be released as hydrolysed DEPETES. Because of the nature of DEPETES, phosphate from DEPETES was incorporated into the glass network by forming covalent Si-O-Si bonds with silica network as T^{n} species were found until the CME DEP glasses were heated to 700^{o}C.

The ^{29}Si and ^{31}P solid state NMR results obtained in this work confirmed the theory of phosphate incorporation from DEPETES into silica network that is stated in Chapter 5. The triethoxysilane end of DEPETES was hydrolysed and formed Si-O-Si bonds with silica network by condensation reaction. The phosphonate end of a DEPETES could also be hydrolysed and then followed by condensation reaction with a hydrolysed phosphonate group from other DEPETES molecules. After 700^{o}C stabilisation, the carbon chain in DEPETES molecules were broken and leave the orthophosphates and pyrophosphates in glass.

6.5 Conclusions

1. Samples synthesised at low temperature (CME DEP 4p 60c and CME DEP 8p 60c) were able to induce HCA formation in SBF.

2. The hypothesis of phosphate incorporation from DEPETES made in Chapter 5 (section 5.4.2), at low temperature, was confirmed.

3. DEPETES is not a suitable phosphate precursor to be used at low temperature as the phosphate species released from the low temperature samples (CME DEP 4p 60c and CME DEP 8p 60c) could not buffer the pH of the surrounding. The phosphate content might be released as hydrolysed DEPETES.

7 Calcium containing PCL hybrids

7.1 Introduction

Data from Chapter 6 suggests that DEPETES is not suitable for low temperature synthesis. Phosphate from 60^{o}C CME DEP gels might release as DEPETES and could not buffer the pH of the surrounding solution. CME incorporated into glass network at 60^{o}C and released as calcium ions. The precursors used to make PCL hybrid in this work were CME and TEP. Because TEP can be hydrolysed to orthophosphate during sol-gel process and incorporated into glass network with calcium ions from CME at low temperature. The low temperature synthesis CME TEP 4p glass (TEOS, TEP and CME) and 6040 glass (TEOS and CME) were made and studied to make sure the glass compositions were bioactive before making the PCL hybrids. The PCL hybrid synthesis used in this project was based on the protocol developed by Francesca Tallia but with additional calcium and phosphate incorporation procedures. In her protocol, GPTMS was chosen as the coupling agent instead of ICPTES and APTES. In fact, during the functionalisation of PCL with GPTMS the unexpected polymerisation of THF into polyTHF occurred, leading to faster gelation (the gelling time reduced from days to hours). This observation was beneficial for the final goal of her project, which was designing PCL hybrid for 3D printing of porous scaffold directly from the sol-gel. Furthermore, it was observed that the resulting hybrid scaffold is tougher due to combination of polyTHF and PCL in the hybrid synthesis. [170]

In this work, compression test was done to investigate the mechanical properties of PCL hybrids with different glass compositions incorporated. Bioactivities of PCL hybrids were also assessed by SBF dissolution study. Characterising tests were applied on the PCL hybrids before and after SBF dissolution (e.g. XRD, FTIR and SEM). Cell cytotoxicity and the cell attachment studies were also being carried out. 3D-printing technique was used to make porous PCL hybrid scaffolds. The aim of this project was to develop non-toxic bioactive PCL hybrid scaffolds with sufficient mechanical strength for bone.

7.2 Materials and methods

7.2.1 Materials

2-Methoxyethanol (anhydrous, 99.8%), calcium pieces (< 1 cm, 99%), Tetraethyl orthosilicate (TEOS, 98%), nitric acid (HNO_3, 69%), pure Ethanol (anhydrous, 200 proof, 99.5%), Triethyl phosphate (TEP, 99%), polycaprolactone diol (PCL diol, average M_n ~ 530), Potassium bromide (KBr, 99%), 2,2,6,6-tetramethyl-1-piperidinyloxy (TEMPO, 98%), sodium bicarbonate ($NaHCO_3$), bleach (NaOCl, 3.5% - 5%), Hydrochloric acid (HCl, 37%), sodium sulfate (Na_2SO_4, anhydrous, 99%), Ethyl acetate (99.5%), acetonitrile (Ch_3CN, 99.8%), (3-Glycidyloxypropyl) trimethoxysilane (GPTMS, 98%), Boron trifluoride diethyl etherate ($BF_3O(C_2H_5)_2$, 46.5% BF_3 basis) and Tetrahydrofuran (THF, 99.9%) were used in PCL hybrid synthesis. The reagents used in cell culture studied are described in section 7.2.5.

Materials used for SBF preparation in this section were the same as described in Section 3.3. Bleach (NaOCl, 3.5% – 5%) was purchased from VWR and all other chemicals were purchased from Sigma-Aldrich. 2-Methoxyethanol and calcium pieces were used in calcium methoxyethoxide (CME) formation. HNO_3 was diluted in deionised water to make the concentration of 2 M. PCL diol was oxidised via TEMPO-mediated oxidation reaction. All the other chemicals were used as purchased.

7.2.2 PCL diol oxidation

PCL diol (530 Da) was oxidised in a biphasic system containing acetonitrile and water via the 2,2,6,6-tetramethyl-1-piperidinyloxy (TEMPO) catalysed oxidation of primary alcohol to carboxylic acid, the reaction is also known as Anelli's oxidation [208]. The mechanism of Anelli's oxidation is schematised in Figure 7.1. Sodium hypochlorite (NaOCl, bleach) form HOCl in water, HOCl is the stoichiometric oxidant which reacts with KBr to form HOBr, that acts as the catalytic secondary oxidant converting TEMPO radical into oxoammonium salt (catalytic primary oxidant), which transforms the alcohol into the corresponding aldehyde. As a result of this reaction, the oxoammonium salt is converted into hydroxylamine, and then the secondary oxidant HOBr transforms hydroxylamine back to TEMPO radical, thus completing the catalytic cycle. The aldehyde, in the presence of water, then equilibrates with the corresponding hydrate that can be further converted into the corresponding carboxylic acid via the same

oxidation mechanism [209]. The concentration of HOBr is low under very basic pH condition and that slows down the oxidation, therefore $NaHCO_3$ is added as buffer to reduce the pH from 12.7 (the pH of commercial bleach) to 8.6.

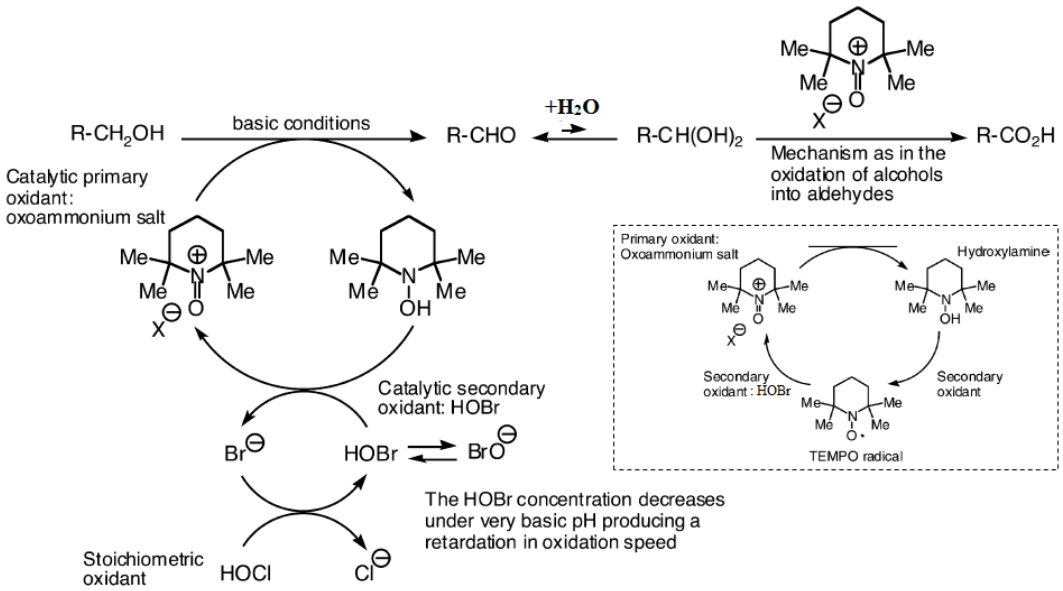


Figure 7.1 Anelli's TEMPO catalysed oxidation mechanism (adapted from [209]).

In this work, 3 g of PCL diol of M_n 530 Da was dissolved in 45.7 ml of acetonitrile under continuous stirring at room temperature. 12.3 ml of saturated $NaHCO_3$ aqueous solution, 4.58 ml of aqueous KBr solution (containing 2.26 mmol of KBr) and the solution containing 1.13 mmol of TEMPO in 11.32 ml of acetonitrile were sequentially added into PCL diol solution. Then 74.04ml of 5% aqueous bleach (NaOCl) solution was added into the PCL solution over a period of 24 h in 4 separate additions: V_1 = 29.02 ml, V_2 = 29.02 ml, V_3 = 8 ml and V_4 = 8 ml at time intervals 1 h, 4 h, 8 h and 24 h, respectively, from the point of the addition of TEMPO solution. After 74.04 ml of bleach solution was added, the resultant solution was left stirring for another 4 h before adjusting the pH to 3 or lower with 37% v/v HCl solution. After 1 h of stirring at room temperature, the acetonitrile in the resultant PCL solution was removed using Rotavapor (Büchi Labortechnik AG, Switzerland) at 60°C and 226 mbar. Then the PCL in the aqueous solution was extracted three times with ethyl acetate by solvent exchange and Na_2SO_4 was used to remove any remaining water from the solution of PCL in ethyl acetate. The ethyl acetate was then removed using Rotavapor at 60°C and 240 mbar in

order to leave the oxidised PCL-diol (PCL-diCOOH). Finally, the PCL-diCOOH was further dried under vacuum at room temperature for at least 12 h to remove any leftover solvent.

7.2.3 PCL hybrid preparation

For the PCL hybrids synthesis in this work, the inorganic glass sol and organic PCL sol were prepared separately. The inorganic bioactive glass sol was first prepared by mixing 2.14 ml (2 g) of TEOS, with the corresponding amount of CME and TEP (for phosphate contain PCL hybrids) under continuous stirring at room temperature in a sealed PTFE container for at least 3 h. The following molar ratios were prepared: 1. TEOS/CME = SiO_2/CaO = 60/40 molar ratio 2. TEOS/CME/TEP = SiO_2/CaO/P_2O_5 = 60/36/4 molar ratio 3. TEOS/CME/TEP = SiO_2/CaO/P_2O_5 = 60/32/8 molar ratio 4. TEOS/CME/TEP = SiO_2/CaO/P_2O_5 = 60/28/12 molar ratio.

For PCL sol, 500 mg of oxidised PCL-diol (PCL-diCOOH) was dissolved in 5 ml of Tetrahydrofuran (THF), then 417 µl of GPTMS (molar ratio of GPTMS : PCL diCOOH = 2:1) was added into the solution. After 10 to 15 minutes of stirring, 58.2 µl of $BF_3O(C_2H_5)_2$ was added into the resultant solution as a catalyst. After 90 minutes of mixing and stirring, the resultant PCL solution was added drop-wise into the inorganic glass sol, then the resultant hybrid sol was left stirring for 1 h (until a homogenous solution was formed) before adding water (molar ratio of water to TEOS was 2:1) and nitric acid (1/6 volume of water). Because of the presence of CME, the resultant hybrid sol gelled fast after water and nitric acid were added, therefore the resultant hybrid sol was transferred into a custom-made PTFE mold insert (Figure 7.2) just before it gelled (usually within 30 minutes after adding water and nitric acid). The PTFE insert was then sealed in a PMP mold and aged at 40^oC for 3 days. The drying stage of the PCL hybrids was well controlled, because the PCL hybrids might crack if they are dried too fast, therefore around 1.5 ml to 2 ml of 70% aqueous ethanol was added in the PMP mould to slow down the drying (Figure 7.2) and the PCL hybrids were first dried at 40^oC for around 2 weeks (until all the ethanol evaporated) then transferred to the 60^oC oven in order to dry the PCL hybrids completely.

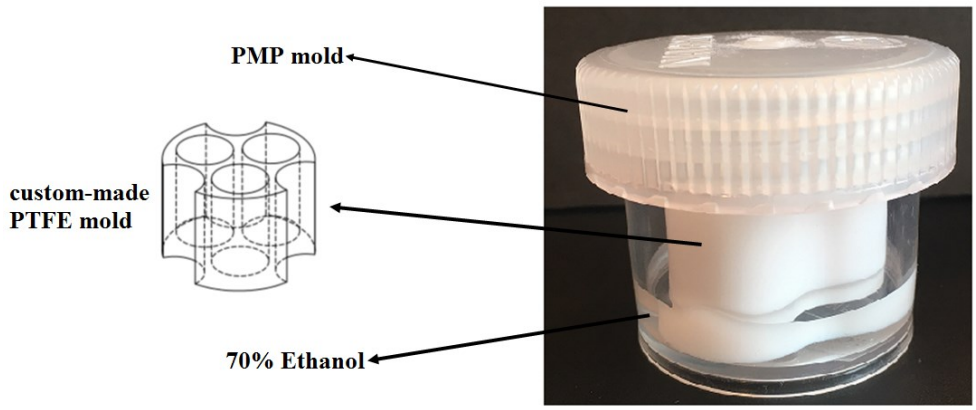


Figure 7.2 Schematic of the PTFE mold for PCL hybrid aging and drying; and a photograph of the PTFE insert within a PMP mold during ageing.

All PCL hybrids in this chapter were made with a TEOS/PCL wt ratio of 80:20 (2.14 ml (2 g) of TEOS and 500 mg of PCL diCOOH) and the corresponding amount of CME and TEP. The samples are named after the inorganic glass compositions incorporated into the hybrids: 6040 PCL was synthesised by incorporating the silica glass of chemical composition 60 mol% SiO_2 (from 2.14 ml of TEOS) and 40 mol% CaO into PCL hybrid (500 mg of PCL diCOOH in 5 ml of THF), TEPXp PCL was synthesised by incorporating a silica glass of 60 mol% SiO2 (from 2.14 ml TEOS), X mol% of P_2O_5 and (40-X) mol% of CaO into PCL hybrid (500 mg of PCL diCOOH in 5 ml of THF). The compositions of the PCL hybrids made in this work are summarised in Table 7.1.

Table 7.1 The compositions of calcium containing PCL hybrids made in this work. * the ratio of TEOS/PCL in wt% where 2.14 ml (2 g) of TEOS and 500 mg of PCL were used. ** the sol of inorganic component for hybrid synthesis was prepared separately by mixing 2.14 ml of TEOS + corresponding amount of CME (CaO precursor) and TEP (P_2O_5 precursor) to make up the chemical composition (in mol%) shows in the table.

Sample	Ratio of TEOS/PCL in hybrid (wt%)*	Composition of inorganic component incorporated into PCL hybrid (mol%)**		
		SiO_2	CaO	P_2O_5
6040 PCL	80:20	60	40	0
TEP4p PCL	80:20	60	36	4
TEP8p PCL	80:20	60	32	8
TEP12p PCL	80:20	60	28	12

Previous work by Tallia found that [170], in this system, THF reacts with GPTMS forming polyTHF, in the presence of $BF_3O(C_2H_5)_2$. Therefore, the hybrids made in this work contained two types of polymers, PCL and polyTHF. The mechanism of THF polymerisation is shown in Figure 7.3.

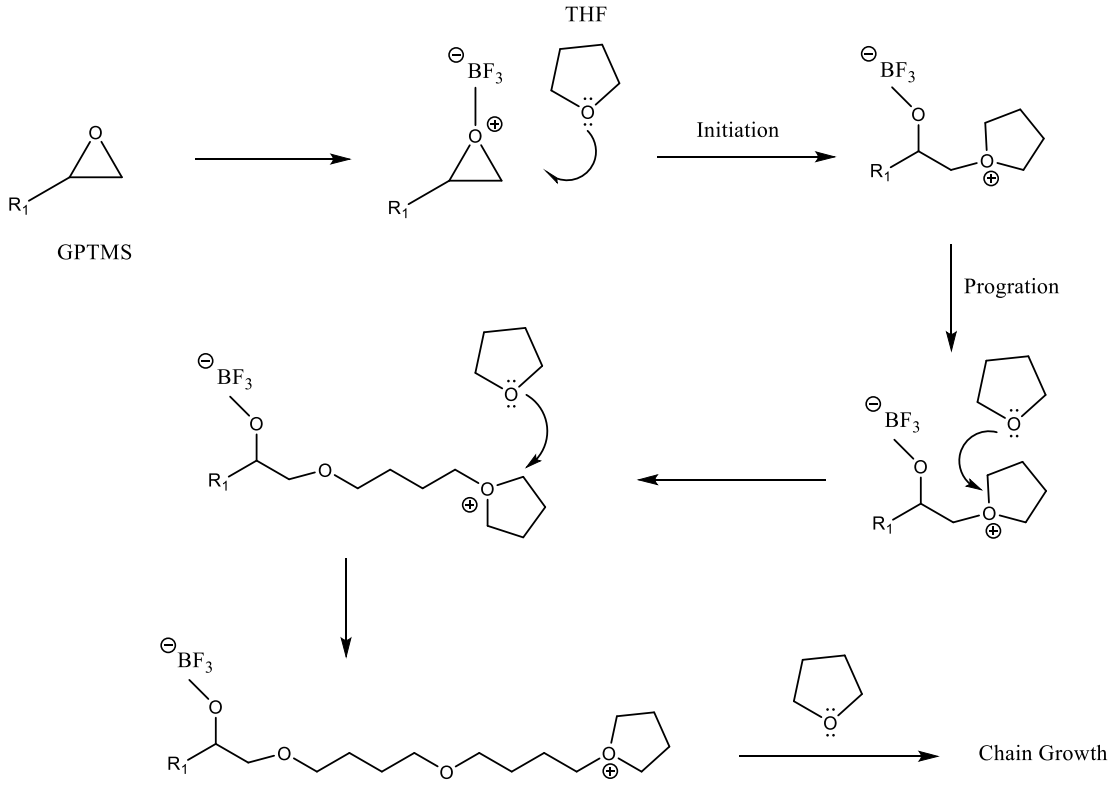


Figure 7.3 Mechanism of THF polymerisation [170].

However, the additional PCL-diCOOH also contributes to the reactivity of the system. A possible reaction is that the PCL-diCOOH may act as terminator of the THF polymerisation (Figure 7.4a). The other possible reaction occurs in the system is that the PCL-diCOOH may compete with THF polymerisation for GPTMS, giving nucleophilic attack on GPTMS (Figure 7.4b). It can also be the combination of both reactions. Because of the polyTHF formation during PCL hybrid synthesis, the true inorganic/organic ratio of a PCL hybrid needed to be determined using TGA.

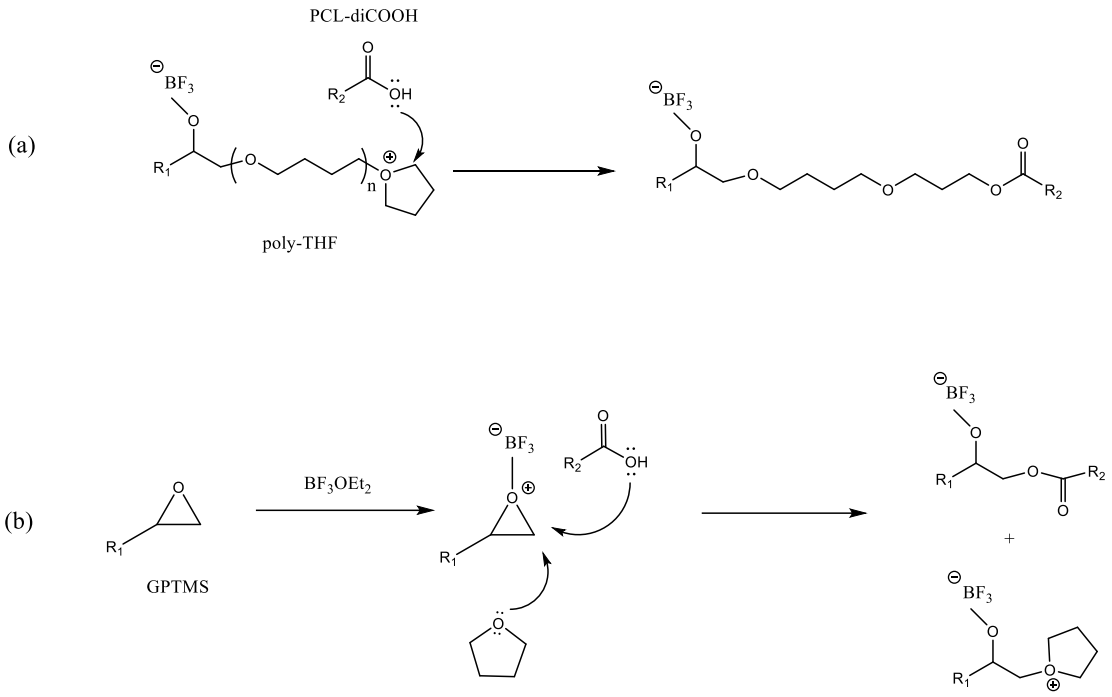


Figure 7.4 Hypothesised reaction mechanism of (a) THF polymerisation terminated by PCL-diCOOH (b) PCL-diCOOH compete with THF for GPTMS [170].

7.2.4 3D printing

PCL scaffolds were printed using Robocaster (3D inks LLC, USA) and the operating software was Robocad. The hybrid ink was prepared via the same route as described in section 7.2.3 but with more water and nitric acid added (molar ratio of water : TEOS = 4:1, volume of 2 M nitric acid = 1/6 volume of water). Hybrid sol was transferred into a 3 ml printing syringe before it gelled and the printing tip used was Nordson tapered dispense tip of 27 gauge (clean, inside diameter: 0.2 mm). A porous cube was printed layer by layer with a pre-set printing program, 2 layers were repeating themselves to form a 3D structure, the 3D printing design is schematised in Figure 7.5.

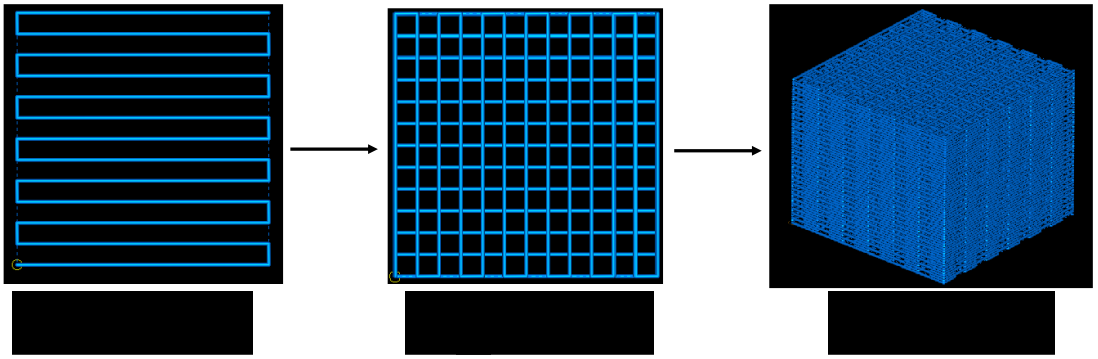


Figure 7.5 Schematic of the 3D grid like structure printing design.

Scaffolds were printed with different printing setting (Including: Horizontal/vertical channel width, Z-space and printing speed) in order to determine the optimal printing setting for 6040 PCL hybrid. Horizontal/vertical channel width is the space between each ink strut and that affect the average pore size of a scaffold. Z-spacing is the space between each printing layers, and it is also the most important parameter and need to be controlled precisely, ideally the Z-spacing should be equal to the diameter of the ink struts, therefore to find an appropriate z-spacing for 6040 scaffold is the biggest challenge in this work.

7.2.5 Cell culture study of PCL hybrids

In vitro cell culture

Cell culture study was carried out by Dr Siwei Li. MC3T3-E1 preosteoblast cell line (ATCC, UK) was monolayer culture expanded in basal α-MEM supplemented with 10% (v/v) FCS (foetal calf serum), 100 U ml^{-1} penicillin and 100 μg ml^{-1} streptomycin. Cultures were maintained in humidified atmosphere at 37°C, 5% CO_2 and 21% O_2. 500 μg ml^{-1} trypsin-EDTA (ethylene diamine tetra-acetic acid) was then used to passage the cells when confluent. Cell culture reagents were purchased from Sigma-Aldrich and ThermoFisher Scientific (Invitrogen UK) unless specified otherwise.

Cytotoxicity test

Potential *in vitro* cytotoxicity effects of PCL hybrid materials on MC3T3-E1 cells were assessed in accordance to ISO 10993-5 (Tests for *in vitro* cytotoxicity) [210] and ISO 10993-12 (Sample preparation and reference materials) [211] standards. Dissolution products released by the hybrid samples in powder form (0.2 g ml^{-1} in fresh serum free α-MEM at 37°C) over a period of 72 h were prepared. Medical grade polyethylene (PE) was used as negative control (non-cytotoxic) and polyurethane (PU) containing 0.1% (w/w) zinc diethyldithiocarbamate (ZDEC) was used as positive control (reproducible cytotoxic). Sterilisation was achieved by filtering dissolution products through a membrane with particle retention of 0.2 μm. Dilution series of 25%, 50%, 75% and 100% were prepared and supplemented with 10% (v/v) FCS before use in cell viability assays.

Calorimetric metabolic activity assay was carried out to assess cell viability based on the conversion of 3-(4,5-dimethylthiazol-2-yl)-2,5-diphenyltetrazolium bromide (MTT) into (purple) formazan crystals. 96-well plates were used, where each well contained 1×10^4 MC3T3-E1 cells and cells were allowed to grow in basal α-MEM for 24 h until a sub-confluent monolayer was formed. The culture media was removed and, MC3T3-E1 cells were then incubated with fresh basal α-MEM or the dissolution products of PCL hybrid materials as well as controls for further 24 h (100 µl $well^{-1}$). Used media was replaced with solutions of MTT in serum-free α-MEM at a concentration of 1 mg ml^{-1} (50 µl $well^{-1}$). After 2 h of incubation, the MTT solution was removed and 100 µl of isopropanol was added to dissolve the formazan derivatives (formazan crystals). Finally, a microplate reader (SpectraMax M5) was used to measure the optical density of the resultant solution at 570 nm spectrophotometrically.

Cell culture on PCL hybrid disks

For cell attachment studies, PCL hybrid disks (approximately $5\times5\times1$ mm^3) were prepared and sterilised with 70% ethanol for 1 minute, followed by washing with phosphate buffered saline (PBS). Then each sample disk was immersed in fresh serum free α-MEM for 30 minutes before cell seeding to prepare the surface of the sample (let amino acids absorb on the surface of the sample). MC3T3-E1 cells were harvested and suspended in basal α-MEM at a concentration of 1×10^6 cells ml^{-1}. 10 µl of cell suspension was seeded onto each PCL hybrid disk and incubated in humidified atmosphere at 37°C, 5% CO_2 and 21% O_2 for 2 h. Then fresh basal α-MEM was added to submerge each cell-seeded disk and samples were cultured for further 24 h.

Immunohistochemistry staining and confocal microscopy

4% paraformaldehyde (PFA) was used to fix the cell-seeded membranes, which were going to be used for immunohistochemical analysis of cell attachment. Buffered 0.5% Triton X-100 in PBS (300 mM sucrose, 50 mM NaCl, 3 mM $MgCl_2$, 20 mM HEPES and pH 7.2) was used for permeabilisation of cell membranes and 10 mg ml^{-1} Bovine Serum Albumin (BSA) in PBS was used for blocking of nonspecific epitopes. Samples were then incubated with anti-Tubulin antiserum (1:200 dilution in 10 mg ml^{-1} BSA/PBS, rabbit polyclonal, IgG, Abcam, Cambridge, UK) at 4°C for 1 h. This was followed by 1 h incubation with Alexa Fluor® 488-conjugated secondary antibody

(1:1000 dilution in 10 mg ml^{-1} BSA/PBS, goat IgG, Abcam, Cambridge, UK). Negative controls (omission of the primary antisera with the presence of secondary antibodies) were performed in all immunohistochemistry procedures. No staining was observed in the samples used as negative controls.

F-actin was labelled using CytoPainter F-actin staining kit (Abcam, Cambridge, UK) following the manufacture's instruction. Briefly, Alexa Fluor® 568-conjugated phalloidin (1:1000 dilution in labelling buffer) was added simultaneously with the secondary antibody during the incubation period. All samples were counter-stained with DAPI (0.1 μg ml^{-1} in PBS) nuclei stain. Then the samples were imaged under confocal microscopy (Leica SP5 MP laser scanning confocal microscope and software, Leica Microsystems, Wetzlar, Germany).

7.2.6 Characterisation techniques

The Characterisation techniques used in this chapter were FTIR, XRD, MAS-NMR, SEM, TGA-DSC, SBF dissolution study, TRIS buffer dissolution study (1 week), compression test and OES-ICP. Refer to chapter 3 for the details of the characterisation techniques used in this chapter.

7.3 Results

7.3.1 Apatite formation on inorganic synthesised at low temperature

Before incorporating the CME TEP glass composition into the PCL hybrid system, a preliminary experiment was done to make sure the inorganic components (made with TEP and CME) were able to induce HCA formation in SBF, without the polymer present (only the time point at 2 weeks of SBF dissolution was included in this preliminary experiment). Samples were aged and dried at 60°C, as they would be during hybrid synthesis. 6040 glass 60c and CME TEP4p 60c were made. 6040 glass 60c has a chemical composition of 60 mol% SiO_2 and 40 mol% CaO; CME TEP 4p 60c has a chemical composition of 60 mol% SiO_2, 4 mol% P_2O_5 and 36 mol% CaO.

The appearance of crystal HCA peaks at 25.7°, 31.78°, 32.19°, 38.8°, 46°, 49.3° and 54° 2θ in XRD patterns (Figure 7.6c and d) indicate the formation of HCA on both samples after 2 weeks of SBF immersion. Figure 7.7 shows the FTIR spectra of 6040glass 60c and CME TEP4p 60c before and after SBF dissolution. After 2 weeks of SBF immersion, the appearances of P-O bending double bands at 546 cm^{-1} and 585 cm^{-1} and P-O stretching band at 1010 cm^{-1} indicate the presence of HCA. The presence of C-O stretching at 875 cm^{-1} and C-O bending band at 1450 cm^{-1} after 2 weeks of SBF dissolution suggest that the apatite formed during SBF dissolution was HCA [72]. XRD and FTIR data have confirmed both low temperature synthesised glass compositions (6040glass 60c and CME TEP4p 60c) were potentially bioactive, therefore they were ready to be incorporated into the PCL hybrid system.

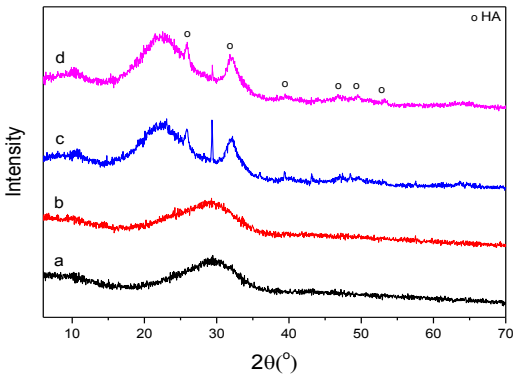


Figure 7.6 XRD patterns of (a) 6040 glass 60c before SBF (b) CME TEP 4p 60c before SBF (c) 6040 glass 60c after 2weeks (d) CME TEP 4p 60c after 2 weeks of SBF dissolution.

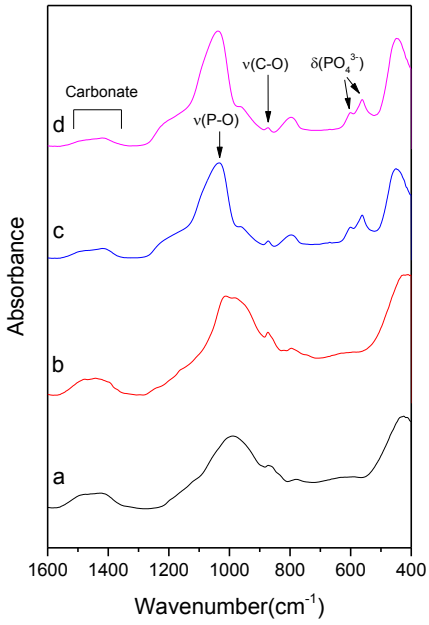


Figure 7.7 FTIR spectra of (a) 6040 glass 60c before SBF (b) CME TEP 4p 60c before SBF (c) 6040 glass 60c after 2weeks (d) CME TEP 4p 60c after 2 weeks of SBF dissolution.

7.3.2 TGA-DSC

TGA-DSC was used to determine the organic/inorganic ratio of each PCL hybrid. Each PCL hybrid was heated to 750°C and the real-time measurement of weights were collected. From the TGA curves, most of the organic components were burned and removed when the temperature reached 600°C. Therefore, when heating the PCL hybrids to 750°C, only the inorganic component from the hybrids remained. Because of the unexpected formation of polyTHF, there was always be a small difference in organic/inorganic ratio between every PCL hybrids. But in general, the inorganic content of all the PCL hybrids (80 wt% TEOS and 20 wt% PCL) made in this work was around 30±2 wt%. The DSC measures the heat flux of the sample. The burn-out of the organic components in a hybrid material is an exothermic reaction, therefore exothermic peaks were obtained by DSC. There are two peaks in DSC curves for all the hybrids, a sharp peak at around 210°C and a broad peak at around 350°C. This suggests that there were two types of polymers were found in the PCL hybrid. According to Francesca Tallia's research [170], the peak at 210°C can be attributed to the burn-out of polyTHF in the hybrid and the broad peak at 350°C indicates the burn-out of PCL.

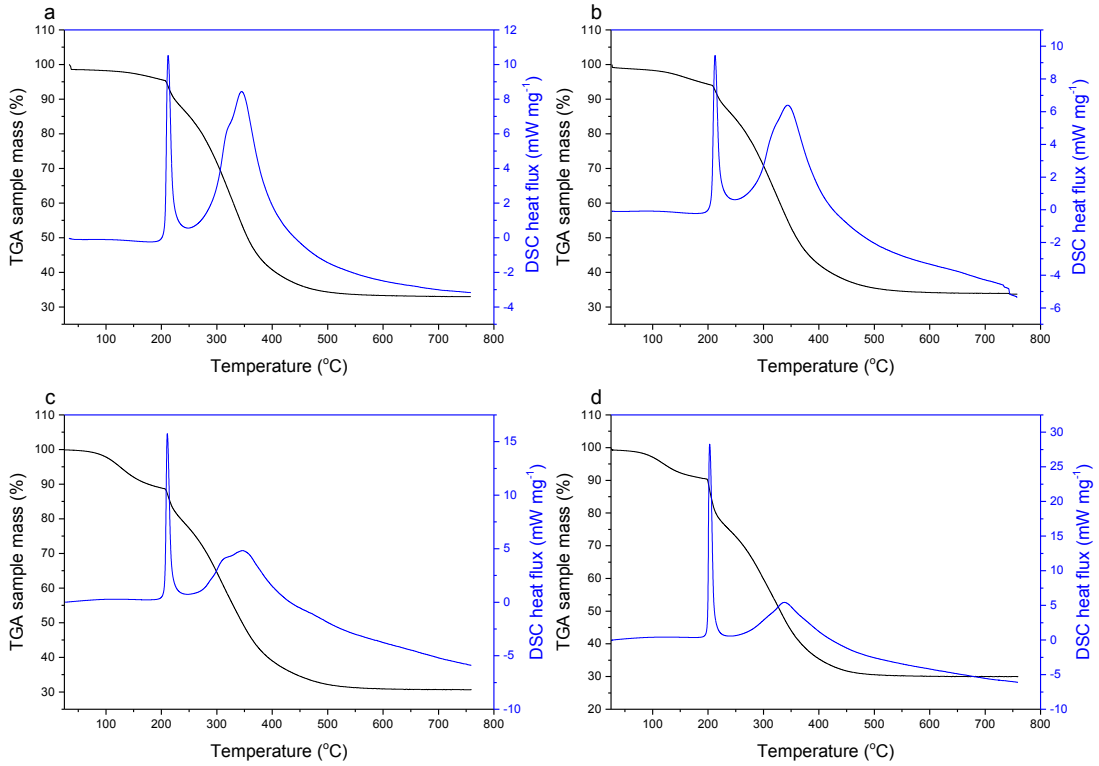


Figure 7.8 TGA and DSC curves of (a) 6040 PCL (b) TEP4p PCL (c) TEP8p PCL (d) TEP12p PCL. All PCL hybrids in this figure were made with a TEOS/PCL wt ratio of 80:20 (2.14 ml of TEOS and 500 mg of PCL diCOOH in 5 ml of THF) and the corresponding amount of CME and TEP.6040 PCL was synthesised by incorporating the silica glass of chemical composition 60 mol% SiO_2 and 40 mol% CaO into PCL (500 mg of PCL in 5 ml of THF) to make a hybrid, TEPXp PCL was synthesised by incorporating a silica glass of 60 mol% SiO_2 (from 2.14 ml TEOS), X mol% of P_2O_5 and (40-X) mol% of CaO into PCL hybrid (500 mg of PCL diCOOH in 5 ml of THF).

7.3.3 Compression test

A preliminary experiment was done to decide the organic/inorganic ratio to be used in the PCL hybrid system. The organic/inorganic ratio of a hybrid is important, if there is too much inorganic glass in it, the hybrid will be brittle and less tough. If a hybrid contains too little of inorganic bioactive glass in it, the hybrid will lose its bioactivity and might also be too soft.

Because of polyTHF formation in the PCL hybrid system, the true organic/inorganic ratio of PCL hybrids were different to the ration of PCL/TEOS added for sol-gel hybrid synthesis. When making the 6040 PCL hybrid with 90 wt% of TEOS (plus corresponding amount of CME) and 10 wt% of PCL, the final true ratio of inorganic in the hybrid was 50.4 wt% (determined by TGA). The final true inorganic ratio of the 6040 PCL hybrid which made with 80 wt% of TEOS (plus corresponding amount of

CME) and 20wt% of PCL was 29.2 wt%. From the compression test, the 6040 PCL hybrid with 29.2 wt% inorganic exhibited much better mechanical property than the PCL hybrid of 50.4 wt% inorganic and 100 wt% inorganic glass samples, where the stress and strain at failure of PCL hybrid with 29. 2 wt% inorganic were much higher (stain is around 52% and stress is around 50 MPa). The stress and strain were calculated by the Equation 7.1 and Equation 7.2:

$$\sigma = \frac{F}{A_0} \tag{7.1}$$

$$\varepsilon = \frac{\Delta L}{L_0} \tag{7.2}$$

Where σ is the stress, F is the standard force perpendicular to the transversal section of specimens, A_0 is the initial transversal area of the specimens, ε is the strain, L_0 is the initial length of the specimens and ΔL is the length change.

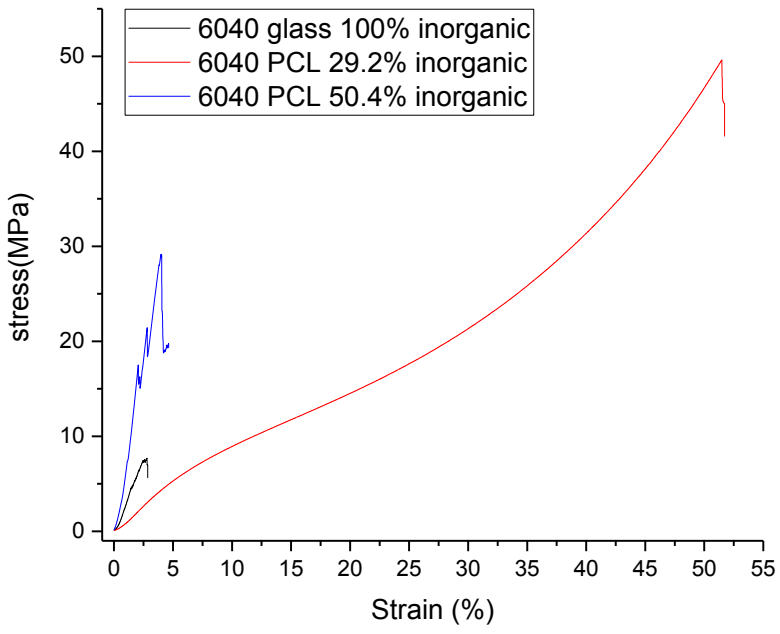


Figure 7.9 Compression test curves of pure 6040 glass (60 mol% SiO_2 and 40 mol% CaO) which was 100% inorganic, 6040 PCL hybrid made with 20wt% PCL (500 mg of PCL), 80wt% TEOS (2.14 ml of TEOS) and corresponding amount of CME (the hybrid contained 29.2 wt% of inorganic) and 6040 PCL hybrid made with 10 wt% PCL (500 mg of PCL), 90wt% TEOS (4.815 ml of TEOS) and corresponding amount of CME (the hybrid contained 50.4 wt% of inorganic). 6040 PCL was synthesised by incorporating the silica glass of chemical composition 60 mol% SiO_2 (from 2.14 ml or 4.815 ml of TEOS) and 40 mol% CaO (from the corresponding amount of CME) into PCL hybrid (500 mg of PCL diCOOH in 5 ml of THF).

From Francesca Tallia's research, the PCL hybrid with true inorganic ratio lower than

30 wt% was too soft, therefore to compare the mechanical properties between each PCL hybrid composition, the true ratio of inorganic in the PCL hybrids was decided to be around 30 wt% in this work. In order to have that final true inorganic ratio of 30 wt% (Figure 7.8), the wt ratio of TEOS/PCL of 80:20 was chosen, where the inorganic component of the hybrid was prepared from 2.14 ml (2 g) of TEOS and the corresponding amount of CME and TEP; the organic component of the hybrid was prepared from 500 mg of PCL in 5ml of THF with the presences of catalyst and coupling agent.

The inorganic ratio of all the PCL hybrids chosen for compression test in this chapter was between 29 wt% to 30 wt% and the difference in inorganic ratio between each PCL hybrids was smaller than 1 wt%. Three cylindrical monoliths were chosen from each PCL hybrid composition for compression tests (compression data for CME-free PCL hybrid was from Francesca Tallia). Figure 7.10 shows the compression curves for each PCL composition, 6040 PCL exhibited best mechanical property among all the PCL hybrid compositions. The first thing to be noticed from the compression curves was that the CME free PCL hybrid was stiffer than any of the calcium containing PCL hybrids made in this work. It might be because that the CME-free PCL hybrid had a slightly higher inorganic content (32.8 wt%) than other PCL hybrids. However, 6040 PCL expressed much greater stress and strain at failure during compression when compared to CME free PCL hybrid. It was clearly shown that the presence of calcium in 6040 PCL strengthened its mechanical property, where the stress and strain at failure for Ca free PCL hybrid was around 30 MPa and 27% deformation, but 6040 PCL had stress and strain at failure of 88 MPa and 60% deformation. The possible explanation for that might be: In the PCL hybrid system, calcium interacts with the hybrid by ionic bonding to the COO^- groups from PCL chains and this makes the PCL hybrid tougher. The ionic crosslinking between PCL and silica network by calcium might also be present in the hybrid and contribute to the mechanical properties of the hybrid. However further investigation is needed to confirm this hypothesis.

A trend was found from the compression curves, the higher the phosphate content in a PCL hybrid the softer the PCL hybrid was. All the calcium containing PCL hybrids in the compression test had similar strain at failure (at the range between 45 % to 55%) apart from one of 6040 PCL specimens. But as the phosphate content increased, the stress at failure of the PCL hybrid decreased. It suggests that the incorporation of

phosphate can affect the mechanical strength of the PCL hybrid by softening the PCL hybrid. The cause of that is still uncertain, but the phosphates can incorporate into the PCL hybrid with calcium by charge balancing with the calcium ions and that might have a softening effect on the PCL hybrids. The stress-strain (compression test) curves of all the calcium containing PCL hybrids expressed a non-linear relationship (Figure 7.10), where the PCL hybrids tended to be stiffer at higher strain, suggesting the viscoelastic property of the calcium containing PCL hybrids.

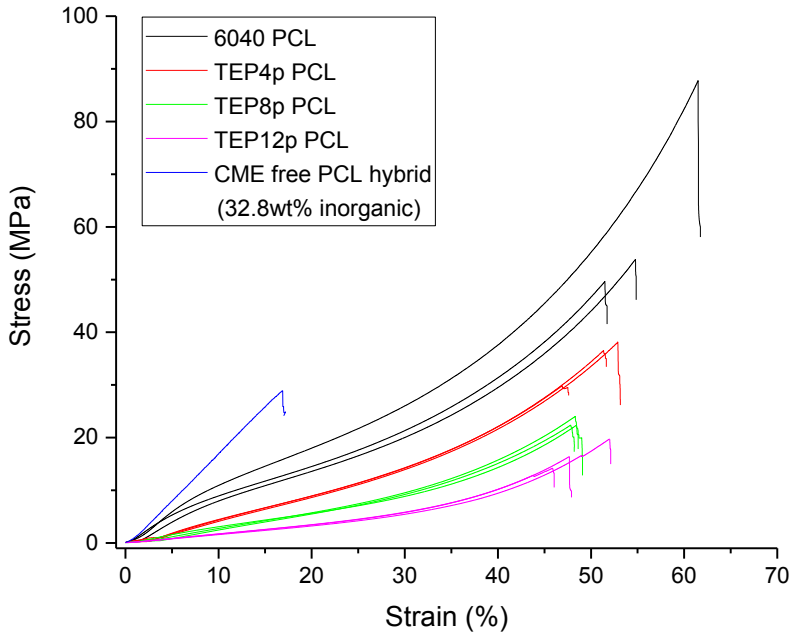


Figure 7.10 Compression curves of calcium containing PCL hybrid monoliths (cylindrical) made in this work and CME free PCL hybrid monolith from Francesca Tallia. All PCL hybrids in this figure were made with a TEOS/PCL wt ratio of 80:20 (2.14 ml of TEOS and 500 mg of PCL diCOOH in 5ml of THF) and the corresponding amount of CME and TEP. The true inorganic/organic ratio difference between the calcium containing PCL hybrids used in the compression test was smaller than 1wt%, all of them contained 29 wt% to 30 wt% of inorganic. 6040 PCL was synthesised by incorporating the silica glass of chemical composition 60 mol% SiO_2 (from 2.14 ml of TEOS) and 40 mol% CaO into PCL hybrid (500 mg of PCL in 5 ml of THF), TEPXp PCL was synthesised by incorporating a silica glass of 60 mol% SiO_2 (from 2.14 ml TEOS), X mol% of P_2O_5 and (40-X) mol% of CaO into PCL hybrid (500 mg of PCL diCOOH in 5 ml of THF).

Before compression test, the top and bottom surfaces of PCL hybrid cylinders were flattened and polished by SiC paper. It was noticed that how the PCL hybrid cylinder was being sanded can actually affect the outcome of the compression test, therefore it was important to flatten and polish the specimens well. In addition, some specimens were not in perfect cylindrical shape because of shrinkage during drying. These were the two main limitations for the compression test. Therefore, abnormal compression

results for some specimens which were not well prepared were excluded from the data base.

Cyclic loading (compressive) test

Since the PCL hybrids made in this work was designed to be used as the scaffolding material for bone regeneration, it is important to investigate the behaviour of the PCL hybrid materials under cyclic loads. 6040 PCL hybrid was chosen for cyclic loading test in this work, because it exhibited best mechanical property among all of the PCL hybrid compositions (Figure 7.10).

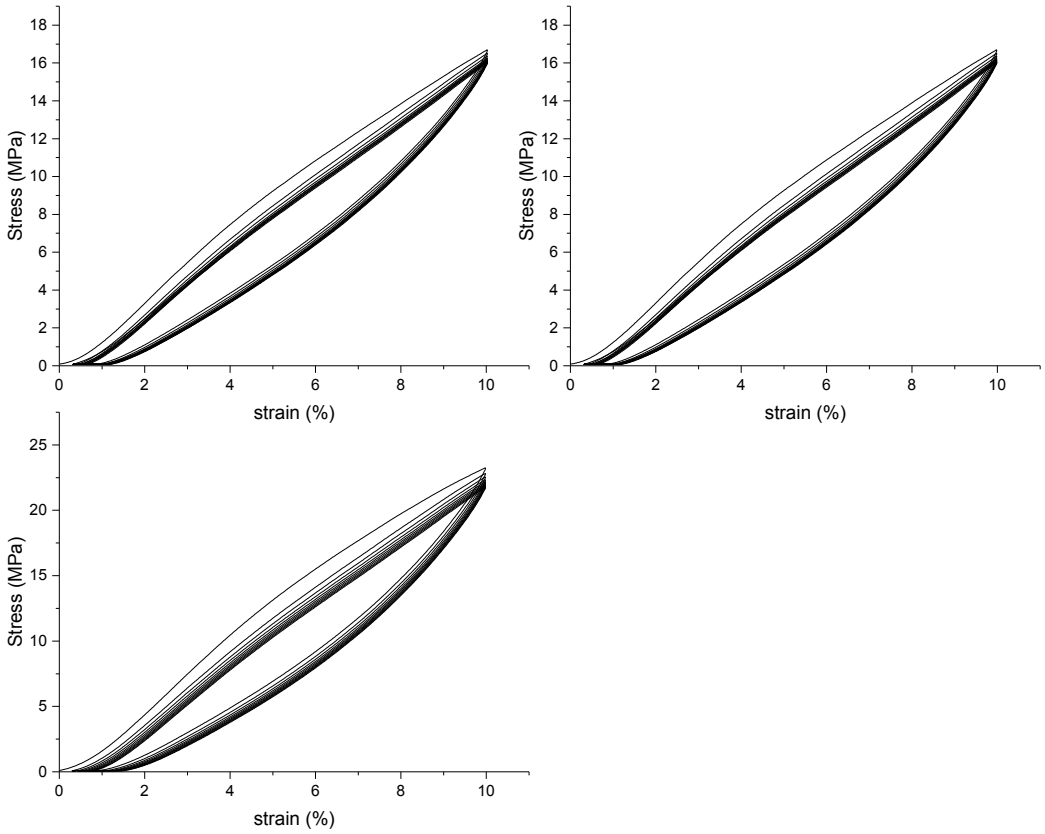


Figure 7.11 Cyclic loading stress-strain curves for 6040 PCL hybrid cylindrical monoliths. In each of the 10 cycles the 6040 PCL cylindrical monolith was compressed up to 10% of their initial height.

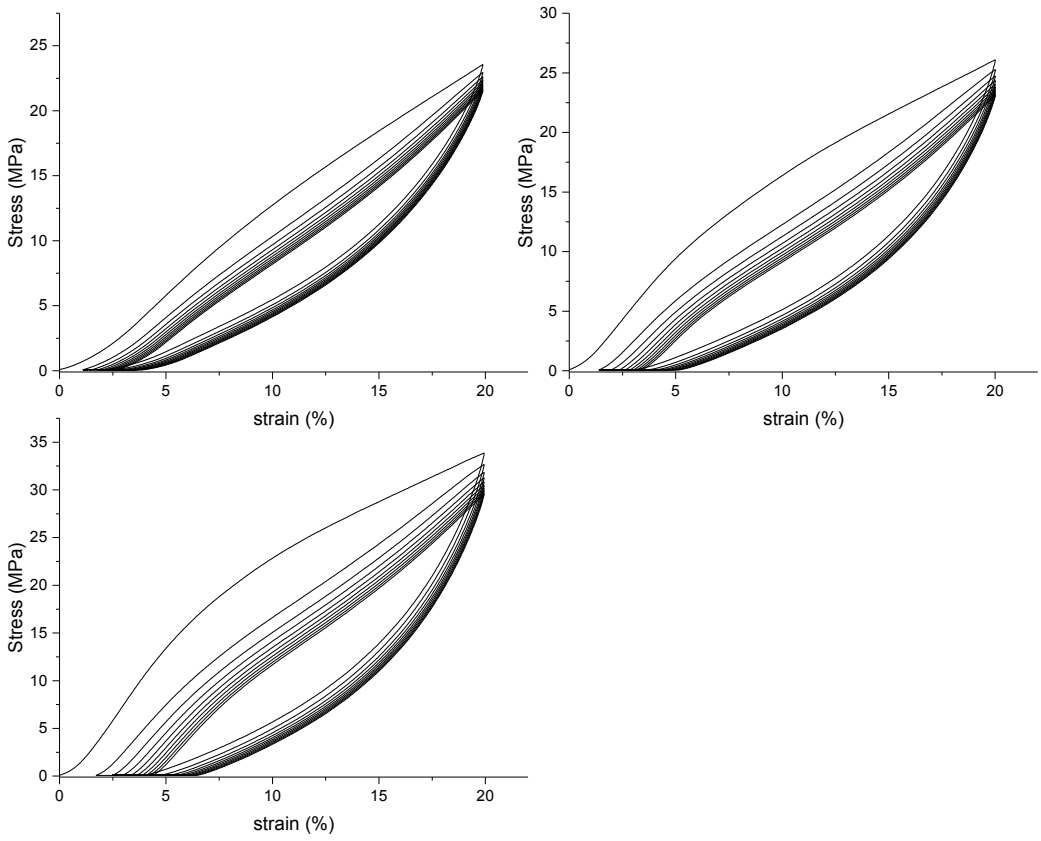


Figure 7.12 Cyclic loading stress-strain curves for 6040 PCL hybrid cylindrical monoliths. In each of the 10 cycles the 6040 PCL cylindrical monolith was compressed up to 20% of their initial height.

When 6040 PCL was compressed up to 10% of its initial height for 10 cycles, the first cycle showed a similar stress-strain behaviour to the other 9 cycles and all 10 cycles almost overlapped (Figure 7.11). The hold time between each cycle was set to 3 minutes and that was enough for the hybrid to recover the 10% deformation, which is why all the cycles were almost overlapping.

When 6040 PCL was compressed up to 20% or 30% of its initial height for 10 loading-unloading cycles (Figure 7.12 and Figure 7.13), the first cycle showed a very different stress-strain behaviour to the following 9 cycles. 3 minutes hold time between each cycle was not enough for the hybrid to fully recover the deformation (20% or 30%). This is quite common for this type of test.

The stress softening effect was observed, where the stress at a given strain (20% or 30%) dropped between the successive loading cycles. The drop of the stress between the first cycle and second cycles were significant and became negligible after 5 or 6 cycles. The possible explanation for the stress softening effect observed during cyclic loading can be: under mechanical stress, the PCL chains can slip over one another and

rearrange to accompany the stress, causing temporary elimination of the entanglement in the PCL hybrid [212]. As the rearrangement of PCL occurs, it creates an internal stress in the hybrid, after the external stress is removed the accumulated internal stress causes the hybrid to return to the original form and the entanglements can also recover slowly. When the hybrid was compressed up to 10% deformation, most of the entanglements were recovered within 3 minutes, it explains why the stress softening effect was negligible in 10% deformation cyclic loading.

When the hybrid was compressed by up to 20% or 30% deformation, some entanglements were not able to be recovered and other entanglements might take longer to fully recover (longer than 3 minutes). The most of unrecovered entanglements were removed in the first few cycles, causing the significant reduce in stress at a given strain between the first and second cycles and the drop in stress become negligible after about 5 or 6 cycles.

Hysteresis between loading and unloading was observed for all 10 cycles in all the cyclic loading tests, indicating that 6040 PCL hybrid was viscoelastic. Since bone is also a viscoelastic material [213-215], therefore it is good that the PCL hybrids had the similar property to bone. But the delay of deformation recovery might cause instability of the hybrid scaffold after implantation.

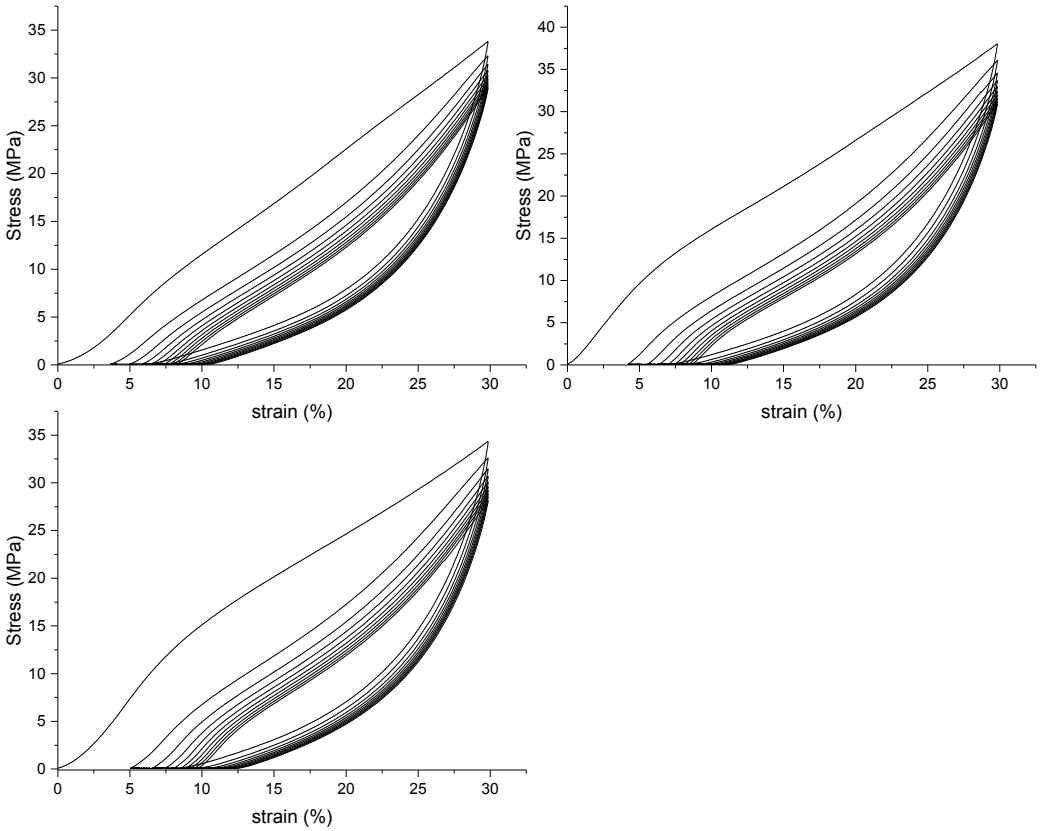


Figure 7.13 Cyclic loading stress-strain curves for 6040 PCL hybrid cylindrical monoliths. In each of the 10 cycles the 6040 PCL cylindrical monolith was compressed up to 30% of their initial height.

7.3.4 SBF dissolution

The amounts of dissolution products from each hybrid were measured by ICP. The pH of SBF was initially pH 7.4 (at 0 time point). All the hybrids increased the pH of SBF after 8 h of SBF dissolution and had very similar pH buffering ability. The pH buffering ability was mainly attributed to the inorganic glass part of the hybrid. The amount of inorganic in each hybrid was around 30wt% (refer to TGA data from section 7.3.2) and that amount of glass was too little to exhibit the significant difference in pH buffering ability between different compositions.

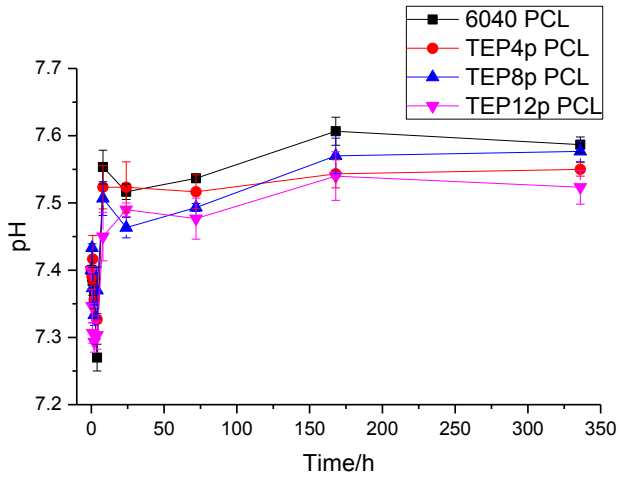


Figure 7.14 pH change profile of PCL hybrids made by incorporating different glass compositions into PCL hybrids. 6040 PCL was synthesised by incorporating the silica glass of chemical composition 60 mol% SiO_2 (from 2.14 ml of TEOS) and 40 mol% CaO into PCL hybrid (500 mg of PCL diCOOH in 5 ml of THF), TEPXp PCL was synthesised by incorporating a silica glass of 60 mol% SiO_2 (from 2.14 ml TEOS), X mol% of P_2O_5 and (40-X) mol% of CaO into PCL hybrid (500 mg of PCL diCOOH in 5 ml of THF).

The phosphate was released from all the phosphate containing PCL hybrids rapidly within the first 30 minutes of SBF immersion (Figure 7.15). After 30 minutes of SBF immersion, TEP4p PCL increased the [P] in SBF from 30 μg ml^{-1} (initial [P] of SBF) to around 45; TEP8p PCL and TEP12p PCL increased the [P] to around 55 μg ml^{-1}. Between 8 h to 144 h of SBF immersion, the phosphate concentration of SBF containing TEP8p PCL and TEP12p PCL reduced significantly. But the phosphate level in SBF 6040 PCL and TEP4p PCL soaked stayed constant and started dropping after 72 h of SBF immersion. The drop in the concentrations of phosphate and calcium indicates the deposition of phosphate and calcium to form amorphous calcium phosphate on the surface of the hybrid. The ICP profile of calcium (Figure 7.15) shows rapid releases of calcium from all the PCL hybrids within first 8 h of SBF dissolution. The [Ca] in SBF at time point 0 was around 100 μg ml^{-1}, after 8 h of SBF immersion 6040 PCL increased the [Ca] to 112 μg ml^{-1}; TEP4p PCL increased [Ca] to 120 μg ml^{-1}; TEP8p PCL increased [Ca] to 118 μg ml^{-1} and TEP12p PCL increased [Ca] to around 110 μg ml^{-1}. The concentration of calcium in the SBF for TEP8p PCL and TEP12p PCL dropped after 24 h of SBF immersion. But 6040 PCL and TEP4p PCL exhibited a consistent release of calcium until 72 h after soaked in SBF and then followed by a significant drop in the concentration of calcium in SBF. There are two possible explanations for the calcium and phosphate ICP profiles: first, all the PCL hybrids released calcium ions

consistently but the calcium and phosphate deposited faster onto TEP8p PCL and TEP12p PCL when compared to 6040 PCL and TEP4p PCL. Second, there was a consistent release of ions from 6040 PCL and TEP4p PCL until 72 h after soaked in SBF, but not from TEP8p PCL and TEP12p PCL.

The consistent release of calcium from 6040 PCL and TEP4p PCL could possibly be because of the presence of PCL in the hybrids. As previous chapters suggested the calcium and phosphate ions were released rapidly from bioactive glasses, but the calcium and phosphate releases from PCL hybrid could be slowed down because of the hydrophobic property of PCL.

An unexpected result was obtained for Si ICP profile. The degradation rate of inorganic glass part of the PCL hybrid can be determined by the Si release rate from PCL hybrid. Figure 7.15 shows that the higher the calcium content in the PCL hybrid the slower the Si release from PCL hybrids, and it also suggests that the inorganic glass in the PCL hybrid degraded slower when the calcium content is higher. It is completely opposite to the results of bioactive glasses obtained previously. A hypothesis can be made from the SBF profile: Calcium ions can be incorporated into a PCL hybrid in two ways, it can incorporate into the inorganic glass part of the PCL hybrid and also it can incorporate into the organic PCL part of the hybrid by ionic bonding to COO^- groups in PCL. It is possible that some PCL-COO^- groups were available for Ca chelation as the GPTMS reacted with the THF, causing its polymerisation, thus leaving an excess of PCL-COO^- groups. The phosphate then incorporates into the PCL hybrid with calcium by charge balancing to the calcium ions. The ionic interaction between calcium and PCL chains might be the other possible explanation for the consistent release of calcium from 6040 PCL and TEP4p PCL. However, further studies are needed to confirm the hypothesis.

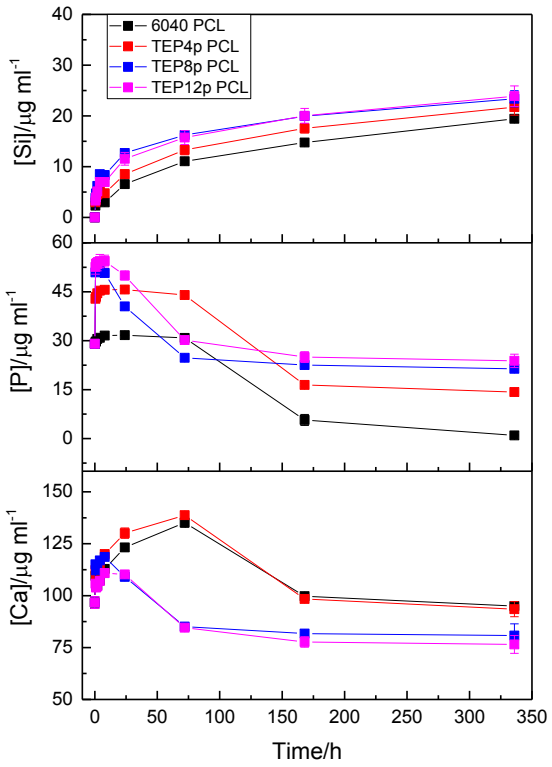


Figure 7.15 ICP SBF dissolution profiles of 6040 PCL, TEP4p PCL, TEP8p PCL and TEP12p PCL. 6040 PCL was synthesised by incorporating the silica glass of chemical composition 60 mol% SiO_2 (from 2.14 ml of TEOS) and 40 mol% CaO into PCL hybrid, TEPXp PCL was synthesised by incorporating a silica glass of 60 mol% SiO_2 (from 2.14 ml TEOS), X mol% of P_2O_5 and (40-X) mol% of CaO into PCL hybrid (500 mg of PCL diCOOH in 5 ml of THF).

7.3.5 TRIS degradation study

The PCL hybrids were soaked in TRIS buffer for 1 week to determine the degradation rate and organic/inorganic ratio before and after soaking in TRIS buffer. Figure 7.16 shows the photographs of cylindrical hybrid monoliths before TRIS buffer and after 1 week of TRIS dissolution. All the cylindrical PCL hybrids monoliths maintained their shape after 1 week of TRIS dissolution but there were many cracks in them after drying. However, only few cracks were observed in all cylindrical PCL hybrids monoliths after 1 week of TRIS dissolution before drying (in wet environment). Since all the PCL hybrids made in this work had the inorganic/organic ratio which is near the critical point for crack forming. According to Francesca Tallia's work, the critical inorganic/organic ratio for crack forming is around 34 – 40 wt%, as she stated that the PCL hybrid which contained inorganic less than 34 wt% did not crack after 1 week of immersion in PBS before drying (in wet environment), but cracks formed after the hybrid was dried. The PCL hybrid which contained 21 wt% inorganic did not form any crack after been

completely dried after 1 week of PBS soaking [170]. Table 7.2 shows that there was not a strong correlation between the weight loss and the hybrid compositions. The organic/inorganic ratio before and after TRIS buffer dissolution were within 3 wt% difference for all the PCL hybrids. It means that the PCL hybrid lost its organic and inorganic at similar rate in TRIS buffer. During TRIS buffer dissolution, water could enter the cylindrical PCL hybrid monolith and degrade the silica network. When silica network degraded, polymer chains were released to the surrounding.

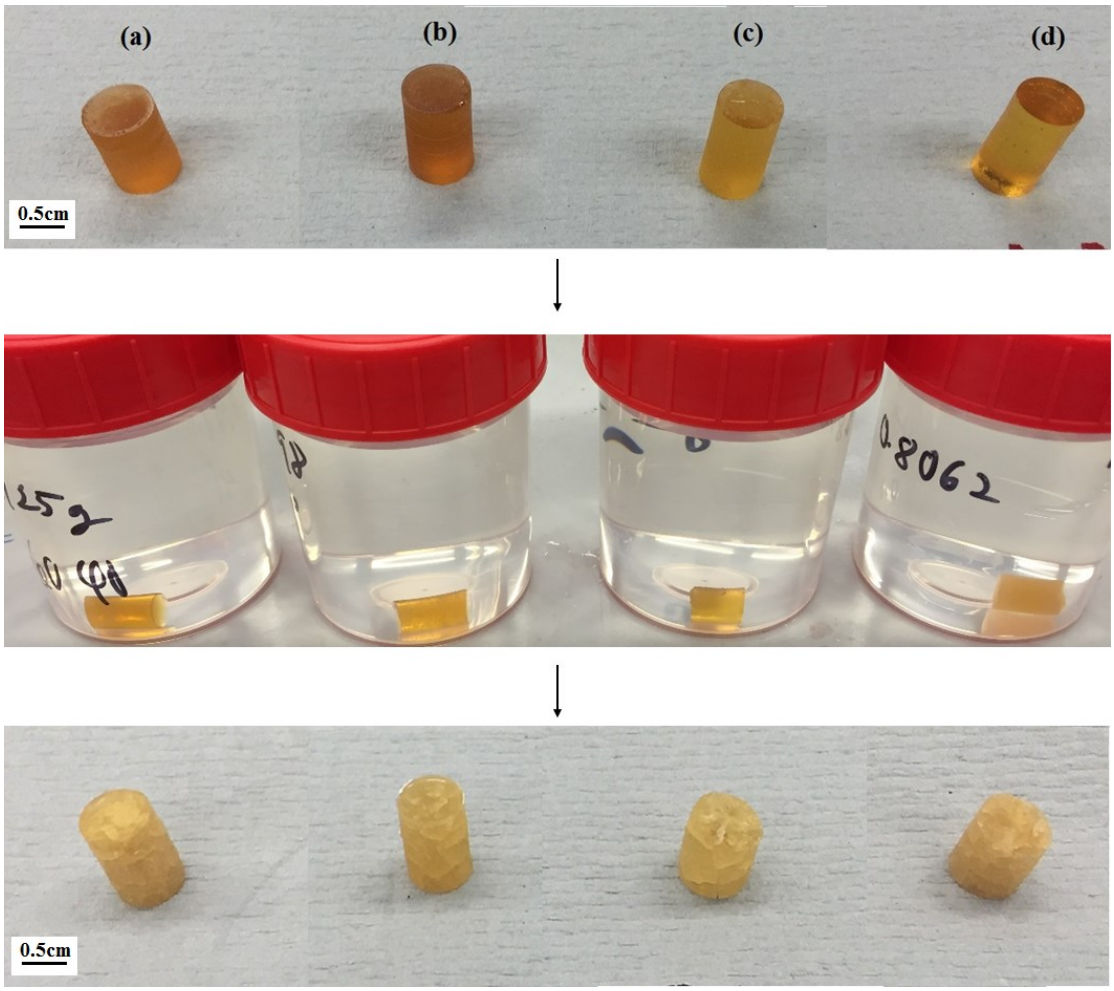


Figure 7.16 Diagram for TRIS buffer dissolution of PCL hybrids (a) 6040 PCL (b) TEP4p PCL (c) TEP8p PCL (d) TEP12p PCL. 6040 PCL was synthesised by incorporating the silica glass of chemical composition 60 mol% SiO_2 (from 2.14 ml of TEOS) and 40 mol% CaO (from the corresponding amount of CME) into PCL (500 mg of PCL in 5 ml of THF) hybrid, TEPXp PCL was synthesised by incorporating a silica glass of 60 mol% SiO_2 (from 2.14 ml TEOS), X mol% of P_2O_5 and (40-X) mol% of CaO into PCL hybrid (500 mg of PCL diCOOH in 5 ml of THF).

Table 7.2 Weight loss after 1 week of TRIS buffer dissoltuion, the inorganic ratios in the PCL hybrids before and after TRIS dissolution.

Hybrids	Original weight (g)	Weight after 1 wk in TRIS (g)	Weight loss (wt%)	Original inorganic ratio (wt%)	Inorganic ratio after 1 wk in TRIS (wt%)
6040 PCL	0.993	0.851	14.2	32.9	34.0
TEP4p PCL	0.980	0.830	15.3	33.6	35.0
TEP8p PCL	0.806	0.741	8.06	30.6	31.2
TEP12p PCL	0.806	0.719	10.8	30.0	34.0

7.3.6 FTIR

The bands from 450 cm^{-1} to 1250 cm^{-1} are mainly attributed to the bioactive glass part in PCL hybrid. The peak at around 1250 cm^{-1} is assigned to the stretching C-O-C from the organic part of the hybrid. The band at around 1700cm^{-1} is ascribed to the carbonyl (C=O) of PCL. The peaks at 2949 cm^{-1} and 2865 cm^{-1} are attributed to asymmetric CH_2 stretching and symmetric CH_2 stretching of PCL respectively [216]. The broad shoulder from 3000 cm^{-1} to 3500 cm^{-1} is assigned to the hydroxyl (OH) stretching vibration of water molecules. The band at 1660 cm^{-1} is assigned to the H-O-H deformation and indicate molecular water in the hybrid [200, 204]. All the bands between 1250 cm^{-1} to 1500 cm^{-1} are assigned to CH_2 groups from both PCL and poly THF in the hybrid.

The band at 470 cm^{-1} is attributed to the vibration of the bridging oxygen atoms perpendicularly to the Si-O-Si plane, and the band at 800 cm^{-1} is caused by the bending motions of oxygen atoms alone the bisector of Si-O-Si groups [193]. The band at around 950 cm^{-1} is assigned to the stretching vibration of two non-bridging oxygen atoms in the Q^2 tetrahedral unit of Si-O-Si [194, 195]. A weak Si-OH band at 960 cm^{-1} is superposed over the Q^2 tetrahedral Si-O-Si band [196] [197]. The double bands at 546 cm^{-1} and 585 cm^{-1} are attributed to the P-O asymmetric bending motion in the orthophosphates, and the other band at 1010 cm^{-1} corresponds to P-O stretching vibration of PO_4^{3-}. These three bands are used to indicate the presence of crystal apatite in the PCL hybrids. The C-O stretching single peak at 862 cm^{-1} indicates the apatite formed was HCA. From the FTIR spectra, all the PCL hybrids induced HCA formation

on the surface just after 3 days of SBF dissolution (time point shorter than 3 days was not done in this work). There was no difference in the HCA formation ability between each PCL hybrid with different glass compositions incorporated.

The additional calcium from CME make the PCL hybrid bioactive as calcium free PCL hybrid is not able to trigger HCA formation during SBF dissolution (Figure 7.18).

The difference in phosphate content between each PCL hybrid might be too small to affect the bioactivity of PCL hybrid.

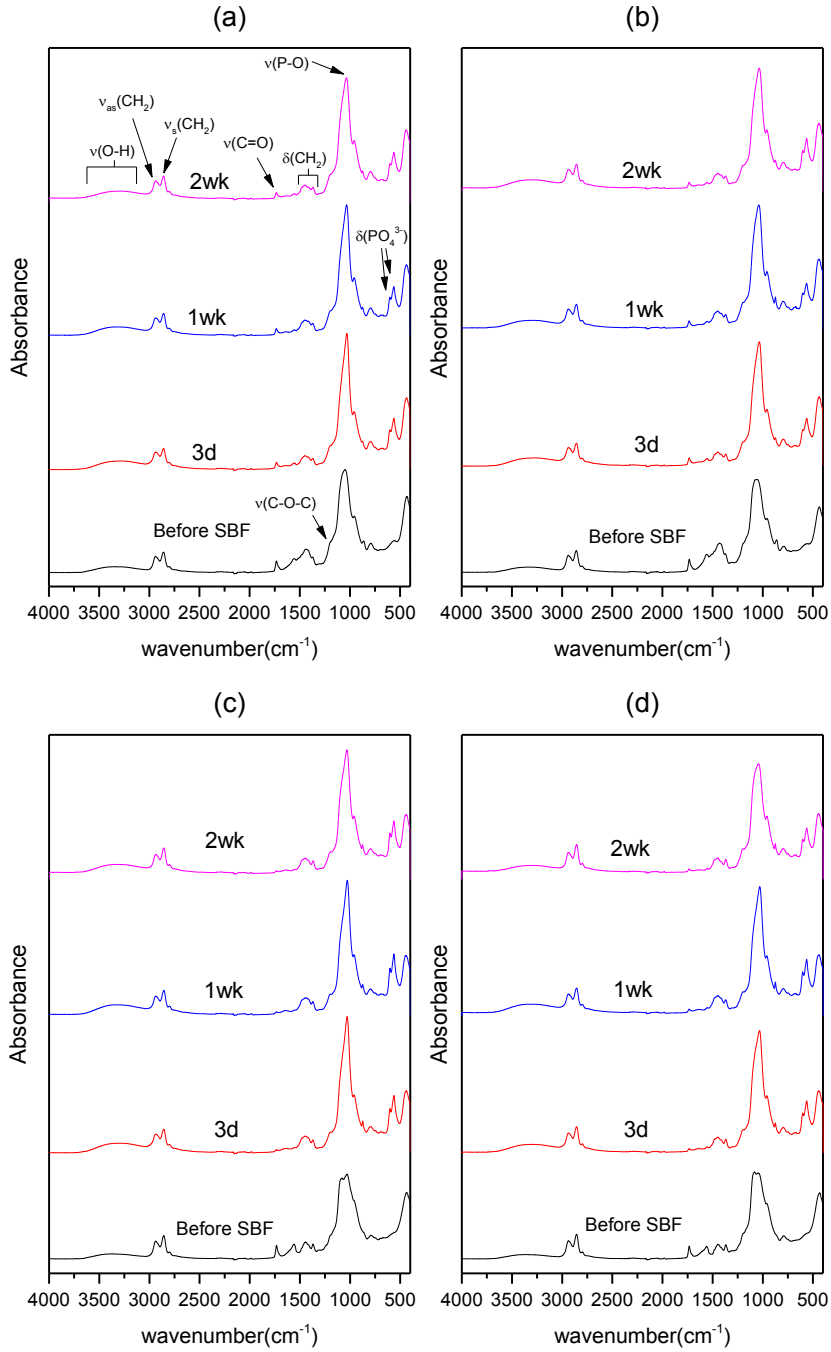


Figure 7.17 FTIR spectra of (a) 6040 PCL (b) TEP4p PCL (c) TEP8p PCL (d) TEP12p PCL at differnet time points of SBF dissolution. 6040 PCL was synthesised by incorporating the silica glass of chemical composition 60 mol% SiO_2 (from 2.14 ml of TEOS) and 40 mol% CaO (from the corresponding amount of CME) into PCL (500 mg of PCL in 5 ml of THF) hybrid, TEPXp PCL was synthesised by incorporating a silica glass of 60 mol% SiO_2 (from 2.14 ml TEOS), X mol% of P_2O_5 and (40-X) mol% of CaO into PCL hybrid (500 mg of PCL diCOOH in 5 ml of THF).

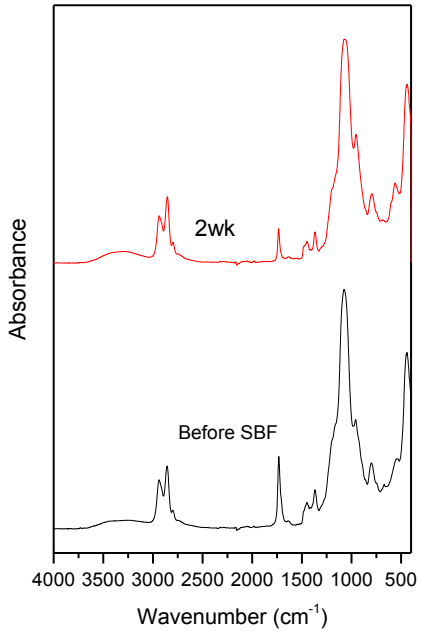


Figure 7.18 FTIR spectra of calcium free PCL hybrid (500 mg of PCL + 2.14 ml of TEOS) before and after 2 weeks of SBF dissolution

7.3.7 XRD

Figure 7.19 shows XRD patterns for PCL hybrids before and after SBF dissolution. The broad peak from the XRD patterns of PCL hybrids before SBF was assigned to amorphous PCL region and silica glass phase of the hybrid. The peaks at around 25°, 32°, 46° and 49° 2θ were attributed to the HCA formed during SBF immersion. However, the HCA peaks detected in PCL hybrids were slightly different to those of bioactive glasses. It indicates that the HCA crystals formed on PCL hybrids have slightly different preferred growth orientation to the HCA crystal formed on bioactive glasses (TEP and DEPETES glasses).

The XRD data suggests all the calcium containing PCL hybrids were able to induce HCA formation just after 3 days of SBF dissolution (time point shorter than 3 days was not done in this work). But the additional phosphate did not affect HCA forming ability of the PCL hybrid. The XRD data (Figure 7.20) also shows that no apatite was formed on the calcium free PCL hybrid after 2 weeks of SBF immersion which agree with the FTIR data obtained (Figure 7.18) and further confirm that the additional calcium from CME make the PCL hybrid bioactive.

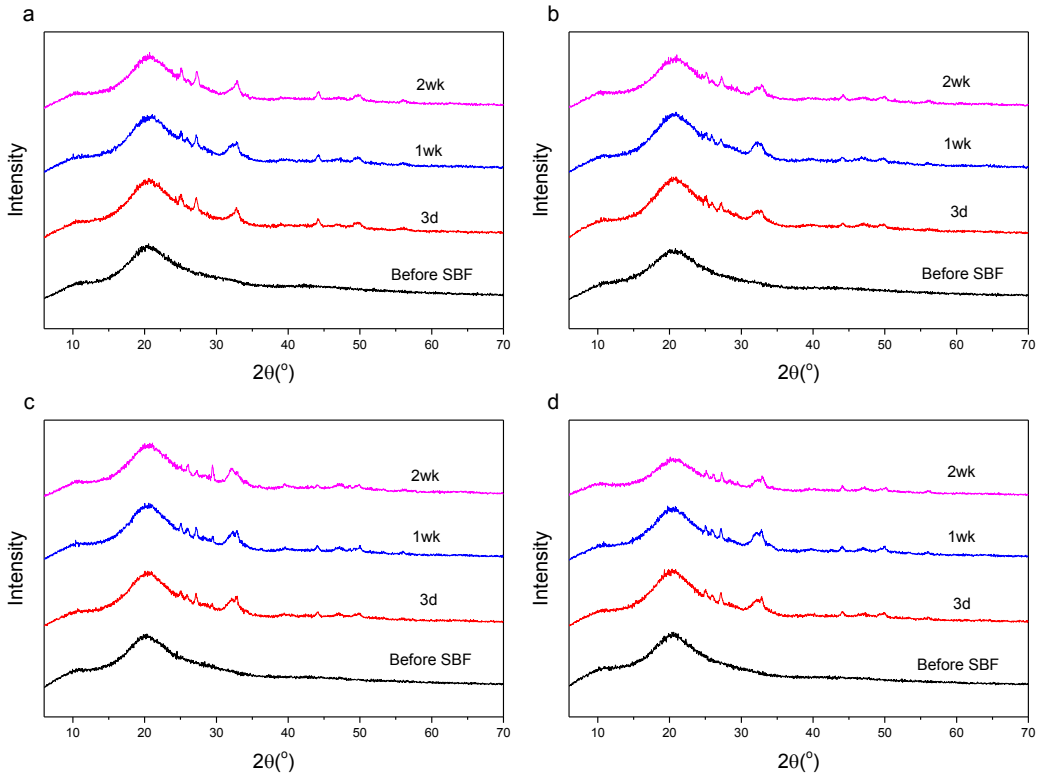


Figure 7.19 XRD patterns of (a) 6040 PCL (b) TEP4p PCL (c) TEP8p PCL (d) TEP12p PCL at differnet time point of SBF dissolution. 6040 PCL was synthesised by incorporating the silica glass of chemical composition 60 mol% SiO_2 (from 2.14 ml of TEOS) and 40 mol% CaO (from the corresponding amount of CME) into PCL (500 mg of PCL in 5 ml of THF) hybrid, TEPXp PCL was synthesised by incorporating a silica glass of 60 mol% SiO_2 (from 2.14 ml TEOS), X mol% of P_2O_5 and (40-X) mol% of CaO into PCL hybrid (500 mg of PCL diCOOH in 5 ml of THF).

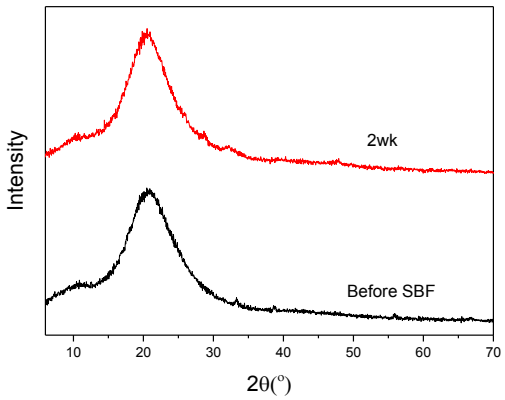


Figure 7.20 XRD patterns of calcium free PCL hybrid (500 mg of PCL + 2.14 ml of TEOS) before and after 2 weeks of SBF dissolution.

7.3.8 Solid state MAS-NMR

Solid state ^{29}Si NMR of PCL hybrids was carried out to identify the molecular conditions of silane groups from GPTMS and TEOS. It gives the information on the silica network formed in the PCL hybrid (Figure 7.21a). Table 7.3 shows the relative quantities of each Q^n and T^n species and the corresponding chemical shift. The degree of condensation was calculated using Equation 3.5 in section 3.8 and is also listed in Table 7.3.

Unexpectedly, the PCL hybrid contained more calcium had slightly higher degree of condensation. As calcium is a network modifier for silica network, in theory, an increase in calcium content should decrease the network connectivity, but the ^{29}Si NMR shows the opposite result. One of the possible cause for it can be the calcium might be incorporated into the PCL by ionic bonding to the COO^- from PCL. The ^{31}P NMR suggests that only orthophosphate was found in all the phosphate containing PCL hybrids (Figure 7.21b).

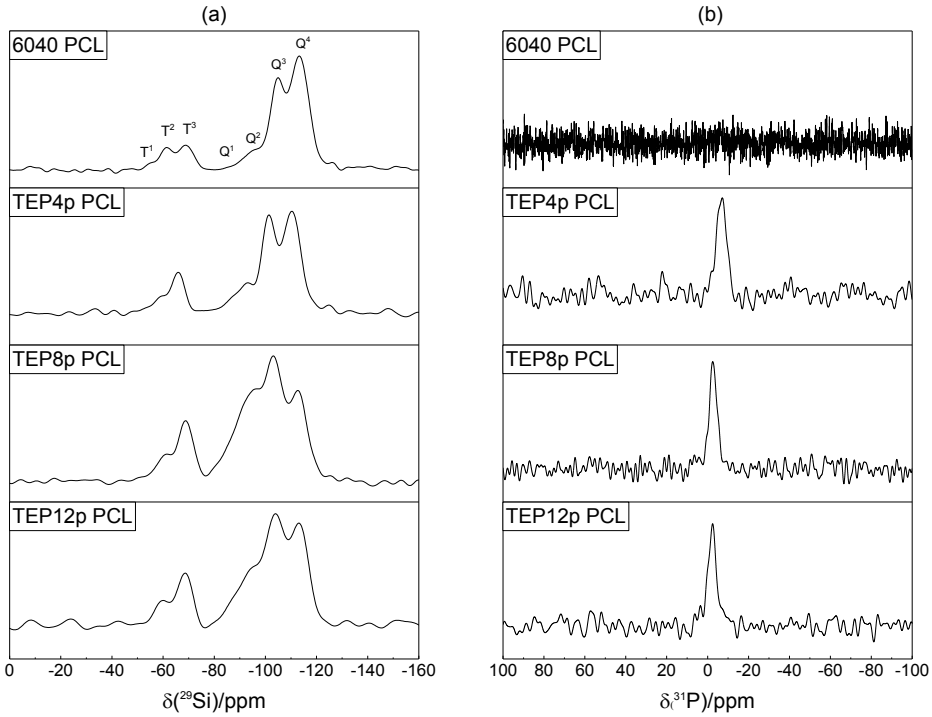


Figure 7.21 Solid state (a) ^{29}Si NMR (b) ^{31}P NMR of the PCL hybrids.

Table 7.3 T^n and Q^n distributions and degree of condensations of silica network in the PCL hybrids.

Sample	T^1		T^2		T^3		Q^1		Q^2		Q^3		Q^4		D_c[%]
	δ [ppm]	I [%]	δ [ppm]	I [%]	δ [ppm]	I [%]	δ [ppm]	I [%]	δ [ppm]	I [%]	δ [ppm]	I [%]	δ [ppm]	I [%]	
6040 PCL	-55.0	1.7	-61.3	5.7	-68.7	8.3	-84.3	1.0	-97.0	12.0	-104.6	21.1	-113.2	50.1	84.8
TEP4p PCL	-54.1	2.3	-59.6	3.9	-66.0	11.0	-80.0	2.6	-92.9	15.6	-101.3	22.3	-110.3	42.3	81.8
TEP8p PCL	-52.1	1.3	-60.5	5.2	-69.0	12.6	-82.4	2.7	-95.0	38.8	-103.6	15.5	-112.7	23.8	72.0
TEP12p PCL	-	-	-60.4	7.9	-68.8	11.2	-82.9	0.4	-95.0	27.8	-104.3	24.5	-113.4	28.1	76.9

7.3.9 Cell culture study

Cytotoxicity and cell attachment test were also performed. The cells used in the test were MC3T3-E1 preosteoblast cell line. The optical density of isopropanol dissolved formazan was measured spectrophotometrically at 570 nm using a microplate reader (SpectraMax M5). The higher the absorbance the more metabolically active the cells are. For a material to pass ISO, the viability of cells when in contact with the dissolution products (from the testing material) needs to be above 70% in comparison to basal and negative control. For 6040 PCL and TEP4p PCL samples, the viability of cells after exposure to the material dissolution products were approximately 70% (Figure 7.22). For TEP8p PCL and TEP12p PCL were approximately 87% (Figure 7.22). All of the PCL hybrids made in this work passed the ISO standard cytotoxicity test and do not induce cytotoxicity effect. Therefore, these materials have potential in biological applications.

Cell attachment was examined by immunohistochemistry and confocal microscopy. Green fluorescence indicated the expression of tubulin, red fluorescence indicated the expression of F-actin and blue fluorescence indicated the expression of nucleus (Figure 7.23). All of the PCL hybrids materials were capable of supporting good cell attachment and spreading, therefore have potential to be used as scaffolding materials in bone tissue engineering applications. It is noticeable that the expression of tubulin on 6040 PCL appeared more prominent. This can be an indication of better cell migration, spreading and potentially differentiation [217, 218]. In addition, cells attached on 6040 PCL and

TEP4p PCL demonstrated better spreading than TEP8p PCL and TEP12p PCL. A number of material surface properties can affect cell attachment, including wettability, stiffness, surface structure etc. At this stage, the comment on what was causing the difference cannot really be made and further studies are required.

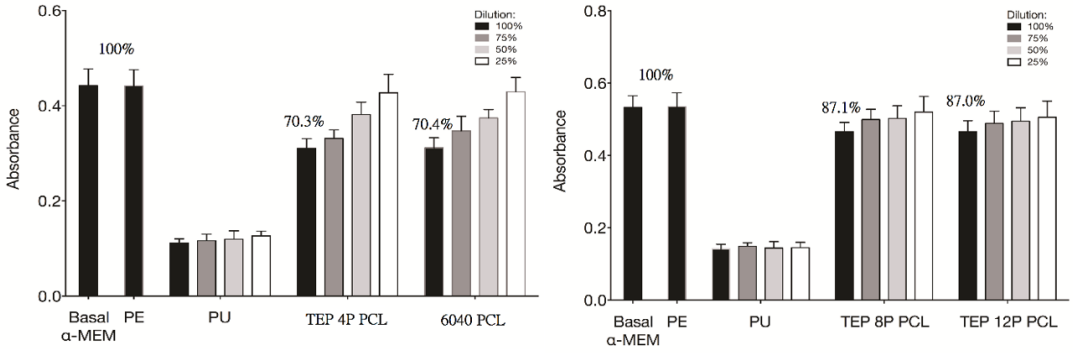


Figure 7.22 Metabolic activity of the preosteoblst cells after 24 hours of incubation with the dissolution products of each PCL hybrid.

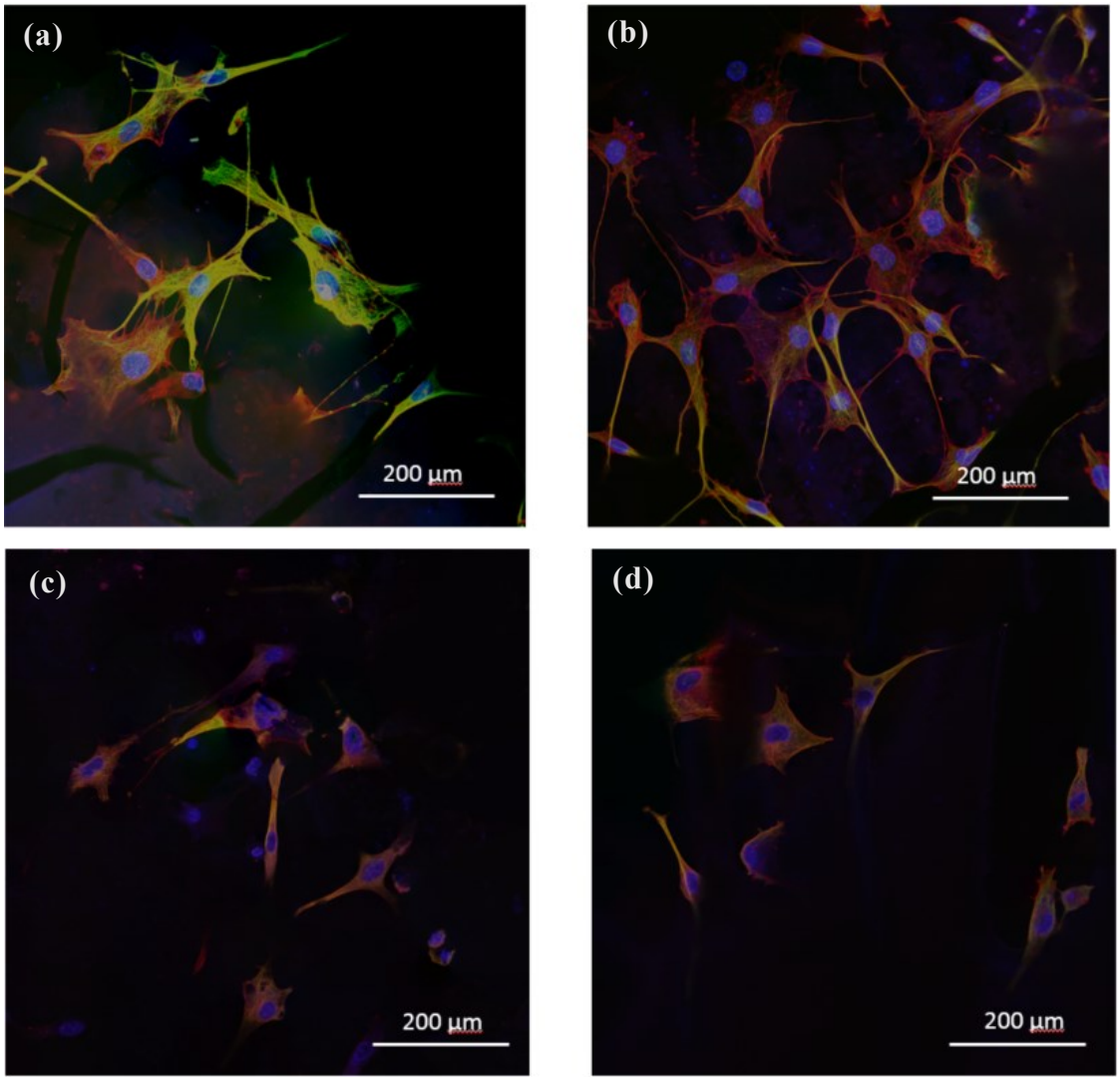


Figure 7.23 Confocal microscopy images of the preosteoblast cells cultured on the surface of (a) 6040 PCL (b) TEP4p PCL (c) TEP8p PCL (d) TEP12p PCL.

7.3.10 3D printing

6040 PCL scaffolds were made using 3D printing technique. Because of the presence of CME in 6040 PCL, the hybrid sol gelled 5 to 10 minutes after water and nitric acid were added. Before it was completely gelled, the sol was transferred into a 3D printing syringe. The viscosity of printing ink is a very important parameter and needs to be controlled carefully, if the ink is not viscous enough, the 3D printing scaffold will not be able to maintain its shape. If the ink is too gelled, it cannot pass through the tip smoothly. The printing window for 6040 PCL was around 30 to 40 minutes (between 5 minutes to 45 minutes after adding water). Within the printing window, hybrid ink expressed a shear thinning-like property, where the viscosity of the hybrid ink

decreased under shear strain therefore the hybrid ink could pass through the tip smoothly and also maintain its 3D shape. The further investigation to rheology of the hybrid ink is needed to confirming the shear thinning property of the hybrid ink.

6040 PCL scaffold was printed layer by layers, the Z-spacing (space between each layer) needs to be controlled carefully. If Z space is too big the ink struts will not be straight and flat; if the Z space too small the layer is printed into the layer below and the scaffold will be less porous, therefore the Z space needs to be just equal to the diameter of the ink strut. The porosity of the hybrids is dependent on the horizontal/vertical channel width (space between ink struts). The pore size suitable for bone ingrowth is thought to be between 200 μm to 500 μm [219]. The scaffold shrank during drying, therefore if the horizontal/vertical channel width setting is too small the scaffold will lose its porosity after drying. On the other hands, larger the pore size can weaken the mechanical property of the scaffold. Each 6040 PCL 3D printing scaffold with different printing setting was studied and came out with the best 3D printing setting for 6040 PCL scaffold. In order to check if the scaffold is porous inside, 3D printing scaffolds were cut, and the top, bottom, horizontal section and vertical section of the 3D printing scaffolds were studied under SEM. The pore sizes and the diameter of the hybrid struts were also measured under SEM.

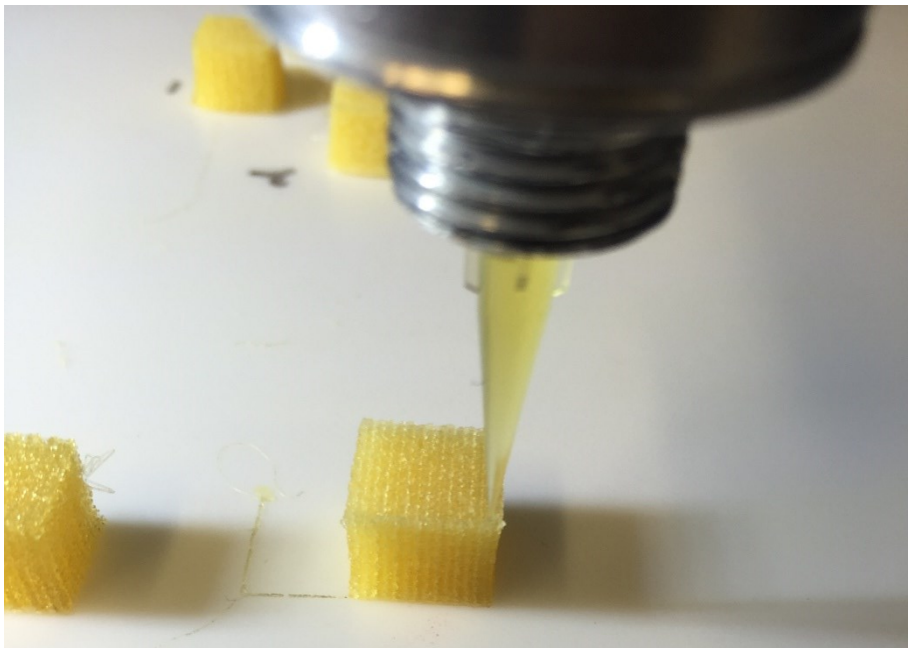


Figure 7.24 Photograph taken during 3D printing.

The 6040 PCL 3D printing scaffolds with the following printing setting were thought

to be the best scaffolds in this work at this stage: Z spacing: 0.18 mm, horizontal/vertical channel width: 0.8 mm and printing speed: 15 mm s^{-1} (depends on how gelled the hybrid ink is, could also use printing speed 10 mm s^{-1}). The 3D printer controls the flow rate of the ink automatically by selecting the sizes of syringe and printing tip. Changing the size of printing tip in the setting can change the ink printing flow rate.

Figure 7.25 shows the SME images of the 3D scaffold taken from different directions. Figure 7.25 b is an SEM image of the horizontal section of the 3D scaffold, it shows that the inside of the 3D scaffold was also porous in the horizontal direction. The pores inside the 3D scaffold were around 326 μm x 316 μm (rectangle shape). The sizes of the pores at the bottom of the scaffold (336 μm x 216 μm) were slightly smaller because of the shrinkage during the drying stage. But they were all within 200 μm to 500 μm range therefore suitable for bone ingrowth. The size of hybrid struts gradually decreased from 253 μm (bottom layers) to 167 μm (top layers) during 3D printing (Figure 7.25a, b and c). because the hybrid solution ink gelled over time while printing, the gelled ink could not pass through the tip smoothly therefore the size of hybrid struts at the top layers were slightly thinner than the struts at the bottom layers.

Figure 7.25d is the SEM image of the vertical section of the scaffold. The SEM image suggests that some layers of the 3D printing scaffold were fused into each other, it decreased the porosity of the scaffold in the horizontal direction significantly. It was the main difficulty in this 3D printing work, in theory this problem can be overcome by simply increasing the Z spacing during 3D printing. But in fact, when increased Z spacing beyond 0.18 mm, zigzag hybrid struts were printed and the printed layers were not flat. During 3D printing, the printed layers must be completely flat, a small bump can affect the 3D printing outcome by interfering the 3D printing tip.

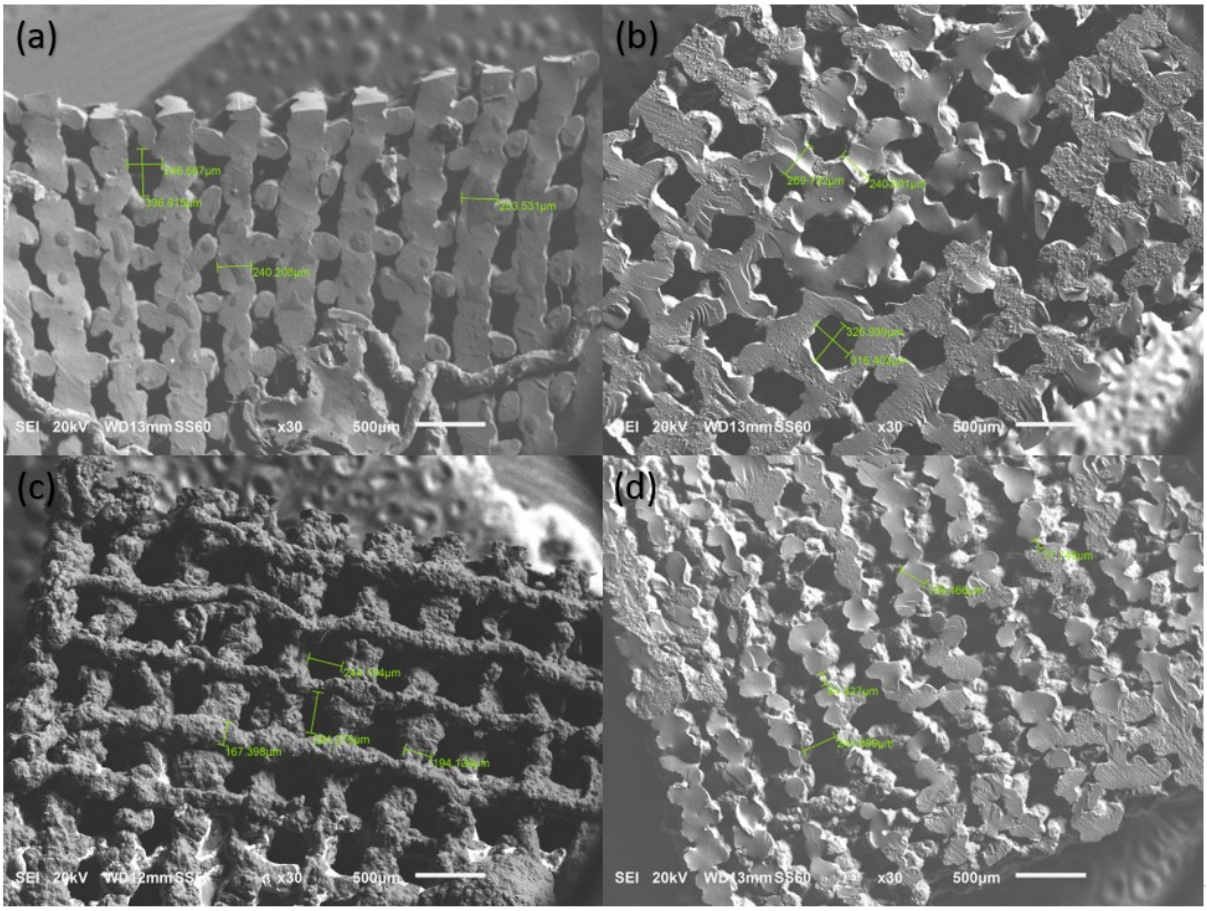


Figure 7.25 Low magnification SEM images of 6040 PCL 3D printing scaffold with 3D printing setting: Z space: 0.18mm, horizontal/vertical road width: 0.8mm and printing speed: 10mm taken from (a) bottom (b) horizontal section (c) Top (d) vertical section of the scaffold.

Micro CT images were taken by Xiaomeng Shi, a PhD student from our lab, to reveal the 3D structure of the scaffold and the porosity of the scaffold was also measured from the 3D images taken. Figure 7.26 shows CT images of a 3D printing scaffold with the following printing setting: Z space: 0.18 mm, horizontal/vertical road width: 0.8 mm and printing speed: 15 mm s^{-1}. The porosity of the scaffold was also calculated from micro CT image by Xiaomeng shi and that was 51.6% v/v. Figure 7.26b is the 3D image of a $1.8\ mm \times 1.8\ mm \times 1.8\ mm$ cube cropped from the inside of hybrid scaffold and the CT image confirmed that the scaffold was porous inside.

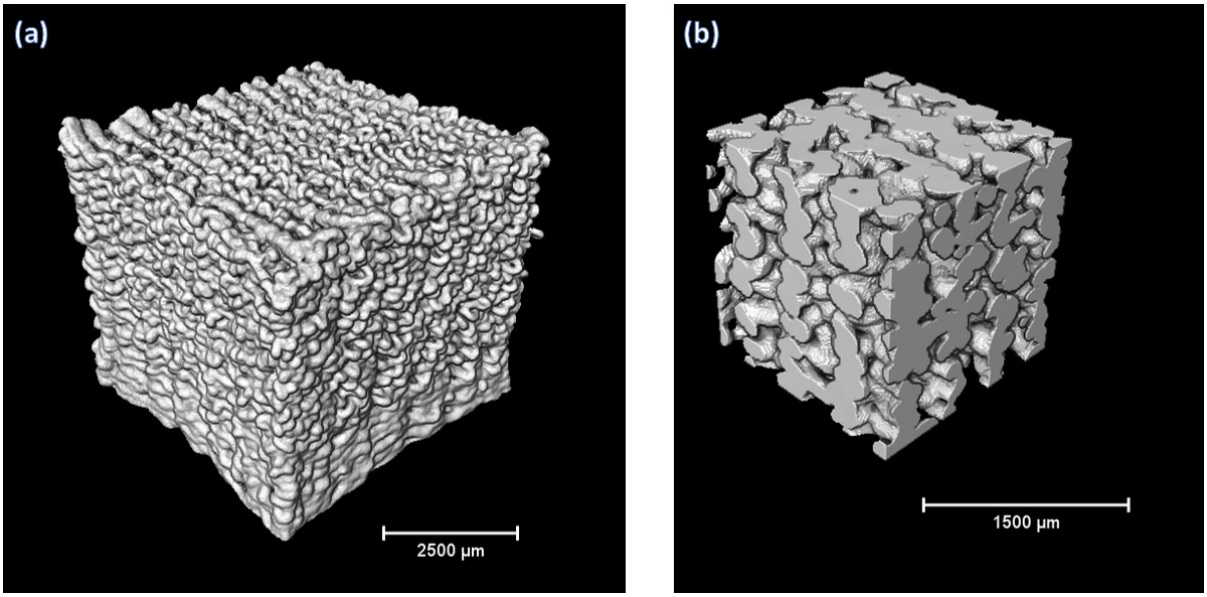


Figure 7.26 Micro CT 3D image of a 3D printing scaffold with the following print setting: Z space: 0.18mm, Horizontal/vertical road width: 0.8mm and printing speed: 15mm s^{-1}. (a) whole scaffold (b) 1.8mmX1.8mmX1.8mm cube cropped from the inside the scaffold. 150X150X150 voxels, voxel size:12µm.

The printing speed could be reduced to 10 mm s^{-1} if the ink was more viscous and gelled. The 3D scaffold is not optimal yet; the mechanical strength of the scaffold was much weaker than the cylindrical hybrid monolith because it is porous (Figure 7.27). Many factors can affect the mechanical properties of a 3D printing scaffold, including the pore size of the scaffold, the diameter of the hybrid struts, air bubbles trapped inside hybrid ink during printing and uneven shrinkage of the scaffold during drying. Reducing the horizontal/vertical channel width from 1 mm to 0.8 mm during printing improved the mechanical strength (stress at failure increased from around 1 MPa to 5 MPa) of the scaffold but the scaffold was still not strong enough (Figure 7.27). In order to improve the mechanical properties, different printing settings and structures of the scaffold need to be tried and studied. However, what can be confirmed at this stage of work is that 6040 PCL material is 3D printable and has the potential to be used as a 3D scaffold in bone tissue engineering applications. It has also been believed that the other PCL hybrid compositions will have the similar behaviour as 6040 PCL does during 3D printing, because of the presence of CME that working as a gelling agent when contact with water.

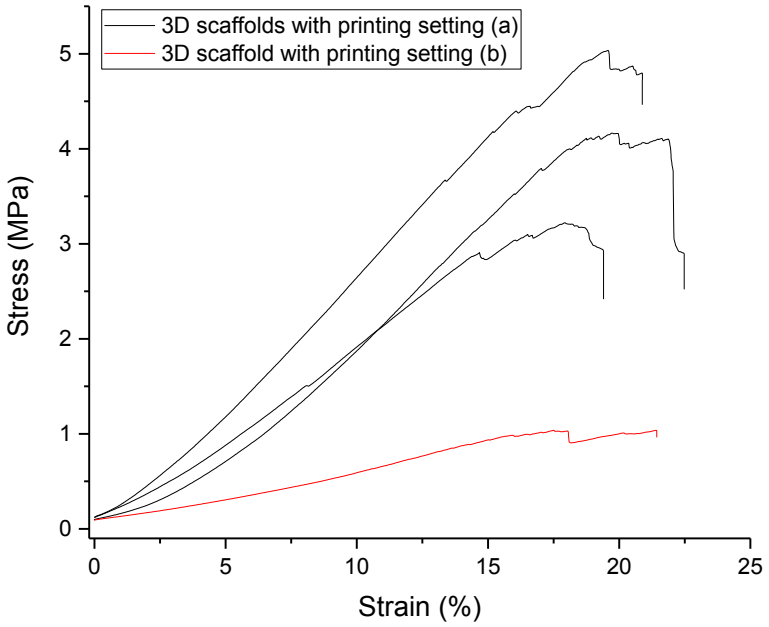


Figure 7.27 Compression curves of scaffolds with the print setting (a) Z space: 0.18mm, Horizontal/vertical channel width: 0.8mm (b) Z space: 0.18mm, Horizontal/vertical channel width: 1mm.

7.3.11 SEM images of PCL hybrid powder particles

High magnification SEM (SEM, LEO Gemini 1525 FEGSEM) images were taken to examine the surface microstructure of the PCL hybrids before and after 2 weeks of SBF immersion. Figure 7.28 shows the surface structure of each PCL hybrid, the surfaces of the PCL hybrids were smoother compared to TEP bioactive glasses and no nanopores could be seen on the surface under SEM. Nitrogen sorption could not be applied to the PCL hybrids, because the PCL hybrids did not absorb nitrogen well and it also suggests that PCL hybrids were not porous.

Figure 7.29b c and d are the SEM images of 6040 PCL hybrid after 2 weeks of SBF dissolution with different magnifications. Figure 7.29a is the low magnification SME image of 6040 PCL powder granules before SBF dissolution, the white (HCA) patches formed on the surface of 6040 PCL after 2 weeks of SBF dissolution (Figure 7.29b). Rod shape HCA structures were found and that suggests HCA crystals were well spread on the surface of 6040 PCL hybrids after 2 week of SBF immersion. The SME images for other PCL hybrids after SBF immersion were similar to 6040 PCL, therefore only SEM images of 6040 PCL are shown here. HCA patches were found in all the PCL hybrids after SBF immersion in this work.

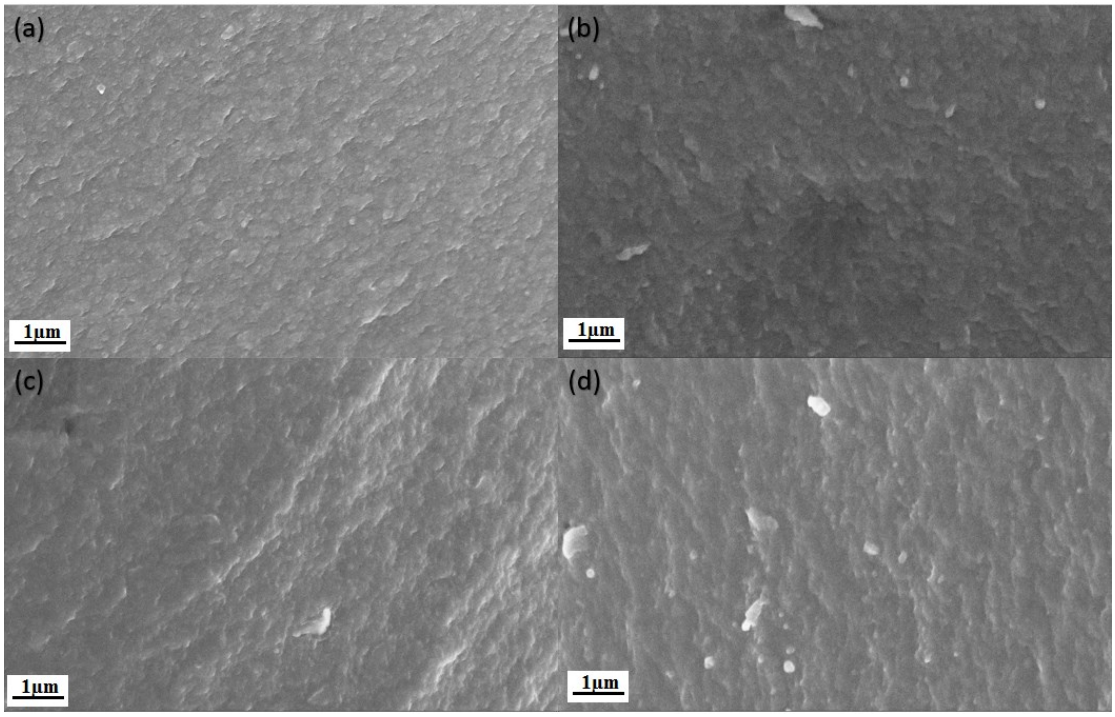


Figure 7.28 SEM images of (a) 6040 PCL (b) TEP4p PCL (c) TEP8p PCL (d) TEP12p PCL before SBF dissolution.

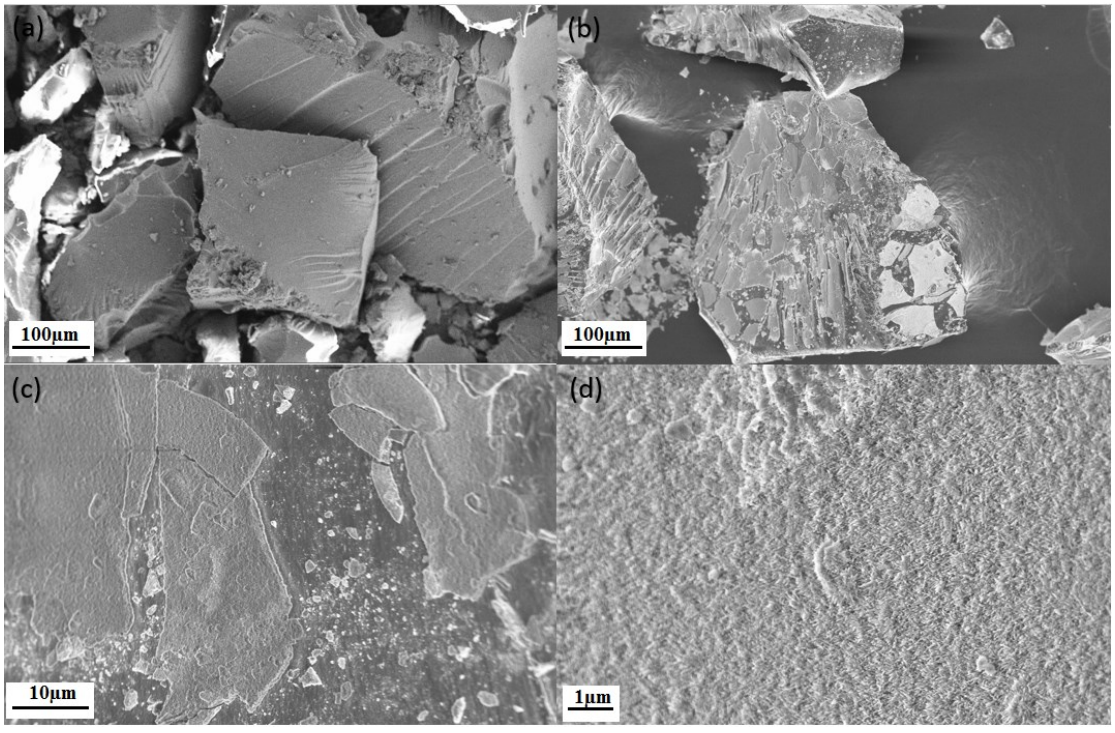


Figure 7.29 SEM images of (a) 6040 PCL before SBF dissolution; (b, c, d) 6040 PCL after 2 weeks of SBF dissolution.

7.4 Discussion

7.4.1 Properties of calcium containing PCL hybrids

The calcium containing silica was successfully incorporated into the PCL hybrid system and homogeneous calcium containing PCL hybrids were made. All the PCL hybrids in this work were capable of triggering HCA formation when soaked in SBF. The XRD and FTIR data suggest that HCA formed on the surfaces of all PCL hybrids just after 3 days of SBF dissolution, and HCA layer were well spread on the surface of each hybrid powder granule. Furthermore, all the PCL hybrids made in this work were able to support good cell attachment and passed the ISO standard cell cytotoxicity test. In addition, 6040 PCL hybrid was proved to be 3D printable although the 3D printing scaffolds made in this work were not perfect yet but the further improvement to the 3D printing scaffold is achievable. Therefore, the PCL hybrids have the promising potential to be used as scaffolds in bone tissue engineering applications.

All the PCL hybrids were soaked in TRIS buffer for a week to investigate their degradation rates. The organic/inorganic ratio of each PCL hybrid was similar before and after TRIS dissolution, this proved that the inorganic glass and organic polymer chains left the PCL hybrid at similar rate. However, cracks appeared in all the cylindrical PCL hybrids monoliths after 1 week of TRIS dissolution and this limits the potential of the PCL hybrid. Increase the organic PCL content in the hybrid can probably solve the problem, but the bioactivity of the hybrid might decrease. Therefore, further studies are required to optimise the PCL hybrids. Compression test indicates that all the PCL hybrids made in this work was viscoelastic. The cyclic loading test further suggest that 6040 PCL has the potential to be used as the scaffolding material at the defect sites that are under cyclic loads.

7.4.2 The role of calcium and phosphate in PCL hybrids

SBF dissolution profiles suggest that 6040 PCL and TEP4p PCL gave consistent release of calcium up to 72 h and it might be because of the hydrophobicity of PCL which slowed down the ions release from the hybrid.

When comparing the calcium containing PCL hybrid (6040 PCL) with calcium free PCL hybrid, 6040 PCL cylindrical monolith had greater stress and strain at failure than calcium free PCL hybrid cylindrical monolith. When phosphate was added into the PCL

hybrid by substituting certain amount of calcium with phosphate, it changed the mechanical properties of the PCL hybrid. The phosphate containing hybrids (TEP4p PCL, TEP8p PCL and TEP12p PCL) were much softer than 6040 PCL and the calcium free PCL hybrids. From the compression test data, it can be confirmed that calcium plays an important role in strengthening the mechanical property of PCL hybrids. But the additional phosphate softens the PLC hybrids. In calcium free PCL hybrids (TEOS, PCL and poly THF), hydrogen bonds may form between carboxyl groups (COOH) in the PCL chains within the hybrid. When calcium was incorporated into the PCL hybrid system, calcium may ionically bond to the COO^- groups at the PCL chain terminus and that make the PCL hybrid tougher. The ionic crosslinking between PCL and silica network by calcium might also be presence in the hybrids. Furthermore, another hypothesis can be made: Phosphate can probably incorporate into PCL chain with calcium by charge balance with calcium ions and that further soften the phosphate containing PCL hybrid. However at this stage, there is no evident to confirm those hypothesises.

From the ^{29}Si solid state NMR data, the PCL hybrid with more calcium had the lower degree of condensation. Calcium is the network modifier for silica network and it can interfere the formation of silica network. Therefore, in theory, the higher the calcium content in the PCL hybrid the lower the degree of condensation of silica network. But the ^{29}Si Solid state NMR result was unexpected. One of the possible causes of that might be when the calcium content was high, the calcium tended to incorporate into the PCL rather than the silica network. The other possible cause might be that the additional phosphate somehow interferes the incorporation of calcium into PCL, therefore when the phosphate was present calcium tend to incorporate in silica network rather than PCL. It can also be the combination of both possible causes. The interference effect of phosphate to calcium incorporation might also contribute to the mechanical property changes in phosphate containing PCL hybrids. Further study on the interaction between calcium and PCL chain is needed to confirm the hypothesises made in this works.

In conclusion, 6040 PLC hybrid should be the best hybrid material made in this work. However, all the PCL hybrids made in this work express similar bioactivity and all of them passed the ISO standard cytotoxicity test, but 6040 PCL had the best mechanical properties and the cells attached on it were better spread. All the data obtained suggest that 6040 PCL seems to be the best PCL hybrid out of four at this stage of the work.

7.5 Conclusions

1. Silica/PCL hybrids which contain calcium and phosphate were successfully made by using CME and TEP as the calcium and phosphate precursors respectively.
2. All the PCL hybrids made in this work were capable of inducing HCA formation in SBF.
3. The PCL hybrids lost their organic and inorganic components through dissolution at similar rate in TRIS buffer.
4. All the PCL hybrids made in this work passed the ISO standard cell cytotoxicity test and could support good MC3T3-E1 (preosteoblast) cell attachment. Cells on 6040 PCL demonstrated better cell migration, spreading and potentially differentiation than other three PCL hybrids.
5. 6040 PCL hybrids exhibited the best mechanical property (highest stress at failure) among all the PCL hybrid compositions. The results of compression tests also suggest that calcium is beneficial to the mechanical property of the PCL hybrid.
6. 6040 PCL hybrid has been proved to be 3D printable.

8 Conclusions and further work

8.1 Conclusions

The effect of phosphate content on the properties of the sol-gel derived bioactive glass was investigated, where calcium nitrate and TEP were used as the calcium and phosphate precursors respectively. The glass compositions were based on the 58S glass but with different ratios of phosphate to calcium. The results show that HA formed during glass synthesis in the low phosphate containing glass (4 mol% and 8 mol%) but when the phosphate content in the sol-gel glass was high enough (around 24 mol% phosphate) a phosphate network (polyphosphate) formed within the silica based sol-gel glass instead of forming HA. The high phosphate glass lost its ability to induce HCA formation in SBF. HCA formed on the low phosphate glasses just after 8 h of immersion in SBF. The glass containing intermediate amount of phosphate (12 mol%) exhibited an intermediate level of HCA forming ability in SBF (HCA formed after 1 week of SBF immersion) and pyrophosphate formed within the glass during glass synthesis.

The effect of phosphate precursor on the properties of the sol-gel glass was subsequently investigated by using DEPETES as the phosphate precursor. Because of the nature of DEPETES, the HA formation during glass synthesis was inhibited by preventing orthophosphate formation in sol. The results suggest that DEPETES might have incorporated into the silica network via a different route to TEP. Where the triethylsilane end of DEPETES can be hydrolysed in sol, then condense with silanol group in silica network (or hydrolysed TEOS). During the heat treatment, the carbon chain within DEPETES broke (removed as carbon dioxide) and left the silica and phosphate alone in the glass. All the sol-gel glasses made with DEPETES and calcium nitrate could induce HCA formation in SBF. Even though there was not HA formed during glass preparation, the glasses still released calcium and phosphate ions rapidly in SBF.

In order to incorporate the glass composition into a hybrid system, a preliminary experiment was conducted to investigate the calcium (CME) and phosphate (DEPETES) incorporations from the chosen precursors at low temperature (60^{o}C). The results showed that the calcium from CME is suitable to be used in hybrid synthesis since the calcium from CME can be incorporated into the glass network at low temperature. Whereas DEPETES might not be a suitable phosphate precursor for hybrid synthesis

as the phosphate might be released as hydrolysed DEPETES from the sol-gel derived sample synthesised at low temperature with DEPETES, therefore it losses the ability to buffer the pH and the *in vivo* effect of the DEPETES released from the glass is still unknown.

The chosen glass compositions were successfully incorporated into PCL hybrid system (using a synthesis protocol developed by Francesca Tallia) using CME and TEP as the calcium and phosphate precursors respectively. The calcium containing hybrids made in this work exhibited the abilities to induce HCA formation in SBF and supported good cell (preosteoblast cell line) attachment. It has also been proven in this work that the dissolution products released from the hybrids do not induce any cytotoxicity effect *in vitro*. The presence of calcium does not only endow the hybrid with ability to induce HCA formation in SBF, but can also improve the mechanical properties of the hybrid (both stress and strain at failure were much higher for 6040 PCL than Ca-free PCL hybrid). Consistent release of calcium from 6040 PCL and TEP4p PCL were observed during the first 3 d of SBF immersion, it might be caused by the incorporation of calcium into both organic and inorganic phases of the hybrid, or it might be just because of the hydrophobic property of PCL which slowed down the ions releases from the hybrid. Lastly, the porous scaffold of 6040 PCL hybrid was fabricated using 3D printing technique, however the 3D printing scaffold was not perfect yet but it has confirmed that 6040 PCL hybrid is 3D printable.

8.2 Further work

The future work of this project will focus on the long-term effect of the PCL hybrids both *in vivo* and *in vitro*. Since polyTHF forms in the PCL hybrid system used in this work, polyTHF is considered as a non-degradable polymer, therefore a long-term degradation study in TRIS will be done to investigate the degradation behaviour of the PCL hybrid materials *in vitro*. The hybrid immersed TRIS solution will be collected and analysed by ICP and liquid NMR. Solid-state NMR and TGA will be applied to check the atomic structure and organic/inorganic ratio of the hybrid material at various time points of TRIS immersion. In addition, the long-term cell culture study will be conducted to investigate the differentiation behaviour of the cells that attached on the PCL materials. *In vivo* studies on the PCL hybrids also need to be done to see if the additional phosphates in the hybrids improve bioactivity of hybrid *in vivo*.

Shear thinning of the ink for 3D printing was not observed from any of the calcium free PCL hybrid ink. But 6040 PCL ink prepared in this project might potentially have the shear thinning property. It suggests the additional CME may provide the shear thinning property to the hybrid ink. In order to confirm shear thinning property, the rheology of the hybrid ink will be studied using a rheometer. Additionally, hybrid scaffolds with different 3D structures and printing parameters will be fabricated and studied to improve the mechanical properties of the hybrid scaffolds.

Lastly, once the 3D printing scaffold with sufficient mechanical strength is successfully fabricated, the *in vivo* testing of the 3D printing hybrid scaffold is needed to investigate the tissue response to the implanted hybrid scaffold (e.g. bone ingrowth) and bioresorption behaviour of the hybrid scaffold *in vivo*.

9 Reference

1. Hench, L.L., *8 - The skeletal system*, in *Biomaterials, Artificial Organs and Tissue Engineering*. 2005, Woodhead Publishing. p. 79-89.
2. Spicer, P.P., et al., *Evaluation of Bone Regeneration Using the Rat Critical Size Calvarial Defect.* Nature protocols, 2012. **7**(10): p. 1918-1929.
3. Kneser, U., et al., *Tissue engineering of bone.* Minimally Invasive Therapy & Allied Technologies, 2002. **11**(3): p. 107-116.
4. Jones, J.R., P.D. Lee, and L.L. Hench, *Hierarchical porous materials for tissue engineering.* Philosophical Transactions of the Royal Society a-Mathematical Physical and Engineering Sciences, 2006. **364**(1838): p. 263-281.
5. Hench, L.L. and J.M. Polak, *Third-Generation Biomedical Materials.* Science, 2002. **295**(5557): p. 1014-1017.
6. Hench, L.L., *Biomaterials.* Science, 1980. **208**(4446): p. 826-831.
7. Hench, L.L. and J. Wilson, *Surface-active biomaterials.* Science, 1984. **226**(4675): p. 630-636.
8. Xynos, I.D., et al., *Bioglass (R) 45S5 stimulates osteoblast turnover and enhances bone formation in vitro: Implications and applications for bone tissue engineering.* Calcified Tissue International, 2000. **67**(4): p. 321-329.
9. Xynos, I.D., et al., *Gene-expression profiling of human osteoblasts following treatment with the ionic products of Bioglass (R) 45S5 dissolution.* Journal of Biomedical Materials Research, 2001. **55**(2): p. 151-157.
10. Xynos, I.D., et al., *Ionic products of bioactive glass dissolution increase proliferation of human osteoblasts and induce insulin-like growth factor II mRNA expression and protein synthesis.* Biochemical and Biophysical Research Communications, 2000. **276**(2): p. 461-465.
11. Hench, L.L., et al., *BONDING MECHANISM AT THE INTERFACE OF CERAMIC PROSTHETIC MATERIALS.* Journal of Biomedical Materials Research Biomedical Materials Symposium, 1972. **2**: p. 117-141.
12. Li, R., A.E. Clark, and L.L. Hench, *AN INVESTIGATION OF BIOACTIVE GLASS POWDERS BY SOL-GEL PROCESSING.* Journal of Applied Biomaterials, 1991. **2**(4): p. 231-239.
13. Rho, J.-Y., L. Kuhn-Spearing, and P. Zioupos, *Mechanical properties and the hierarchical structure of bone.* Medical Engineering & Physics, 1998. **20**(2): p. 92-102.
14. Wise, E.R., et al., *The Organic–Mineral Interface in Bone Is Predominantly Polysaccharide.* Chemistry of Materials, 2007. **19**(21): p. 5055-5057.
15. Stayton, P.S., et al., *Molecular recognition at the protein-hydroxyapatite interface.* Critical Reviews in Oral Biology & Medicine, 2003. **14**(5): p. 370-376.
16. Hench, J.W., *6 - Cells and tissues*, in *Biomaterials, Artificial Organs and Tissue Engineering*. 2005, Woodhead Publishing. p. 59-70.
17. Hench, L.L., *12 - Repair of skeletal tissues*, in *Biomaterials, Artificial Organs and Tissue Engineering*. 2005, Woodhead Publishing. p. 119-128.
18. Jones, J.R., *Review of bioactive glass: From Hench to hybrids.* Acta Biomaterialia, 2013. **9**(1): p. 4457-4486.
19. Hench, L.L., *Bioactive Ceramics: Theory and Clinical Applications*, in *Bioceramics*. 1994, Pergamon: Oxford. p. 3-14.
20. Hench, L.L., J.R. Jones, and M.B. Fenn, *New Materials and Technologies for Healthcare*. 2012: Imperial College Press.
21. Oonishi, H., et al., *Quantitative comparison of bone growth behavior in granules of Bioglass (R), A-W glass-ceramic, and hydroxyapatite.* Journal of Biomedical Materials Research, 2000. **51**(1): p. 37-46.

22. Clare, A.G., *The Unique Nature of Glass*, in *Bio-Glasses*. 2012, John Wiley & Sons, Ltd. p. 1-12.
23. Vallet-Regi, M., *Ceramics for medical applications.* Journal of the Chemical Society, Dalton Transactions, 2001(2): p. 97-108.
24. Oonishi, H., et al., *Particulate bioglass compared with hydroxyapatite as a bone graft substitute.* Clinical Orthopaedics and Related Research, 1997(334): p. 316-325.
25. Ducheyne, P. and Q. Qiu, *Bioactive ceramics: the effect of surface reactivity on bone formation and bone cell function.* Biomaterials, 1999. **20**(23–24): p. 2287-2303.
26. Ducheyne, P., S. Radin, and L. King, *The effect of calcium phosphate ceramic composition and structure on in vitro behavior. I. Dissolution.* Journal of Biomedical Materials Research, 1993. **27**(1): p. 25-34.
27. Scheffler, M., P. Colombo, and I. Wiley, *Cellular ceramics : structure, manufacturing, properties and applications.* 2005.
28. Legeros, R.Z., et al., *Biphasic calcium phosphate bioceramics: preparation, properties and applications.* Journal of Materials Science-Materials in Medicine, 2003. **14**(3): p. 201-209.
29. Brauer, D.S., *Phosphate Glasses*, in *Bio-Glasses*. 2012, John Wiley & Sons, Ltd. p. 45-64.
30. Uo, M., et al., *Properties and cytotoxicity of water soluble Na2O-CaO-P2O5 glasses.* Biomaterials, 1998. **19**(24): p. 2277-2284.
31. Ahmed, I., et al., *Phosphate glasses for tissue engineering: Part 1. Processing and characterisation of a ternary-based P2O5–CaO–Na2O glass system.* Biomaterials, 2004. **25**(3): p. 491-499.
32. Franks, K., et al., *Investigation of thermal parameters and crytallisation in a ternary CaO-Na2O-P2O5-based glass system.* Biomaterials, 2001. **22**(5): p. 497-501.
33. Knowles, J.C., *Phosphate based glasses for biomedical applications.* Journal of Materials Chemistry, 2003. **13**(10): p. 2395-2401.
34. Salih, V., et al., *Development of soluble glasses for biomedical use Part II: The biological response of human osteoblast cell lines to phosphate-based soluble glasses.* Journal of Materials Science: Materials in Medicine, 2000. **11**(10): p. 615-620.
35. Hench, L.L., *The story of Bioglass (R).* Journal of Materials Science-Materials in Medicine, 2006. **17**(11): p. 967-978.
36. Hench, L.L., *Bioceramics.* Journal of the American Ceramic Society, 1998. **81**(7): p. 1705-1728.
37. Hench, L.L., *BIOCERAMICS - FROM CONCEPT TO CLINIC.* Journal of the American Ceramic Society, 1991. **74**(7): p. 1487-1510.
38. O'Donnell, M.D., *Melt-Derived Bioactive Glass*, in *Bio-Glasses*. 2012, John Wiley & Sons, Ltd. p. 13-27.
39. Wilson, J., et al., *TOXICOLOGY AND BIOCOMPATIBILITY OF BIOGLASSES.* Journal of Biomedical Materials Research, 1981. **15**(6): p. 805-817.
40. Greenspan, D.C. and L.L. Hench, *CHEMICAL AND MECHANICAL-BEHAVIOR OF BIOGLASS-COATED ALUMINA.* Journal of Biomedical Materials Research, 1976. **10**(4): p. 503-509.
41. Wu, Z.Y., et al., *Melt-derived bioactive glass scaffolds produced by a gel-cast foaming technique.* Acta Biomaterialia, 2011. **7**(4): p. 1807-1816.
42. Lin, S., et al., *Nanostructure evolution and calcium distribution in sol-gel derived bioactive glass.* Journal of Materials Chemistry, 2009. **19**(9): p. 1276-1282.
43. Jones, J.R., *Sol-Gel Derived Glasses for Medicine*, in *Bio-Glasses*. 2012, John Wiley & Sons, Ltd. p. 29-44.

44. Sepulveda, P., J.R. Jones, and L.L. Hench, *In vitro dissolution of melt-derived 45S5 and sol-gel derived 58S bioactive glasses.* Journal of Biomedical Materials Research, 2002. **61**(2): p. 301-311.
45. Hench, L.L. and J.K. West, *Biological applications of bioactive glasses.* Life Chemistry Reports, 1996. **13**: p. 187 - 241.
46. Sepulveda, P., J.R. Jones, and L.L. Hench, *Characterization of melt-derived 45S5 and sol-gel-derived 58S bioactive glasses.* Journal of Biomedical Materials Research, 2001. **58**(6): p. 734-740.
47. Hamadouche, M., et al., *Long-term in vivo bioactivity and degradability of bulk sol-gel bioactive glasses.* Journal of Biomedical Materials Research, 2001. **54**(4): p. 560-566.
48. Wheeler, D.L., et al., *Assessment of resorbable bioactive material for grafting of critical-size cancellous defects.* Journal of Orthopaedic Research, 2000. **18**(1): p. 140-148.
49. Hench, L.L., D.L. Wheeler, and D.C. Greenspan, *Molecular control of bioactivity in sol-gel glasses.* Journal of Sol-Gel Science and Technology, 1998. **13**(1-3): p. 245-250.
50. Bielby, R.C., et al., *Time- and concentration-dependent effects of dissolution products of 58S sol-gel bioactive glass on proliferation and differentiation of murine and human osteoblasts.* Tissue Engineering, 2004. **10**(7-8): p. 1018-1026.
51. Bielby, R.C., et al., *Enhanced derivation of osteogenic cells from murine embryonic stem cells after treatment with ionic dissolution products of 58S bioactive sol-gel glass.* Tissue Engineering, 2005. **11**(3-4): p. 479-488.
52. Christodoulou, L., et al., *Characterization of human fetal osteoblasts by microarray analysis following stimulation with 58S bioactive gel-glass ionic dissolution products.* Journal of Biomedical Materials Research Part B-Applied Biomaterials, 2006. **77B**(2): p. 431-446.
53. Saravanapavan, P. and L.L. Hench, *Mesoporous calcium silicate glasses. I. Synthesis.* Journal of Non-Crystalline Solids, 2003. **318**(1–2): p. 1-13.
54. Saravanapavan, P., et al., *Binary CaO-SiO2 gel-glasses for biomedical applications.* Bio-Medical Materials and Engineering, 2004. **14**(4): p. 467-486.
55. Brinker, C.J. and G.W. Scherer, *Sol-gel science : the physics and chemistry of sol-gel processing*. 1990, Boston: Academic Press.
56. Buckley, A.M. and M. Greenblatt, *The Sol-Gel Preparation of Silica Gels.* Journal of Chemical Education, 1994. **71**(7): p. 599.
57. Brinker, C.J. and G.W. Scherer, *Sol → gel → glass: I. Gelation and gel structure.* Journal of Non-Crystalline Solids, 1985. **70**(3): p. 301-322.
58. Iler, R.K., *The chemistry of silica : solubility, polymerization, colloid and surface properties, and biochemistry*. 1979, New York: Wiley.
59. Labbaf, S., et al., *Spherical bioactive glass particles and their interaction with human mesenchymal stem cells in vitro.* Biomaterials, 2011. **32**(4): p. 1010-1018.
60. Milea, C.A., B. C, and A. Duta, *The influence of parameters in silica sol-gel process.* Bulletin of the Transilvania University of Braşov. Series I, Series I, 2011. **4**(53): p. 59-66.
61. Aelion, R., A. Loebel, and F. Eirich, *Hydrolysis of Ethyl Silicate*.* Journal of the American Chemical Society, 1950. **72**(12): p. 5705-5712.
62. Hench, L.L. and J.K. West, *The sol-gel process.* Chemical Reviews, 1990. **90**(1): p. 33-72.
63. Colby, M.W., A. Osaka, and J.D. Mackenzie, *Effects of temperature on formation of silica gel.* Journal of Non-Crystalline Solids, 1986. **82**(1): p. 37-41.
64. Zarzycki, J., M. Prassas, and J. Phalippou, *Synthesis of glasses from gels: the problem of monolithic gels.* Journal of Materials Science, 1982. **17**(11): p. 3371-3379.

65. Whitaker, S., *Simultaneous heat, mass, and momentum transfer in porous media: a theory of drying.* Advances in heat transfer, 1977. **13**: p. 119-203.
66. Hench, L.L. and M.J.R. Wilson, *Processing of gel-silica monoliths for optics.* Journal of Non-Crystalline Solids, 1990. **121**(1): p. 234-243.
67. Sherwood, T.K., *The Drying of solids—II.* Industrial & Engineering Chemistry, 1929. **21**(10): p. 976-980.
68. Hench, L.L. and S.H. Wang, *The sol-gel glass transformation of silica.* Phase Transitions, 1990. **24-26**(2): p. 785-834.
69. Arcos, D., D.C. Greenspan, and M. Vallet-Regí, *Influence of the Stabilization Temperature on Textural and Structural Features and Ion Release in SiO2−CaO−P2O5 Sol−Gel Glasses.* Chemistry of Materials, 2002. **14**(4): p. 1515-1522.
70. Martin, R.A., et al., *Characterizing the hierarchical structures of bioactive sol-gel silicate glass and hybrid scaffolds for bone regeneration.* Philosophical Transactions of the Royal Society a-Mathematical Physical and Engineering Sciences, 2012. **370**(1963): p. 1422-1443.
71. Hill, R., *An alternative view of the degradation of bioglass.* Journal of Materials Science Letters, 1996. **15**(13): p. 1122-1125.
72. Yu, B., et al., *Effect of Calcium Source on Structure and Properties of Sol-Gel Derived Bioactive Glasses.* Langmuir, 2012. **28**(50): p. 17465-17476.
73. Pedone, A., et al., *New Insights into the Atomic Structure of 45S5 Bioglass by Means of Solid-State NMR Spectroscopy and Accurate First-Principles Simulations.* Chemistry of Materials, 2010. **22**(19): p. 5644-5652.
74. Elgayar, I., et al., *Structural analysis of bioactive glasses.* Journal of Non-Crystalline Solids, 2005. **351**(2): p. 173-183.
75. Mercier, C., et al., *Influence of P2O5 content on the structure of SiO2-Na2O-CaO-P2O5 bioglasses by Si-29 and P-31 MAS-NMR.* Journal of Non-Crystalline Solids, 2011. **357**(24): p. 3901-3909.
76. Tilocca, A. and A.N. Cormack, *Structural Effects of Phosphorus Inclusion in Bioactive Silicate Glasses.* The Journal of Physical Chemistry B, 2007. **111**(51): p. 14256-14264.
77. Carta, D., et al., *A structural study of sol–gel and melt-quenched phosphate-based glasses.* Journal of Non-Crystalline Solids, 2007. **353**(18–21): p. 1759-1765.
78. Carta, D., et al., *Structural studies of bioactive sol-gel phosphate based glasses.* Physics and Chemistry of Glasses, 2005. **46**(4): p. 365-371.
79. Farzad, F., et al., *Sol–gel synthesis of quaternary (P 2 O 5) 55 –(CaO) 25 –(Na 2 O) (20– x) –(TiO 2) x bioresorbable glasses for bone tissue engineering applications (x = 0, 5, 10, or 15).* Biomedical Materials, 2015. **10**(4): p. 045025.
80. Carta, D., et al., *Sol-gel synthesis of the P(2)O(5)-CaO-Na(2)O-SiO(2) system as a novel bioresorbable glass.* Journal of Materials Chemistry, 2005. **15**(21): p. 2134-2140.
81. Carta, D., et al., *Sol-gel synthesis and structural characterisation of P2O5-B2O3-Na2O glasses for biomedical applications.* Journal of Materials Chemistry, 2009. **19**(1): p. 150-158.
82. Carta, D., et al., *Sol-gel produced sodium calcium phosphosilicates for bioactive applications: Synthesis and structural characterisation.* Materials Chemistry and Physics, 2011. **130**(1-2): p. 690-696.
83. Lee, I.H., et al., *Sol-gel synthesis and structural characterization of P2O5-CaO-Na2O glasses.* Physics and Chemistry of Glasses-European Journal of Glass Science and Technology Part B, 2013. **54**(3): p. 115-120.
84. Foroutan, F., et al., *Novel sol–gel preparation of (P2O5)0.4–(CaO)0.25–(Na2O)X–(TiO2)(0.35−X) bioresorbable glasses (X = 0.05, 0.1, and 0.15).* Journal of Sol-Gel Science and Technology, 2015. **73**(2): p. 434-442.

85. Pickup, D.M., et al., *New sol-gel synthesis of a (CaO)(0.3)(Na2O)(0.2)(P2O5)(0.5) bioresorbable glass and its structural characterisation.* Journal of Materials Chemistry, 2007. **17**(45): p. 4777-4784.
86. Pickup, D.M., R.J. Newport, and J.C. Knowles, *Sol-Gel Phosphate-based Glass for Drug Delivery Applications.* Journal of Biomaterials Applications, 2012. **26**(5): p. 613-622.
87. Pickup, D.M., et al., *Sol-gel synthesis and structural characterisation of binary TiO(2)-P(2)O(5) glasses.* Materials Research Bulletin, 2008. **43**(2): p. 333-342.
88. Pickup, D.M., et al., *Preparation, structural characterisation and antibacterial properties of Ga-doped sol–gel phosphate-based glass.* Journal of Materials Science, 2009. **44**(7): p. 1858-1867.
89. Pickup, D.M., et al., *Sol-gel preparation and high-energy XRD study of (CaO)(x)(TiO(2))(0.5-x)(P(2)O(5))(0.5) glasses (x=0 and 0.25).* Journal of Materials Science-Materials in Medicine, 2008. **19**(4): p. 1661-1668.
90. Qiu, D., et al., *A comparative study of the structure of sodium borophosphates made by sol-gel and melt-quench methods.* Journal of Non-Crystalline Solids, 2010. **356**(9-10): p. 490-494.
91. Foroutan, F., et al., *Sol-Gel Synthesis and Electrospraying of Biodegradable (P2O5)(55)-(CaO)(30)-(Na2O)(15) Glass Nanospheres as a Transient Contrast Agent for Ultrasound Stem Cell Imaging.* Acs Nano, 2015. **9**(2): p. 1868-1877.
92. Vrouwenvelder, W.C.A., C.G. Groot, and K. Degroot, *HISTOLOGICAL AND BIOCHEMICAL EVALUATION OF OSTEOBLASTS CULTURED ON BIOACTIVE GLASS, HYDROXYLAPATITE, TITANIUM-ALLOY, AND STAINLESS-STEEL.* Journal of Biomedical Materials Research, 1993. **27**(4): p. 465-475.
93. Ohtsuki, C., et al., *Compositional dependence of bioactivity of glasses in the system CaO-SiO2-P2O5: its in vitro evaluation.* Nippon Seramikkusu Kyokai Gakujutsu Ronbunshi, 1991. **99**(1): p. 1-6.
94. Ebisawa, Y., et al., *Bioactivity of CaO·SiO2-based glasses:in vitro evaluation.* Journal of Materials Science: Materials in Medicine, 1990. **1**(4): p. 239-244.
95. Salinas, A.J., A.I. Martin, and M. Vallet-Regí, *Bioactivity of three CaO–P2O5–SiO2 sol-gel glasses.* Journal of Biomedical Materials Research, 2002. **61**(4): p. 524-532.
96. Vallet-Regi, M., I. Izquierdo-Barba, and A.J. Salinas, *Influence of P2O5 on crystallinity of apatite formed in vitro on surface of bioactive glasses.* Journal of Biomedical Materials Research, 1999. **46**(4): p. 560-565.
97. Cao, W. and L.L. Hench, *Bioactive materials.* Ceramics International, 1996. **22**(6): p. 493-507.
98. Clark, A.E., C.G. Pantano, and L.L. Hench, *AUGER SPECTROSCOPIC ANALYSIS OF BIOGLASS CORROSION FILMS.* Journal of the American Ceramic Society, 1976. **59**(1-2): p. 37-39.
99. Lobel, K.D. and L.L. Hench, *In-vitro protein interactions with a bioactive gel-glass.* Journal of Sol-Gel Science and Technology, 1996. **7**(1): p. 69-76.
100. Kawamura, M., et al., *CHONDROOSTEOGENETIC RESPONSE TO CRUDE BONE-MATRIX PROTEINS BOUND TO HYDROXYAPATITE.* Clinical Orthopaedics and Related Research, 1987(217): p. 281-292.
101. Ripamonti, U., et al., *OSTEOGENIN, A BONE MORPHOGENETIC PROTEIN, ADSORBED ON POROUS HYDROXYAPATITE SUBSTRATA, INDUCES RAPID BONE DIFFERENTIATION IN CALVARIAL DEFECTS OF ADULT PRIMATES.* Plastic and Reconstructive Surgery, 1992. **90**(3): p. 382-393.
102. Green, A.M., et al., *Fibroblast response to microtextured silicone surfaces: Texture orientation into or out of the surface.* Journal of Biomedical Materials Research, 1994. **28**(5): p. 647-653.

103. Carlisle, E.M., *Silicon as an Essential Trace Element in Animal Nutrition*, in *Ciba Foundation Symposium 121 - Silicon Biochemistry*. 2007, John Wiley & Sons, Ltd. p. 123-139.
104. Keeting, P.E., et al., *ZEOLITE-A INCREASES PROLIFERATION, DIFFERENTIATION, AND TRANSFORMING GROWTH-FACTOR-BETA PRODUCTION IN NORMAL ADULT HUMAN OSTEOBLAST-LIKE CELLS-INVITRO.* Journal of Bone and Mineral Research, 1992. **7**(11): p. 1281-1289.
105. Yamaguchi, T., et al., *Mouse Osteoblastic Cell Line (MC3T3-E1) Expresses Extracellular Calcium (Ca2+o)–Sensing Receptor and Its Agonists Stimulate Chemotaxis and Proliferation of MC3T3-E1 Cells.* Journal of Bone and Mineral Research, 1998. **13**(10): p. 1530-1538.
106. Beck, G.R., B. Zerler, and E. Moran, *Phosphate is a specific signal for induction of osteopontin gene expression.* Proceedings of the National Academy of Sciences, 2000. **97**(15): p. 8352-8357.
107. Sepulveda, P., J.R. Jones, and L.L. Hench, *Bioactive sol-gel foams for tissue repair.* Journal of Biomedical Materials Research, 2002. **59**(2): p. 340-348.
108. Jones, J.R., *Bioactive Glass as Synthetic Bone Grafts and Scaffolds for Tissue Engineering*, in *Bio-Glasses*. 2012, John Wiley & Sons, Ltd. p. 177-201.
109. Chen, Q.Z.Z., I.D. Thompson, and A.R. Boccaccini, *45S5 Bioglass (R)-derived glass-ceramic scaffolds for bone tissue engineering.* Biomaterials, 2006. **27**(11): p. 2414-2425.
110. Fu, Q., E. Saiz, and A.P. Tomsia, *Bioinspired Strong and Highly Porous Glass Scaffolds.* Advanced Functional Materials, 2011. **21**(6): p. 1058-1063.
111. Poologasundarampillai, G., et al., *Compressive Strength of Bioactive Sol–Gel Glass Foam Scaffolds.* International Journal of Applied Glass Science, 2016. **7**(2): p. 229-237.
112. Chen, Q.Z. and A.R. Boccaccini, *Poly(D,L-lactic acid) coated 45S5 Bioglass (R)-based scaffolds: Processing and characterization.* Journal of Biomedical Materials Research Part A, 2006. **77A**(3): p. 445-457.
113. Yang, J., et al., *Fabrication and surface modification of macroporous poly(L-lactic acid) and poly(L-lactic-co-glycolic acid) (70/30) cell scaffolds for human skin fibroblast cell culture.* Journal of Biomedical Materials Research, 2002. **62**(3): p. 438-446.
114. Lu, H.H., et al., *Three-dimensional, bioactive, biodegradable, polymer–bioactive glass composite scaffolds with improved mechanical properties support collagen synthesis and mineralization of human osteoblast-like cells in vitro.* Journal of Biomedical Materials Research Part A, 2003. **64A**(3): p. 465-474.
115. Rezwan, K., et al., *Biodegradable and bioactive porous polymer/inorganic composite scaffolds for bone tissue engineering.* Biomaterials, 2006. **27**(18): p. 3413-3431.
116. Blaker, J.J., et al., *Premature degradation of poly(alpha-hydroxyesters) during thermal processing of Bioglass (R)-containing composites.* Acta Biomaterialia, 2010. **6**(3): p. 756-762.
117. Shirosaki, Y., et al., *Inorganic-Organic Sol-Gel Hybrids*, in *Bio-Glasses*. 2012, John Wiley & Sons, Ltd. p. 139-158.
118. Niemela, T., et al., *Self-reinforced composites of bioabsorbable polymer and bioactive glass with different bloactive glass contents. Part 1: Initial mechanical properties and bioactivity.* Acta Biomaterialia, 2005. **1**(2): p. 235-242.
119. Valliant, E.M. and J.R. Jones, *Softening bioactive glass for bone regeneration: sol-gel hybrid materials.* Soft Matter, 2011. **7**(11): p. 5083-5095.
120. Novak, B.M., *Hybrid Nanocomposite Materials—between inorganic glasses and organic polymers.* Advanced Materials, 1993. **5**(6): p. 422-433.

121. Pereira, M.M., et al., *Preparation of bioactive glass-polyvinyl alcohol hybrid foams by the sol-gel method.* Journal of Materials Science-Materials in Medicine, 2005. **16**(11): p. 1045-1050.
122. Martin, A.I., A.J. Salinas, and M. Vallet-Regi, *Bioactive and degradable organic-inorganic hybrids.* Journal of the European Ceramic Society, 2005. **25**(16): p. 3533-3538.
123. Gomide, V.S., et al., *In vitro and in vivo osteogenic potential of bioactive glass-PVA hybrid scaffolds colonized by mesenchymal stem cells.* Biomedical Materials, 2012. **7**(1).
124. Services, N.P.C., C. Board of, and Engineers, *The complete book on water soluble polymers*. 2009, Delhi: Asia Pacific Business Press.
125. Yabuta, T., et al., *Synthesis of PDMS-based porous materials for biomedical applications.* Journal of Sol-Gel Science and Technology, 2003. **26**(1-3): p. 1219-1222.
126. Tsuru, K., et al., *Synthesis and in vitro behavior of organically modified silicate containing Ca ions.* Journal of Sol-Gel Science and Technology, 2001. **21**(1-2): p. 89-96.
127. Tsuru, K., S. Hayakawa, and A. Osaka, *Synthesis of bioactive and porous organic-inorganic hybrids for biomedical applications.* Journal of Sol-Gel Science and Technology, 2004. **32**(1-3): p. 201-205.
128. Chen, Q., et al., *Preparation of Bioactive PDMS-Modified CaO–SiO2–TiO2 Hybrids by the Sol-Gel Method.* Journal of Sol-Gel Science and Technology, 2000. **19**(1): p. 101-105.
129. Kickelbick, G., *The search of a homogeneously dispersed material—the art of handling the organic polymer/metal oxide interface.* Journal of Sol-Gel Science and Technology, 2008. **46**(3): p. 281-290.
130. Witucki, G.L., *A silane primer:chemistry and applications of alkoxy silanes.* Journal of Coatings Technology, 1992. **65**(822): p. 57-60.
131. Mahony, O., et al., *Silica-Gelatin Hybrids with Tailorable Degradation and Mechanical Properties for Tissue Regeneration.* Advanced Functional Materials, 2010. **20**(22): p. 3835-3845.
132. Guiver, M.D., et al., *SYNTHESIS AND CHARACTERIZATION OF CARBOXYLATED POLYSULFONES.* British Polymer Journal, 1990. **23**(1-2): p. 29-39.
133. Sun, H., et al., *Novel Ternary Molecular Composites Prepared by a Sol–Gel Process and Their Conversion into Microcellular Foams.* Journal of Macromolecular Science, Part A, 2004. **41**(9): p. 981-1000.
134. Hsu, Y.G. and F.J. Lin, *Organic–inorganic composite materials from acrylonitrile–butadiene–styrene copolymers (ABS) and silica through an in situ sol-gel process.* Journal of Applied Polymer Science, 2000. **75**(2): p. 275-283.
135. Helminen, A., H. Korhonen, and J.V. Seppälä, *Biodegradable crosslinked polymers based on triethoxysilane terminated polylactide oligomers.* Polymer, 2001. **42**(8): p. 3345-3353.
136. Hüsing, N., et al., *Formation and Structure of Porous Gel Networks from Si(OMe)4 in the Presence of A(CH2)nSi(OR)3 (A = Functional Group).* Chemistry of Materials, 1998. **10**(10): p. 3024-3032.
137. Hüsing, N., et al., *Formation and Structure of Gel Networks from Si(OEt)4/(MeO)3Si(CH2)3NR‘2 Mixtures (NR‘2 = NH2 or NHCH2CH2NH2).* Chemistry of Materials, 1999. **11**(2): p. 451-457.
138. Heinemann, S., et al., *A Novel Biomimetic Hybrid Material Made of Silicified Collagen: Perspectives for Bone Replacement.* Advanced Engineering Materials, 2007. **9**(12): p. 1061-1068.

139. Olsen, D., et al., *Recombinant collagen and gelatin for drug delivery.* Advanced Drug Delivery Reviews, 2003. **55**(12): p. 1547-1567.
140. van den Bosch, E. and C. Gielens, *Gelatin degradation at elevated temperature.* International Journal of Biological Macromolecules, 2003. **32**(3–5): p. 129-138.
141. Falini, G., et al., *Films of self-assembled purely helical type I collagen molecules.* Journal of Materials Chemistry, 2004. **14**(14): p. 2297-2302.
142. Ogunleye, A., et al., *Poly-γ-glutamic acid: production, properties and applications.* Microbiology, 2015. **161**(1): p. 1-17.
143. Sung, M.-H., et al., *Natural and edible biopolymer poly-γ-glutamic acid: synthesis, production, and applications.* The Chemical Record, 2005. **5**(6): p. 352-366.
144. Poologasundarampillai, G., et al., *Synthesis of bioactive class II poly(gamma-glutamic acid)/silica hybrids for bone regeneration.* Journal of Materials Chemistry, 2010. **20**(40): p. 8952-8961.
145. Valliant, E.M., et al., *Bioactivity in silica/poly(γ-glutamic acid) sol–gel hybrids through calcium chelation.* Acta Biomaterialia, 2013. **9**(8): p. 7662-7671.
146. Middleton, J.C. and A.J. Tipton, *Synthetic biodegradable polymers as orthopedic devices.* Biomaterials, 2000. **21**(23): p. 2335-2346.
147. Bergsma, J.E., et al., *Late degradation tissue response to poly(l-lactide) bone plates and screws.* Biomaterials, 1995. **16**(1): p. 25-31.
148. Rhee, S.-H. and S.J. Lee, *Effect of acidic degradation products of poly(lactic-co-glycolic)acid on the apatite-forming ability of poly(lactic-co-glycolic)acid-siloxane nanohybrid material.* Journal of Biomedical Materials Research Part A, 2007. **83A**(3): p. 799-805.
149. Woodruff, M.A. and D.W. Hutmacher, *The return of a forgotten polymer—Polycaprolactone in the 21st century.* Progress in Polymer Science, 2010. **35**(10): p. 1217-1256.
150. Rhee, S.H., J.Y. Choi, and H.M. Kim, *Preparation of a bioactive and degradable poly(epsilon-caprolactone)/silica hybrid through a sol-gel method.* Biomaterials, 2002. **23**(24): p. 4915-4921.
151. Rhee, S.-H., *Effect of molecular weight of poly(ε-caprolactone) on interpenetrating network structure, apatite-forming ability, and degradability of poly(ε-caprolactone)/silica nano-hybrid materials.* Biomaterials, 2003. **24**(10): p. 1721-1727.
152. Rhee, S.-H., *Bone-like apatite-forming ability and mechanical properties of poly(ε-caprolactone)/silica hybrid as a function of poly(ε-caprolactone) content.* Biomaterials, 2004. **25**(7–8): p. 1167-1175.
153. Song, S.-H., S.J. Lee, and S.-H. Rhee, *Synthesis of biodegradable poly(ε-caprolactone)-organosiloxane hybrid with carboxylate groups.* Journal of Biomedical Materials Research Part B: Applied Biomaterials, 2012. **100B**(5): p. 1289-1297.
154. Yoo, J.J. and S.-H. Rhee, *Evaluations of bioactivity and mechanical properties of poly (ε-caprolactone)/silica nanocomposite following heat treatment.* Journal of Biomedical Materials Research Part A, 2004. **68A**(3): p. 401-410.
155. Rhee, S.-H., *Effect of calcium salt content in the poly(ε-caprolactone)/silica nanocomposite on the nucleation and growth behavior of apatite layer.* Journal of Biomedical Materials Research Part A, 2003. **67A**(4): p. 1131-1138.
156. Tian, D., P. Dubois, and R. Jerome, *A new poly(ε-caprolactone) containing hybrid ceramer prepared by the sol-gel process.* Polymer, 1996. **37**(17): p. 3983-3987.
157. Tian, D., et al., *A Novel Biodegradable and Biocompatible Ceramer Prepared by the Sol−Gel Process.* Chemistry of Materials, 1997. **9**(4): p. 871-874.
158. Tian, D., P. Dubois, and R. Jérôme, *Biodegradable and biocompatible inorganic–organic hybrid materials. I. Synthesis and characterization.* Journal of Polymer Science Part A: Polymer Chemistry, 1997. **35**(11): p. 2295-2309.

159. Tian, D., et al., *Biodegradable and biocompatible inorganic-organic hybrid materials: 2. Dynamic mechanical properties, structure and morphology.* Polymer, 1998. **39**(4): p. 855-864.
160. Sun, H., et al., *The in vivo degradation, absorption and excretion of PCL-based implant.* Biomaterials, 2006. **27**(9): p. 1735-1740.
161. Pitt, C.G., et al., *Aliphatic polyesters. I. The degradation of poly(ϵ-caprolactone) in vivo.* Journal of Applied Polymer Science, 1981. **26**(11): p. 3779-3787.
162. Jenkins, M.J. and K.L. Harrison, *The effect of crystalline morphology on the degradation of polycaprolactone in a solution of phosphate buffer and lipase.* Polymers for Advanced Technologies, 2008. **19**(12): p. 1901-1906.
163. Jenkins, M.J. and K.L. Harrison, *The effect of molecular weight on the crystallization kinetics of polycaprolactone.* Polymers for Advanced Technologies, 2006. **17**(6): p. 474-478.
164. Shih, T.Y., et al., *Synthesis and Properties of Biodegradable Segmented Poly-epsilon-caprolactone.* Journal of Medical and Biological Engineering, 2014. **34**(3): p. 238-242.
165. Lam, C.X.F., et al., *Evaluation of polycaprolactone scaffold degradation for 6 months in vitro and in vivo.* Journal of Biomedical Materials Research Part A, 2009. **90A**(3): p. 906-919.
166. Woodward, S.C., et al., *The intracellular degradation of poly(ε-caprolactone).* Journal of Biomedical Materials Research, 1985. **19**(4): p. 437-444.
167. Pol, B.J.M., et al., *In vivo testing of crosslinked polyethers .1. Tissue reactions and biodegradation.* Journal of Biomedical Materials Research, 1996. **32**(3): p. 307-320.
168. Pol, B.J.M., et al., *In vivo testing of crosslinked polyethers .2. Weight loss, IR analysis, and swelling behavior after implantation.* Journal of Biomedical Materials Research, 1996. **32**(3): p. 321-331.
169. Anderson, J.M. and Q.H. Zhao, *Biostability of Biomedical Polymers.* MRS Bulletin, 1991. **16**(9): p. 75-77.
170. Tallia, F., *3-D printed flexible hybrids for tissue regeneration*. 2016, Imperial College London.
171. Allo, B.A., A.S. Rizkalla, and K. Mequanint, *Synthesis and Electrospinning of epsilon-Polycaprolactone-Bioactive Glass Hybrid Biomaterials via a Sol-Gel Process.* Langmuir, 2010. **26**(23): p. 18340-18348.
172. Pereira, M.M., A.E. Clark, and L.L. Hench, *CALCIUM-PHOSPHATE FORMATION ON SOL-GEL-DERIVED BIOACTIVE GLASSES IN-VITRO.* Journal of Biomedical Materials Research, 1994. **28**(6): p. 693-698.
173. Poologasundarampillai, G., et al., *Poly(gamma-glutamic acid)/Silica Hybrids with Calcium Incorporated in the Silica Network by Use of a Calcium Alkoxide Precursor.* Chemistry-a European Journal, 2014. **20**(26): p. 8149-8160.
174. Sing, K.S.W., et al., *REPORTING PHYSISORPTION DATA FOR GAS SOLID SYSTEMS WITH SPECIAL REFERENCE TO THE DETERMINATION OF SURFACE-AREA AND POROSITY (RECOMMENDATIONS 1984).* Pure and Applied Chemistry, 1985. **57**(4): p. 603-619.
175. Brunauer, S., P.H. Emmett, and E. Teller, *Adsorption of Gases in Multimolecular Layers.* Journal of the American Chemical Society, 1938. **60**(2): p. 309-319.
176. E, B.P., J.G. L, and H.p. P, *The determination of pore volume and area distributions in porous substances. I. Computations from nitrogen isotherms.* Journal of the American Chemical Society, 1951. **41**(780): p. 373.
177. Rouquerol, J., et al., *RECOMMENDATIONS FOR THE CHARACTERIZATION OF POROUS SOLIDS.* Pure and Applied Chemistry, 1994. **66**(8): p. 1739-1758.
178. Kokubo, T. and H. Takadama, *How useful is SBF in predicting in vivo bone bioactivity?* Biomaterials, 2006. **27**(15): p. 2907-2915.

179. Jones, J.R., P. Sepulveda, and L.L. Hench, *Dose-dependent behavior of bioactive glass dissolution.* Journal of Biomedical Materials Research, 2001. **58**(6): p. 720-726.
180. Maçon, A.L.B., et al., *A unified in vitro evaluation for apatite-forming ability of bioactive glasses and their variants.* Journal of Materials Science: Materials in Medicine, 2015. **26**(2): p. 1-10.
181. Thompson, M. and J.N. Walsh, *Handbook of inductively coupled plasma spectrometry*. 1989, Glasgow; New York: Blackie ; Chapman and Hall.
182. Rosenberg, H.M., *The solid state : an introduction to the physics of crystals for students of physics, materials science, and engineering*. 1978, Oxford: Clarendon Press.
183. Smith, B.C., *Fundamentals of Fourier transform infrared spectroscopy*. 1996, Boca Raton: CRC Press.
184. Reimer, L., *Scanning electron microscopy : physics of image formation and microanalysis*. 1985, Berlin; New York: Springer-Verlag.
185. Chescoe, D., P.J. Goodhew, and S. Royal Microscopical, *The operation of transmission and scanning electron microscopes*. 1990, Oxford; New York; Oxford: Oxford University Press ; Royal Microscopical Society.
186. Reimer, L., *Transmission electron microscopy : physics of image formation and microanalysis*. 1989, Berlin; New York: Springer-Verlag.
187. Abraham, R.J., et al., *Introduction to NMR spectroscopy*. 1988: Wiley.
188. Hore, P.J., *Nuclear magnetic resonance*. 1995, Oxford; New York: Oxford University Press.
189. Harris, R.K., et al., *NMR nomenclature: nuclear spin properties and conventions for chemical shifts. IUPAC Recommendations 2001. International Union of Pure and Applied Chemistry. Physical Chemistry Division. Commission on Molecular Structure and Spectroscopy.* Magnetic Resonance in Chemistry, 2002. **40**(7): p. 489-505.
190. Connell, L.S., et al., *Chemical characterisation and fabrication of chitosan-silica hybrid scaffolds with 3-glycidoxypropyl trimethoxysilane.* Journal of Materials Chemistry B, 2014. **2**(6): p. 668-680.
191. Hatakeyama, T. and F.X. Quinn, *Thermal analysis : fundamentals and applications to polymer science*. 1999, Chichester; New York: Wiley.
192. Brauer, D.S., M. Mneimne, and R.G. Hill, *Fluoride-containing bioactive glasses: Fluoride loss during melting and ion release in tris buffer solution.* Journal of Non-Crystalline Solids, 2011. **357**(18): p. 3328-3333.
193. Chrissanthopoulos, A., N. Bouropoulos, and S.N. Yannopoulos, *Vibrational spectroscopic and computational studies of sol-gel derived CaO-MgO-SiO2 binary and ternary bioactive glasses.* Vibrational Spectroscopy, 2008. **48**(1): p. 118-125.
194. Domine, F. and B. Piriou, *STUDY OF SODIUM-SILICATE MELT AND GLASS BY INFRARED REFLECTANCE SPECTROSCOPY.* Journal of Non-Crystalline Solids, 1983. **55**(1): p. 125-130.
195. Pryce, R.S. and L.L. Hench, *Tailoring of bioactive glasses for the release of nitric oxide as an osteogenic stimulus.* Journal of Materials Chemistry, 2004. **14**(14): p. 2303-2310.
196. Stolen, R.H. and G.E. Walrafen, *WATER AND ITS RELATION TO BROKEN BOND DEFECTS IN FUSED SILICA.* Journal of Chemical Physics, 1976. **64**(6): p. 2623-2631.
197. Melinte, G., et al., *Hydrogen peroxide versus water synthesis of bioglass–nanocrystalline hydroxyapatite composites.* Journal of Materials Science, 2011. **46**(23): p. 7393-7400.
198. Laczka, M., et al., *Gel-derived materials of a CaO-P2O5-SiO2 system modified by boron, sodium, magnesium, aluminum, and fluorine compounds.* Journal of Biomedical Materials Research, 2000. **52**(4): p. 601-612.

199. Lei, B., et al., *Synthesis and bioactive properties of macroporous nanoscale SiO2-CaO-P2O5 bioactive glass.* Journal of Non-Crystalline Solids, 2009. **355**(52-54): p. 2678-2681.
200. Balamurugan, A., et al., *Synthesis and characterisation of sol gel derived bioactive glass for biomedical applications.* Materials Letters, 2006. **60**(29-30): p. 3752-3757.
201. Sannigrahi, P. and E. Ingall, *Polyphosphates as a source of enhanced P fluxes in marine sediments overlain by anoxic waters: Evidence from (31)P NMR.* Geochemical Transactions, 2005. **6**(3): p. 52-52.
202. Rabadjieva, D., et al., *Biomimetic Modifications of Calcium Orthophosphates*, in *On Biomimetics*, D.L. Pramatarova, Editor. 2011, InTech.
203. Skipper, L.J., et al., *The structure of a bioactive calcia-silica sol-gel glass.* Journal of Materials Chemistry, 2005. **15**(24): p. 2369-2374.
204. Zhang, X., et al., *Structural characterization of sol–gel composites using TEOS/MEMO as precursors.* Surface and Coatings Technology, 2007. **201**(12): p. 6051-6058.
205. Lambert, J.B., *Introduction to Organic Spectroscopy*. 1987: Macmillan.
206. Zhang, J., et al., *Self-healable and recyclable triple-shape PPDO-PTMEG co-network constructed through thermoreversible Diels-Alder reaction.* Polymer Chemistry, 2012. **3**(6): p. 1390-1393.
207. Godinot, C., et al., *On the use of P-31 NMR for the quantification of hydrosoluble phosphorus-containing compounds in coral host tissues and cultured zooxanthellae.* Scientific Reports, 2016. **6**.
208. Lucio Anelli, P., et al., *Fast and selective oxidation of primary alcohols to aldehydes or to carboxylic acids and of secondary alcohols to ketones mediated by oxoammonium salts under two-phase conditions.* The Journal of Organic Chemistry, 1987. **52**(12): p. 2559-2562.
209. Tojo, G. and M. Fernández, *Oxidation of primary alcohols to carboxylic acids : a guide to current common practice*. 2007, New York: Springer.
210. Ch, *BS EN ISO 10993- 5: 2009 - Biological evaluation of medical devices. Tests for in vitro cytotoxicity*. Biologische Beurteilung von Medizinprodukten. Prüfungen auf In-vitro-Zytotoxizität. 2009.
211. Ch, *BS EN ISO 10993- 12: 2012 - Biological evaluation of medical devices. Sample preparation and reference materials*. Biologische Beurteilung von Medizinprodukten. Probenvorbereitung und Referenzmaterialien. 2012.
212. Cantournet, S., R. Desmorat, and J. Besson, *Mullins effect and cyclic stress softening of filled elastomers by internal sliding and friction thermodynamics model.* International Journal of Solids and Structures, 2009. **46**(11–12): p. 2255-2264.
213. Lakes, R.S., J.L. Katz, and S.S. Sternstein, *Viscoelastic properties of wet cortical bone—I. Torsional and biaxial studies.* Journal of Biomechanics, 1979. **12**(9): p. 657-675.
214. Wu, Z., T.C. Ovaert, and G.L. Niebur, *Viscoelastic properties of human cortical bone tissue depend on gender and elastic modulus.* Journal of Orthopaedic Research, 2012. **30**(5): p. 693-699.
215. Mano, J.F., *Viscoelastic properties of bone: Mechanical spectroscopy studies on a chicken model.* Materials Science and Engineering: C, 2005. **25**(2): p. 145-152.
216. Elzein, T., et al., *FTIR study of polycaprolactone chain organization at interfaces.* Journal of Colloid and Interface Science, 2004. **273**(2): p. 381-387.
217. Ganguly, A., et al., *The Role of Microtubules and Their Dynamics in Cell Migration.* The Journal of Biological Chemistry, 2012. **287**(52): p. 43359-43369.
218. Schlunck, G.n., et al., *Substrate Rigidity Modulates Cell–Matrix Interactions and Protein Expression in Human Trabecular Meshwork Cells.* Investigative Ophthalmology & Visual Science, 2008. **49**(1): p. 262-269.

219. Hulbert, S.F., S.J. Morrison, and J.J. Klawitter, *Tissue reaction to three ceramics of porous and non-porous structures.* Journal of Biomedical Materials Research, 1972. **6**(5): p. 347-374.